12-2021

Computational investigations of the photochemical properties of B12-dependent systems: from solution to enzymes.

Megan Toda Mackintosh
University of Louisville

COMPUTATIONAL INVESTIGATIONS OF THE PHOTOCHEMICAL PROPERTIES OF B_{12}-DEPENDENT SYSTEMS: FROM SOLUTION TO ENZYMES

By

Megan Joy Toda Mackintosh
B.S., Misericordia University, 2015
M.S. University of Louisville, 2019

A Dissertation
Submitted to the Faculty of the
College of Arts and Sciences of the University of Louisville
in Partial Fulfillment of the Requirements
for the Degree of

Doctor of Philosophy in Chemistry

Department of Chemistry
University of Louisville
Louisville, Kentucky

December 2021

COMPUTATIONAL INVESTIGATIONS OF THE PHOTOCHEMICAL PROPERTIES OF B_{12}-DEPENDENT SYSTEMS: FROM SOLUTION TO ENZYMES

By

Megan Joy Toda Mackintosh

A Dissertation Approved on

September 15, 2021

By the following Dissertation Committee:

_____

Dr. Pawel M. Kozlowski, Dissertation Chair

_____

Dr. Craig Grapperhaus, Committee member

_____

Dr. Lee Thompson, Committee member

_____

Dr. Robert Bert, Committee member

DEDICATION

So, whether you eat or drink, or whatever you do, do all to the glory of God.

This dissertation is dedicated to

my kind and loving parents, Mark and Ruth Toda,

and

my dear and loving husband and the family we've started;

Timothy,

you have given me a life full of light and laughter.

ACKNOWLEDGMENTS

…give thanks in all circumstances…thanks be to God for His inexpressible gift…

I wish to thank and acknowledge those people who have made this work possible, both professionally and personally.

To my PhD mentor, Dr. Pawel M. Kozlowski, thank you for your support, guidance, and encouragement. Especially for teaching me how to be a researcher who thinks critically and creatively. Thank you for your encouragement and support in my future endeavors.

To my group members past and present, Dr. Brady Garabato, Dr. Abdullah Al Mamun, Arghya Pratim Ghosh, and Saurav Parmar, thank you for your collaboration, friendship, and support.

To my dissertation committee, Dr. Craig Grapperhaus, Dr. Lee Thompson, and Dr. Robert Bert, thank you for your constructive and thoughtful feedback throughout my candidacy. Thank you especially to Dr. Grapperhaus, for your encouragement and support in my future endeavors.

To my undergraduate mentor, Dr. Anna Fedor, thank you for all your support and encouragement and for inspiring me to pursue a post-baccalaureate degree. Thank you for introducing me to computational chemistry.

To the National Science Foundation Research Experience for Undergraduates mentors at North Carolina State University, Dr. Elena Jakubikova, Dr. Elon Ison, Dr. Reza Ghiladi, Dr. Felix N. Castellano, and Dr. Catherine McCusker. Especially to Dr. Castellano who welcomed me into his research group and to Dr. McCusker who mentored me in the techniques of experimental photochemistry of inorganic systems.

To the doctors and therapists at the Frazier Rehabilitation Institute and Baptist Health, for helping me recover from serious illness during my graduate studies, I could not accomplish this task without you.

To my parents Mark and Ruth Toda, thank you for your lovingkindness and all that you have instilled in me. I will never be able to thank you and honor you enough for all that you have given me.

To my siblings, David, Brian, and Rachel, thank you for infusing my life with adventure, you are so dear to me.

To Mark and Connie Mackintosh, thank you for your love, support, and prayers.

To my late grandparents, especially to my dear grandma Kate, thank you for always seeing me. Oh how I wish to live a life as impactful as yours.

To my friends and mentors, Ted and Dawn Sandquist. Thank you for your kindness, prayers, and love on this journey. Thank you for your integral part bringing joy and healing to my life.

To my friends…Sue Boldrick, thank you for all of the love and care you've shown me. Melissa Sandquist, thank you for supporting me and loving me throughout this journey. The Moel's, time spent with you is a highlight of my Louisville life. Maevers – oh how I love you and all of our memories.

To my church family at In Christ Church and Ministries, Louisville, Kentucky for your love, prayers, and support on this journey.

Lastly, to my dear, sweet husband, Timothy Ira Mackintosh. You are a bright light, who inspires all around you. Thank you for your unending support, your steadfast love, and your incredible humor. Someday we will reminisce on these days with a family that's grown. What a beautiful life we live!!!

ABSTRACT

COMPUTATIONAL INVESTIGATIONS OF THE PHOTOCHEMICAL PROPERTIES OF B_{12}-DEPENDENT SYSTEMS: FROM SOLUTION TO ENZYMES

Megan Joy Toda Mackintosh

September 15, 2021

The photochemical properties of the B_{12} family of molecules (cobalamins = Cbls) have been known for many years yet only until the 21st century have applications for the light-sensitivity of Cbls come to the surface. Photolabile Cbls can be used for the delivery of therapeutics with spatial and temporal control, in the generation of hydroxyl radicals, and in nature, as demonstrated in the catalytic cycle of coenzyme B_{12}-dependent photoreceptors. This dissertation describes the use of computational methods to explore the photochemical properties of Cbl systems including antivitamins B_{12}, a thiolato-cobalamin, and the coenzyme B_{12}-dependent photoreceptor CarH.

Chapter 1 includes explanation of the light-sensitivity of B_{12} derivatives from both technical and historic standpoints. Descriptions of the structure and functions Cbls are included. The main target of Chapter 2 is to describe how experimental observations can inform theoretical investigations. The computational approach is also described.

Chapter 3 describes the photolytic properties of two synthetic antivitamins B_{12} including ethylphenylcobalamin (EtPhCbl) and phenylethynylcobalamin (PhEtyCbl). EtPhCbl is photoactive and excitation leads to a branching between internal conversion (IC) to the ground state and photodissociation. PhEtyCbl is remarkably photostable and IC is the major photophysical event with nearly unit quantum yield (QY). The photolytic properties of a thiolato-cobalamin, N-acetylcysteinylcobalamin (NACCbl) are described in Chapter 4. Photoexcitation of NACCbl leads to Co(II)/Ado• radical pair (RP) formation from the ligand field region of the S_1 potential energy surface (PES). A key difference in comparison to other photoactive Cbls is that the S_1 LF field region can be directly accessed via $S_2 \rightarrow S_1$ IC bypassing the involvement of the S_1 metal-to-ligand charge transfer (MLCT) minimum. Also unique to NACCbl is that the LF region contains two local minima from which RP formation can occur from.

Chapters 5-7 are devoted to the coenzyme B_{12}-dependent photoreceptor CarH. While coenzyme B_{12} (aka adenosylcobalamin = AdoCbl) is best known as a ubiquitous cofactor, in CarH, AdoCbl takes on a new function as a chromophore. In Chapter 5, the evidence for how CarH operates using light linstead of substrate binding in its catalytic cycle is presented. Chapter 6 focuses on the description of the electronic and photolytic properties of hydridocobalamin (HCbl) and explores its potential role as an intermediate in CarH. Chapter 7 is devoted to proposing a mechanism for how CarH uses light to form the photoproduct, 4′,5′-anhydroadenosine (anhAdo) using insights from Chapters 5 and 6 as well as comparisons to experimental works.

TABLE OF CONTENTS

LIST OF TABLES

LIST OF FIGURES

CHAPTER 1

INTRODUCTION

1.0 Light-Sensitivity of B_{12} Derivatives

Vitamin B_{12} and its family of derivatives, known as cobalamins (Cbls, Figure 1.1), are among the most complex organometallic naturally occurring compounds which are best known as critical bioinorganic cofactors for a variety of biological processes.[1-15] Cbls are a ubiquitous family of corrinoid metabolites which are the subject of an active area of multidisciplinary research as a result of their biological and medical relevance as well as their photolytic properties.[16, 17] Exciting applications for the light-sensing abilities of Cbls include the generation of hydroxyl (OH) radicals,[18] drug delivery,[16, 19, 20] antivitamins B_{12},[21] coenzyme B_{12}-dependent photoreceptors,[22, 23] and mimicking enzymatic catalysis.[24, 25] OH radicals can be generated *in situ* from the aerobic photolysis of hydroxocobalamin (HOCbl), and this can be used to study DNA structure and binding.[18] Cbls can also be synthetically altered to be used as scaffolds for the targeted release of therapeutics via light.[19, 20] Recently, two synthetic antivitamins B_{12}, namely 4-ethylphenylcobalamin (EtPhCbl) and phenylethynylcobalamin (PhEtyCbl), were developed and represent an interesting group of derivatives that can counteract the physiological effects of the biologically relevant forms of B_{12} by various types of inhibition.[26-31] EtPhCbl and PhEtyCbl also represent an important step toward the design of Cbl-based agents that would serve as scaffolds for therapeutic light-activated reagents. The photochemistry of

B_{12} goes beyond synthetic applications as nature harnessed the light sensitivity of B_{12} as exemplified by the activity of the transcription regulator CarH.[23, 32-37] This coenzyme B_{12} (AKA adenosylcobalamin = AdoCbl)-dependent enzyme is representative of an entirely new class of photoreceptors, whose existence has only recently been determined. There is also a debate in the field of B_{12} chemistry as to whether B_{12} photochemistry can be used to mimic or to elucidate details of native enzymatic catalysis. For instance, the enzymes ethanolamine ammonia-lyase (EAL) and glutamate mutase (GLM) represent two AdoCbl-dependent enzymes that were studied with advanced spectroscopic techniques in order to assess the photolytic properties of AdoCbl bound to enzymes with the hope that photochemical analyses will shed light on the native catalytic reactions.[25, 38-41] This hypothesis has been essentially refuted in a recent computational study of EAL.[24] Nevertheless, a connection of native catalysis to photochemistry of B_{12} derivatives is likely inevitable considering the discovery of B_{12}-dependent enzymes that use light instead of substrate binding for activation. The focus of this dissertation is the analysis of photolytic properties of Cbls that are representative examples of these synthetic and natural applications for the light-sensing abilities of various derivatives including antivitamins B_{12}, thiolato-Cbls (SCbls), and the photoreceptor CarH.

2.0 Properties of Cbls

2.1 Function

In their roles as cofactors, the biologically active Cbls catalyze several enzymatic reactions in both bacteria and mammals. Vitamin B_{12}, also called cyanocobalamin (CNCbl), is not biologically active itself but it is the precursor to the biologically active cofactors, namely methylcobalamin (MeCbl) and adenosylcobalamin (AdoCbl).[6] MeCbl is

involved in methyl transfer reactions in methyltransferases both in bacteria and mammals.[15, 42, 43] Among them, methionine synthase (MetH) is a very well-known MeCbl-dependent mammalian enzyme that has attracted attention due to its critical role in mammalian metabolism. This methyl transferase facilitates the conversion of homocysteine to methionine. Other well-studied methyltransferases include methanol:CoM (MtaBCA) and corrinoid-iron/sulfur protein methyltransferase (CFeSP).[15, 42, 43] On the other hand, the AdoCbl cofactor catalyzes complex molecular transformations through radical chemistry.[38, 44-52] AdoCbl-dependent enzymes are typically involved in carbon skeletal rearrangement, heteroatom elimination, and intermolecular amino group migration.[6, 38] Examples of AdoCbl-dependent enzymes found in bacteria include GLM,[53-59] diol dehydratase (DDH),[12, 46] and EAL.[52, 60] Methylmalonyl-CoA mutase (MCM) is among the most thoroughly investigated AdoCbl-dependent enzymes.[15, 42, 43]

2.2 Structure

Cbls contain over one hundred eighty atoms.[3] There are certain features of these compounds that remain constant across the entire family of derivatives. All B_{12} derivatives contain a corrin macrocycle with a central cobalt (Co) ion that is equatorially ligated to four nitrogens of the corrin ring. There are several side chains attached to the corrin ring that include methyl, acetamide, and propionamide groups. In the Co(III) form, the metal center is axially ligated to an upper and lower ligand. The lower ligand is a dimethylbenzimidazole (DBI) base in what is known as the base-on form. The upper axial ligand is variable and can be used to distinguish cobalamins from each other. For the case of CNCbl, the upper ligand is a cyano group (CN). There are several other upper axial ligands that are known to occur naturally as well as various synthetic derivatives. For

MeCbl the upper ligand is a methyl (Me) group and for AdoCbl the upper axial ligand is 5′-deoxy-5′-adenosyl (Ado).

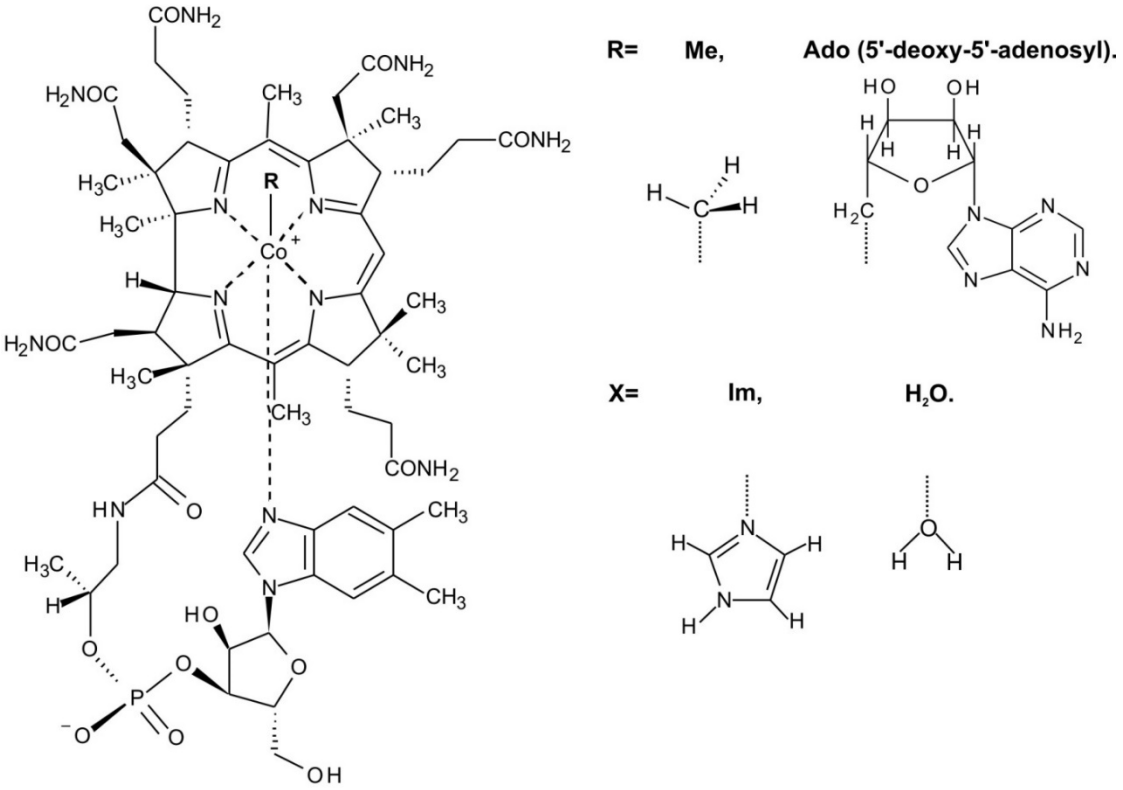

Figure 1.1. Left: General molecular structure of Cbls. Right: Molecular structure of upper axial ligands for methylcobalamin (R=Me) and adenosylcobalamin (R=Ado). Molecular structure of lower axial ligands for base-on (X=Im) and base-off (X=H2O).

The binding of the axial base is an important characteristic to discuss as Co(III)-based Cbls can either exist in the base-on or base-off forms. Of particular relevance to this dissertation is, the binding mode of the axial base affects the photolytic properties of Cbls.[1] In solution, the attachment of the axial base (DBI) can be modulated by pH. So, in highly acidic environments such as pH 2, the axial base will be detached when the DBI is protonated. The Co will remain Co(III) by becoming weakly coordinated to a water molecule, thus adopting the base-off form. Alternatively, the lower ligand may be water or

can be a histidine (His) residue in certain enzymatic environments. In cases where the axial base becomes detached in an enzyme, a His residue will coordinate to the Co on the lower face. This is known as the base-off/His-on form, and the Co will coordinate to the δ nitrogen of the His. In the base-on form, whether in solution or in an enzyme, the Co will coordinate to the nitrogen of the benzimidazole ring.

2.3 Electronic Structure

Cbls typically exist as low spin octahedral Co(III) complexes with d^6 electronic configuration of Co. The splitting of Co d orbitals is more in line with axially perturbed square planar geometry, with local D4h symmetry. The equatorial corrin ligand resembles the porphyrin macrocycle, while the upper and lower positions can be occupied by a variety of different ligands. Although Cbls tend to exist in the Co(III) form, other coordination environments are important to highlight. These other low oxidation states include the Co(II) and Co(I) species, which have roles in the context of enzymatic catalysis and in various photochemical reactions. The Co(II) form, where paramagnetic Co center has d^7 electronic configuration, is produced by one-electron reduction of Co(III)Cbls and is a five-coordinate species. It can be also generated upon homolytic cleavage of the Co-C bond, thus forming Co(II)Cbl. Co(II)Cbl is a common intermediate formed in enzymatic reactions catalyzed by coenzyme B_{12} (aka AdoCbl). In all AdoCbl-dependent enzymes, the presence of Co(II) can be detected via electron paramagnetic resonance (EPR) spectroscopy. Alternatively, Co(II)-based species can also be generated photochemically when the Co-C bond is cleaved with light. Regardless of environment, solution versus enzyme, homolytic cleavage of the Co-C bond will lead to a radical pair (RP) formation. One-electron reduction of a Co(II)Cbl leads to a low-spin Co(I) compound, which has

complex electronic structure involving mixture of Co(d^8) and Co(d^7)/corrin($\pi*$)[1] configurations. The four-coordinate Co(I) form is known as the super-reduced form of vitamin B_{12} and has also been deemed a super-nucleophile due to its high reactivity. Heterolytic cleavage of the Co-C bond in MeCbl-dependent enzymes leads to a Co(I) species. The resulting Co(I)Cbl plays key mechanistic roles in B_{12}-dependent methyltransferases such as MetH.

3.0 B_{12} Historical Significance

The field of B_{12} chemistry is diverse and has a long and rich history. The discovery of vitamin B_{12}, the elucidation of its role in metabolism, structural characterization, total synthesis, as well as the discovery of B_{12}-dependent enzymes occurred over the course of more than 100 years. It was the subject of two separate Nobel Prizes. Vitamin B_{12} was discovered in 1926 by Georg R. Minot and William P. Murphy.[61] In 1934, both scientists, as well as George Whipple, won a Nobel Prize for their work in the treatment of pernicious anemia.[62] Vitamin B_{12} was not officially isolated until 1948.[63-67] The vitamin was crystallized and characterized in the laboratory of Dorothy Hodgkin in 1954-1955.[68-70] Her contributions to X-ray crystallography, through the determination of the structures of important biochemical substances, including vitamin B_{12}, were recognized when she was awarded the Nobel Prize in chemistry in 1964.[71, 72]

Beyond the enzymatic roles of Cbls, it has also been known for nearly five decades that the Co-C bond is light-sensitive.[73-77] Originally, the photo-reactivity was viewed as an unwanted side-reaction.[77] Nonetheless, this attribute has intrigued researchers since its original discovery and the photolytic properties of B_{12} derivatives have been scrutinized for decades. Barker, *et al*. first reported the light sensitivity of Cbls in 1958.[77] This was

discovered based on the studies of a coenzyme isolated from a pseudovitamin B_{12}. The absorption (Abs) spectrum of this coenzyme was obtained with visible light irradiation from a tungsten lamp. In the subsequent papers in 1960, Barker, *et al*.[78, 79] reported a more detailed study of the photochemical cleavage and photolysis products were observed. Later on, Johnson, Hogenkamp, Schrauzer and others identified the photolysis product of coenzyme B_{12}.[80-86] It was also shown that the fate of photolysis also depends on the presence of O_2. There is a difference in the photolysis products based on the presence and absence of O_2.[83]

Since these important contributions, photochemistry of Cbls has continued to gain interest among the scientific community. In the 1960s, Dolphin and co-workers studied the photochemical reactions of alkylCbls including MeCbl.[87] The photochemical properties of non-alkylCbls were also studied by Pratt, *et al*. in 1964.[74] The photochemical reactions of aquacobalamin (H_2OCbl^+), CNCbl, HOCbl, MeCbl were studied and it was shown that non-alkylCbls were insensitive to light (i.e. are photostable).[74] One of the first theoretical efforts to study the optical properties and the electronic structure of vitamin B_{12} derivatives was conducted by Day in 1967 with the use of Huckel and Pariser-Parr-Pople methods.[88] The major outcome of this study was the quantitative explanation of the Abs bands (α, γ, δ) for different types of Cbls. In the 1970s, using self-consistent HMO method, a theoretical study of the photochemistry of Cbls was conducted by Schrauzer, *et al*.[86] It was shown that photolysis of the Co-C bond is induced by charge transfer (CT) from a bonding axial molecular orbital to the antibonding axial orbital. Furthermore, the photo-resistivity of Cbls seems to increase by increasing the energy of the Co-C CT transition.

With the advancement of laser spectroscopic techniques such as ultrafast transient absorption spectroscopy (TAS), the photochemistry of Cbls continued to gain interest in the 1990's. Simultaneously the magnetic field effect (MFE) of Cbls became an important research area in B_{12} chemistry. In the early 1990s, Chen and Chance published a series of studies which were the first examples of using modern spectroscopic techniques including nanosecond TAS to elucidate the photodissociation mechanisms of Cbls.[89, 90] The quantum yield (QY or Φ) of photolysis was reported for the nanosecond time scale. The difference in photochemistry based on the binding mode (base-on versus base-off) was also reported. Another important contribution from this work was a proposed scheme representative of the mechanism of the photophysical and photochemical process. Since the mid-90s and into the twenty-first century, Sension and co-workers used ultrafast TAS to study the photochemical and photophysical properties of Cbls in solution[30, 91-101] as well as in coenzyme B_{12}-dependent enzymes.[37, 40, 41, 102, 103] Several other researchers including Warncke and co-workers,[25, 104-106] Scrutton and co-workers,[107-109] and Jones and coworkers[17, 34] used various spectroscopic techniques to investigate the photolytic properties of Cbl-dependent enzymes.

Interest in Cbl photochemistry has not waned in the 21st century and today, there are several examples where the light sensitivity of Cbls is harnessed including, OH radical generation and drug-delivery.[18-20] Recently, an AdoCbl-dependent photoreceptor, called CarH, was discovered and the crystal structures for various intermediates of its catalytic cycle were resolved.[23, 32, 33, 35, 36] CarH regulates the transcription of DNA, which results in the synthesis of carotenoids in certain bacteria.[33] A crucial step in this catalytic cycle is the cleavage of the Co-C bond via light. It is the first known example of a naturally occurring

physiological role for light in B_{12} systems.[17, 23, 32, 34, 35] What was once considered a nuisance, has now opened an entirely new area of research, B_{12} photoreceptors.[23] With these applications in mind, molecular level understanding is crucial. In short, this dissertation is aimed at using computational techniques to study the photolytic properties of various Cbls with these important applications in mind.

4.0 Dissertation Structure and Research Targets

Chapter 2

Emphasis is given to the computational approach for studying the photolytic properties of Cbls. The photolytic properties of MeCbl and AdoCbl will be highlighted as representative systems.[*]

Chapter 3

The research target is to determine the properties which are indicative of photolability and, conversely, photostability in antivitamins B_{12}. Comparisons to experimental work included.[†]

---

[*] Toda, M. J., Lodowski, P., Mamun, A. A., Jaworska, M., Kozlowski, P. M. Photolytic Properties of the Biologically Active Forms of Vitamin B_{12}. *Coord. Chem. Rev.* 2019, 385, 20-43. *and* Toda, M. J., Kozlowski, P. M., Andruniow, T. Assessing Electronically Excited States of Cobalamins via Absorption Spectroscopy and Time-Dependent Density Functional Theory. In book: *Transition Metals in Coordination Environments: Computational Chemistry and Catalysis Viewpoints*. Springer. **2019**, Chapter 8, Pages 219-258. DOI: 10.1007/978-3-030-11714-6_8.

[†] Lodowski, P., Toda, M. J., Ciura, K., Jaworska, M., Kozlowski, P. M. Photolytic Properties of Antivitamins B_{12}. *Inorg. Chem.* **2018**, 57, 7838-7850. *and* Lodowski, P., Ciura, K., Toda, M. J., Jaworska, M., Kozlowski, P. M. Photodissociation of Ethylphenylcobalamin Antivitamin B_{12}. *Phys. Chem. Chem. Phys.* **2017**, 19, 30310-30315.

Chapter 4

The research target is to determine the mechanism of photo-induced radical pair formation in a non-alkylCbl with a Co-S bond to the upper ligand. Comparisons to experimental works included.[‡]

Chapter 5

The research target is to determine why the Co-C bond of AdoCbl in photoreceptor CarH is activated by light instead of substrate binding in the initiation of the catalytic cycle. Comparisons to experiment and to the photolytic properties of other AdoCbl-dependent enzymes, GLM and EAL, included.[§]

Chapter 6

The research target is to analyze the electronic and photolytic properties of hydridocobalamin (HCbl). Main aim is to determine whether a proton, hydrogen, or hydride binds as the upper ligand. Formation of HCbl in CarH is also explored via quantum mechanics/molecular mechanics (QM/MM) calculations. Comparisons to experiment included.[**]

[‡]Toda, M. J., Lodowski, P., Thurman, T. M., Kozlowski, P. M. Light Mediated Properties of a Thiolato-derivative of Vitamin B_{12}. *Inorg. Chem.* **2020**, 59, 17200-17212.

[§]Toda, M. J., Mamun, A. A., Lodowski, P. Kozlowski, P. M. Why is CarH Photolytically Active in Comparison to other B_{12}-dependent Enzymes? *J. Photochem. Photobiol. B: Biol.* **2020**, 111919. *and* Mamun, A. A., Toda, M. J., Lodowski, P., Kozlowski, P. M. Photolytic Cleavage of Co-C Bond in Coenzyme B_{12}-Dependent Glutamate Mutase. *J. Phys. Chem. B* **2019**, 12, 2585-2598. *and* Mamun, A. A., Toda, M. J., Lodowski, P., Jaworska, M., Kozlowski, P. M. Mechanism of Light Induced Radical Pair Formation in Coenzyme B_{12} Dependent Ethanolamine Ammonia-Lyase. *ACS Catal*. **2018**, 8, 7164-7178.

[**]Toda, M. J., Lodowski, P., Mamun, A. A., Kozlowski, P. M. Electronic and Photolytic Properties of Hydridocobalamin. *J. Photochem. Photobio. B* **2021**, https://doi.org/10.1016/j.jphotobiol.2021.112295.

Chapter 7

The research target is to propose a mechanism of action for photoproduct formation in CarH. Emphasis is placed on determining whether HCbl can be formed in concert with 4′,5′-anhydroadenosine (anhAdo).[††]

[††]Toda, M. J., Lodowski, P., Mamun, A. A., Kozlowski, P. M. Exploring the Mechanisms of Action of Photoreceptor CarH. *ACS Catal.* **2021**, *submitted.*

CHAPTER 2

COMPUTATIONAL APPROACH

1.0 Introduction

Cbls exhibit complex photolytic properties based on a variety of different factors. Upon illumination with light, the upper ligand can be dispelled from the Cbl scaffold. The major target of recent computational studies is to determine the mechanism of photodissociation of the upper ligand. The main focus of this chapter is to highlight the theoretical protocol for elucidating photoreaction mechanisms and to provide insights into experimental data. Computational modeling of photolytic properties of Cbls should take into account observations from experimental studies including photostability versus photolability, wavelength dependence, the influence of environment, the divergent photochemistry of the base-on/base-off forms, MFEs, and the influence of oxygen. These subtopics are key foundational points to the research work outlined throughout this dissertation and are summarized here.

2.0 Experimental Observations

2.1 Photolability versus Photostability

It is generally accepted, with some exceptions, that nonalkylCbls are typically photostable while alkylCbls such as MeCbl and AdoCbl are photoactive (also called photolabile).[103, 110] Figure 2.1 shows schemes of photoreaction mechanisms for the base-

on and base-off forms of MeCbl and AdoCbl as well as the non-alkylCbl, CNCbl. These observations have been known for a long time but can be further understood based on modern spectroscopic investigations, particularly from Sension and co-workers.[91-95] Generally speaking, the electronic excitation of non-alkylCbls results in a series of internal conversion (IC) processes to the S_1 state that finally result in nonradiative decay to the ground state.[100] Non-alkylCbls are considered photostable because there is little to no photoproduct formation as evidenced by TAS studies of CNCbl, H_2OCbl^+, HOCbl, and N_3Cbl.[100, 101, 111] Some exceptions involve HOCbl,[101, 111] antivitamins B12[30, 31, 112, 113] (Chapter 3), and thiolato-Cbls (SCbls)[19, 114, 115] (Chapter 4). In particular, two synthetic antivitamins B_{12}, PhEtyCbl and EtPhCbl, were analyzed for their spectroscopic properties.[30] PhEtyCbl is photostable while EtPhCbl, a conditional antivitamin B_{12}, is photochemically active but has a very low yield of photoproducts.

AlkylCbls are considered photolabile because electronic excitation leads to cleavage of the Co-C bond which occurs from the S_1 state.[89-92, 96] Prior to this, electronic excitation cascades through various states until reaching the S_1 state (Figure 2.1). In the terminal phase of the photoreaction, RPs are generated from the S_1 state. Photoproducts in the form of alkyl radicals can either escape the solvent cage or can recombine and this would result in the return to the ground state. The explanation for the differences between the photo-induced characteristics of alkylCbls versus non-alkylCbls is apparent based on inspection of the S_0 and S_1 PESs as a function of axial bond lengths.[110] For alkylCbls, including MeCbl and AdoCbl, the S_0 and S_1 PESs are clearly separated by an energy gap.[110, 116-119] For the non-alkylCbls, such as HOCbl and CNCbl, the energy gap between the S_0 and S_1 surfaces is especially small at longer bond distances.[101, 120] As a result, IC to

the ground state is preferred over the photolysis of the upper axial bond in non-alkylCbls (Figure 2.1).

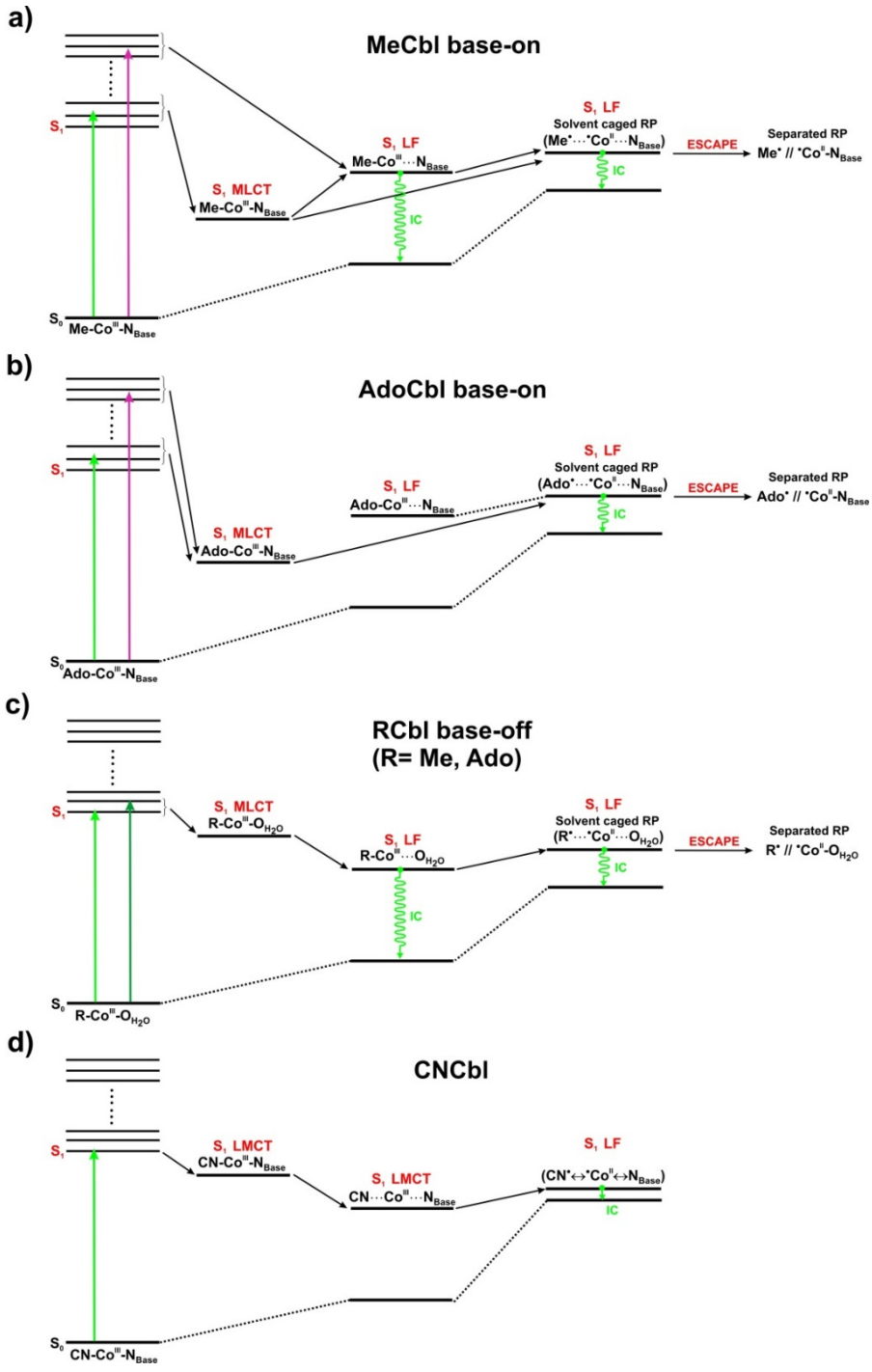

Figure 2.1. Schemes of photoreaction mechanism for **(a)** base-on form of methylcobalamin, MeCbl base-on, **(b)** base-on form of adenosylcobalamin, AdoCbl base-on **(c)** base-off form of alkylcobalamin, RCbl base-off, R=Me, Ado **(d)** non-alkyl cobalamin – cyanocobalamin, CNCbl.

2.2 Wavelength Dependence

The photolysis of MeCbl is wavelength dependent while the photolysis of AdoCbl is wavelength independent.[92, 93] As the photolysis of MeCbl is wavelength dependent, the QY is also wavelength dependent.[93] In other words, for MeCbl, the photolytic properties are different based on excitation wavelength. More specifically, there is a branching between bond scission and IC when MeCbl is excited at 400 nm. The photoproducts from bond homolysis include Co(II)/Me• RP as well as some metastable species consistent with Co(III)Cbl. At 520 nm excitation, Co-C bond cleavage is observed but the mechanism of the photoreaction is different than at 400 nm. Upon excitation with 520 nm, only the formation of the metastable product is observed, without prompt photolysis, which again branches between Co-C bond photolysis (14%) and reversion to the ground state. The photolysis of AdoCbl is wavelength independent because excitation at either 400 or 520 nm for AdoCbl results in Co-C bond cleavage on the picosecond timescale, with a QY of nearly one.

2.3 Influence of Environment

While photolysis occurs at either wavelength for AdoCbl, there is an additional observation from these studies that is worthy of note, namely that the environment effects the nature of the S_1 state for AdoCbl.[94, 103, 121] This is evidenced by the comparison between the absorption spectrum of the S_1 state of AdoCbl in ethylene glycol and of AdoCbl in water.[94] The ligand field (LF) state of the S_1 PES is stabilized in water in comparison to ethylene glycol. For the spectrum in the more viscous ethylene glycol, the S_1 state looks very similar to the non-alkylCbls. For AdoCbl in water, IC from an upper excited state to the S_1 state is observed and there is a blue shift in the absorption spectrum. This likely

indicates a lengthening of the lower axial Co-N bond or perhaps even a momentary dissociation of the axial base. In addition to the differences observed in the S_1 state of AdoCbl based on different solvents, the protein environment also affects the S_1 state. Inside enzymes, the mechanism of photolytic cleavage occurs in a fashion that is not significantly different than the isolated cofactor but there are some differences in terms of energetics.[40, 41, 102, 103] This is apparent based on TAS measurements and computatiaonal studies of AdoCbl-dependent GLM.[40, 41, 122] The spectrum of the S_1 state of AdoCbl bound to GLM is quite similar to other alkylCbls including MeCbl, EtCbl, and n-propylcobalamin (PrCbl).[95]

2.4 Base-on versus Base-off

There are divergent characteristics of the S_1 state when comparing the base-on alkylCbls to the base-off forms. An ultrafast TAS study that included the base-off derivatives of three Cbl species including AdoCbl, MeCbl, and PrCbl displays this.[99] For the base-off analogues, it was shown that there is an active channel for fast nonradiative decay to the ground state via IC when the axial base is displaced. This controls the photolysis yield. So, for the base-off forms there is a competition between IC and photolysis. This is traditionally not the case for the base-on alkylCbls. Rather, the photolysis yield for alkylCbls is controlled by the competition between geminate recombination and cage escape, with both photo-physical events occurring after photolysis. As an example, the photolysis of base-on AdoCbl results in a QY for bond homolysis of essentially one whereas in the base-off analogue this value is approximately 0.12.[92] The changes in the electronic structure between the base-on and base-off forms is attributed to being responsible for these differences in the S_1 state.[1]

The details related to the different photolytic properties of the biologically active forms of Cbls are key foundational points to the research work outlined throughout this dissertation. The biologically active forms of Cbls, both in their base-on and base-off forms have been extensively studied both experimentally[91-95] and computationally.[110, 116-119, 123-126] In sum, MeCbl and AdoCbl, are photoactive in comparison to the non-alkylCbls.[17, 102, 103, 110] While it is true that the biologically active forms are photolabile, there are differences concerning the photolytic properties including the mechanism of photodissociation, deactivation, QY, and wavelength dependence. Interestingly, the S_1 PESs that describe the mechanism of photodissociation for the base-off analogues of MeCbl and AdoCbl are very similar.[110]

2.5 Magnetic Field Effects

The MFE of photolysis of MeCbl and AdoCbl was initially reported by Grissom and co-workers in 1990s.[127-130] It was shown that photolytic cleavage of the Co-C bond varies with the magnitude of the magnetic field. In addition, the QY of RP generation decreases with certain magnitudes of the magnetic field. MFEs in Cbl systems has been a contested topic in the literature. MFE of the photolysis of AdoCbl in solution was studied by Chagovetz and Grissom.[128] There was a magnetic dependence observed for the photolysis of the Co-C bond of isolated AdoCbl in glycerol but no MFE was observed in water. The MFE in enzymes was first reported by Harkins and Grissom in 1994 for EAL, an AdoCbl-dependent enzyme found in bacteria.[129] It was suggested that this was caused by a magnetic field-induced change in the rate of intersystem crossing (ISC) between the singlet and triplet spin states of the Co(II)/Ado• RP. The issue of MFEs in EAL was reinvestigated in 2007 by Scrutton and co-workers who called MFEs into question and

reported much more in-depth analyses of MFE in both Cbls in solution and protein-bound alkylCbls.[107, 109, 131, 132] Stopped flow (pre-steady-state) studies were used and it was found that in the presence of substrate, Co-C bond homolysis in EAL is insensitive to the magnetic field. More recently, MFEs in AdoCbl-dependent lysine 5,6-aminomutase (LAM) was studied by Chen and Ke.[133] It was observed that the catalytic efficiency of LAM decreased upon the application of a magnetic field. While MFE studies of AdoCbl in solution and enzymes provided evidence related to catalytic processes there is still a need for computational studies to fully understand magnetic effects.

2.6 Influence of Oxygen

Anaerobic and aerobic conditions also play an important role in Cbl chemistry. Consider the photolysis of free AdoCbl in solution as an example. The photolysis product of AdoCbl in the presence of O_2 is adenosine-5′-aldehyde.[83] This reaction was revisited in 2007 by Frey and co-workers.[134] They found that 5′-peroxyadenosine is the initial product of the AdoCbl photolysis reaction in O_2 and there is a decomposition to the adenosine-5′-aldehyde product. On the other hand, in anaerobic conditions, the main photoproducts are Co(II)-Cbl and 5′-deoxy-5′,8-cycloadenosine. The reaction in aerobic conditions requires the insertion of O_2 between the Co and the upper axial ligand to form the peroxy intermediate. Insights from calculations are still required to understand all details of this mechanism. However, based on present information it can be summarized as follows. Upon excitation of AdoCbl, formation of the Co(II)/Ado• RP occurs. In the aerobic environment, the 5′-peroxy-adenosylcobalamin intermediate is formed via O_2 insertion. This first hydrolyses to 5′-peroxyadenosine and HOCbl and then the peroxyalkyl irreversibly

decomposes to adenosine-5′-aldehyde. Anaerobic versus aerobic conditions come into play in the mechanism of action of photoreceptor of CarH. This will be discussed in Chapter 7.

The wealth of experimental data from the aforementioned research groups provided the appropriate references for the theoretical studies which are summarized throughout this dissertation.[112, 113, 115, 135, 136] A driving force for the use of calculations is providing a molecular level understanding of the geometric and electronic properties that contribute to Cbl photolytic properties. Due to the size and complexity of Cbls, density functional theory (DFT)[137] and time-dependent DFT (TD-DFT)[138] became the method of choice for these systems.[119, 139-144] Potential energy surfaces (PESs) generated by DFT for the ground state (S_0) and TD-DFT for the low-lying electronically excited states (S_1, S_2, . . .) are reliable tools for understanding the mechanism of photodissociation of Cbls.[1, 101, 110-113, 115-120, 123-126, 139, 145-149]

3.0 Use of DFT and TD-DFT

The ground- and excited-state properties of Cbls can be represented well by using DFT and TD-DFT methods, respectively. Although wave function-based methods can be more accurate for certain systems, they are simply far too expensive to apply to molecules as large as Cbls. Benchmark studies have shown that high-level calculations such as complete active space self-consistent field (CASSCF)[150] combined with CASSCF-based complete active space second-order perturbation theory (CASPT2)[151, 152] are far too expensive because the appropriate active space for Cbls would be enormous.[139, 148] Alternatively, DFT is a method not based on the wave function but is based on inhomogeneous electron gas, typically referred to as electron density.[153] DFT efficiently scales with system size and is applicable to large systems. TD-DFT can be viewed as an

extension of DFT but is used to study properties related to time-dependent potentials. Analogous to the Hohenberg–Kohn theorem in DFT is the Runge–Gross theorem in TD-DFT.[138] In TD-DFT, the many-body time-dependent Schrodinger equation is replaced with a set of time-dependent single-particle equations.[154]

TD-DFT has become a widely used tool to study the electronically excited states of complex systems, including Cbls. Vertical excitation energies and transition dipole moments at a particular geometry can be calculated using TD-DFT. Excitation energies tend to agree with experiment within 0.3 eV, but typically calculated excitation energies require a shift to the red to yield much better agreement with experiment.[155] With that said, the proper description of electronically excited states within the TD-DFT framework is dependent on functional choice. A common practice is to rely on benchmark studies to determine the most appropriate functional to use for a particular system. There have been several studies that sought to determine the proper functionals to use for both ground- and excited-state properties of Cbls, and these will be discussed in this chapter.

3.1 Theoretical Benchmarks

3.1.1 Co-C Bond Strength

There are several challenges to overcome when studying Cbls computationally, including the system size and the presence of a transition metal. The former can be resolved by using a truncated cofactor in simulations (Figure 2.2). This typically involves replacing all side chains with hydrogens, replacing the lower axial DBI base with a much simpler imidazole (Im) ligand, while maintaining the structural integrity of the upper axial ligand. These truncated models have less than 70 atoms and provide a good agreement with relevant known structural details from high-quality crystal structures. In fact, there is very

little difference in computed bond dissociation energies (BDEs) whether the full cofactor or truncated model is used in calculations.[143]

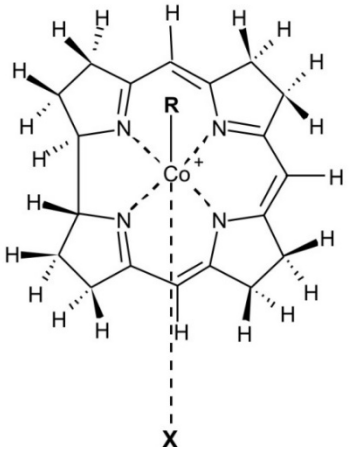

Figure 2.2. General form of truncated model used in calculations.

As far as determining the proper functional to use within the DFT framework to study Cbls, one must rely on benchmark calculations. With access to over three hundred density functionals, it is not automatically apparent which functional is appropriate to study a particular system, including Cbls. The key parameter that is targeted for benchmark studies, in addition to comparison with relevant crystal structures, is the BDE of the Co-C bond. Reproducing this energy (Table 2.1) accurately is a key standard for evaluating whether a particular theoretical method or density functional, in the case of DFT, is suitable to analyze these complex bioinorganic systems. In order to draw meaningful conclusions in studies where understanding various aspects of catalysis or photochemistry of Cbls are the target, only functionals that can determine the strength of the Co-C bond accurately should be considered. Table 2.1 collects the experimentally computed BDE for MeCbl and AdoCbl. Recalling from the Introduction, the cleavage of the Co-C bond is the key step in

Table 2.1. Experimental values of Co-C BDEs (kcal/mol) in selected Cbls.

Cobalamin	BDE	Experimental Method
MeCbl	37 ± 3	Thermolysis[156, 157]
MeCbl	36 ± 4	Calorimetry[158]
AdoCbl	31.5 ± 1.3	Thermolysis[159, 160]
AdoCbl	30.9 ± 4.1	Calorimetry[161]

reactions catalyzed by the biologically active forms of B_{12}. Additionally, the photo-cleavage of the Co-C bond is the key step in photolytic mechanisms. A number of thorough benchmark studies report computational estimations for the dissociation of the Co-C bond in Cbls.[140, 144, 162-164] The major conclusion of these studies is that hybrid functionals

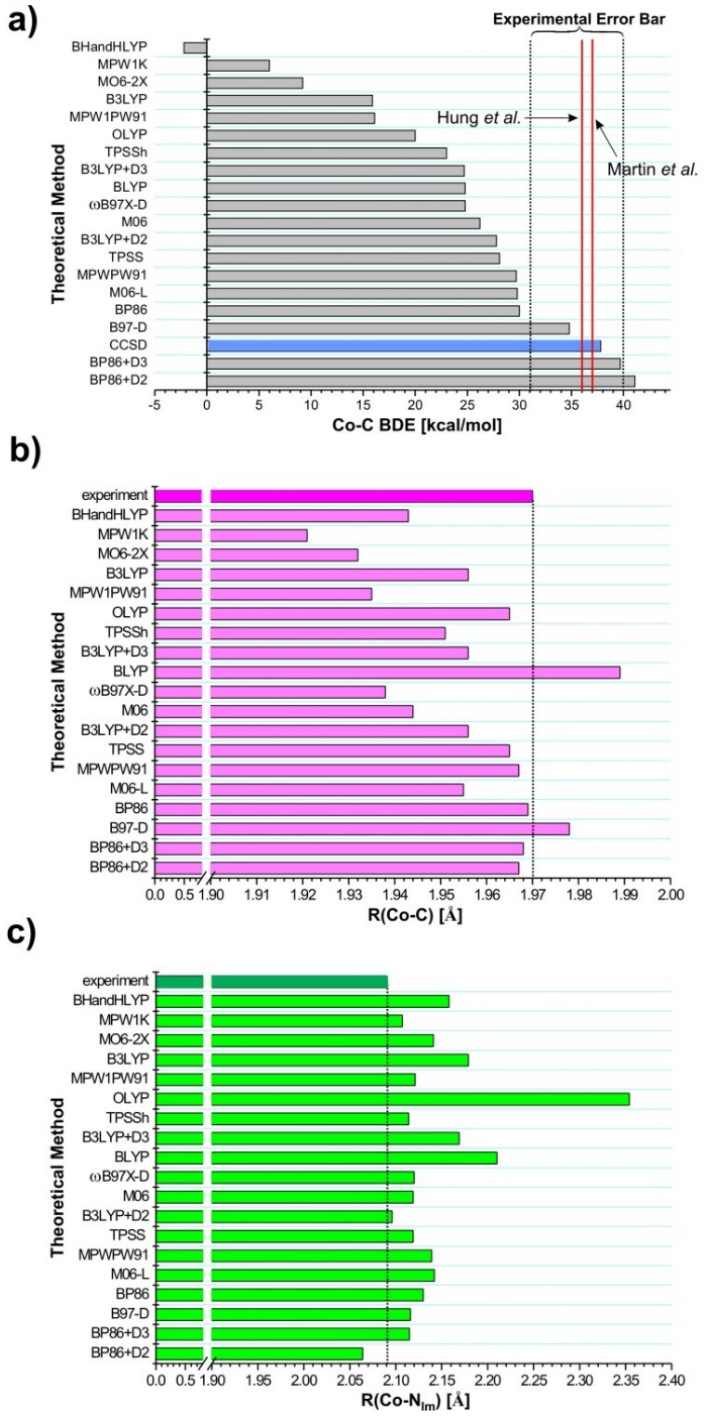

Figure 2.3. **(a)** A comparison of the ZPE and BSSE-corrected BDE values characterizing Co-C axial bond in the Im-[Co^{III}(corrin)]-Me^{+} model system resulting from various DFT calculations using the 6-311++G** basis set. The extrapolated ZPE-corrected CCSD BDE value is presented as the blue-colored bar. In the case of the DFT approaches, the optimized geometry and ZPE correction were obtained with the 6-31G* basis set using the respective functional. In the case of CCSD calculations, the ZPE correction was obtained in the BP86/6-31G* calculations, whereas BSSE correction was ignored. A comparison of the **(b)** Co-C and **(c)** Co-N_{Im} axial bond lengths for the Im-[Co^{III}(corrin)]-Me^{+} model complex, obtained with various DFT/6-31G* approaches with the experimental data. The vertical lines corresponding to the experimental data.

significantly underestimate the experimentally determined BDE, while pure GGA functionals like BP86 with dispersion correction (D3) provide BDE with reliable agreement with experiment. Figure 2.3 shows a comparison of theoretically determined BDEs of MeCbl as well as axial bond lengths with experimental values. All presented results in Figure 2.3 originate from the appended reference.[163]

A benchmark analysis of the Co-C_{Me} BDE in MeCbl was performed in order to determine the most appropriate functional to use within the DFT framework for studying ground-state properties.[163] In this study, coupled cluster (CC), DFT, CASSCF, and CASPT2 were used to predict BDE in the Im-[Co^{III}-corrin]-Me^{+} model system, a representative of MeCbl. There are several important conclusions that are of note. The benchmark *ab initio* potential energy curve (PEC) for the Co-C_{Me} dissociation was determined using the canonical CC approach with singles and doubles (CR-CC(2,3)/CCSD) (Figure A.2.1). Upon introduction of zero-point energy (ZPE) and basis set superposition error corrections (BSSE), BDEs were produced in excellent agreement with experiment. For instance, with the 6-311++G** basis set, BDE was calculated to be 38 kcal/mol.[163] The experimental range for Co–C_{Me} BDE for MeCbl falls within the range of 32-40 kcal/mol, including error (Table 2.1).[156-158] It was found that among all of the hybrid functionals tested, including the popular B3LYP, the strength of the Co-C_{Me} bond is always underestimated (Figure 2.3). The underestimation correlates with the percentage of Hartree–Fock (HF) exchange that is included in calculations. It was suggested that the neglect of dispersion interactions at shorter Co-C_{Me} bond lengths is a contributing factor to the poor performance of the hybrids. Alternatively, pure functionals give much better agreement with experiment, and addition of dispersion corrections tends to bring the

predicted BDEs to even closer agreement with experiment. The best-performing DFT functionals, with the 6-311++G** basis set, were B97D and BP86 corrected for dispersion as these predicted Co-C_{Me} BDE to be 35 and 40 kcal/mol, respectively. A further conclusion of this study is that high-level calculations such as CASSCF and CASPT2 seem to be far too expensive for any realistic study of Cbls because appropriate active space would be prohibitively large.

Previously, the Co-C bond strength was studied in the context of determining why B3LYP, the density functional of choice for an enormous majority of computational studies, performed so poorly in determining BDE in MeCbl.[140] It was suggested that this error comes from the HF exchange and the LYP functional. This study also indicated that BP86 is an appropriate functional to use for the analysis of cobalamins, especially over MP2 and B3LYP, citing several reasons. BP86 is much less expensive than MP2. There is a smaller basis set dependence for DFT methods than for *ab initio* methods and finally BP86 gives better agreement with experimentally determined structural details than B3LYP and MP2. It was further suggested that the B3LYP functional is a problematic choice in general for determining homolytic metal-carbon BDEs in tetrapyrroles and other highly conjugated systems.

Co-C BDE was also studied in AdoCbl.[143, 144] These benchmark studies yielded similar conclusions to those where MeCbl was the cofactor under study. Namely, it was found that BP86 is an appropriate functional to predict BDE in AdoCbl. B3LYP significantly underestimates the strength of the Co-C_{Ado} bond. Beyond the poor performance of B3LYP in predicting Co-C_{Ado} BDE, this functional does not properly reproduce axial bond distances from crystal structures in cobalamins in the base-on form.

It was also shown that B3LYP underestimates the energies of the bonding orbitals and overestimates the energies of the antibonding orbitals.

3.1.2 Electronically Excited States

In order to use calculations to aid in the interpretation of experimental spectroscopic data, benchmarks for electronically excited states within the TD-DFT framework are critical. Results from benchmarks can be relied upon to choose the proper functional that will ensure meaningful conclusions. These have been performed for both CNCbl[145] and MeCbl.[139, 163, 165] In particular for CNCbl, which has been referred to as the paradigm system for the evaluation of excited states of Cbls, a benchmark analysis targeting the manifold of low-lying excited states was performed.[145] TD-DFT calculations were compared with high-level *ab initio* calculations and experimental results in order to analyze the nature of the low-lying excited states. The performance of three density functionals, B3LYP, BP86, and LC-BLYP, representing hybrids, GGAs, and range-separated functionals, respectively, was investigated (Figure A.2.2).[145] Both BP86 and LC-BLYP, with range-separation parameter $\mu \sim 0$, yielded results that were consistent with experimental results and high-level *ab initio* calculations. The electronic properties of CNCbl were most appropriately described when employing the BP86 functional. The α/β region of the Abs spectrum was once interpreted as a vibrational progression of one intense $\pi \rightarrow \pi*$ electronic transition. This is not necessarily supported by circular dichroism (CD) and magnetic circular dichroism (MCD) spectra. Rather this region of the spectrum can be dominated by both $d/\pi \rightarrow \pi*$ and $\pi \rightarrow \pi*$ transitions. The S_4 transition, which is primarily a $\pi \rightarrow d$ excitation, may also contribute the α/β band. The BP86 functional can reliably predict these excitations.

Additional insights can be gained from studies associated with Co(I)Cbl. Electronically excited states of this compound can be assessed through various types of spectroscopy including Abs, CD, and MCD spectroscopy techniques.[166] Each of these types of spectra can be readily simulated using TD-DFT. For the test case of Co(I)Cbl, Abs, CD, and MCD spectra were simulated using a GGA functional, BP86, and a hybrid functional, CAM-B3LYP.[167] Extended second-order multiconfigurational quasi-degenerate perturbation theory (XMCQDPT2), a high level *ab initio* method, was used as a reference to explore the nature of the low-lying electronic transitions. It is apparent from this study,[167] involving both a truncated model and calculations with the full structure, that BP86 performs better than the hybrid functional in describing the excitations associated with Co d and corrin π localized transitions. Another important implication from this work was that the lowest energy band was associated MLCT excitations, a finding that is distinct from the widely presumed assignment of a single $\pi \rightarrow \pi^*$ transition followed by a vibrational progression for this state.

TD-DFT calculations involving various functionals were also benchmarked against XMCQDPT2 and equation-of-motion coupled-cluster singles and doubles (EOM-CCSD) calculations with MeCbl as a test case.[139] These were compared with the low-lying excited states with the aim of determining the proper density functional to describe the S_1 state as MLCT, a finding that has been experimentally confirmed via TAS and resonance Raman spectroscopy.[91, 93, 95, 102]

The choice of functional is paramount in providing the proper description of the character of the S_1 state. The hybrid functionals tested (B3LYP, MPW1PW91, and TPSSh) provide a description of the S_1 state representative of a pure $\pi \rightarrow \pi^*$ transition localized on

the corrin. Alternatively, the GGA (BP86, BLYP, MPWPW91), the meta-GGA (TPSS), and range-separated LC-BLYP describe the S_1 consistently with experiment as MLCT. In summary, it would seem that, at the time this chapter was written, DFT and TD-DFT employing the BP86 functional is the most economical and reliable way to study Cbls in both the ground and excited states, respectively.

3.2 Ground and Excited State Geometries

Axial bonding is one of the most important issues that needs to be considered in studies involving Cbls. Crystallography of isolated B_{12} cofactors reached its apogee more than 50 years ago, when several crystal structures from the laboratory of Dorothy Hodgkin were reported including vitamin B_{12}, coenzyme B_{12}, and several other B_{12} derivatives.[68] Some of these structures were re-determined using synchrotron radiation by Randaccio and coworkers.[168-171] This high-resolution crystallographic data is an excellent source for computational studies and has allowed for the in-depth exploration of axial bonding and the inverse trans influence. In general, structural properties associated with electronic excitations cannot be easily accessed experimentally. However, this situation has changed recently because it has been shown that structural changes can be probed via X-ray absorption near edge structure (XANES) spectroscopy.[172] It is evident, based on XANES measurements of CNCbl, that upon excitation the axial bonds undergo the most significant changes, namely elongation, when compared to the equilibrium geometry. As previously stated, it is well understood based on the work of Sension and co-workers that photodissociation or deactivation to the ground state occurs from the S_1 state. With these points in mind, PESs as a function of axial bond lengths for both the S_0 and S_1 state can be used to understand the mechanisms of the photoreactions.

Figure 2.4 depicts bond length comparisons between MeCbl and AdoCbl base-on and base-off derivatives in both the ground and first excited state.[110] DFT/BP86 and TD-DFT/BP86 were employed for optimization geometries of the S_0 and S_1 electronic states, respectively. In all calculations, the conductor-like screening model (COSMO) for solvation was used. For the MeCbl and AdoCbl base-on forms, high-resolution X-ray crystal structures are available and optimized bond lengths can be readily compared with those from experiment. However, for base-off MeCbl and AdoCbl, there are no available crystal structures, so calculations must be solely relied upon. For the S_1 state geometries, there is not an experimental reference for axial bond lengths so only optimized bond lengths are shown for the S_1 geometries. The optimized Co-N_{Im} and Co-C ground state (S_0) bond lengths for MeCbl and AdoCbl base-on are in very good agreement with experiment. For each of the derivatives understudy, the Co-X bond (X = N_{Im} and OH_2O for base-on and base-off forms, respectively) is shorter for the optimized S_1 geometries than the S_0. For the base-on forms, the S_1 Co-C bond lengths is slightly longer than the S_0 experimental and optimized lengths. This was not observed in the base-off forms. For base-off MeCbl, the S_1 Co-C bond is just slightly shorter than the optimized S_0 Co-C bond length. For base-off AdoCbl, the S_0 and S_1 optimized Co-C bond lengths are essentially identical. It is apparent based on these comparisons that the axial bond lengths are sensitive to electronic excitation.

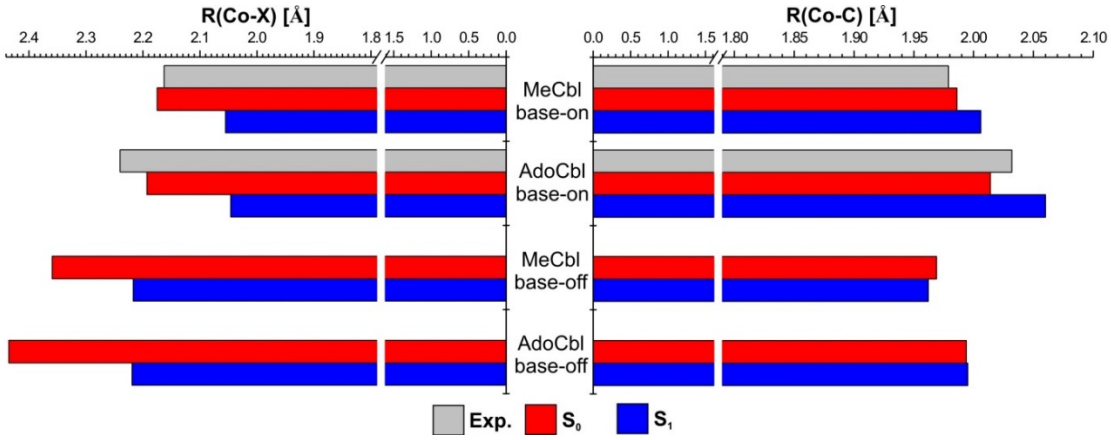

Figure 2.4. Experimental and optimized axial bond lengths at the DFT/BP86 level, for S_0 and TD-DFT/BP86 for S_1 excited states of the cobalamins under consideration (X= Im and H_2O for *base-on* and *base-off* form, respectively). In all calculations the same basis sets, TZVPP for Co, C, N, and TZVP for H were used, employing the COSMO solvent model.

4.0 Reaction Coordinates for Photodissociation of Cbls

4.1 Potential Energy Curves

Upon irradiation with light, the Co-C bond in alkylCbls is cleaved to generate RPs. The straightforward computational approach to investigate photo-induced homolytic bond cleavage is analysis of the low-lying excited states along the reaction coordinate associated with bond scission. The proper way to construct the corresponding PECs is to elongate and freeze the specific photo-activated bond systematically and relax the rest geometrical parameters for the ground and excited states. This approach to describe photodissociation has been shown to be useful in systems like CO- or O_2-ligated models of myoglobin where the photo-induced coordinate was Fe-CO or Fe-O_2, respectively, phosphine-substituted transition metal carbonyl complexes $Cr(CO)_5PH_3$, and Si-C bond in Siphthalocyanine.[173-178] However, such an approach is only valid if the changes associated with photodissociation involve a single coordinate. The most obvious reaction coordinate to be considered for photolysis of alkylCbls is the Co-C bond but a more detailed picture can be obtained by considering the involvement of the lower axial bond as well. PECs with a

single reaction coordinate (Co-C distance) can be used to get an idea about the low-lying excited states of Cbls. To get a more realistic picture of the photodissociation mechanism PESs should be constructed considering both axial bonds.

The importance of the lower axial ligand in the photodissociation mechanism of Cbls is further evident from the analysis of the PECs of base-off MeCbl and AdoCbl (Figure 2.5). For these base-off models, the PECs of S_1 electronic state are very shallow in energy. The character of selected points along the curves indicate the dominant transitions are from the $d_{yz} + p \rightarrow \sigma^*$ excitation. The LF character of the S_1 states matches well with several other triplet states with the similar orbital contributions (Figure A.2.3). Thus, at the vicinity of the equilibrium length of the Co-C bond, the S_1 state can couple with the triplet states, opening the channel for ISC and photodissociation with production of the RPs in triplet state.

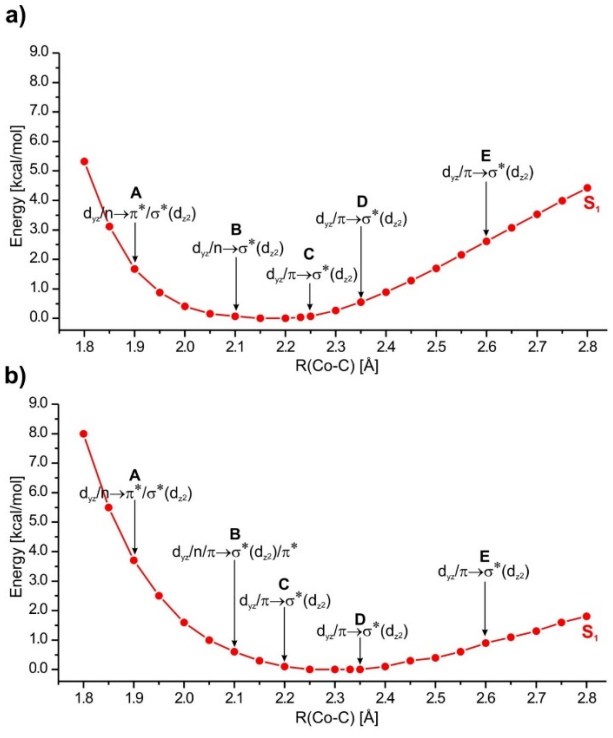

Figure 2.5. PESs as a function of Co-C bond distance for S_1 optimized geometry of the **(a)** [Co^{III}(corrin)]-Me^+ and **(b)** [Co^{III}(corrin)]-Ado^+ model complexes.

4.2 Potential Energy Surfaces

A schematic representation for the construction of S_0 and S_1 PESs by systematic elongation of the axial bonds is shown in Figure 2.6. To construct an S_0 PES, the axial bonds Co-C and Co-X, (X=N_{Im}, or X=O_{H2O}, for base-on and base-off forms, respectively) are systematically elongated using a step size of 0.05 Å and the corresponding ground state geometries of each point are optimized. The ground state geometry of each point can used to calculate the vertical excitation energies of the S_1 state. The projection of the S_1 state with the S_0 allows for visualization of the energetic barrier between the two states. The contour representations of both surfaces are also shown in Figure 2.6. Similar methodology was used in the case of relaxed S_1 PESs, where the geometries associated with individual points on the S_1 PES were optimized.

The topology of the S_0 state carries a single energy minimum whereas the S_1 PES contains two energy minima. In the case of S_1 PESs of various Cbl derivatives, the two energy minima are the result of two distinct electronic states namely MLCT and the LF.[101, 110-113, 115-120] These two states cross and are separated by a seam. The corresponding orbital contribution for the MLCT state is primarily metal d orbitals to the corrin π* whereas in the LF state the major orbital contribution is coming from the metal d orbitals to the π*. Conceptually, there is a parallel between electronic excitations and the one electron reduction of the cofactor. Upon addition of an electron to the cofactor, the electron delocalizes on the corrin ring at equilibrium Co-C bond lengths. After elongating the Co-C bond the electron will be promoted from corrin π orbitals to $\sigma^*_{Co\text{-}C}$ orbitals.[179-181] This is analogous to excitation via light.

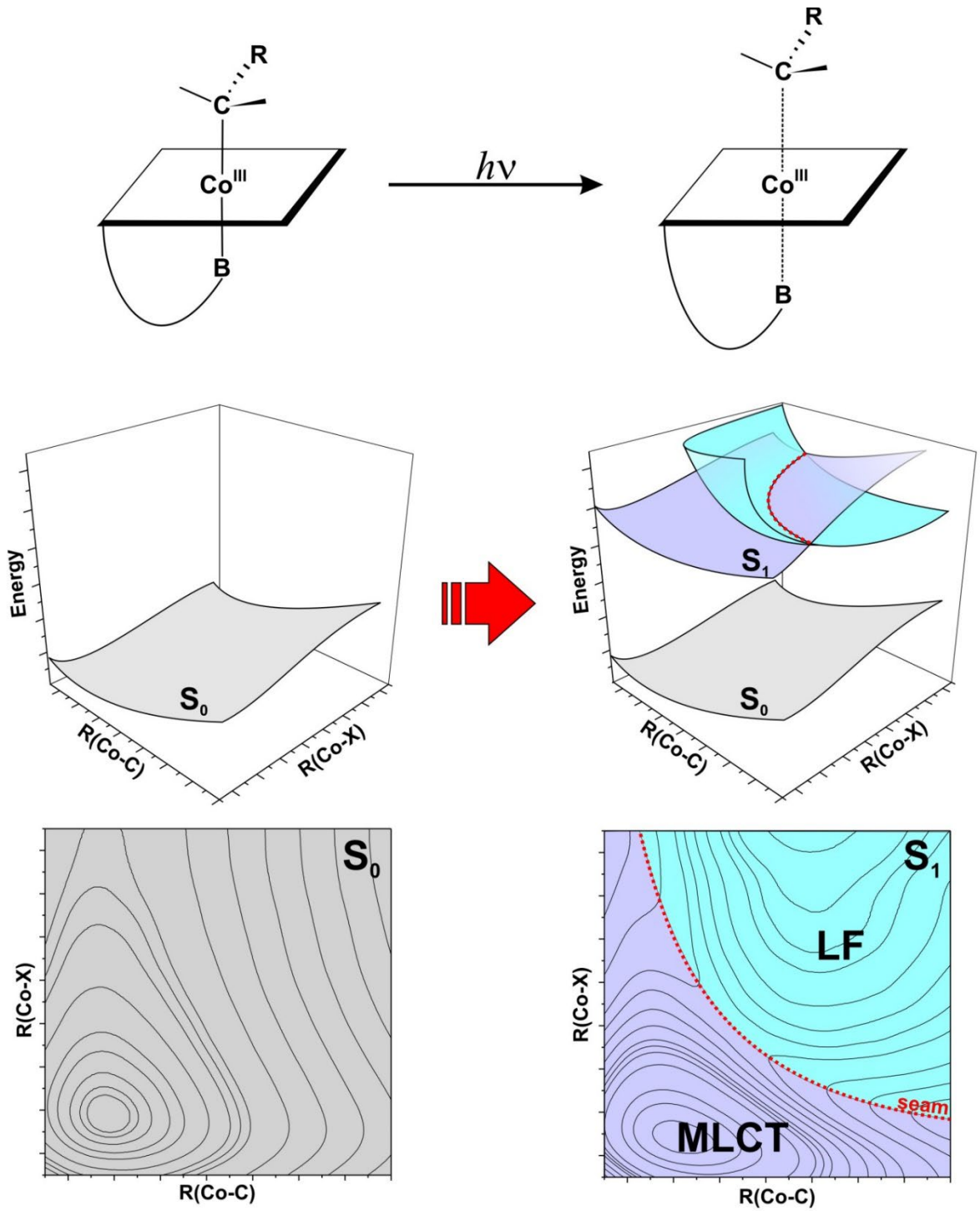

Figure 2.6. Work-flow for the construction of S_0 and S_1 PESs by systematic elongation of the axial bonds. Top row: S_0 geometry (left) and S_1 geometry, with elongated axial bonds, resulting from excitation with light (right). Middle row: S_0 PES as a function of axial bond lengths (left). S_1 PES based on vertical excitation from S_0 (right panel). S_1 surface is characterized as a crossing of two states, MLCT (purple) and LF (cyan), where the dotted line (seam, red) marks the crossing of the two states. Last row: Contour view of PESs. DFT calculations are used to construct the S_0 surface. TD-DFT calculations are used to construct S_1 surfaces based on the S_0 optimized geometries.

5.0 Determination of the Photoreaction Mechanism

5.1 Photolysis Pathways

The challenge in describing the photodissociation mechanism is to connect the MLCT to the LF. Two pathways are identifiable, called Path A and Path B, and connect the MLCT to LF state as shown in Figure 2.7. Path A involves the initial elongation of the Co-C bond from the MLCT minimum followed by the elongation of the Co-X bond. Path B initiates from the MLCT minimum and the initial elongation is with the Co-X bond followed by the elongation of the Co-C bond. The active pathway is dependent upon energetics and is specific to each Cbl. However, both routes end in the LF region where photodissociation and formation of the RPs occurs.

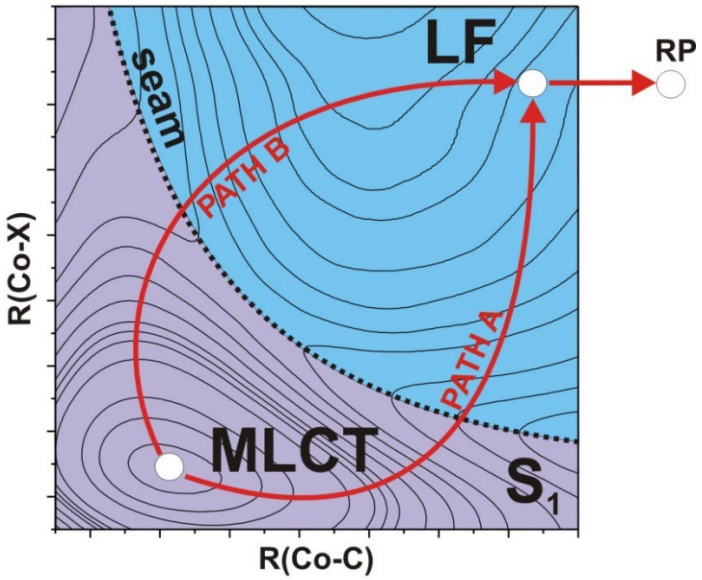

Figure 2.7. Schematic representation of S_1 potential energy surface and the corresponding pathways for photodissociation from the MLCT to LF state. RP are generated from the LF state. Path A involves elongation of the Co-C bond followed by elongation of the Co-X bond. Path B results from the initial elongation of the Co-X bond followed by elongation of the Co-C bond.

5.2 Topology and Electronic States

Here the base-on and base-off models of isolated MeCbl and AdoCbl will be used to demonstrate how to use PESs to determine the mechanism of RP formation in the excited state of Cbls. The topologies of the S_0 and S_1, S_2 excited states, based on vertical excitations, for the base-on and base-off model complexes for both MeCbl and AdoCbl are depicted in Figure 2.8. For Im-[Co^{III}(corrin)]-Me^+ and Im-[Co^{III}(corrin)]-Ado^+, the surfaces are constructed based on Co-C and Co-N_{Im} bond lengths.[116, 117] For the base-off forms, H_2O-[Co^{III}(corrin)]-Me^+ and H_2O-[Co^{III}(corrin)]-Ado^+, the PESs are based on Co-C and Co-O bond lengths.[118] Upon visual inspection, there are some apparent similarities and differences that are of note.

The topologies of the S_0 state are quite similar, regardless of the axial base. Each S_0 state contains a single energy minimum. This low energy region is shallow and extends along the lower axial base bond length. The S_0 surfaces have a substantially greater gradient of increase in energy during elongation of Co-C bond. Unlike non-alkylCbls, such as CNCbl and HOCbl, there is a distinct energetic gap between the S_0 and S_1 states for MeCbl and AdoCbl base-on and base-off forms.[110] Moving on to the S_1 surfaces, similarities are noted based on binding mode. In other words, the topologies of the S_1 surfaces for Im-[Co^{III}(corrin)]-Me^+ and Im-[Co^{III}(corrin)]-Ado^+ are quite similar. The same is true for the topologies of the S_1 surfaces for the base-off forms. For Im-[Co^{III}(corrin)]-Me^+ (Figure 2.8a), the S_1 surface contains two low energy regions separated by a seam. The minima region localized between Co-C bond lengths of 1.9-2.3 Å and Co-N_{Im} of 1.9-2.4 Å is of MLCT character. The second minima region, of LF character, is much larger and is located at Co-C bond distances of 2.1-2.6 Å and Co-N_{Im} of 2.5-3.5 Å. Here, the MLCT region is

lower in energy than the LF region. For Im-[Co^{III}(corrin)]-Ado^{+} (Figure 2.8b), two minima regions are also observed and are separated by a seam. The MLCT region is found between Co-C bond lengths of 1.95-2.45 Å and Co-N_{Im} bond lengths of 1.8-2.3 Å. The LF region is broad and is between Co-C distances of 2.1-2.6 Å and Co-N_{Im} distances of 2.5-3.5 Å. From an energetic standpoint, the minima of each of these regions is comparable. The S_1 PESs' topologies for relaxed geometries of the base-on forms, Figure 2.9 a and b, are very similar to those obtained from vertical excitations, only the energetic relation and height of the barrier between the MLCT and LF regions undergoes a slight change.

The S_1 PESs for the base-off forms are essentially indistinguishable between the MeCbl and AdoCbl models, Figure 2.8 c and d, respectively. These have a large minima region located between Co-C distances of 2.0-2.6 Å and Co-O distances of 2.3-3.5 Å and this is designated as the LF region. Another minima region, characterized as MLCT is located between Co-C 1.9-2.1 Å and Co-O of 2.1-2.6 Å for the base-off MeCbl model complex and between Co-C 1.9–2.1 Å and Co-O 2.1-2.5 Å in the case of the AdoCbl base-off model complex. For the adiabatic PESs of the base-off forms shown in Figure 2.9 c and d, the two minima regions, MLCT and LF, are more distinct. At this point, two generalizations are apparent upon comparison of the base-on and base-off surfaces based on vertical projections. First, both forms of MeCbl and AdoCbl have two distinct minima regions separated by the seam. Second, the topology of S_1 PESs of the base-off forms are markedly different than their base-on counterparts. The LF region is more extensive and clearly lower in energy than the region represented by the MLCT electronic state. The MLCT region covers much less of the S_1 state and the transition to LF region by direct elongation of the lower axial bond is practically barrierless. The topology of the S_1 PES

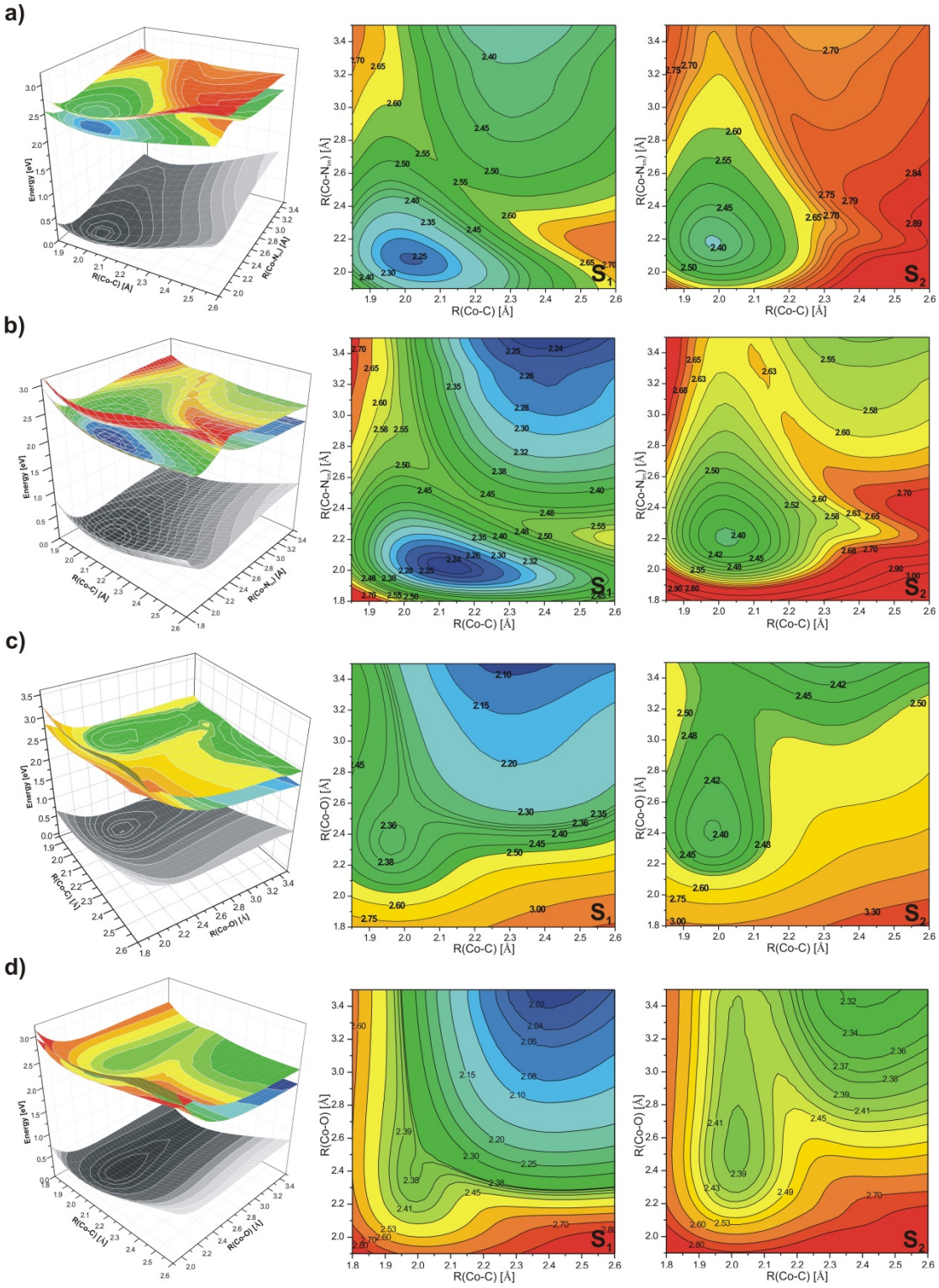

Figure 2.8. Potential energy surfaces as a function of axial bond lengths of the singlet ground states (S_0) and the lowest two singlet excited states (S_1 and S_2), shown as vertical projections for **(a)** Im-[Co^{III}(corrin)]-Me^+, **(b)** Im-[Co^{III}(corrin)]-Ado^+, **(c)** H_2O-[Co^{III}(corrin)]-Me^+, and **(d)** H_2O-[Co^{III}(corrin)]-Ado^+ model complexes.

for the base-off forms thus has a strong influence on the course of the photoreaction. For the S_2 states of all the derivatives understudy, the corresponding PESs have topologies that are relatively similar to their S_1 states.

The key issue for using PESs to describe the mechanism of photodissociation of Cbls is to connect the minima regions of the S_1 surfaces and extrapolate towards RP formation. As shown in Figure 2.8 for the S_1 surfaces of Cbls, two possible routes for photodissociation can be identified, Path A and Path B, respectively. Both pathways will end in LF region, although the instability of the wavefunction associated with TD-DFT at longer bond distances limits the range of the PES that is generated. As a result, extrapolations must be relied upon for Co-C bond distances longer than ~2.6 Å to fully visualize Path A's progression to the LF region. Path A involves the elongation of the Co-C bond while the Co-X bond remains essentially unchanged. It proceeds through the MLCT region along the Co-C coordinate. Path B initiates with the elongation of the Co-X bond followed by the elongation of the Co-C bond, which involves crossing of the seam into the LF region where photodissociation or IC to the ground state occurs. The active pathway is determined based on energetics and intuitively, the path with a smaller energetic barrier will be favored. For the base-off forms, Path A is a closed channel to photodissociation. For the base-on forms the photoreaction activity along Path A or Path B is determined by the height of the energy barrier during elongation of the lower or upper axial bond.

The adiabatic PES for the MeCbl base-on model structure (Im-[Co^{III}(corrin)]-Me^{+}) indicates two minima regions, the MLCT and LF (Figure 2.9).[117] Both Path A and B initiate from the MLCT minimum, denoted I (S_{1min}) in Figure 2.9. Path A proceeds along the Co-

C_{Me} coordinate. In order to reach the LF region, Path B crosses the seam at IIB. At this point the Co-N_{Im} bond is ~2.8 Å and the Co-C bond is ~2.15 Å. Rather uniquely, each of these paths can be explained through the experimentally observed wavelength dependence for MeCbl. Path A represents the photoreaction mechanism after excitation at 520 nm whereas Path B after 400 nm excitation. Based on the S_1 PES for base-on AdoCbl (Figure 2.8b), Path A is explicitly more favorable energetically and this step of the photoreaction begins with elongation Co-C_{Ado} bond.[116] Path B remains rather inactive for base-on AdoCbl, however in the enzymatic environment energy preferences may be reversed to such an extent, that the photodissociation initially begins with the elongation of Co-N_{Im} bond to the axial base.[182] For the base-off forms of MeCbl (Figure 2.9c) and AdoCbl (Figure 2.9d), Path A is inactive based on energetic grounds while Path B is active. The base-off S_1 surfaces are unique in comparison to the base-on forms in that the LF region is stabilized. This means that the LF region is lower in energy than the MLCT region, for both MeCbl and AdoCbl base-off models. Put in another way, the LF region is repulsive in comparison to the MLCT region. Overall, the topologies of the S_1 surfaces, based on their respective binding modes, are very similar.

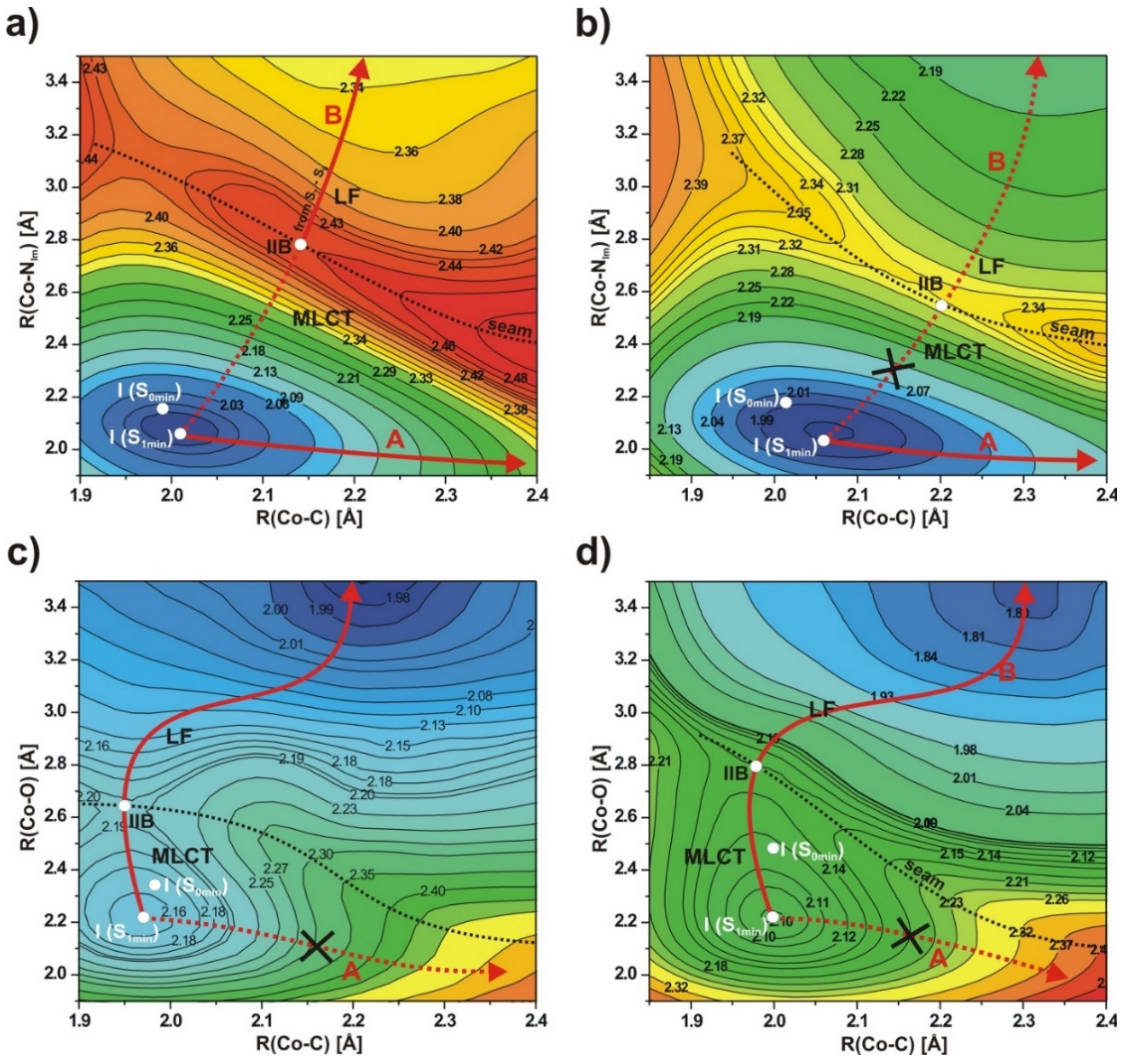

Figure 2.9. PESs as a function of axial bond lengths with photodissociation paths for (a) Im-[Co^{III}(corrin)]-Me^{+}, (b) Im-[Co^{III}(corrin)]-Ado^{+}, (c) H_2O-[Co^{III}(corrin)]-Me^{+}, and (d) H_2O-[Co^{III}(corrin)]-Ado^{+} model complexes.

5.3 Deactivation

While considering photodissociation, a natural competition event to consider is deactivation to the S_0 state. Here we can recall that RP formation occurs from the LF region where the axial base is detached, or the axial Co-N bond is significantly elongated. In the case of solution-based studies, these RP can diffuse from the solvent cage in a process also known as cage escape. The RP can also recombine and be deactivated to the S_0 state via

geminate recombination. Alternatively, IC to the S_0 state can occur. For deactivation to take place, the S_1 and S_0 states should cross with a small energy barrier.

In light of our theoretical investigations, there are two possible channels for IC that can be considered for alkylCbls and these are depicted in Figure 2.10. One possible option for IC labeled as, IC channel 1, involves de-excitations of Co(II) by changing the electronic configuration from $(d_{yz})^1(d_{z2})^2$ to $(d_{yz})^2(d_{z2})^1$. As shown in Figure 2.10, the significant elongation of the axial bonds leads to a small energy gap between the S_0 and S_1 PESs and the electronic configuration of the cobalt center can be formally considered Co(II). As a result, de-excitations involving Co(II) are possible. The second possible option, IC channel 2, involves the distortion of the corrin ring. Upon inspection of the S_0 and S_1 PESs as a function of Co-C distance and N-Co-N valence angle, it is apparent that these cross. At this seam, IC to the ground state will take place. For solution-based studies, both channels may be active. In the enzymatic environment we have proposed that that only IC channel 1 is active as an enzyme imposes constraints on the corrin macrocycle that prevents the distortion.

IC channel 1 can be further understood by considering the mechanism of excited state quenching as shown in Figure 2.11. After initial excitation with light, MLCT occurs and an electron (represented as a green dot in Figure 2.11) from a metal d orbital is transferred to a π^* orbital of the corrin ring because the corrin ring is capable of strong delocalization of the electron. This leaves behind a hole in the metal d orbital, shown in red in Figure 2.11. Subsequently the Co-C bond is elongated, and this forms a Co(II) structure. After elongation of the Co-C bond, the axial base is lengthened as well. At this point, an electron from the corrin ring is back promoted to the d_{z2} Co orbital and this

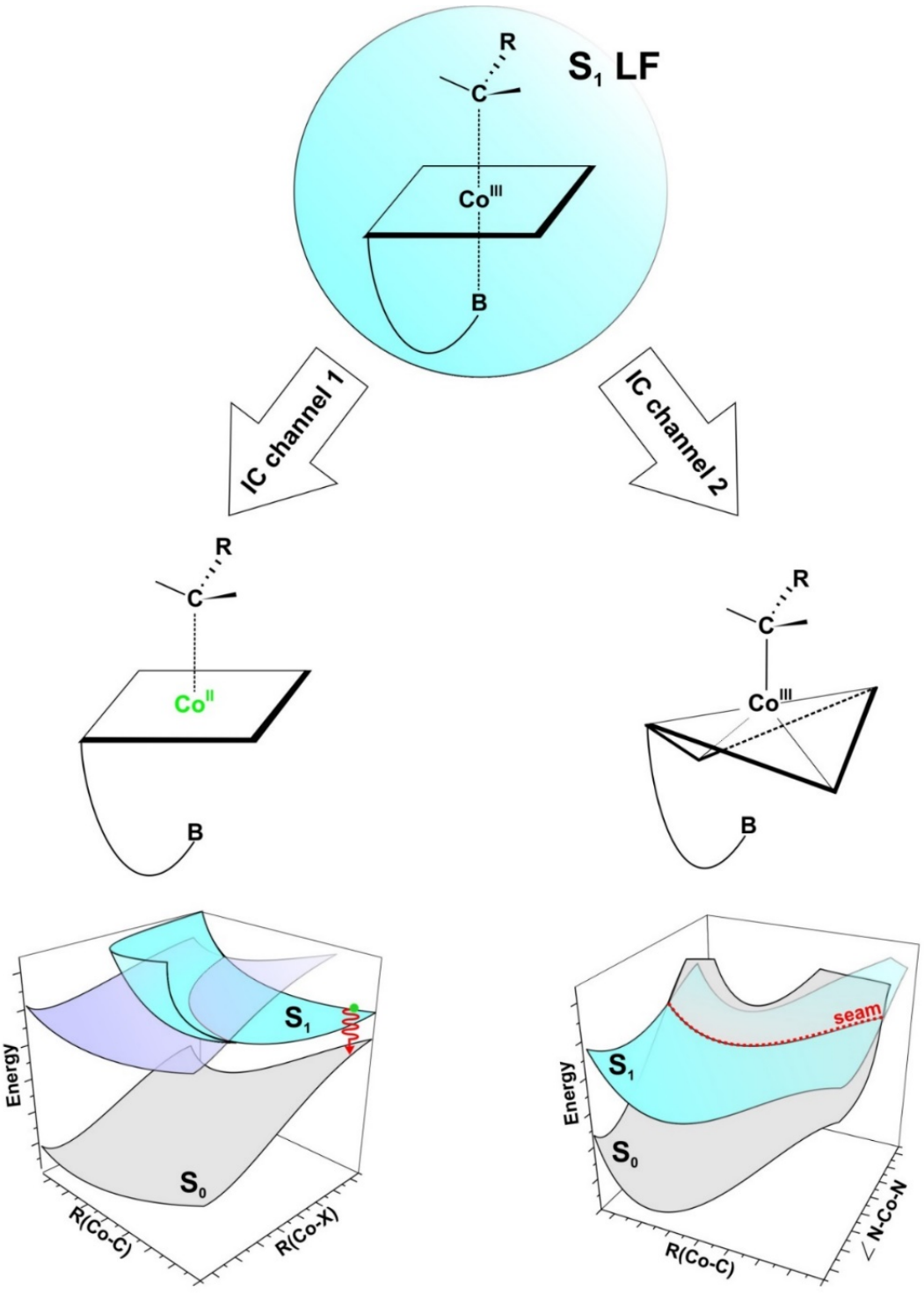

Figure 2.10. Scheme depicting general deactivation ($S_1 \rightarrow S_0$) based on two possible channels. IC channel 1 involves electronic de-excitations of Co^{II} from the LF (cyan) region. IC channel 2 involves corrin ring distortion after the axial base is detached, resulting in a crossing of the S_0 and S_1 PESs based on Co-C bond length and N-Co-N valence angle.

provides the geometry of the LF region. This species can be described as a Co(II) radical, D_1[Co(II)]*, which is formally a doublet electronic state. The electronic configuration of this species is $(d_{yz})^1(d_{z2})^2$. From this electronic configuration, deactivation can follow. The deactivation process of $D_1 \rightarrow D_0$ is shown in the blue box in Figure 2.11. For the deactivation to occur, there will be a transfer of the electron in the d_{z2} orbital to the metal d_{yz} orbital. This configuration is Co(II)$(d_{yz})^2(d_{z2})^1$ and the Co atom will adopt the ground state electronic configuration: Co(II)$(d_{yz})^2(d_{z2})^1$. The process concludes with the binding of the ligands to the Co and relaxation to the S_0 state will occur. This channel for IC can be active for alkylCbls in solution or in enzymes.

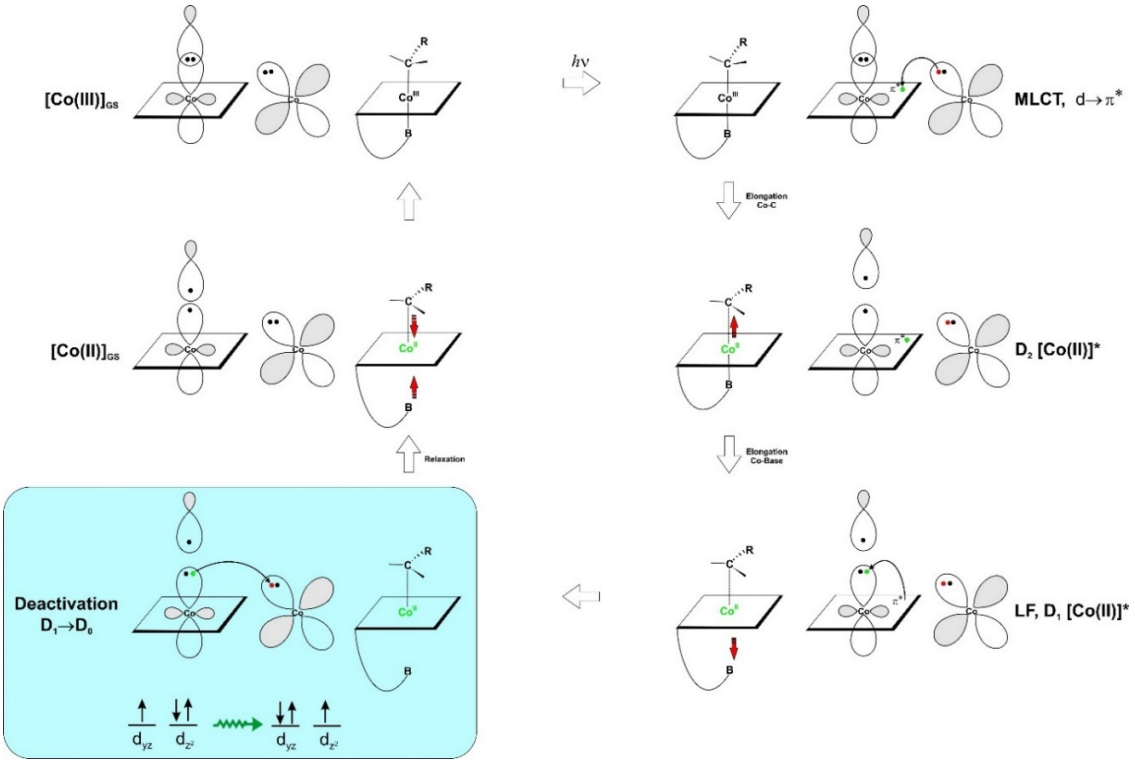

Figure 2.11. General scheme of excited state quenching along the photoreaction.

PECs and PESs as a function of Co-C bond length and N_{21}-Co-N_{23} valence angle provide further insight into the mechanism of IC via corrin ring distortion. The left panel of Figure 2.11 shows the cooperativity of the N_{21}-Co-N_{23} valence angle and Co-C_{Me} bond length in the S_1 state for MeCbl base-off model complex, [Co^{III}(corrin)]-Me^+. Point IIIB (S_{1min}) corresponds to the energy minimum of the S_1 state. As the Co-C_{Me} bond elongates, the valence angle increases linearly from 160° to 170°. As the Co-C_{Me} bond shortens to ~2.0 Å, there is a sharp decrease in the valence angle (160°-143°) at bond distances between 1.8 Å and 2.0 Å there is no change in the valence angle. Figure 2.12 shows the PES as a function of N_{21}-Co-N_{23} valence angle and Co-C_{Me} bond length. The pathway for IC shown on the PES initiates from the S_1 state minimum and proceeds to the seam where IC will ultimately take place. At this point (IVB (IC)), the valence angle is ~113° and the Co-C_{Me} bond is ~2.05 Å. This geometry is shown in Figure 2.12. Several structural configurations may be possible for IC to occur from because the energy change along the N_{21}-Co-N_{23} angles from 165° to 135° and the Co-C_{Me} distances, from 2.25 Å to 1.90 Å is small. The calculated barrier for the S_1/S_0 crossing is 9.9 kcal/mol but this is likely overestimated because several other coordinates may be involved in the IC process and only two are considered here. Similarities are observed for the base-off AdoCbl model complex (Figure 2.12, right panels) with only slight differences in numeric values.

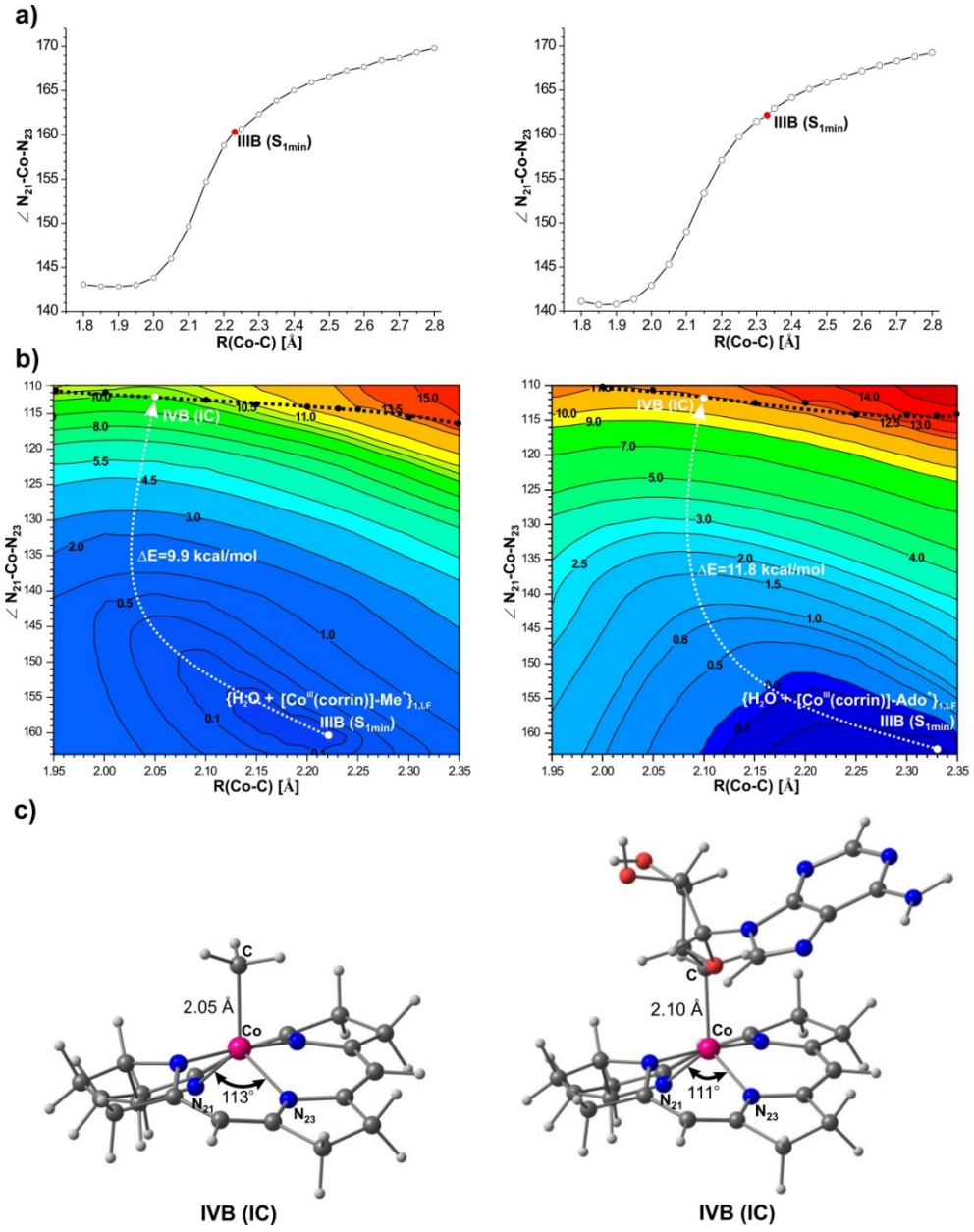

Figure 2.12. (a) N_{21}-Co-N_{23} valence angles as functions Co-C bond length in the LF electronic states of the {[Co^{III}(corrin)]-Me^{+}}^{1},LF (left), and the {[Co^{III}(corrin)]-Ado^{+}}^{1},LF (right) model complexes. (b) Potential energy surfaces for the S1 optimized geometry of the {[Co^{III}(corrin)]-Me^{+}}^{1},LF (left), and the {[Co^{III}(corrin)]-Ado^{+}}^{1},LF (right) model complexes as functions of N_{21}-Co-N_{23} valence angle and Co-C bond length, with minimum energy paths for S_1/S_0 internal conversion depicted. The seams along the intersections of the S_1/S_0 PESs are marked with black dotted line. (c) Geometries of the {[Co^{III}(corrin)]-Me^{+}}^{1},LF (left), and the {[Co^{III}(corrin)]-Ado^{+}}^{1},LF (right) model complexes at their points of internal conversion.

CHAPTER 3

PHOTOLYTIC PROPERTIES OF ANTIVITAMINS B_{12}

Synopsis

Biologically active forms of Cbls are crucial cofactors in biochemical reactions and these metabolites can be inhibited by their structurally similar analogues known as antivitamins B_{12}. PhEtyCbl or EtPhCbl exemplify recently synthesized and structurally characterized antivitamins B_{12}. These molecules represent an important class of vitamin B_{12} analogues that are of recent interest particularly for their application in drug design. From a spectroscopic point of view, EtPhCbl is photolabile with a very low QY of photoproducts, while PhEtyCbl is incredibly photostable. Herein, DFT and TD-DFT computations are provided to explore the photolytic properties of these compounds to shed light on the electronic properties that are indicative of these differences. PESs were constructed to investigate the mechanisms of photodissociation leading to RP formation and the mechanisms of deactivation to the ground state. The S_1 PESs for each antimetabolite contain two energy minima, one being the MLCT and another the LF state. There are two possible pathways for photodissociation that can be identified for EtPhCbl but only one (path B) is energetically feasible and involves the lengthening of the Co-N_{Im} bond through the MLCT region followed by the lengthening of the Co-C bond through the LF region. For PhEtyCbl, there is not an energetically favorable path for photolysis; rather, IC is the significantly preferred photophysical event.

1.0 Introduction ‡‡

Antivitamins are unique metabolites that are structurally similar to their respective vitamin analogues yet they counteract the physiological effects of those counterparts by various types of inhibition.[16, 29, 183] Despite their inhibitory nature, antivitamins can have useful medicinal applications.[21] For instance, vitamin K antagonists are used to reduce blood clotting by preventing thrombosis.[184, 185] There is an interest in the study of antivitamins B_{12}, which are structurally similar to vitamin B_{12} and other Cbls (Figure 3.1), to unearth whether medical or biological applications are possible for these antimetabolites as well.[186, 187] Recently, two antivitamins B_{12}, EtPhCbl and PhEtyCbl, were synthesized and these are structurally similar to the relevant B_{12} derivatives (Figure 3.1) involved in enzymatic catalysis.[26, 28] EtPhCbl and PhEtyCbl differ from other known B_{12} antagonists in that they bind well to the proteins of the human B_{12}-transport system including intrinsic factor, haptocorrin, and transcobalamin. They can also bind to the B_{12}-processing protein CblC. EtPhCbl and PhEtyCbl are unaffected in this environment and do not convert to the biologically active B_{12}-cofactors, MeCbl and AdoCbl, as is the case when CNCbl is bound to CblC.[26, 28, 188] This new class of organometallic Cbls offers opportunities to explore B_{12} chemistry and the pathophysiological implications associated with the metabolism of B_{12} in humans further.

‡‡ *Chapter 3 adopted from*: Lodowski, P., Ciura, C., Toda, M.J., Kozlowski, P.M. Photodissociation of ethylphenylcobalamin antivitamin B_{12}. *Phys. Chem. Chem. Phys.* **2017**, 19, 30310-30315. *and* Lodowski, P., Toda, M.J., Ciura, C., Kozlowski, P.M. Photolytic Properties of Antivitamins B_{12}. *Inorg. Chem.* 2018, 57, 7838-7850.

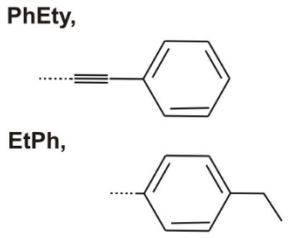

Figure 3.1. Molecular structure of upper ligands PhEty and EtPh of PhEtyCbl and EtPhCbl, respectively.

Both EtPhCbl and PhEtyCbl maintain all the key structural features of Cbls, with the exception being the nature of the upper axial ligand (Figure 3.1). As described in Chapter 1, for the biochemically important derivatives of B_{12}, CNCbl, MeCbl, and AdoCbl, the upper axial ligands are cyano, methyl, and adenosyl groups, respectively.[3, 5] In the case of the antivitamins B_{12}, EtPhCbl and PhEtyCbl, the upper axial ligands are 4-ethylphenyl (EtPh) and 2-phenylethynyl (PhEty), respectively (Figure 3.1). The other structural features of Cbls, including the antivitamins B_{12} understudy, were described in Chapter 1 Section 2.2. EtPhCbl and PhEtyCbl also have unique properties from both a biochemical and spectroscopic perspective.

EtPhCbl is the first organometallic aryl Cbl and is non-natural and chemically inert.[26] EtPhCbl has been used to induce functional vitamin B_{12} deficiency, also known as pernicious anemia, in laboratory mice.[27] EtPhCbl has also been called a conditional antivitamin B_{12} despite the difficulty in cleaving the Co-C bond in the enzymatic environment because it is possible to cleave this bond with light, albeit with a very low QY of photoproducts.[30] TAS studies indicated that photolysis results in the formation of Co^{II}Cbl with a QY of <1%. PhEtyCbl represents an organometallic alkynyl-Cbl which is structurally similar to CNCbl and is stable both thermally and photochemically.[28] Alkynyl-

Cbls may be representative of an entire group of B_{12} derivatives that are photostable.[31] From a spectroscopic point of view, PhEtyCbl is photostable, and the Co-C bond to the upper axial ligand does not cleave in the presence of light.

The divergent photochemical properties of these two antimetabolites provide an opportunity for theoretical insights. Understanding the mechanism of photodissociation for a conditional antivitamin B_{12} like EtPhCbl, and conversely why PhEtyCbl is so remarkably photostable, is the motivation behind the work presented in this chapter. This study provides a detailed analysis of the photochemical properties of both of these antivitamins B_{12} as well as the mechanisms of photodissociation of the upper axial ligand. This theoretical perspective can be used to guide future experimental work in the area of B_{12} photochemistry while offering important insights into the electronic structure properties that facilitate photolability as well as those that are representative of photostability. The presented results are crucial in the context of designing aryl- and alkynl- Cbls that are suitable agents for use in light-activated pharmaceutical applications.

2.0 Computational Details

2.1 Model Preparation

The structural models were derived from X-ray crystallographic data available for EtPhCbl and PhEtyCbl.9,10 The full structures of antivitamins were truncated to reduce computational cost. The side chains of the corrin macrocycle were replaced with hydrogens and the axial base was simplified by replacing the DBI axial ligand with Im (Figures 3.1). The nucleotide loop contains a phosphate ion (PO_4^-), so when this was removed, the truncated model had a positive charge. The geometries corresponding to the EtPhCbl and PhEtyCbl model complexes are denoted Im-[Co^{III}(corrin)]-$EtPh^+$ and Im-[Co^{III}(corrin)]-

PhEty^{+}, respectively. These models are analogous to the base-on form. In the models for the base-off forms, the Im ligand is removed, and these structures are labeled as [Co^{III}(corrin)]-EtPh^{+} and [Co^{III}(corrin)]-PhEty^{+}. A full molecular skeleton the crystal structures and the model geometries for both antivitamins are depicted in Figure 3.2.

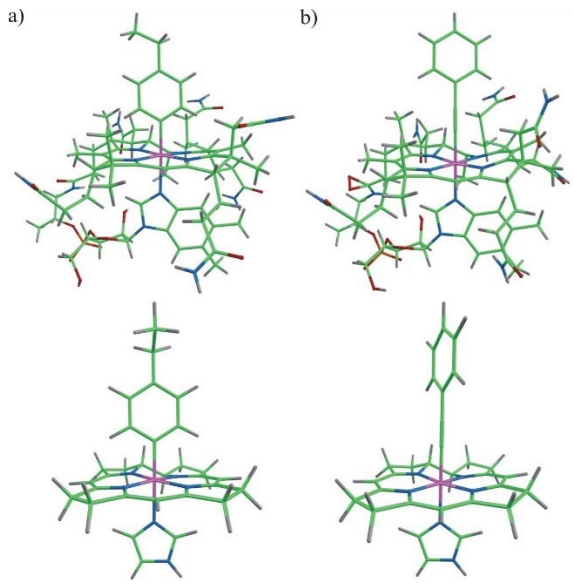

Figure 3.2. a) Crystal structure of EtPhCbl and the corresponding model complex (bottom left), described as Im-[Co^{III}(corrin)]-EtPh^{+} in the main text. b) Crystal structure of PhEtyCbl, and the corresponding model complex (bottom right), described as Im-[Co^{III}(corrin)]-PhEty^{+} model complex used in calculations. The truncated model system of EtPhCbl is modeled based on the crystallographic data from M. Ruetz, C. Gherasim, K. Gruber, S. Fedosov, R. Banerjee, B. Kräutler, Access to Organometallic Arylcobaltcorrins through Radical Synthesis: 4-Ethylphenylcobalamin, a Potential"Antivitamin B_{12}", *Angew. Chem. Int. Ed.* 2013, **52**, 2606 –2610, and CCDC 848663 data obtained from the Cambridge Crystallographic Data Centre via www.ccdc.cam.ac.uk/data_request/cif. The full structure of PhEtyCbl is drawn based on the crystallographic data from M. Ruetz, R. Salchner, K. Wurst, S. Fedosov, B. Kräutler, Phenylethynylcobalamin: A Light-Stable and Thermolysis-Resistant Organometallic Vitamin B_{12} Derivative Prepared by Radical Synthesis, *Angew. Chem. Int. Ed.* 2013, **52**, 11406 –11409, and CCDC 939826 data obtained from the Cambridge Crystallographic Data Centre via www.ccdc.cam.ac.uk/data_request/cif .

2.2 Level of Theory

The calculations for this study were all carried out using DFT and TD-DFT employing resolution of identity (RI)[189] with the GGA-type BP86[153, 190] functional and the TZVPP basis set for Co, C, N, and the TZVP basis set for H.[191, 192] In addition, the COSMO[193, 194] with water as the solvent was employed. All calculations were completed

using the TURBOMOLE[195] software with the exception of the Λ parameter[155] calculations which were obtained with the GAMESS[196] program.

DFT and TD-DFT employing BP86/TZVP(P) was successfully applied to other Cbls.[1, 101, 110, 111, 115, 117-119, 123-126, 146] Particularly, benchmark calculations for the electronically excited states of CNCbl and MeCbl were performed.[139, 145-147] These calculations are a relevant basis for determining the proper computational approach for EtPhCbl and PhEtyCbl. CNCbl has been referred to as the 'paradigm system' for the evaluation of excited states in biological cofactors including Cbl derivatives.[100] CNCbl is quite similar to antivitamins B_{12} as both are biologically inactive derivatives due to the difficulty in photo-cleaving the bond to the upper axial ligand. More specifically, there are key similarities between CNCbl and PhEtyCbl in that the there is no photoproduct formation for either species following excitation.[30] This was attributed to the strength of the Co-C bond in PhEtyCbl and CNCbl where the sp hybridization results in a strong sigma bond in addition to π-bonding interactions that stabilize the bond against cleavage.[30] PhEtyCbl and CNCbl are similar in that both involve a triple bond in their upper ligands. In PhEtyCbl, there is a triple bond between the Co and the PhEty ligand and in CNCbl there is a triple bond between the carbon and nitrogen of the cyano upper ligand.

The use of non-DFT methods has been explored previously for CNCbl, methylcobalamin (MeCbl) as well as one- and two-electron reduced forms of vitamin B_{12}, namely Co(II)Cbl and Co(I)Cbl, where TD-DFT calculations were benchmarked against CASSCF/MC-XQDPT2 and EOM-CCSD calculations.[139, 145, 148, 167] These high-level *ab initio* calculations were compared with low-lying excited states to describe the S_1 state in MeCbl as having MLCT character, a conclusion that has also been confirmed

experimentally with transient absorption and resonance Raman experiments.[139, 145, 147] A major conclusion of this work was that the choice of functional in TD-DFT was paramount in obtaining an accurate description of electronically excited states in MeCbl. In particular, the hybrid functionals (B3LYP, MPW1PW91, and TPSS-h) did not corroborate the experimental and theoretical (CASSCF/MC-XQDPT2 or EOM-CCSD) MLCT assignment, rather they indicated $\pi \rightarrow \pi^*$ character for the $S_0 \rightarrow S_1$ transition. It was shown that the pure GGA (BP86, BLYP, and MPWPW91), meta-GGA (TPSS), and range-separated (LC-BLYP; $\mu = 0$) functionals produced results that are consistent with the MLCT assignment.[139] It should be further noted that CC2 does not work well for cobalamins as exemplified by CNCbl where the energy is significantly underestimated.[145] CASSCF/MC-XQDPT2 as well as EOM-CCSD are computationally very expensive and thus these more much more demanding calculations are essentially not practical for computing PESs of electronically excited states. As a result of the literature precedence, the use of TD-DFT/BP86 is an appropriate way to analyze the excited state properties of antivitamins B_{12}.

2.3 Long Range Charge Transfer

In regard to the potential for underestimation of long-range charge-transfer (LRCT) type excitations energies, Λ parameters[155] were calculated for the antivitamins. These calculations were used to determine whether or not CT-type excitation energies are underestimated. If excitation energies are underestimated, then it is likely due to poor overlap between the occupied and virtual orbitals involved in the transition. The Λ diagnostic results, in the range from 0 to 1, can indicate whether or not poor overlap persists between orbitals involved in the electronic excitation. For GGA-type functionals, if Λ is

less than 0.4, then excitations are likely to be significantly underestimated; conversely, if Λ is greater than 0.4, then excitations are most likely not underestimated.

The results from the Λ diagnostic calculations shown in Tables 3.1 and 3.2 demonstrate that CT-type excitation energies are not significantly underestimated in the investigated antivitamin systems. The results show that Λ is greater than 0.4 for these transitions, particularly for the S_1 and S_2 states the Λ parameter is 0.541 and 0.712, respectively. It should be further noted that due to the dominant cobalt d → d character, CT states were not observed as axial bonds were elongated. These results imply that there is a good degree of spatial overlap between the occupied and virtual orbitals and thus there is confidence that the CT-type excitations energies are not significantly underestimated for either EtPhCbl or PhEtyCbl.

Table 3.1. The four lowest, vertical singlet states and the value of the $S_1 \rightarrow S_0$ transition for Im-[Co^{III}(corrin)]-$EtPh^+$ and [Co^{III}(corrin)]-$EtPh^+$ model complexes.

	E [eV]	λ [nm]	*f*	Λ[a)]	%	Character		Exp. λ[nm] (eV)
					Im-[Co^{III}(corrin)]-$EtPh^+$ (*base-on*)			
S_1	2.22	557.5	0.0002	0.541	50.9	H-1 → L	$\pi + d_{xz} \rightarrow \pi^*$	
					46.3	H-2 → L	$d_{xz} + \pi_{Ph} \rightarrow \pi^*$	
S_2	2.44	506.9	0.0314	0.712	73.5	H → L	$d_{yz} + \pi \rightarrow \pi^*$	525 (2.36)
					11.8	H-1 → L	$\pi + d_{xz} \rightarrow \pi^*$	
S_3	2.48	500.3	0.0462	0.550	46.4	H-2 → L	$d_{xz} + \pi_{Ph} \rightarrow \pi^*$	
					34.6	H-1 → L	$\pi + d_{xz} \rightarrow \pi^*$	
					11.3	H → L	$d_{yz} + \pi \rightarrow \pi^*$	
S_4	2.66	466.6	0.0004	0.302	97.2	H-3 → L	$d_{x2-y2} \rightarrow \pi^*$	
S_{1min}	1.72	720.4	0.0015	0.490	96.6	H → L	$d_{xz} + \pi_{Ph} \rightarrow \pi^*$ (MLCT/LL)	
					[Co^{III}(corrin)]-$EtPh^+$ (*base-off*)			
S_1	2.19	566.8	0.0006	0.506	81.8	H-1 → L	$\pi_{Ph} + d_{xz} \rightarrow \pi^*$	

					14.8	H → L+1	$d_{yz} + \pi \rightarrow \sigma^*(d_z^2)$
S_2	2.22	558.5	0.0064	0.532	62.3	H → L+1	$d_{yz} + \pi \rightarrow \sigma^*(d_z^2)$
					13.6	H-1 → L	$\pi_{Ph} + d_{xz} \rightarrow \pi^*$
					13.5	H → L	$d_{yz} + \pi \rightarrow \pi^*$
S_3	2.33	531.3	0.0040	0.567	84.9	H-1 → L+1	$\pi_{Ph} + d_{xz} \rightarrow \sigma^*(d_z^2)$
S_4	2.42	512.7	0.0307	0.698	67.4	H → L	$d_{yz} + \pi \rightarrow \pi^*$
					13.4	H → L+1	$d_{yz} + \pi \rightarrow \sigma^*(d_z^2)$
$S_{1\ min1}$	1.68	738.8	0.0019	0.482	92.9	H → L	$(d_{xz} + d_{yz}) + \pi_{Ph} \rightarrow \pi^*$ (MLCT/LL)
$S_{1\ min2}$	1.40	888.1	0.0013	0.612	99.0	H → L	$(d_{xz} + d_{yz}) + \pi_{Ph} \rightarrow$ □$^*(d_z^2)$ (LF)

[a] Λ parameters were obtained from TD-DFT/BP86/TZVPP calculations with use Gamess quantum chemistry program.

Table 3.2. The four lowest, vertical singlet states and the value of the $S_1 \rightarrow S_0$ transition for Im-[Co^{III}(corrin)]-$PhEty^+$ and [Co^{III}(corrin)]-$PhEty^+$ model complexes.

	E [eV]	λ [nm]	*f*	Λ[a]	%	Character		Exp. λ[nm] (eV)
					Im-[Co^{III}(corrin)]-$PhEty^+$ (*base-on*)			
S_1	2.05	603.1	0.0019	0.459	93.2	H → L	$\pi_{PhEty} + d_{yz} \rightarrow \pi^*$	
S_2	2.33	531.1	0.0029	0.610	59.9	H-2 → L	$\pi_{Ety} + d_{yz} \rightarrow \pi^*$	
					22.6	H-1 → L	$\pi + d_{z2} \rightarrow \pi^*$	
					14.3	H-3 → L	$\pi_{Ety} + d_{yz} + \pi \rightarrow \pi^*$	
S_3	2.51	493.6	0.0558	0.609	66.5	H-1 → L	$\pi + d_z^2 \rightarrow \pi^*$	550 (2.25)
					21.6	H-2 → L	$\pi_{Ety} + d_{yz} \rightarrow \pi^*$	
S_4	2.56	483.9	0.0034	0.460	87.9	H → L+1	$\pi_{PhEty} + d_{yz} \rightarrow d_{xy}$ - n	
S_{1min}	1.59	777.9	0.0008		97.6	H → L	$\pi_{PhEty} + d_{yz} \rightarrow \pi^*$ (MLCT/LL)	
					[Co^{III}(corrin)]-$PhEty^+$ (*base-off*)			
S_1	1.64	756.9	0.0006	0.528	99.3	H→ L	$\pi_{PhEty} + d_{yz} \rightarrow \sigma^*(d_{z2})$ - n	
S_2	1.94	637.5	0.0017	0.444	93.0	H→ L+1	$\pi_{PhEty} + d_{yz} \rightarrow \pi^*$	
S_3	2.03	609.5	0.0022	0.590	96.3	H-1→ L	$\pi_{Ety} + d_{yz} \rightarrow \sigma^*(d_{z2})$ - n	
S_4	2.29	541.3	0.0021	0.600	74.9	H-1→ L+1	$\pi_{Ety} + d_{yz} \rightarrow \pi^*$	
					14.1	H-2→ L	$\pi_{Ety} + \pi + d_{xz} \rightarrow \sigma^*(d_{z2})$ - n	
S_{1min}	0.98	1259.8	0.0002		99.8	H→ L	$\pi_{PhEty} + d_{xz} \rightarrow \sigma^*(d_{z2})$ – n (LF)	

[a)] Λ parameters were obtained from TD-DFT/BP86/TZVPP calculations with use Gamess quantum chemistry program.

3.0 Results and Discussion

3.1 Structural Properties of Antivitamins

Selected geometric parameters of the S_0 and S_1 optimized structures for the base-on and base-off forms of EtPhCbl and PhEtyCbl model complexes are gathered in Table 3.3. A more detailed list of the geometric parameters for the coordination sphere of cobalt are provided in the Appendix, Tables A.3.1 and A.3.2. The optimized structures for the ground and the excited state are presented in the Appendix, Figures A.3.1 and A.3.2. For the base-on form of both model complexes, the optimized S_0 structural parameters were compared to the corresponding parameters in the crystal structures. The axial bond lengths, valence angles, and the dihedral angles around the coordination sphere of Co all showed good agreement between the optimized geometries and the crystal structures.

Table 3.3. Selected geometric parameters of *base-on* and *base-off* forms of Im-Co^{III}(corrin)]-$EtPh^+$ and Im-[Co^{III}(corrin)]-$PhEty^+$ model complexes for optimized geometries in the ground state (S_0) and in the first excited state (S_1).

Parameter	Im-[Co^{III}(corrin)]-$EtPh^+$ *base-on*			[Co^{III} (corrin)]-$EtPh^+$ *base-off*		
	S_0	Exp.[26]	S_{1min}	S_0	$S_{1\,(min1)}$	$S_{1\,(min2)}$
r[Å]						
Co - C_{1Ph}	1.973	1.981	1.927	1.939	1.847	2.018
Co - N	2.197	2.230	2.107			
Valence angle[°]						
C_{1Ph} -Co - N	179.4	176.5	171.1			
N_{21} - Co – N_{23}	171.7	172.9	170.9	164.7	155.6	145.8
N_{22} - Co – N_{24}	173.4	171.6	172.8	171.1	167.6	171.1
Dihedral angle [°]						
N_{21} – N_{22} – N_{23} - Co	-3.9	-3.6	-4.3	-10.0	-16.6	-23.1

	Im-[Co^{III}(corrin)]-$PhEty^+$ *base-on*			[Co^{III}(corrin)]-$PhEty^+$ *base-off*	
	S_0	Exp.[28]	S_{1min}	S_0	S_{1min}
r[Å]					
Co – C_{1Ety}	1.860	1.861	1.775	1.820	1.857
Co - N	2.084	2.084	2.057		
Valence angle[°]					
C_{1Ety}-Co - N	179.2	178.6	178.7		
N_{21} - Co – N_{23}	173.0	173.4	170.7	165.5	148.0
N_{22} - Co – N_{24}	172.3	172.1	172.6	172.0	168.8
Dihedral angle [°]					
N_{21} – N_{22} – N_{23} - Co	-1.9	-0.5	-4.0	-9.3	-21.9

For Im-[Co^{III}(corrin)]-$EtPh^+$, the optimized axial bond lengths are 1.973 and 2.197 Å for the Co-C_{1Ph} and Co-N_{Im}, respectively. In the crystal structure, these bonds are 1.981 and 2.230 Å. For Im-[Co^{III}(corrin)]-$PhEty^+$, the optimized bond lengths of the Co-C_{1Ety} and Co-N_{Im} axial bonds are 1.860 and 2.084 Å, respectively. In the crystal structure these bonds are 1.861 and 2.084 Å. The axial bonds in the optimized geometries of the lowest singlet excited state (S_{1min}) are slightly shorter compared to the geometry of the S_0. Shortening of the axial bonds is observed for both of the S_1 model complexes. The optimized geometry of the S_0 for the base-off models is also characterized by a small shortening of the Co-C axial bond in comparison to the S_0 for the base-on form. According to the results from Table 3.3, the length of Co-C_{1Ph} and Co-C_{1Ety} axial bonds is 1.939 and 1.820 Å for [Co^{III}(corrin)]-$EtPh^+$ and [Co^{III}(corrin)]-$PhEty^+$, respectively. Generally, for the base-on and base-off forms of both antivitamins, the calculated valence and dihedral angles from the optimizations showed good agreement with experiment (Table 3.3). However, it should be noted that for the S_0 and S_1 optimized geometries, the coordination sphere of the base-off form is more distorted. This is clearly visible when comparing the N_{21}-Co-N_{23} and N_{21}-

N_{22}-N_{23}-Co angle values between the base-off and base-on forms of the model complexes. For the base-off forms, the valence angles (N_{21}-Co-N_{23}) are smaller, whereas the dihedral angles (N_{21}-N_{22}-N_{23}-Co) are larger in comparison to those of base-on form (Table 3.3).

3.2 Absorption Spectra of Antivitamins

The characteristic features of the Abs spectra of Cbls arise from the oxidation state of the Co as well as the nature of the upper and lower axial ligands.[2, 5, 197-199] When comparing Abs spectrum of Cbls to each other, and variations in the spectra are accompanied by changes in oxidation and ligation. These variations have been intensively scrutinized and are the topic of two important contributions in B_{12} literature.[197, 198] The features in the UV-visible spectra of Co corrinoids are usually designated by, α, β, γ , and δ. The α and β bands are typically referred to as the α/β region, and these are located in the visible region (ε ~8,000 - 10,000 M^{-1} cm^{-1}). The γ band is found in the UV (ε ~ 25,000 $M^{-1}cm^{-1}$) and can also be referred to as the Soret band. The δ band occurs in the region less than 300 nm. In addition, low-intensity bands around 400 nm are referred to as D and E as these are separate transitions from those designated with the Greek letters. As a side note, the naming system for the Abs spectra of Co corrinoids is based on the Abs nomenclature used for porphyrins.

Cbls' Abs spectra can be designated as normal or anomalous[73] and sometimes as typical or unique.[200] Normal Abs spectra are marked by an α band that is more intense than the β band. For anomalous spectra, this is reversed and the β band is more intense than the α band. However, the major difference between the normal and anomalous Abs spectra is with the γ band. In normal spectra, the γ band is quite obviously the Soret band and is the most intense feature. An intense γ band is not present in anomalous Abs spectra. Rather,

transitions that would correspond to an intense γ band in a normal spectrum are distributed over a larger range of wavelengths in the UV region. Notably, the Abs spectra for CNCbl and H_2OCbl^+ are representative of the normal type, while MeCbl and AdoCbl Abs spectra can be classified as anomalous. The spectra of some lesser-known derivatives, NO_2Cbl, SCNCbl, ClCbl, N_3Cbl, CNCbl, and (i-Pr)$_2$-phosphitoCbl, could be classified as typical and those of SO_3Cbl, SeCNCbl, MeCbl, AdoCbl and isoamylCbl as unique.

For CNCbl, there are two distinctive bands including the γ and α/β bands.[100] The γ band (360 nm) is located in the UV part of the Abs spectrum, whereas the α/β band, with a maximum at 550 nm, occurs in the visible region. The α/β bands arise primarily from the $\pi \rightarrow \pi^*$ transition, and the α-band is more intense than the β band. AlkylCbls such as MeCbl and AdoCbl differ in their UV-visible spectra when compared to the "typical" CNCbl spectrum.[200] In the region of the α/β band, the β-band is more intense. PhEtyCbl has an α/β band that is similar to that of CNCbl and has a very pronounced γ band.[30] EtPhCbl's α/β band is blue-shifted and is more similar to AdoCbl's UV-visible spectrum.[30]

To obtain the electronic spectra of the two antivitamins under study, 25 singlet electronic transitions were calculated using TD-DFT from the S_0 optimized geometries (Table A.3.3 and A.3.4). The calculated excitations (black lines) along with the corresponding simulated Abs spectra are shown in Figure 3.3 and 3.4. In order to allow a comparison with the simulations, the experimental Abs spectra (blue lines) are also presented in the figures. The simulated spectra for both models of antivitamins are slightly shifted by about 25-50 nm in the direction of higher energy in relation to experiment. Such a shift, as a consequence of an overestimation of transition energy, is characteristic of TD-DFT results for non-alkylCbls, e.g., CNCbl.[145] Despite this, the resulting shape of the

simulated spectral lines are very similar to the experimental spectra. For both model complexes, the simulated spectra have a visible band in the range from ~450 to ~550 nm which can be assigned to the *α/β* band from experiment. In this range, the simulated spectrum for Im-[Co^{III}(corrin)]-$EtPh^+$ contains four singlet electronic transitions, S_1-S_4. For the second model, Im-[Co^{III}(corrin)]-$PhEty^+$, the low energy part of calculated spectrum is determined by six excitations, S_1-S_6. The calculated transitions in the range of the *α/β* band have different values for the oscillator strength, but one transition (S_3) in the case of Im-[Co^{III}(corrin)]-$PhEty^+$ and two transitions (S_2 and S_3) in the case of Im-[Co^{III}(corrin)]-$EtPh^+$ have relatively large intensity. The remaining transitions have medium or very small oscillator strengths. It is worth mentioning that in the case of both model complexes there are low-lying excited states for which electronic transitions have very small oscillator strengths. Two such transitions at 603 and 531 nm and one at 557 nm exist for Im-[Co^{III}(corrin)]-$PhEty^+$ and Im-[Co^{III}(corrin)]-$EtPh^+$, respectively. These transitions are very interesting because they can play a crucial role in photochemical processes.

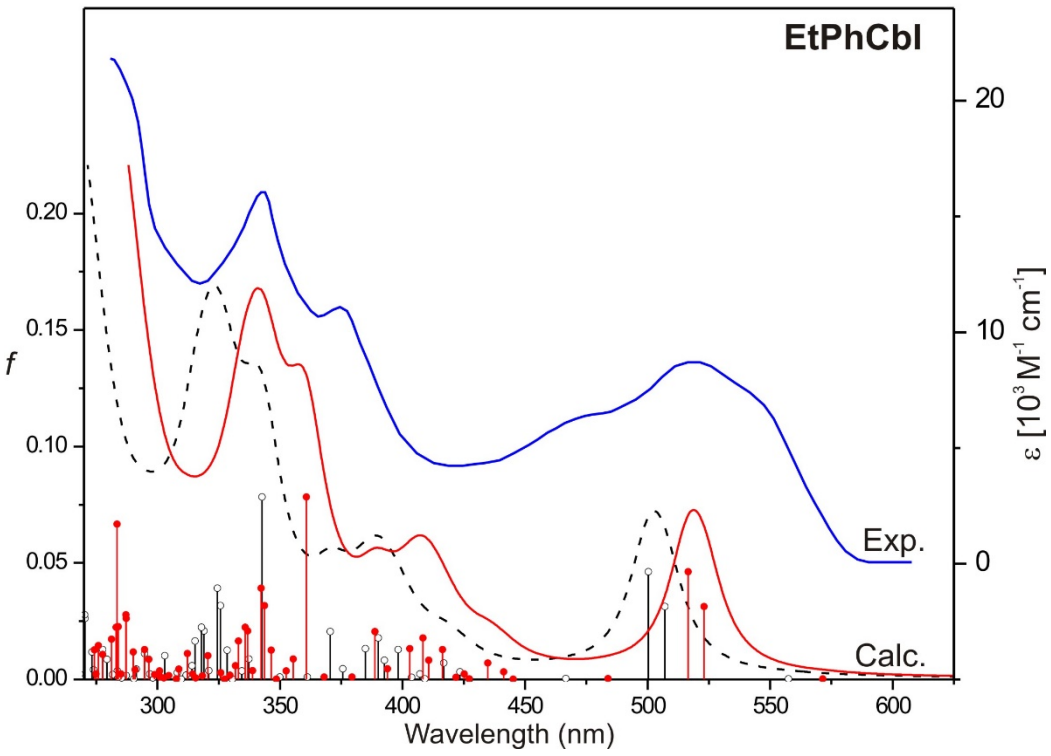

Figure 3.3. The experimental (blue) and the TD-DFT simulated Abs spectra for Im-[Co^{III}(corrin)]-$EtPh^+$ model complex: not scaled (black) and scaled (red) with □(S_3) and □(S_{25}). Simulation based on TD-DFT/BP86 calculations in water solution. Experimental spectra from Miller, *et al*. *J. Am. Chem. Soc.* **2016,** *138* (43), 14250-14256.

The second characteristic band for cobalamins, the *γ* band, can be also identified in the simulated electronic spectra, especially for Im-[Co^{III}(corrin)]-$EtPh^+$. The two maxima between 300 nm -360 nm in the simulated spectrum of the Im-[Co^{III}(corrin)]-$EtPh^+$ can be ascribed to the two separated peaks that are observed in the *γ* band region of the experimental spectrum. The transition with the largest oscillator strength in this part of the calculated spectrum is S_{19} at 343 nm (Table A.3.3) and can be attributed to the first peak at ~375 nm in the experimental spectrum. The second peak, which is apparent both in the simulated and experimental spectrum, is a superposition of several close electronic transitions, S_{24}-S_{29}, which have moderate oscillator strength. Two of them, S_{24} at 326 nm and S_{25} at 324 nm (Table A.3.3), should have the greatest impact on the location and

intensity of the second peak in the γ region. For Im-[Co^{III}(corrin)]-$PhEty^{+}$, the γ band is less pronounced in the simulated spectrum because the intensity of this band is not well reproduced in calculations. The experimental γ band reasonably correlates to the maximum of the simulated spectrum located between ~345 nm and ~390 nm. In this range, nine electronic transitions S_{15}-S_{23} are identifiable (Table A.3.4). The excitations forming the γ band have rather moderate or small oscillator strengths except for one transition at 360 nm. This transition (S_{19}) has a large oscillator strength value (f = 0.0742) and correlates with the maximum of the experimental γ band.

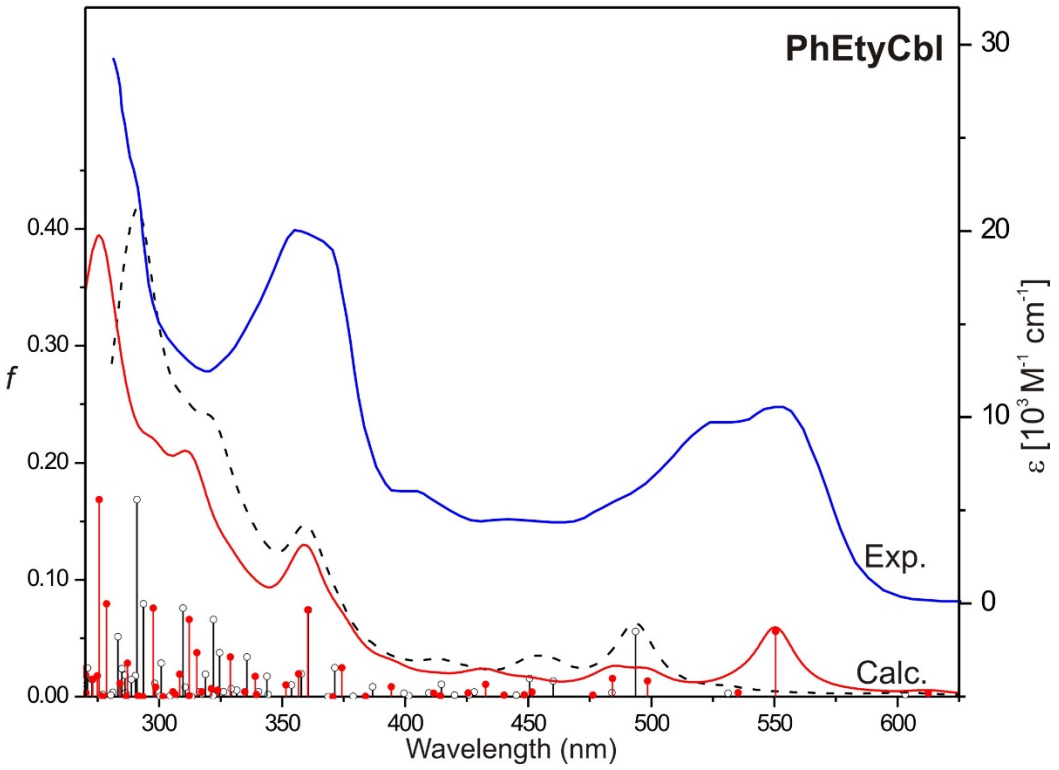

Figure 3.4. The experimental (blue) and the TD-DFT simulated Abs spectra for Im-[Co^{III}(corrin)]-$PhEty^{+}$ model complex: not scaled (black) and scaled (red) with □(S_3) and □(S_{19}). Simulation based on TD-DFT/BP86 calculations in water solution. Experimental spectra from Miller *et al*. *J. Am. Chem. Soc.* **2016,** *138* (43), 14250-14256.

To further improve the agreement between experiment and theory, a scaling procedure was applied to the electronic transitions. The calculated spectra of both investigated model complexes were scaled using the following equation (2.1) from a previous theoretical study of Cbl Abs spectra.[124, 125]

$$E^{i}_{scaled} = \xi E^{i}_{TDDFT} + E_{shift} \quad (2.1)$$

The *i*th electronic excitations computed via TD-DFT are represented by E^{i}_{TDDFT}. ξ and E_{shift} are empirical parameters used to adjust the computed spectrum to be in-line with the experiment. For each spectrum, an optimal set of two scaling parameters, ξ and E_{shift}, were determined under the assumption that the energies of the electronic excitations associated with the α and γ bands should be reproduced precisely. The most intense $S_0 \rightarrow S_3$ transitions, at 500 and 494 nm for Im-[Co^{III}(corrin)]-$EtPh^+$ and Im-[Co^{III}(corrin)]-$PhEty^+$, respectively, were assigned to the maximum of lowest energy Abs band. For the γ band, several different transitions were tested to determine the optimal scaling parameters. On this basis, it was concluded that the energy of the $S_0 \rightarrow S_{24}$ excitation at 324 nm for Im-[Co^{III}(corrin)]-$EtPh^+$ and the $S_0 \rightarrow S_{19}$ excitation at 360 nm for Im-[Co^{III}(corrin)]-$PhEty^+$ should be assigned to the maximum of the experimental γ band. The results for the scaled spectra are shown in Figures 3.3 and 3.4 (red lines). The simulated spectra for both model complexes are in good accordance with experiment and agree well in regard to the characteristic features of spectral line of Cbls.

The electronic structures of the calculated excited states were obtained on the basis of analysis of the frontier Kohn-Sham molecular orbitals (KS MOs) involved in the TD-DFT electronic excitations. Figures 3.5 and 3.6 contain images of relevant MOs involved in the electronic excitations for the base-on analogues. The characters of the transitions for

the four low-lying singlet excited states of Im-[Co^{III}(corrin)]-$EtPh^+$ and Im-[Co^{III}(corrin)]-$PhEty^+$ are presented in Tables 3.1 and 3.2, respectively. For Im-[Co^{III}(corrin)]-$EtPh^+$ the S_1 state is the result of electronic transitions from the HOMO-1 and HOMO-2 orbitals to the LUMO orbital, and this corresponds to the $\pi + d_{xz} \rightarrow \pi^*$ (51%) and $d_{xz} + \pi_{Ph} \rightarrow \pi^*$ (46%) excitations. Both of these excitations can be characterized as MLCT transitions. The S_1 transition for Im-[Co^{III}(corrin)]-$PhEty^+$ is also MLCT type and has been characterized as HOMO to LUMO, $\pi_{PhEty} + d_{yz} \rightarrow \pi^*$ (93%), excitation. The remaining low-lying singlet states for both species have similar character to the S_1 state. These states are mainly a result of $\pi/d \rightarrow \pi^*$ excitations, excluding the S_4 transition for Im-[Co^{III}(corrin)]-$PhEty^+$ which is $\pi/d \rightarrow d$ type. In the case of the base-off forms, the characters of the low energy transitions are rather diametrically opposed. The lowest singlet states are dominated by $\pi/d \rightarrow \sigma^*(d_{z2})$ excitations, therefore the states are of predominantly the LF type. These results clearly show that detachment of the axial base causes a change in the order of MLCT and LF states. Thus, unlike the base-on forms, the S_1 state of the base-off forms has mostly $d \rightarrow \sigma^*(d_{z2})$ character.

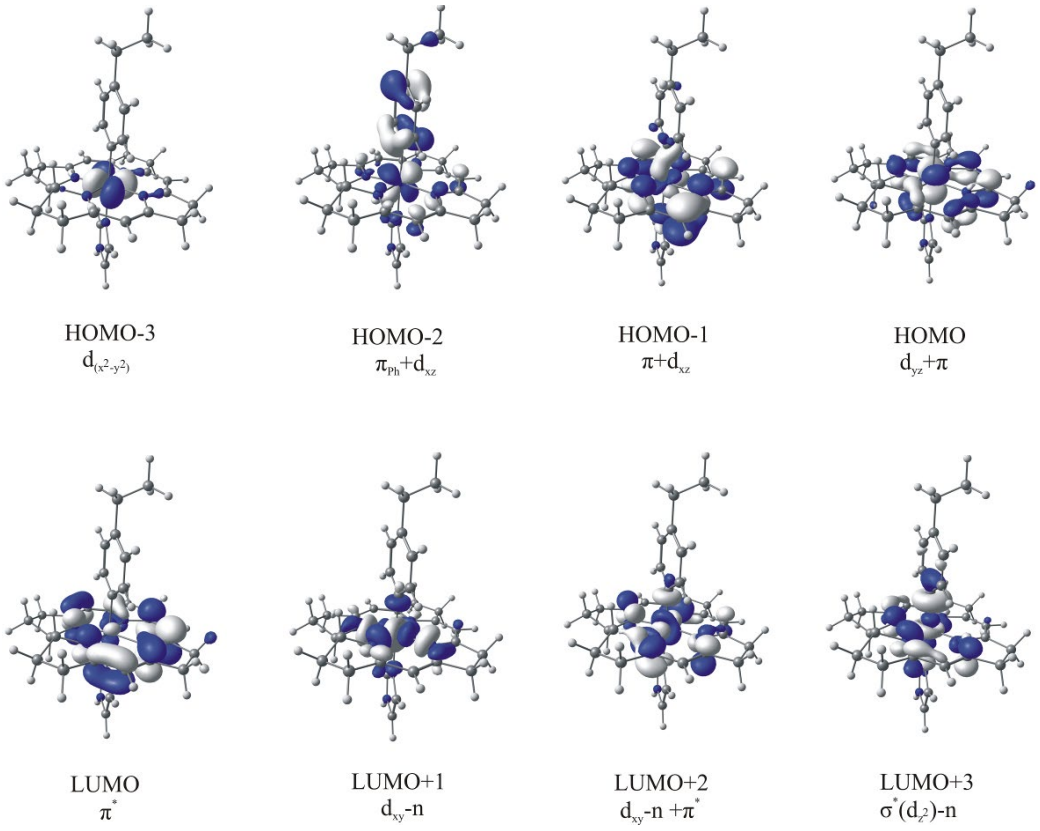

Figure 3.5. Selected molecular orbitals involved in electronic excitations for Im-[Co^{III}(corrin)]-$EtPh^+$

For the optimized S_{1min} geometry of Im-[Co^{III}(corrin)]-$EtPh^+$, the excited state is HOMO → LUMO transition and is characterized as $d_{xz} + \pi_{Ph} \rightarrow \pi^*$ (97%, MLCT/LL, LL = ligand-to-ligand CT). For the base-off form, there are two S_1 minima, $S_{1(min1)}$ and $S_{1(min2)}$, and these are characterized as $(d_{xz} + d_{yz}) + \pi_{Ph} \rightarrow \pi^*$ (93%, MLCT/LL) and $(d_{xz} + d_{yz}) + \pi_{Ph} \rightarrow \sigma^*(d_{z2})$ (99%, LF). The S_{1min} for optimized geometry of Im-[Co^{III}(corrin)]-$PhEty^+$ is characterized as $\pi_{PhEty} + d_{yz} \rightarrow \pi^*$ excitation (98%, MLCT/LL). For [Co^{III}(corrin)]-$PhEty^+$ the S_{1min} is characterized as LF state and corresponds to the $\pi_{PhEty} + d_{xz} \rightarrow \sigma^*(d_{z2})$-n transition (99%). A complete list of the lowest vertical singlet states and their corresponding orbital characterizations for the base-off models can be found in Table A.3.5

for [Co^{III}(corrin)]-$EtPh^+$ and Table A.3.6 for [Co^{III}(corrin)]-$PhEty^+$. Images for the corresponding orbitals are depicted in Figures A.3.3 and A.3.4.

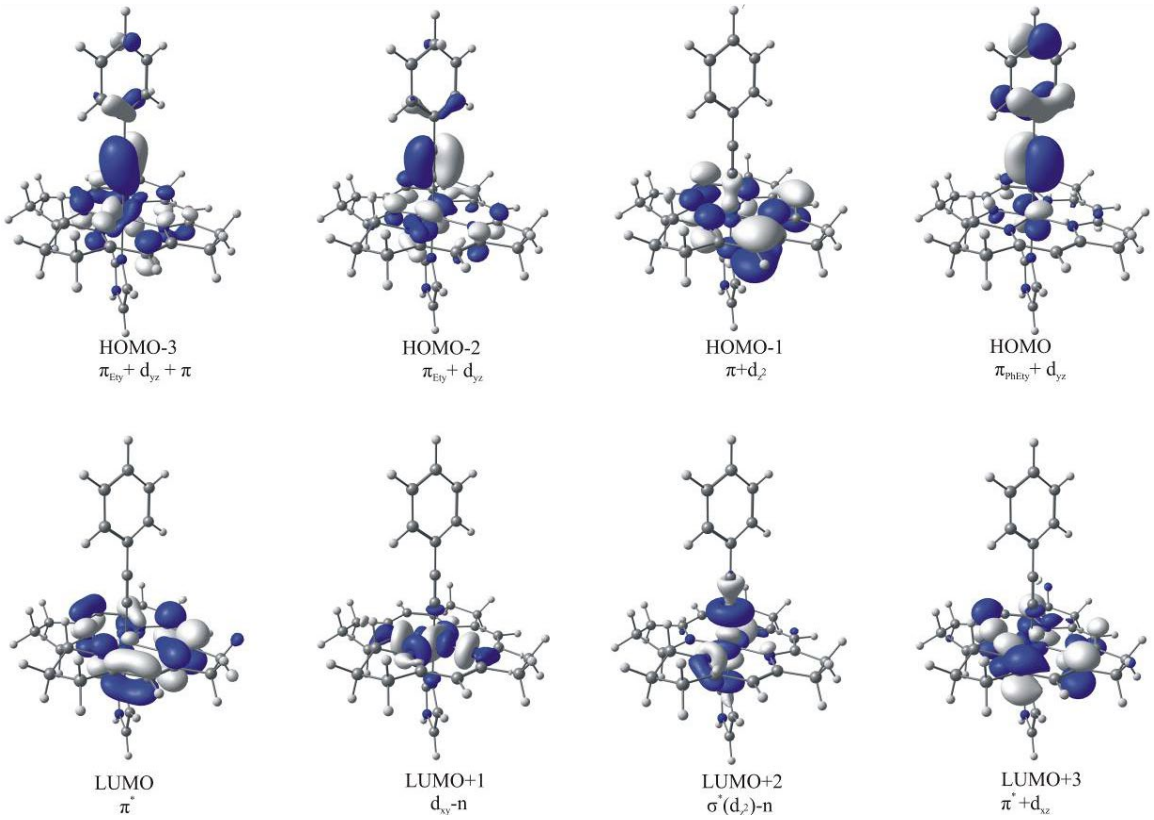

Figure 3.6. Selected molecular orbitals involved in electronic excitations for a) Im-[Co^{III}(corrin)]-$PhEty^+$

3.3 Construction of PESs and Energy Profiles

To explore the mechanism of Co-C bond photodissociation, PESs corresponding to the S_1 state were constructed as a function of axial bond lengths. These bonds experience the most significant changes upon electronic excitations while the corrin structure is maintained. This has been shown theoretically and experimentally with XANES measurements reported for CNCbl.[110, 172] It should be expected, especially in the case of PhEtyCbl, that the XANES spectrum of antivitamins B_{12} and CNCbl would be similar. The involvement of triplet states was not considered, based on magnetic effects measurements

that suggest that this is unlikely.[99, 132] Prior to constructing the S_1 surfaces, the S_0 PESs were constructed by optimizing the geometries associated with the structures resulting from the systematic elongation of the two axial bonds. The PESs for the low-lying S_1 and S_2 states of Im-[Co^{III}(corrin)]-$EtPh^+$ and Im-[Co^{III}(corrin)]-$PhEty^+$ were constructed from the manifold of vertical excitations (Figure A.3.5). The relaxed PESs representing the S_1 state were obtained by optimizing the corresponding excited state geometries (Figures 3.7 and 3.8). Overall, comparison of the S_1 PESs based on vertical excitations (Figure A.3.5) with the relaxed S_1 PESs (Figures 3.7 and 3.8) show that the surfaces do not significantly differ from each other in regard to topology, relative energetics, and the character of the minima regions.

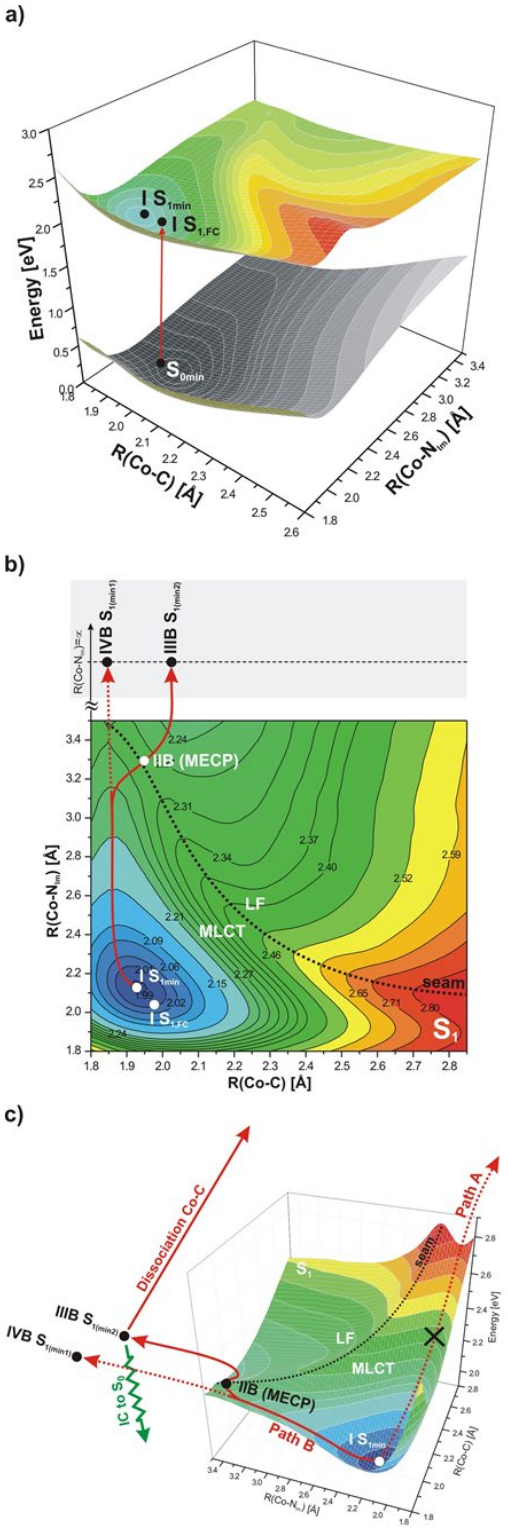

Figure 3.7. a) Potential energy surfaces (PESs) as function of axial bond lengths for optimized geometry of the ground state S_0 and optimized geometry of the S_1 excited state of Im-[Co^{III}(corrin)]-$EtPh^+$ model complex, b) vertical projections of S_1 PES, c) scheme of photoreaction for Im-[Co^{III}(corrin)]-$EtPh^+$ model complex.

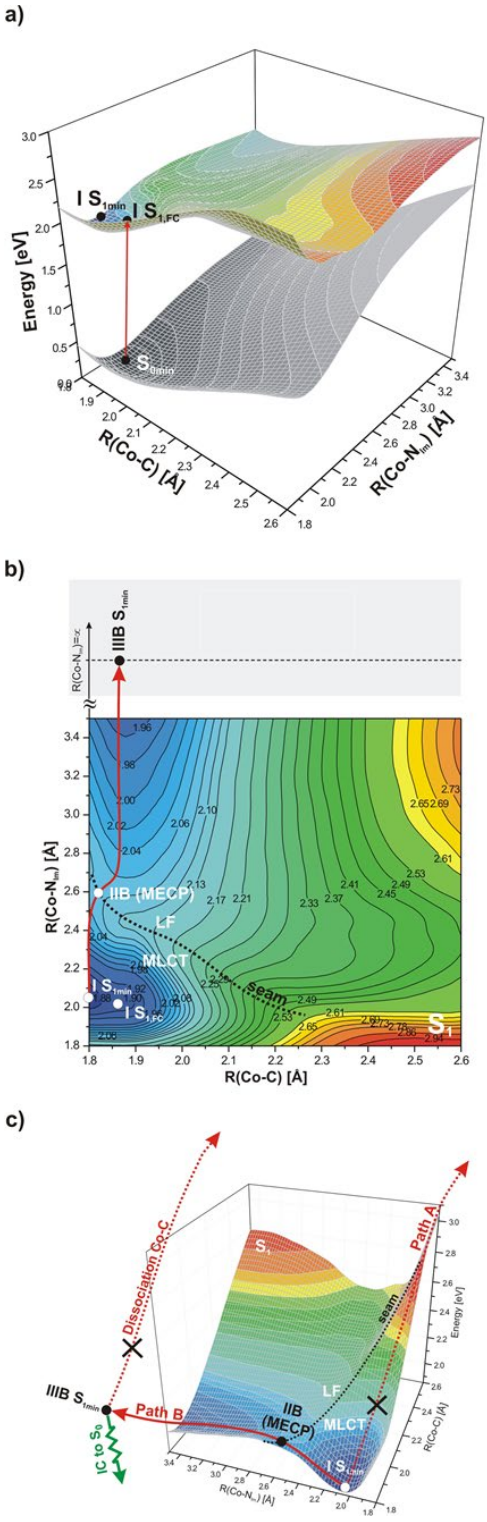

Figure 3.8 a) Potential energy surfaces (PESs) as function of axial bond lengths for optimized geometry of the ground state S_0 and optimized geometry of the S_1 excited state of Im-[Co^{III}(corrin)]-$PhEty^+$ model complex, b) vertical projections of S_1 PES, c) scheme of photoreaction for Im-[Co^{III}(corrin)]-$PhEty^+$ model complex.

3.4. Interpretation of Photochemical Data Based on PESs

The PES of the S_1 state for both antivitamin models have characteristic topology, similar to the S_1 PESs of other Cbls. Basically, the shape of this surface is the result of the intersection between two surfaces of electronic states with different character, MLCT and LF. As a consequence, the surface of the lowest singlet state has two minima: One occurs for shorter axial bonds, while the second corresponds to elongated bonds. Photochemical conversion between the two minima regions requires overcoming an energetics barrier, with localization and height usually dependent upon the character of the upper axial ligand. Among the available photochemical paths, the preference is for the path with the smallest energetic barrier. The energetics profile of the photoreaction on the S_1 surface will be different for each path and depends on the initial reaction step from the MLCT minimum, i.e., from which the axial coordinate undergoes elongation first. There are two possible photoreaction pathways (paths A and B) that were identified. These are depicted on Figures 3.7 and 3.8. Path A involves initially lengthening the Co-C bond from the MLCT I S_{1min} minimum, followed by the subsequent elongation of Co-N_{Im}. In contrast, path B involves the lengthening of the Co-N_{Im} bond through the MLCT region to the LF stationary point. The stable intermediate for path B involves a LF state responsible for Co-C bond dissociation. Conversion to the ground state prior to dissociation is possible via out-of-plane distortion of the corrin ring at the stationary point of the LF state. A second possible mechanism of IC can engage deactivation of the electronically excited photoproduct $[Co^{II}(corrin)]^{+}$.[120]

From a theoretical point of view, regardless of whether Co-C photodissociation involves paths A or B, the result is the formation of the same RP products in the case of

homolytic cleavage. The general RP products, for Cbls include $N_{base}\cdots[Co^{II}(corrin)]^* + \bullet R$, where $N_{base}\cdots[Co^{II}(corrin)]^*$ (N_{base} can be DBI, Im, or water) denotes the electronically excited states of the Co^{II}Cbl, while •R is the corresponding radical. It seems as though the Co-N_{base} bond does not ultimately break when the base-on configuration is present, but it is significantly elongated as the upper axial ligand dissociates. It also has been demonstrated that the Co-N_{base} distance controls the nature of the electronically excited states of the Co(II) species. However, whether or not the Co-C bond finally breaks is dependent upon the nature of the upper axial ligand.

3.5 EtPhCbl PES

The PESs gathered in Figures 3.7 and A.3.5 show the locations of the energy minima for the S_0, S_1, and S_2 electronic states of Im-[Co^{III}(corrin)]-$EtPh^+$. The relaxed S_1 PES indicates two distinct regions that are low in energy that are delineated by a seam (Figure 3.7b,c). The first is located in the area of the projection corresponding to shorter Co-C and Co-N_{Im} bond lengths and is denoted by the point I S_{1min}. The second low energy region is located in the area of PES where Co-C distances are short and Co-N_{Im} distances are elongated. The highest energy for both the S_1 and S_2 states is found in the part of the surface that corresponds to the longest Co-C bond lengths and short Co-N bond lengths and this region is shown as a bright red color in the PESs gathered in Figures 4 and S7.

The S_2 state has one particularly shallow energy minima in the region of shorter Co-C and longer Co-N_{Im} bond distances (Figure A.3.5). On the S_1 surface, as shown in Figure 3.7c, there is a steep increase in energy as the Co-C bond is lengthened. This steep increase in energy is not observed as the Co-N_{Im} bond is lengthened simultaneously with Co-C. The S_1 minima regions result from the interaction of at least two different electronic

states. The region associated with shorter Co-C axial bond lengths corresponds to MLCT transition, whereas the minimum associated with longer Co-C and Co-N_{Im} bonds corresponds to LF excitation, which has dominant cobalt d → d character. Charge transfer states for the elongated axial bond were not observed because the LF state primarily involves electronic excitation localized on the Co. Additionally, in Figure 3.7c, besides the minimum I S_{1min} in the MLCT region of the PES, several other stationary points in the LF part of surface are shown. IIB (MECP) denotes the minimum energy crossing point of path B. The two local minima on either side of the seam in the LF region are the MLCT minimum (IVB $S_{1(min1)}$) and the LF minimum (IIIB $S_{1(min2)}$), which correspond to the structure with the completely detached axial base from the Co center.

3.6. Photodissociation and Energy Profiles of EtPhCbl Photoreaction

In the case of Im-[Co^{III}(corrin)]-$EtPh^+$, photodissociation involving path A is ineffective as it is not energetically feasible due to the steep increase in energy. Conversely, path B is effective where elongation of the Co-N_{Im} bond initially involves the MLCT region up to the distance of ~3.4 Å where crossing of the seam through the MECP, labeled as IIB, takes place. At this stage, the crossing between MLCT and LF electronic states is essentially barrierless, as discussed in more detail later, and the photoreaction further proceeds via elongation of the Co-C bond through the LF region. Consequently, the final dissociation of the Co-C bond would start from IIIB $S_{1(min2)}$ point. In addition to photodissociation, IC to S_0 may take place from LF minimum.

The energetics of the photoreaction along path B for the Im-[Co^{III}(corrin)]-$EtPh^+$ model complex is shown in Figure 3.9 for key points along the reaction path. Upon excitation at a wavelength of 557 nm promotion to the S_1 state will occur and

simultaneously, excitation at 507 nm leads to population of the S_2 state. There is an energy difference of 5.1 kcal/mol between these two electronic levels (Figure 3.9). After vertical excitation, the system undergoes relaxation to the energy minimum of the lowest singlet state, thus on the photoreaction path, the first intermediate state corresponds to the minimum in the MLCT region, I S_{1min}. The photoreaction then leads to the MECP, requiring 6.2 kcal/mol. Outside the MECP point, in the area of the LF state there is a relaxation, which ends in IIIB $S_{1(min2)}$ stationary point. At this point of photoreaction, the stable intermediate in the excited state is created. From the IIIB minimum there is a competition between photodissociation and IC to S_0. There is not a significant difference in the energy required to overcome the barrier for either of these processes. IC and photodissociation would require 14.5 and 10.3 kcal/mol, respectively (Figure 3.9), which suggests that both processes can be competitive. These theoretical insights also corroborate recent experimental findings.[30]

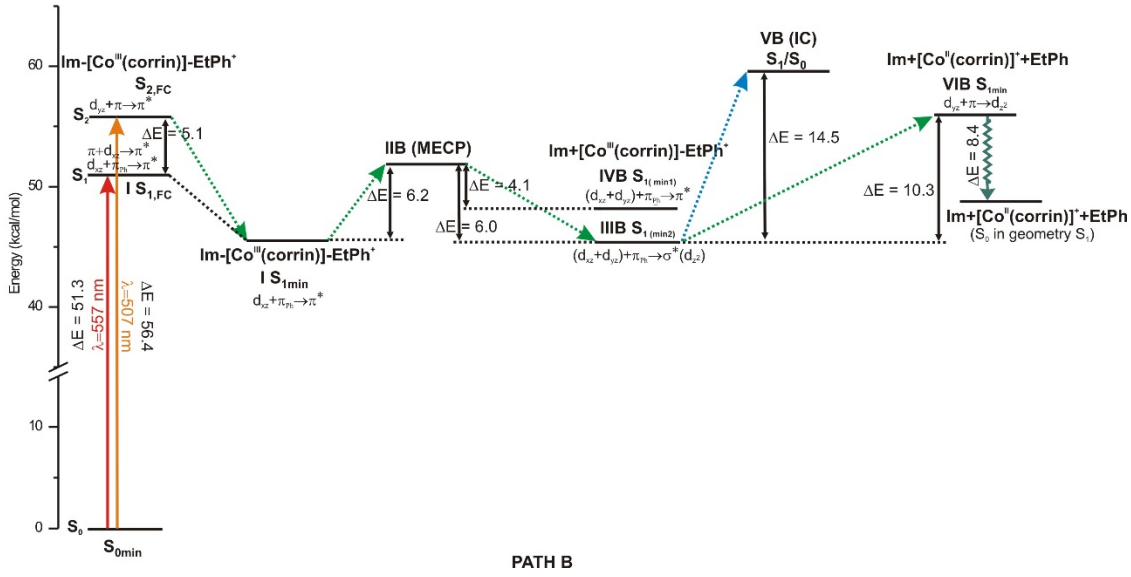

Figure 3.9. Energy diagram of photoreaction on Path B for Im-[Co^{III}(corrin)]-$EtPh^+$ model complex (ΔE values in kcal/mol).

3.7 PhEtyCbl PES

The PESs gathered in Figures 3.8 and A.3.5 show the locations of the energy minima for the S_0, S_1, and S_2 electronic states of Im-[Co^{III}(corrin)]-$PhEty^+$. The relaxed S_1 PES indicate two regions that are low in energy and separated by a seam. The S_1 minima regions result from the interaction of at least two different electronic states. The region associated with shorter Co-C axial bond lengths corresponds to the MLCT transition, whereas the minimum associated with longer Co-C and Co-N_{Im} bonds corresponds to LF excitation. The first minimum is located in the area of the projection corresponding to shorter Co-C and Co-N_{Im} bond lengths and is denoted by the point I S_{1min}. The second low energy region is located in the region where Co-C distances are short (1.8-2.3 Å) and Co-N_{Im} distances are elongated (2.6-3.4 Å). Long Co-C bonds are associated with the high energy regions on the S_1 PES, and a steep increase in energy occurs as the Co-C bond is lengthened while the Co-N bond remains unperturbed.

The PES in Figure 3.8 shows several stationary points. The MLCT minimum is denoted I S_{1min}. IIB (MECP) denotes the minimum energy MLCT/LF crossing point of path B. In the LF region of the surface, the elongation of the Co-N_{Im} bond is associated with the detachment of the axial base from the Co center and point IIIB S_{1min} corresponds to a stable intermediate in the base-off form, which can undergo IC to S_0.

3.8 Ineffective Photodissociation and Energy Profiles of PhEtyCbl Photoreaction

For PhEtyCbl, as for parent CNCbl, photodissociation is not feasible from an experimental point of view.[30] This finding is corroborated by the theoretical results for Im-[Co^{III}(corrin)]-$PhEty^+$. Like Im-[Co^{III}(corrin)]-$EtPh^+$, there are two possible routes for Co-C bond dissociation upon inspection of the S_1 PES (Figure 3.8c). Path A, which involves

the elongation of the Co-C bond while the Co-N bond remains unchanged, is not energetically favorable. Conversely, path B is characterized by a low energy barrier between the MLCT and LF regions and thus it is significantly more energetically advantageous; however, this path will result in IC to S_0 and not in photodissociation. This path involves the elongation of the Co-N bond starting from the MLCT minimum (I S_{1min}, Figure 3.8) and proceeds through the seam at the MECP point until the system reaches the LF region. After crossing the IIB (MECP) point, on the surface of the LF electronic state, the relaxation to III B minimum occurs. Competition between two processes, i.e., IC and photodissociation from this minimum, is dependent upon the height of the energy barrier of these processes. In the case of the discussed complex, IC is the more favorable process.

The energetics for the photoreaction along path B for Im-[Co^{III}(corrin)]-$PhEty^+$ are shown in Figure 3.10. There are some general similarities with the photoreaction of the Im-[Co^{III}(corrin)]-$EtPh^+$ model complex, but the biggest differences are in the magnitude of the energies between the various points along the reaction pathway. The S_1 and S_2 states are populated upon excitation with a wavelength of 603 and 531 nm, respectively, whereby both excitations have small oscillator strength values. From among the remaining electronic states in the α/β region, S_3 is the most probable electronic state, which is populated during absorption at about 550 nm (calculated 493 nm). First, after the initial excitation, there is a relaxation to the MLCT minima, I S_{1min}, which is energetically favorable. To reach the MECP 5.3 kcal/mol of energy is required prior to reaching the second minima IIIB S_{1min}, in the LF region. From this point, there is a significant energetic preference for IC to S_0 instead of photodissociation. On the basis of these calculations, relaxation to S_0 from point IIIB S_{1min} requires overcoming a barrier equal to only 9.7

kcal/mol, whereas the calculated energy for photodissociation is about 39.8 kcal/mol (Figure 3.10).

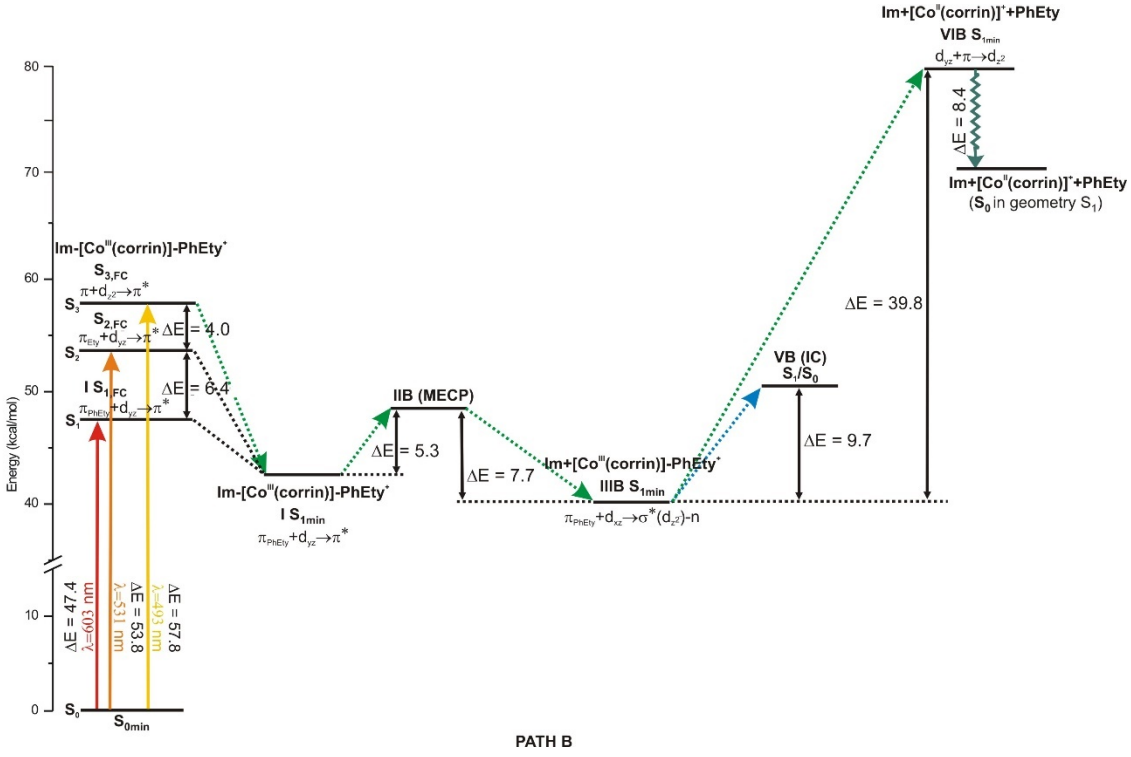

Figure 3.10. Energy diagram of photoreaction on Path B for Im-[Co^{III}(corrin)]-PhEty^{+} model complex (ΔE values in kcal/mol).

3.9 Mechanism of Internal Conversion

The mechanism for IC for the [Co^{III}(corrin)]-EtPh^{+} and [Co^{III}(corrin)]-PhEty^{+} can be understood using a PES constructed as a function of Co-C bond length and N_{21}-Co-N_{23} valence angle (Figure 3.11). The model structures mentioned above correspond to complexes with a fully detached axial base. Upon visual inspection of these PESs, it is apparent that the S_0 and S_1 surfaces cross. It is at this crossing that IC can occur. The minimum energy path for IC with [Co^{III}(corrin)]-EtPh^{+} and [Co^{III}(corrin)]-PhEty^{+} begins at point IIIB and proceeds to VB (IC) which is the point where the S_1 and S_0 surfaces cross.

From IIIB $S_{1(min2)}$ to VB (IC), 14.5 kcal/mol is required to overcome the barrier for IC in the case of the [Co^{III}(corrin)]-$EtPh^+$ complex. The IC process for the second antivitamin, [Co^{III}(corrin)]-$PhEty^+$, is more energetically favorable than for [Co^{III}(corrin)]-$EtPh^+$ as only 9.7 kcal/mol is required from the first point to the second on the path of minimal energy.

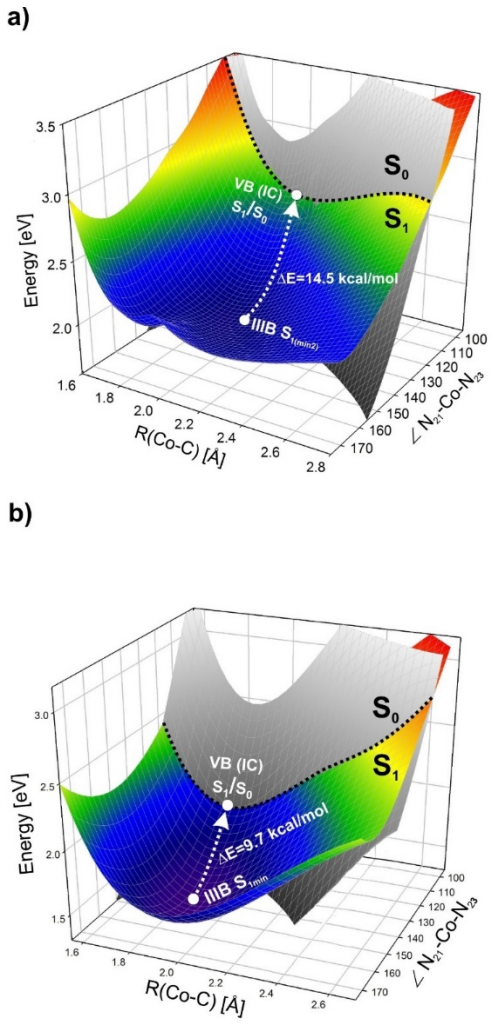

Figure 3.11. Potential energy surface for the S_1 optimized geometry as a function of Co-C bond length and N_{21}-Co-N_{23} valence angle with the minimum energy path for S_1/S_0 internal conversion (IC) depicted for a) [Co^{III}(corrin)]-$EtPh^+$ and b) [Co^{III}(corrin)]-$PhEty^+$ model complexes.

Deactivation can be further considered upon inspection of the PECs in Figure 3.12. These PECs correspond to geometries where the axial base is fully detached, and they are extrapolations of the PESs in Figures 3.7c and 3.8c. For [Co^{III}(corrin)]-$EtPh^+$, Figure 3.12a, it is apparent from the S_1 curve that the photochemical reaction takes place essentially barrierless between the crossing of the two electronic states, MLCT and LF. For [Co^{III}(corrin)]-$PhEty^+$ (Figure 3.12b) is not observed. This is to be expected as the seam for the PES corresponding to the photodissociation (Figure 3.8c) is not as distinctive. It is also of note that the excitation to the S_1 curve for [Co^{III}(corrin)]-$PhEty^+$ (~1.40 eV), is much lower in energy than [Co^{III}(corrin)]-$EtPh^+$ (~2.1 eV). There is a gap between the S_0 curves and the S_1 curve for [Co^{III}(corrin)]-$EtPh^+$ whereas for [Co^{III}(corrin)]-$PhEty^+$ there is a very minimal gap between the S_0 and S_1 curves at bond distances greater than 2.6 Å. The small energetic difference between the S_0 and S_1 curves for [Co^{III}(corrin)]-$PhEty^+$ further corroborate the preference for IC. In fact, this is quite similar to CNCbl and HOCbl, where the S_0 and S_1 PESs nearly meet at long bond distances.[110] The PECs for [Co^{III}(corrin)]-$EtPh^+$ are more similar to the PESs of the photolabile MeCbl and AdoCbl, where a gap in energy remains between the S_0 and S_1 surfaces, even when the axial bonds are elongated.[110] This gap in energy between the S_0 and S_1 curves for [Co^{III}(corrin)]-$EtPh^+$ are further evidence of the potential for photodissociation for this conditional antivitamin B_{12}.

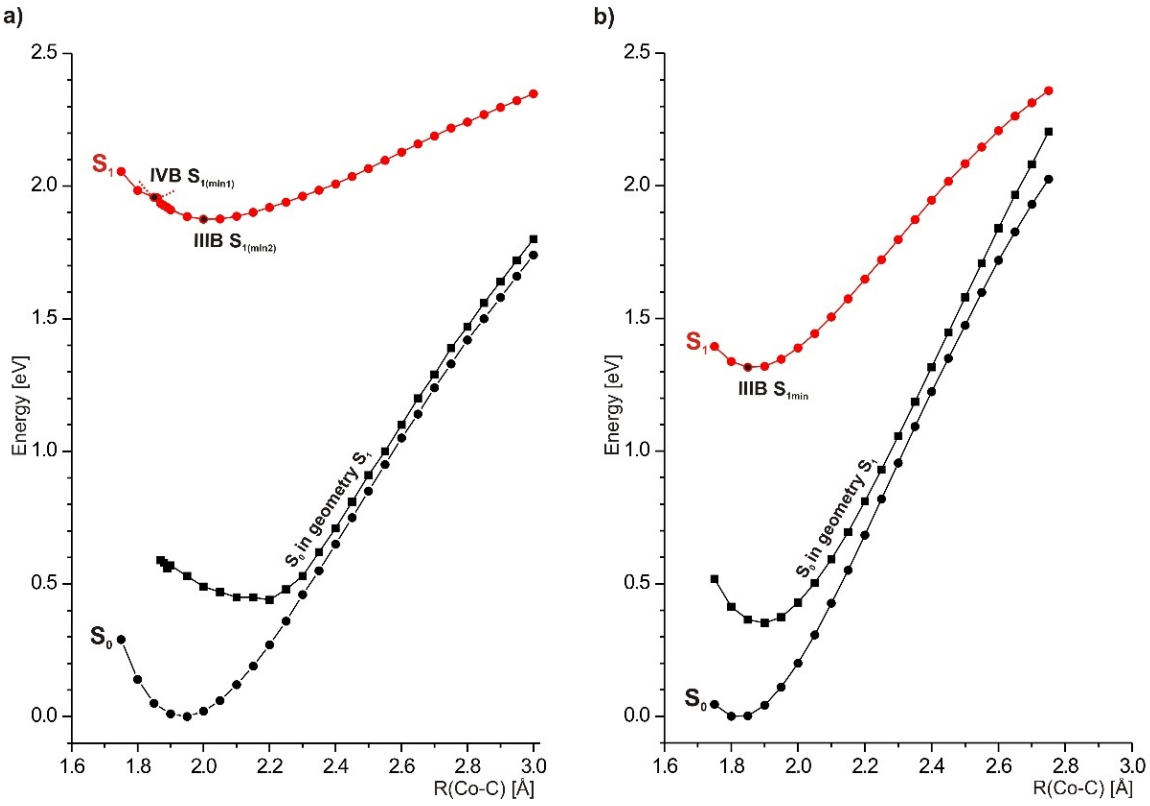

Figure 3.12. Potential energy curves (PECs) for optimized geometries of S_1 state as function Co-C bond length for $[Co^{III}(corrin)]$-$EtPh^+$ (a) and $[Co^{III}(corrin)]$-$PhEty^+$ (b) model complexes.

4.0 Summary and Conclusions

When photochemistry of EtPhCbl is compared to alkylcobalamins such as MeCbl or AdoCbl, which have been thoroughly investigated both experimentally as well as theoretically, one can conclude that EtPhCbl behaves more like Cbls that are in base-off configurations.[1, 30, 110, 116-118] However, unlike MeCbl or AdoCbl, when EtPhCbl is excited in the visible or near-UV regions, significant dissociation of the upper axial ligand is not observed. The Abs spectrum of the excited state indicates a LF minimum with a dissociated lower axial ligand as well as an elongated Co-C bond to the upper axial ligand. In addition, TAS measurements indicate that the lower axial ligand (DBI) is photodetached.[30] PECs for the optimized geometries of S_1 (Figure 3.12) that correspond to the base-off form confirm

these experimental results. The S_1 PEC which is an extrapolation of the PES in the dissociation limit of axial base (Figure 3.7c), indicates that the intersection between the MLCT and LF electronic states is essentially barrierless, and the photoreaction proceeds through the LF region as the Co-C bond undergoes elongation. Experimental results also indicate that IC is observed for EtPhCbl and that a long-lived base-off product is formed.[30] This is a distinct difference in comparison to other Cbls such as MeCbl or HOCbl, where IC between excited states is not observed.[101, 110] The theoretical results validate the categorization of EtPhCbl as a conditional antivitamin B_{12} as we have determined an optimum pathway (path B) for photolysis (Figures 3.8 and 3.9).

The major conclusion associated with PhEtyCbl's photolytic properties is that it is incredibly photostable. TAS measurements indicate that upon excitation PhEtyCbl experiences IC to S_0 with a QY of essentially one. Photoproducts are not detected in such measurements.[30] Results indicate that from the minimum of the LF electronic excited state there is a substantial energetic barrier of 39.8 kcal/mol in order for photodissociation to occur via path B, whereas the energetic barrier for IC is only 9.7 kcal/mol. Sension and co-workers estimated the activation barrier for IC to the S_0 for PhEtyCbl in solution to be ~12.6 kJ/mol (~3.0 kcal/mol) using an Arrhenius Plot.[30] This is higher than the IC barrier for CNCbl in solution ~8.8 kJ/mol (~2.0 kcal/mol). In previous studies, the estimated energy barrier for IC was 5.0 kcal/mol for a truncated model of CNCbl.[120] The calculated barrier for Im-[Co^{III}(corrin)]-$PhEty^+$ is 9.7 kcal/mol, so these theoretical results corroborate the experimental observation that the energetic barrier for S_1/S_0 IC is greater for PhEtyCbl than CNCbl. Additionally, the Co-C bond (1.86 Å) in PhEtyCbl is shorter than those of other Cbls and is sp-hybridized. As a result, the Co-C_{sp} bond is stronger than that of other

alkyl Cbls such as AdoCbl.[26] In addition to photostability, it is also resistant to thermal cleavage of the Co-C bond.

In conclusion, a theoretical analysis of the photolytic properties of two newly characterized non-natural Cbls is provided. These theoretical results provide insights into the electronic structure of the lowest excited state, which directly determines photolability and conversely photostability of the investigated antivitamins. There are two pathways for photolysis, and based on energetics, an optimum path can be determined. EtPhCbl (Im-[Co^{III}(corrin)]-$EtPh^{+}$) can photodissociate via path B through the LF state with a substantially elongated axial base, although the QY of photoproducts is low. Similarly for PhEtyCbl (Im-[Co^{III}(corrin)]-$PhEty^{+}$), two pathways can be identified; however, neither are energetically feasible for Co-C bond photolysis, thus explaining the incredible photostability of this antimetabolite. These results for the model complexes have important implications for understanding experimental results. As a result of the overwhelming energetic favorability for IC, PhEtyCbl is photostable. In contrast, for EtPhCbl, there is a competition between IC and photodissociation due to the comparable energetic barriers between the two photophysical possibilities. It is not surprising that EtPhCbl and PhEtyCbl both exhibit difficulty in dissociating the upper axial ligand as these Cbls have been shown to be metabolically inert. The analysis of these species is an important step towards the design of synthetic B_{12}-based metabolites that are sufficiently photoactive for therapeutic applications. In addition, the results gathered in this study are of particular importance especially as more applications for synthetic vitamin-B_{12} derivatives continue to be realized.

CHAPTER 4

PHOTOLYTIC PROPERTIES OF A THIOLATO-COBALAMIN

Synopsis

Vitamin B_{12} derivatives exhibit photolytic properties upon excitation with light. These properties can be modulated by several factors including the nature of the axial ligands. Upon excitation, homolytic cleavage of the organometallic bond to the upper axial ligand takes place in photo-labile Cbls. The photosensitive nature of Cbls has made them potential candidates for light-activated drug delivery. The addition of a fluorophore to the nucleotide loop of thiolato Cbls has been shown to shift the region of photo-homolysis to within the optical window of tissue (600-900 nm). With this possibility, there is a need to analyze photolytic properties of unique Cbls which contain a Co-S bond. Herein, the photodissociation of one such Cbl, namely N-acetylcysteinylcobalamin (NACCbl), is analyzed based on DFT and TD-DFT calculations. The S_0 and S_1 PESs, as a function of axial bond lengths, were computed to determine the mechanism of photodissociation. Like other Cbls, the S_1 PES contains MLCT and LF regions, but there are some unique differences. Interestingly, the S_1 PES of NACCbl contains three distinct minima regions opening several possibilities for the mechanism of RP formation. The mild photo-responsiveness, observed experimentally, can be attributed to the small gap in energy between the S_1 and S_0 PESs. Compared to other Cbls, the gap shown for NACCbl is neither exactly in line with the alkyl Cbls nor the non-alkyl Cbls.

1.0 Introduction [§§]

The emergence of new applications for the photochemical properties of B_{12} derivatives has spurred on experimental and computational analyses of their complex light-mediated mechanisms of action.[1] These applications include light-activated drug delivery[19, 20, 201] and B_{12}-based photoreceptors.[22, 23, 35, 36] In particular, the photochemical and photophysical properties of parent vitamin B_{12} and its derivatives, namely CNCbl,[100, 110, 120, 145-147, 172, 202] AdoCbl,[37, 99, 116, 119] MeCbl,[117, 118, 149, 203] HOCbl,[101, 110, 111] as well as antivitamins B_{12}[30, 31, 112, 113] were studied extensively in recent years. The photolytic properties of these derivatives are well-understood but missing from these analyses are Cbls containing a Co-S bond.

There are several examples of Cbls with this metal-thiolate bond (SCbls) to an upper ligand.[3, 204-212] Glutathionylcobalamin (GSCbl) is one example and the upper axial ligand, L-glutamyl-L-cysteinylglycine (GS^-) is bound to the Cbl via the Co-S bond.[213] GSCbl appears to have some biological relevance.[212-217] In the presence of glutathione (GSH), H_2OCbl^+ is known to convert irreversibly to GSCbl.[214] In addition to GSCbl, sulfitoCbl (sulfito = SO_3^{2-}) has also been implicated to be biologically relevant and both GSCbl and SO_3Cbl can be extracted from cultured endothelial cells.[212, 215] Another naturally occurring SCbl is cysteinylCbl (CysCbl), where the upper axial ligand is cysteine.[205, 216, 217] CysCbl decomposes easily to Co(II) and the cysteine radical.

[§§] *Chapter 4 adopted from*: Toda, M.J., Lodowski, P., Thurman, T., Kozlowski, P.M. Light Mediated Properties of a Thiolato-Derivative of Vitamin B_{12}. *Inorg. Chem*. **2020**, 59, 17200−17212.

SCbls are of interest to the B_{12} community not only for their biological significance but for their excited state properties. The electronically excited states of both GSCbl and CysCbl have been studied using Abs, CD, and MCD spectroscopy and the electronic transitions were assigned using time-dependent density functional theory (TD-DFT) calculations which employed a combined QM/MM methodology.[218] Birke and co-workers also analyzed the excited state properties of GSCbl using spectroscopic and computational techniques.[219, 220] Even more recently, the photolytic properties of N-acetylcysteinylcobalamin (NACCbl) have been investigated using Abs and electron paramagnetic resonance (EPR) spectroscopy.[114] NACCbl contains all of the characteristic features of Cbls with the exception being the upper ligand, which is depicted in Figure 4.1

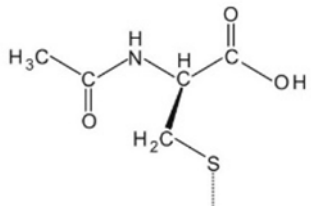

Figure 4.1. Molecular structure of upper ligand of NACCbl. The sulfur atom is bond to the Co of the Cbl.

Lawrence and co-workers investigated the photo-lability of the Co-S bond in NACCbl at various wavelengths of the UV-vis spectrum.[220] It was shown that NACCbl is photoactive, albeit with a reduced quantum yield (Φ) and rate of photolysis compared to alkylCbls. EPR measurements confirmed that the photocleavage of the Co-S bond was homolytic resulting in the formation of Co(II)/NAC• radical pair (RP). While NACCbl exhibits modest photo-responsiveness, the attachment of a fluorophore to the nucleotide loop improves the molecule's photolytic efficiency. Moreover, the addition of a fluorophore to Cbls containing a drug as the upper axial ligand shifts the photo-homolysis

window to within the optical window of tissue (600-900 nm).[114] With this approach, drugs can be launched from the Cbl scaffold by modulating the wavelength of light, making Cbls potential candidates for phototherapeutics.[19, 20, 114] Understanding the factors responsible for the photolytic properties that arise based on the inclusion of a fluorophore to the nucleotide loop of NACCbl is a very complex problem. However, a good starting point is to first analyze the photolytic properties of NACCbl without a fluorophore. In particular, the mechanism of photodissociation of the NAC ligand should be determined. The goal of the work presented in this chapter was to sort out the mechanism of photodissociation of NACCbl absent of a fluorophore.

The excited state properties of Cbls in solution, as well as bound to enzymes,[24, 122, 136, 182, 221] were analyzed extensively, and a streamlined computational protocol for the elucidation of photolytic mechanisms was developed. Several review papers and book chapters resulted from these analyses.[1, 2, 110] Further, the recent experimental analysis of NACCbl, which probed the photolysis of the Co-S bond, opened the door for revisiting the properties of SCbls from a computational perspective. The photolytic properties of NACCbl were explored with a similar computational approach of the studies of CNCbl, MeCbl, AdoCbl, HOCbl, and antivitamins B_{12}. The mechanism for the photoreaction of NACCbl is reported here based on the S_0 and S_1 PESs generated from DFT and TD-DFT calculations, respectively. The S_0 and S_1 PESs exhibit features that are markedly similar to other Cbls but at the same time there are some unique differences. Interestingly, the S_1 PES of NACCbl contains three distinct minima regions opening several possibilities for the mechanism of photodissociation. Unlike other Cbls, contributions of the sulfur-based p orbitals need to be considered in analyzing the electronic excitations.

2.0 Computational Details

In the present study, the photolytic properties of both the base-on and base-off forms of NACCbl were investigated, and the two structures can be used hand-in-hand to elucidate the photolytic properties. The base-on model provides insights into the photocleavage of the Co-S bond while the base-off model can provide insights into the mechanism of deactivation. The crystal structure from Brasch and co-workers[222] was used of the DBI. The structure of the model complex used in calculations is depicted in Figure 4.1. The base-on model is referred to as Im-[Co^{III}(corrin)]-NAC^{+} and the base-off model as [Co^{III}(corrin)]-NAC^{+}. The nonhybrid BP86 functional was used for both the ground state and excited state calculations.[190] The valence triple-ζ basis set with polarization (TZVP) was used for hydrogen atoms.[192] The valence triple-ζ basis set including two sets of polarization functions (TZVPP) was used for the remaining atoms including the Co, O, N, C, and S. In addition, the COSMO, with water as the solvent, was employed. All reported calculations were carried out in the Turbomole suite of programs.[193-195] The efficacy of the DFT/BP86/TZVPP and TD-DFT/BP86/TZVPP levels of theory for ground and excited state properties of Cbls, respectively, have been reported extensively.[2, 139, 143, 146, 163]

Table 4.1. Selected geometric parameters of base-on Im-[CoIII(corrin)]-NAC+and base-off Im-[CoIII(corrin)]-NAC+ forms of model complex for optimized geometries in the ground state S0 and in the excited state S1.

Parameter	base-on			base-off	
	S_0	Exp[53]	S_{1min}	S_0	S_{1min}
r[Å]					
Co – S	2.305	2.251	2.204	2.240	2.256
Co – N	2.056	2.057	1.984		
Valence angle[°]					
S - Co - N	177.5	177.7	176.5		
N_{21} - Co – N_{23}	173.2	173.1	171.8	165.0	152.0

N_{22} - Co – N_{24}	172.7	172.1	172.7	171.2	169.6
Dihedral angle [º]					
N_{21} – N_{22} – N_{23} - Co	-1.8	-2.2	-3.0	-9.8	-19.1
N_{21} – N_{22} – N_{23} - N_{24}	-3.9	-4.5	-2.3	-5.3	-12.7
C_{10} – Co –S-C	0.7	-41.9	-23.0	4.9	45.5

In order to ensure that the reported excited states (Table 4.2) do not result from long-range charge transfer, the Λ diagnostic test was employed.[155] The Λ parameter ranges from 0 to 1 and is used to "weed out" electronic excitations that may result from poor overlap. The recommendation for GGA-type functionals is as follows: if Λ is less than 0.4, then excitation energies are likely to be significantly underestimated; conversely, if Λ is greater than 0.4, then the error in the estimated energy for CT transitions is usually small.

Table 4.2. Lowest, vertical singlet states and S1 → S0 transition for Im-[CoIII(corrin)]-NAC+ and [CoIII(corrin)]-NAC+ model complexes.

	E [eV]	λ [nm]	*f*	□	%	Character		Exp. λ[nm] (eV)[219]
					Im-[Co^{III}(corrin)]-NAC^+ (base-on)			
S_1	1.70	729.6	0.0012	0.435	95	H → L	$p_S + d_{yz} \rightarrow \pi^*$	615 sh (2.02)
S_2	1.85	669.9	0.0002	0.536	96	H → L+1	$p_S + d_{yz} \rightarrow \sigma^*(d_z^2)$	
S_3	2.30	538.1	0.0067	0.401	57	H → L+2	$p_S + d_{yz} \rightarrow d_{xz} - n$	
					26	H-1→ L+1	$\pi + (d_z^2/p_S) \rightarrow \sigma^*(d_z^2)$	
					12	H-1→ L	$\pi + (d_z^2/p_S) \rightarrow \pi^*$	
S_4	2.34	529.5	0.0180	0.634	43	H-1→ L	$\pi + (d_z^2/p_S) \rightarrow \pi^*$	561 (2.21)
					32	H → L+2	$p_S + d_{yz} \rightarrow d_{xz} - n$	
					15	H-1→ L+1	$\pi + (d_z^2/p_S) \rightarrow \sigma^*(d_z^2)$	
S_5	2.38	521.4	0.0207	0.626	49	H-1→ L+1	$\pi + (d_z^2/p_S) \rightarrow \sigma^*(d_z^2)$	
					27	H-1→ L	$\pi + (d_z^2/p_S) \rightarrow \pi^*$	
S_6	2.47	502.3	0.0052	0.649	78	H-2 → L+1	$\pi + (d_{yz}/p_S) \rightarrow \sigma^*(d_z^2)$	
S_7	2.51	493.7	0.0004	0.288	97	H → L+3	$p_S + d_{yz} \rightarrow \pi^*$	
S_8	2.64	470.4	0.0216	0.695	69	H-2 → L	$\pi + (d_{yz}/p_S) \rightarrow \pi^*$	
					11	H-1→ L+3	$\pi + (d_z^2/p_S) \rightarrow \pi^*$	534 (2.32)
S_9	2.71	458.0	0.0233	0.507	69	H-3 → L	$d_{xz} \rightarrow \pi^*$	
					20	H-1→ L+2	$\pi + (d_z^2/p_S) \rightarrow d_{xz} - n$	
S_{10}	2.77	446.9	0.0022	0.570	78	H-3 → L+1	$d_{xz} \rightarrow \sigma^*(d_z^2)$	
					10	H-2 → L+2	$\pi + (d_{yz}/p_S) \rightarrow d_{xz} - n$	
S_{11}	2.79	444.1	0.0139	0.460	67	H-1→ L+2	$\pi + (d_z^2/p_S) \rightarrow d_{xz} - n$	498 (2.49)
					16	H-3 → L	$d_{xz} \rightarrow \pi^*$	
S_{12}	2.85	435.6	0.0039	0.420	91	H-4 → L	$d_x^2\text{-}_y^2 \rightarrow \pi^*$	
S_{1min}	1.13	1092.5	0.0004	0.267	99	H → L	$p_S + d_{yz} \rightarrow \pi^*$	
					[Co^{III}(corrin)]-NAC^+ (base-off)			
S_1	1.05	1183.3	0.0008	0.610	100	H → L	$p_S + d_{yz} \rightarrow \sigma^*(d_z^2)$	
S_2	1.71	723.5	0.0016	0.447	93	H → L+1	$p_S + d_{yz} \rightarrow \pi^*$	

S_3	1.79	693.5	0.0062	0.621	97	H-1→ L	$\pi + ([d_{xz}-d_{yz}]/p_S) \rightarrow \sigma^*(d_z^2)$
S_4	1.90	653.5	0.0022	0.602	97	H-2 → L	$d_{xz} \rightarrow \sigma^*(d_z^2)$
S_5	2.22	558.9	0.0004	0.318	98	H-5 → L	$p_O \rightarrow \sigma^*(d_z^2)$
S_6	2.31	537.8	0.0065	0.416	71	H-3 → L	$[d_x^2-y^2+ d_{xz}]+\pi \rightarrow \sigma^*(d_z^2)$
					11	H-4 → L	$[d_x^2-y^2+ d_z^2]+\pi \rightarrow \sigma^*(d_z^2)$
					10	H-1→ L+1	$\pi + ([d_{xz}-d_{yz}]/p_S) \rightarrow \pi^*$
S_7	2.42	513.1	0.0014	0.648	66	H-4 → L	$[d_x^2-y^2+ d_z^2]+\pi \rightarrow \sigma^*(d_z^2)$
					13	H → L+2	$p_S + d_{yz} \rightarrow d_{xz} - n$
					12	H-3 → L	$[d_x^2-y^2+ d_{xz}]+\pi \rightarrow \sigma^*(d_z^2)$
S_8	2.48	500.9	0.0007	0.449	49	H → L+2	$p_S + d_{yz} \rightarrow d_{xz} - n$
					24	H → L+3	$p_S + d_{yz} \rightarrow \pi^*$
					15	H-4 → L	$[d_x^2-y^2+ d_z^2]+\pi \rightarrow \sigma^*(d_z^2)$
S_9	2.55	486.0	0.0029	0.509	29	H → L+3	$p_S + d_{yz} \rightarrow \pi^*$
					25	H → L+2	$p_S + d_{yz} \rightarrow d_{xz} - n$
					24	H-2 → L+1	$d_{xz} \rightarrow \pi^*$
S_{10}	2.61	474.8	0.0084	0.462	38	H → L+3	$p_S + d_{yz} \rightarrow \pi^*$
					30	H-2 → L+1	$d_{xz} \rightarrow \pi^*$
					18	H-1→ L+1	$\pi + ([d_{xz}-d_{yz}]/p_S) \rightarrow \pi^*$
S_{1min}	0.64	1953.8	0.0001	0.584	100	H → L	$p_S + [d_{xz}+d_{yz}] \rightarrow \sigma^*(d_z^2)$

3.0 Results and Discussion

3.1 Structural Analysis of Model Complexes

The model structures were derived from the high-resolution crystal structure.[222] The most relevant structural parameters for Cbls from the crystal structure were compared to the optimized base-on and base-off models (Table 4.1). For photochemical analysis, the most critical parameters to consider are the axial bond lengths. These bonds exhibit the most significant structural change upon excitation. Additionally, whether a Cbl is in its base-on or base-off form typically affects the photolytic properties. The Co-S bond was 2.251 Å in the crystal structure. For the optimized models, base-on Im-[Co^{III}(corrin)]-NAC^+ and base-off [Co^{III}(corrin)]-NAC^+, the Co-S bond was 2.305 and 2.240 Å, respectively. The bond to the lower axial ligand Co-N, i.e., Co-N_{DBI} for the crystal structure

and Co-N_{Im} for Im-[Co^{III}(corrin)]-NAC^{+} model complex, was found 2.057 and 2.056 Å, respectively. The angle spanning the axial bonds (N_{Im}-Co-S) is essentially unchanged in comparison to the crystal structure and the S_0 base-on structure corresponding to minimum energy. Experimental data is not available for NACCbl structural properties in the excited state such as axial bond lengths, so calculations must be relied on. Recently, structural properties in the excited state for various Cbls have been reported based on XANES measurements[172, 202, 223] but analyses of sulfur-containing Cbls are yet to be completed. The Co-S bond of the base-on model for the S_1 minimum is slightly shorter from the S_0 minimum and is 2.204 Å. However, the S_1 minimum bond length of the base-off model is slightly increased in comparison to its base-on counterpart. Overall, there is a good agreement between the experimentally determined structural parameters and those that were derived computationally.

3.2 Experimental versus Simulated Abs Spectrum

The simulated Abs spectrum of NACCbl (Figure 4.2) was compared to the experimental spectrum of GSCbl. Overall, there is good agreement between the experimental and computed Abs spectrum. The simulated spectrum of NACCbl was compared to the experimental spectrum of GSCbl, because thorough computational investigations of the Abs spectrum of GSCbl have been completed and are a good reference for this study.[219, 220] Additionally, the experimental spectrum of NACCbl is nearly indistinguishable from that of GSCbl.[114] The similarities of Abs spectra of GSCbl and

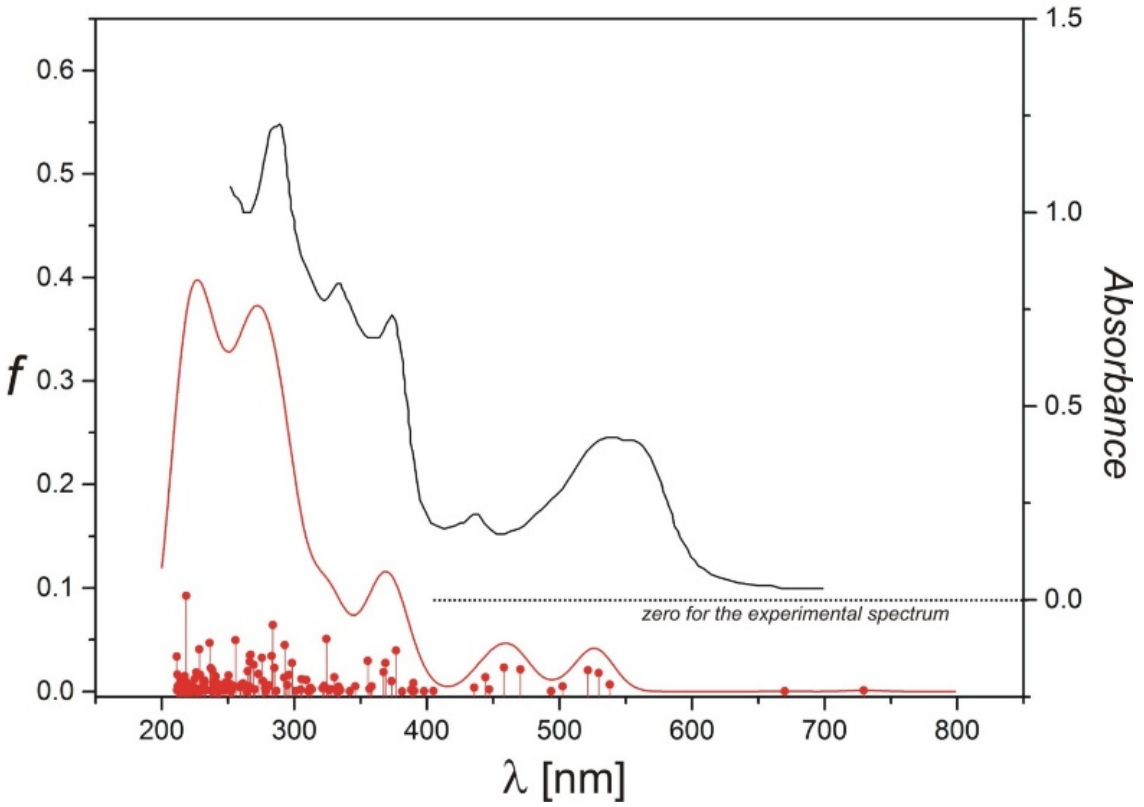

Figure 4.2. TD-DFT excitations (red sticks) and the simulated (red line) electronic spectrum for Im-[Co^{III}(corrin)]-NAC^{+} model complex together with experimental (black line) absorption spectrum for GSCbl. Experimental spectrum is from A. S. Eisenberg, I. V. Likhtina, V. S. Znamenskiy, R. L. Birke. Electronic Spectroscopy and Computational Studies of Glutathionylco(III)balamin. *J. Phys. Chem. A* 2012, 116, 6851-6869. TD-DFT excitations were used to simulation spectral line by modeling each predicted transition as a Gaussian band with a full width at half-maximum of 20 nm.

NACCbl are further observed based on the comparison of the Abs spectra corresponding to the reaction between GSH and H_2OCbl to form GSCbl[219] and the conversion of NACCbl to HOCbl.[114] There is a gradual change in absorption as NACCbl is converted to HOCbl by photolysis at 360 nm with isosbestic points at 340, 365, 404, 418, 446, and 540 nm.[114] These same isosbestic points are observed for the extinction spectra when H_2OCbl is converted to GSCbl.[219] These observations indicate that the Abs spectrum of GSCbl is a fair representation of NACCbl. Nevertheless, the simulated Abs spectrum of NACCbl presented in Figure 4.2 is described as follows.

The simulated electronic spectrum is based on TD-DFT excitations of the base-on model complex, Im-[Co^{III}(corrin)]-NAC^{+}. For both the simulated spectrum and the experimental Abs spectrum, the Soret band is not present. The *α/β* band is between 450 and 600 nm for the experimental spectrum and between 400 and 550 for the simulated spectrum. The electronic transitions that correlate to the experimentally observed peaks for the *α/β* region are listed in Table 4.1. The peak observed experimentally for GSCbl at 615 nm[219] corresponds to contributions from the S_1 and S_2 states of Im-[Co^{III}(corrin)]-NAC^{+}. The S_1 state is 95% HOMO to LUMO and is designated $p_S + d_{yz} \rightarrow \pi^*$, and the S_2 state is 96% HOMO to LUMO+1 and is designated $p_S + d_{yz} \rightarrow \sigma^*(d_{z2})$. The experimental bands at 561, 534, and 498 nm correspond to contributions from the S_3-S_5, S_8-S_9, and S_{10}-S_{12} states of Im-[Co^{III}(corrin)]-NAC^{+}, respectively. For the first two bands, the calculations indicate the presence of excitations of a rather mixed character of electronic transitions, and generally they are of the $p_S/d \rightarrow d$, $\pi/d \rightarrow \pi^*$, $\pi/d \rightarrow \sigma^*$, $p_S/d \rightarrow \pi^*$, and $d \rightarrow \pi^*$ type. In the third mentioned bands, the transition $\pi/d \rightarrow d$ is dominant, accompanied by two less intense $d \rightarrow \sigma^*$ and $d \rightarrow \pi^*$ type excitations.

3.3 NTO Analysis

The excited states in the standard TD-DFT approach are described as a combination of more than one electronic excitation between KS MOs. In addition to these descriptions of the character of the electronic transitions of the Abs spectrum of NACCbl, the natural transition orbital (NTO) hole-particle formalism was applied to verify the character of ten low-lying excited states (Appendix, Figures A.4.1 and A.4.2). The hole and particle plots for the S_4 state at 561 nm for GSCbl with a BP86/6-311(d,p) calculation show that both

Co-S and Co-N axial bonds are antibonding in the Franck-Condon region.[219] The NTO hole/particle analysis of NACCbl shows a similar antibonding nature.

According to the NTO hole and particle isosurfaces, the two lowest excited electronic states (A.4.1 and A.4.2) are a consequence of electron relocation from the p orbital of sulfur (p_S) and d orbital of Co π^* and σ^* orbitals, respectively, where the π^* orbital is localized on the corrin ring, whereas the σ^* is the antibonding orbital in relation to the axial ligands (Figure A.4.1). The S_3 excited state is also a p_S/d excitation; however, these excitations take place on the unoccupied orbital, which is the antibonding combination of the d_{xy} orbital of Co and the nonbonding p orbitals of equatorial nitrogens. The S_4 singlet state is mainly the result of electronic excitation for which the electron hole has mixed π/p_S/d nature, and the particle is almost completely localized on the π^* antibonding orbital of the corrin ligand (Figure A.4.2). Similar to the case in the S_2 state, the S_5 and S_6 states have antibonding character in relation to the axial ligands and the electron excitation occurs from a mixed π/p_S/d orbital to the σ^* antibonding orbital. States S_7-S_9 are the result of electron density transfer from delocalized π/p_S/d, p_S/d, or π/d orbitals on the π^* antibonding orbital (Figure A.4.2). The S_{10} state, which is probably out of the experimental band with maximum at 534 nm (Table 4.2), is result of the almost pure d $\rightarrow$ σ^* transition with very small participation from π/d/p_S $\rightarrow$ d-n excitation (Figure A.4.2).

In sum, the NTO representation of the ten lowest calculated excited states ranging from 450 to 730 nm reveals that the character of the excited states is consistent with the calculated distribution of electronic excitations between KS orbitals where the characters of the particular states are generally determined by KS interorbital excitation with the greatest contribution coefficient to a specific excited state. Among the mentioned excited

singlet states, the S_2, S_5, S_6, and S_{10} states have pronounced antibonding character with respect to bonds with axial ligands. As will be discussed in the next section, the S_2 state for elongated axial bonds becomes the lowest excited electronic state. The NTO analysis supports this assertion as the hole is represented by p_S/d type orbitals and the particle represented by a σ* antibonding orbital in relation to the axial ligands (d_{z2}-type character in the KS analysis (Table 4.2) for the S_2 state). The involvement of the S_2 state in the photodissociation mechanism will be discussed in more detail in the following sections.

3.4 Analysis of PECs

In the initial stage of analysis, key characteristics of the photolytic properties of NACCbl can be deduced upon inspection of the S_0 and S_1 PECs curves whose reaction coordinate is simply the Co-S distance. The PECs for the optimized geometry of the S_0 state and the ten lowest vertical, singlet electronic excited states as a function Co-S bond length for the Im-[Co^{III}(corrin)]-NAC^+ and [Co^{III}(corrin)]-NAC^+ model complexes are shown in Figure 4.3. The optimized S_1 PEC for the base-on and base-off models are shown in the Appendix (Figures A.4.3 and A.4.4). The S_1 PEC for Im-[Co^{III}(corrin)]-NAC^+ appears to be lower in energy as the Co-S distance stretches beyond 2.5 Å (Figure 4.3). This seems to be the result of crossing between two states, the MLCT and LF, at about 2.4-2.5 Å. It also appears that there is a mixing of the S_1 and S_2 states. On the base-off side (Figure 4.3b), the S_0 curve, representative of BDE, steadily increases in energy, whereas the S_0 BDE curve for the base-on case appears to level off. Based on this, the Co-S bond is more easily cleaved in the S_0 state in the base-on configuration. Additionally, the S_0 curve and the S_1 curve appear to nearly degenerate at the Co-S distance of 3.4 Å for the base-off model. This will come into play later when the deactivation mechanism is

discussed. Unlike the base-on situation, the S_1 and S_2 states do not appear to mix for [Co^{III}(corrin)]-NAC^+. Clearly, the departure of the axial base affects the photolytic properties of NACCbl. The KS orbitals involved in electronic excitation at minimum energy on the S_1 PEC of the [Co^{III}(corrin)]-NAC^+ model complex are shown in Figure A.4.5.

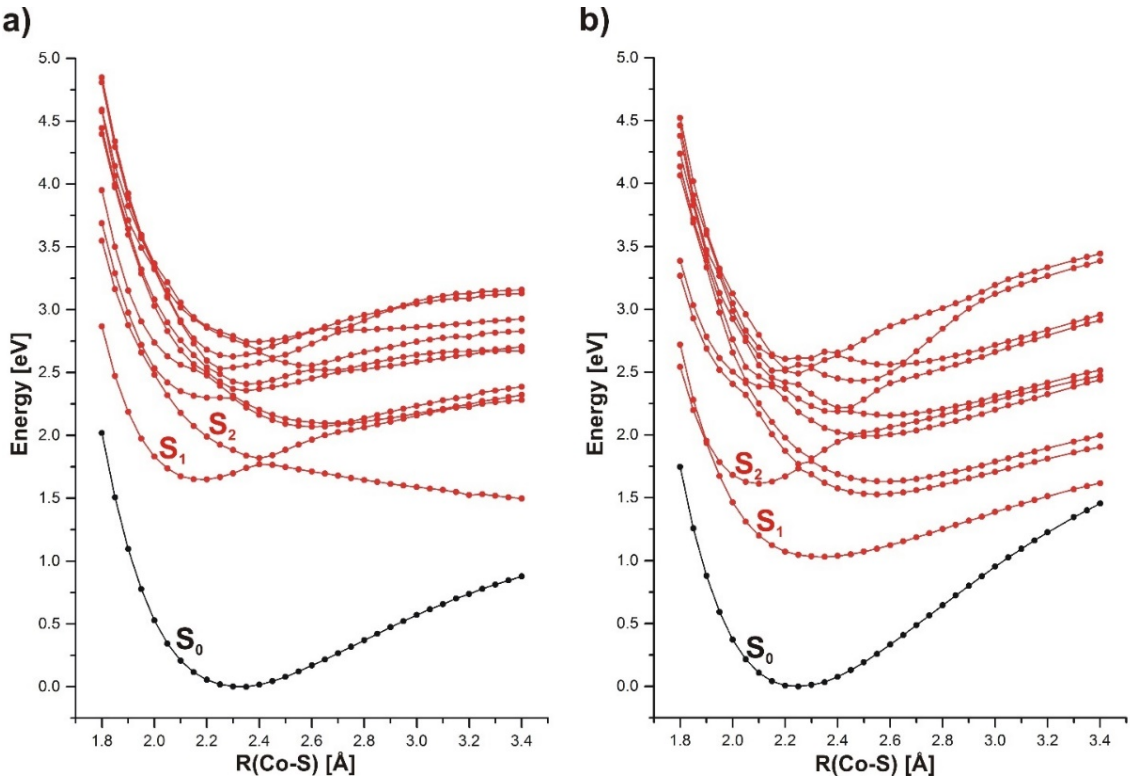

Figure 4.3. Potential energy curves (PECs) for optimized geometry of S_0 state and ten lowest vertical, singlet electronic excited states as function Co-C bond length for (a) Im-[Co^{III}(corrin)]-$NAC^+$and (b) [Co^{III}(corrin)]-NAC^+ model complexes.

There are a few crossings of PECs that are worthy of further discussion. First, it appears that the S_2 state for elongated axial bonds becomes the lowest, excited electronic state. Taking into account the KS orbital analysis and NTO analysis, this state may be directly involved in photochemical dissociation of the NAC ligand, which occurs from a LF state. Based on analysis of KS orbitals (Table 4.2), the S_2 transition is LF type and is

characterized as $p_S + d_{yz} \rightarrow \sigma^*(d_{z2})$. The NTO analysis further supports this assertion and the particle shows antibonding character along the axial ligands. For the base-on form of NACCbl, the S_2 PEC crosses the S_1 PEC at Co-S distance around 2.4-2.5 Å (Figure 4.3a). While the S_2 state is of LF ($p_S/d \rightarrow \sigma^*$) type, the S_1 state is MLCT ($p_S/d \rightarrow \pi^*$) type. The intersection of the S_2/S_1 suggests that there is an effective path between the local minima of the S_1 PES, occurring at short Co-S and Co-N_{Im} distances, and a vast plane of the LF state, from which the Co(II)/NAC• RP is formed directly as a result of dissociation of the Co-S bond.

In the Franck−Condon region, the PEC of S_3 ($p_S/d \rightarrow$ d-n), with local minimum for Co-S distance at around 2.2 Å, intersects with PECs of two states with the $p_S/d \rightarrow \sigma^*$ antibonding character. Similar crossings of $p_S/d \rightarrow \sigma^*$ antibonding states and states of $p_S/d \rightarrow \pi^*$ or $\pi/d \rightarrow \pi^*$ character are also visible for slightly shorter Co-S distances. For elongated Co-S bonds, the $p_S/d \rightarrow \sigma^*$ states are the S_3 and S_4. At distances above 2.6 Å, the PECs of these excited states are close in energy or cross the curve of MLCT ($p_S/d \rightarrow \pi^*$) state, which in the Franck-Condon region is the lowest singlet electronic state of S_1. The layout of the S_1-S_4 PECs for elongated Co-S bond may suggest that after initial excitation to excited states above the S_1 and S_2, a repayable relaxation of the molecular system to the lowest LF state is possible. While these observations have provided some important insights, they do not offer a complete picture of the mechanism of RP formation and the photodissociation of the NAC ligand. It becomes apparent that another coordinate needs to be added to the analysis, and this is the Co-N_{Im} bond distance.

3.5 Analysis of PESs

While PECs only consider one structural parameter, PESs can be constructed which are a function of two coordinates, i.e., both axial bonds. A wealth of information describing the photolytic properties of Cbls is available upon careful inspection of the S_0 and S_1 PESs. It is well understood that photodissociation of the upper ligand of Cbls occurs from the S_1 state.[1, 41, 91-95, 98, 103, 121] At the same time, the axial bonds of Cbls undergo significant changes upon excitation.[110, 172] Accordingly, the mechanism of photolysis can best be understood by analyzing the S_1 PES which is a function of both axial bond lengths. In this case, the axial bonds, Co-S and Co-N_{Im}, of the base-on model Im-[Co^{III}(corrin)]-NAC^+ were used. First, the S_0 PES was computed by systematically stretching the Co-S and Co-N_{Im} bonds with a step size of 0.05 Å. Points between the resulting grid were extrapolated and the S_0 PES is depicted in Figure 4.4a. In total, the S_0 PES spans from Co-S distances of 1.8-3.1 Å and Co-N_{Im} distances of 1.8-3.5 Å. The S_1 PES was generated based on vertical excitations from each of the corresponding optimized ground state structures (Figures 4.5a). For comparison, the S_1 PES was relaxed from Co-S distances of 1.8-2.5 Å and is depicted in Figures 4b and 5b. The single-determinant based wave function in TD-DFT prevents optimization of the PES beyond 2.5 Å, as this would be indicative of RP formation where a multiconfigurational wave function would be required.

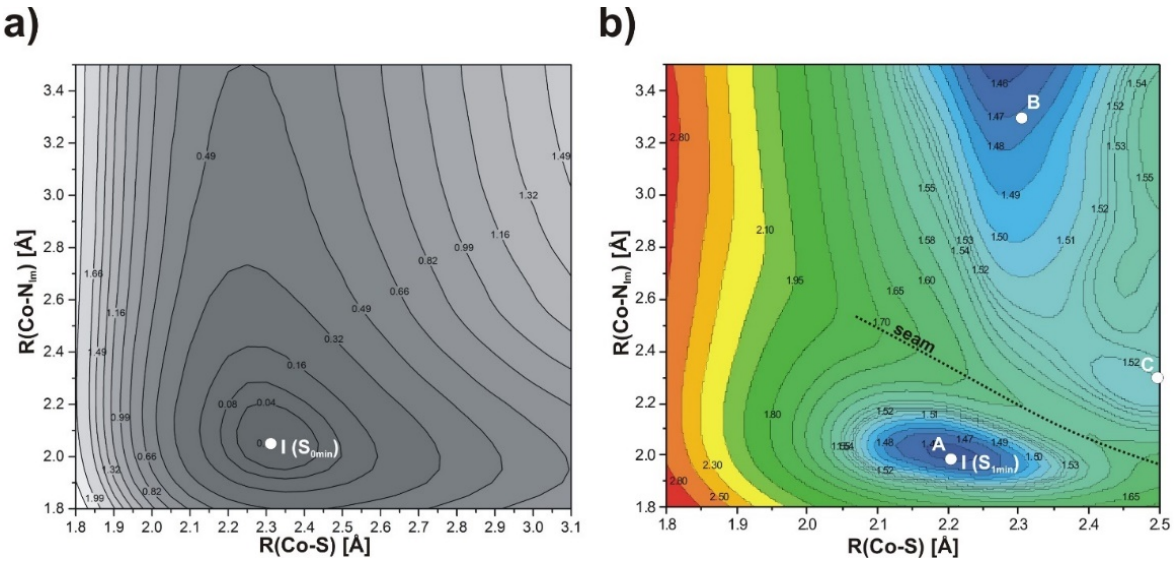

Figure 4.4. Vertical projections of a) S_0 and b) S_1 PESs as function of axial bond lengths for optimized geometry of the S_0 ground state and S_1 excited state of Im-[Co^{III}(corrin)]-NAC^+model complex.

The analysis of the S_0 and S_1 PESs (Figures 4.4 and 4.5) of NACCbl provided insight into the photolytic properties and the resulting photodissociation mechanism. First, the S_0 PES contains a single energy minimum, denoted I ($S_{0\ min}$) in Figure 4.4a. This is characteristic of Cbls. Similarly, the S_1 PES contains key features which can be described based on the energy minima of the surface. The S_1 PES is the result of the crossing of two different electronic states, namely, the MLCT and LF. The crossing of these states results in a "ridge" across the PES, and this energy barrier is referred to as "seam" in Figure 4.4b. Ultimately, the crossing of the MLCT and LF gives rise to the low energy regions of the surface. Typically for Cbls, there are two minima points on the S_1 PES, and each minimum is contained in either the MLCT or LF region. For the base-on model of NACCbl, there are three minima points on the S_1 PES. These are denoted as A I ($S_{1\ min}$), B, and C in Figure 4.4b.

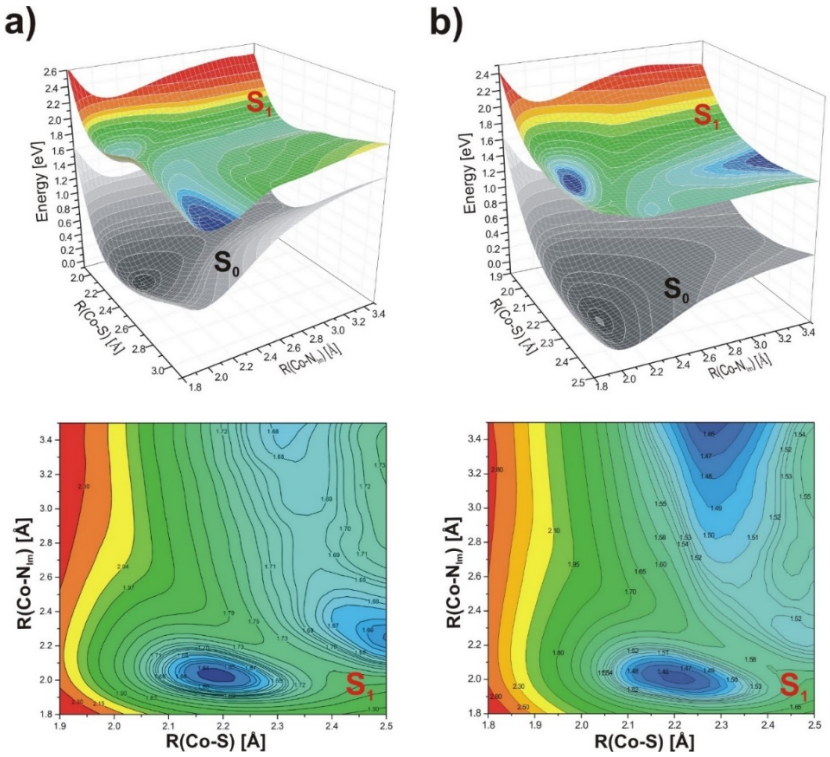

Figure 4.5. Potential energy surfaces as a function of axial bond lengths for (a) optimized geometry of the ground state S_0 and (b) optimized geometry of the S_1 excited state of Im-[Co^{III}(corrin)]-NAC^+ model complex together with projections of PES for vertical and relaxed S_1 state, respectively.

The KS orbitals involved in the electronic transitions at these key points are shown in Figure 4.6. The Co-S bond of NACCbl adds complexity to the orbital analysis, as the p orbitals of sulfur need to be taken into account. Accordingly, the electronic excitations involve a mixing of the metal d orbitals and the sulfur p orbitals. Point A I($S_{1\ min}$) arises from excitations that can be characterized as, $p_S + d_{yz} \rightarrow \pi^*$, with the acceptor π^* orbitals delocalized on the corrin ring. Despite the involvement of the ps orbital, the excitation can still be categorized as MLCT. Points B and C are LF type, and the electronic excitations involved are $p_S + (d_{yz} + d_{xz}) \rightarrow \sigma^*(d_{z2})$ and $p_S + d_{xz} \rightarrow \sigma^*(d_{z2})$, respectively.

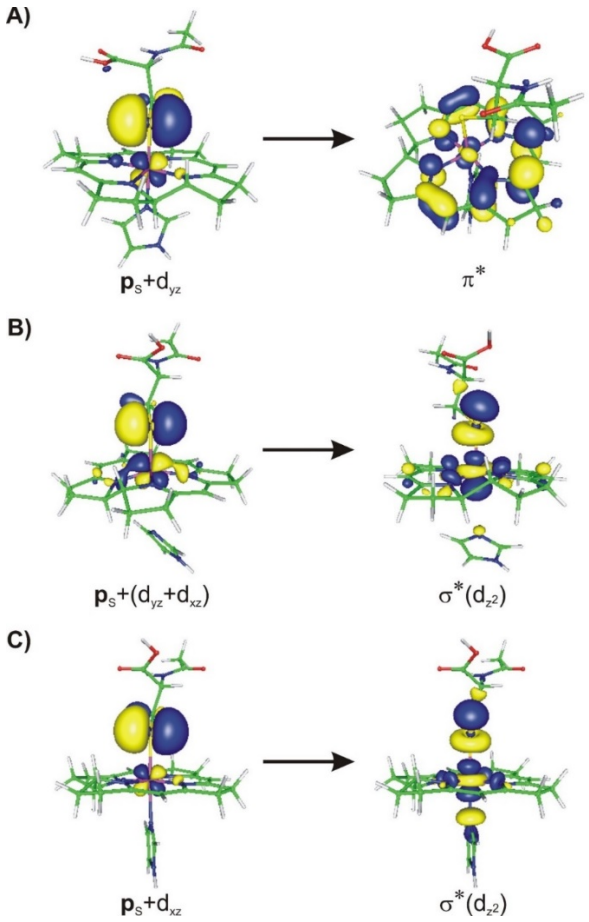

Figure 4.6. KS orbitals involved in electronic excitation at selected points on S_1 PES Im-[Co^{III}(corrin)]-NAC^+ model complex (A, B and C, Figure 4.4).

In addition to the topology of the S_0 and S_1 PESs, the relative energetics associated with the S_0 and S_1 PES provide important information about the photolytic properties of Cbls. The energy gap between the S_0 and S_1 PESs at elongated axial bond lengths provides an indication as to whether a Cbl is photoactive. In other words, if the S_1 PES crosses the S_0 PES, the Cbl is likely photostable.[110] Conversely, if there is a large gap in energy between the S_0 and S_1 PESs, the Cbl likely is photolabile. The energetic difference between the S_0 and S_1 PESs of Im-[Co^{III}(corrin)]-NAC^+ can be visualized in Figure 4.5. Panel A depicts the S_1 state which is based on vertical projections from the optimized geometries

of the corresponding S_1 points and spans from Co-S distances of 1.9-3.1 Å and Co-N_{Im} 1.8-3.5 Å. Panel B shows the relaxed S_1 PES. Regardless of whether the PES based on vertical excitations or excited state optimization, it is apparent that there is a gap in energy between the S_1 and S_0 PESs. Put a different way, the S_1 and S_0 states do not cross or come in close enough proximity for IC to be immediately preferred over Co-S photocleavage. This indicates that a mechanism of photodissociation can be identified from a theoretical perspective. Overall, it appears that NACCbl is somewhere in between the nonalkyl Cbls and alkyl Cbls in terms of this energetic difference. For nonalkyl Cbls, such as CNCbl and HOCbl, the S_1 PES surface meets the S_0 PES at long Co-C and Co-O distances, indicative of IC instead of photodissociation,[110] whereas for base-on nonalkyl Cbls, such as AdoCbl and MeCbl, the S_1 PES is nowhere near crossing with the S_0 PES.[1] Accordingly, AdoCbl and MeCbl are photoactive. For NACCbl, the S_0 state is not as flat as these nonalkyls, but at the same time, it is not fully in-line with its alkyl counterparts, as the increase is not nearly as steep. Nevertheless, in order to sort out whether or not photodissociation is truly feasible for NACCbl, first an optimum path for photolysis should be identified.

3.6 Potential Photolysis Pathways

The first thing to note about Cbl photochemistry is that photodissociation, marked by RP formation, occurs from the LF state. In order to access this portion of the PES, where the upper axial bond is elongated nearly to the point of rupture, the barrier between the MLCT and LF regions needs to be crossed. Intuitively, this should involve the least costly option, namely, the MECP. Recalling that the S_1 PES is a function of axial bond lengths, photodissociation of the upper ligand should be achieved by axial bond elongation. Either the upper axial bond can elongate first followed by the elongation of the lower axial bond

or the reverse can occur, i.e., lower axial bond elongation followed by upper axial bond elongation. This is dictated by energy associated with corresponding structural changes. In our previous analyses, we have designated these two scenarios as Path A and Path B, respectively.[116-120] Typically, one of the routes can be ruled out based on energetics that are simply not feasible. For instance, for base-on AdoCbl, Path A is energetically viable while Path B is not accessible. For the base-off cases of MeCbl and AdoCbl, where the lower axial ligand is a water molecule, Path B is active, while Path A is not energetically favorable. The difference between these cases and NACCbl is that the energetically feasible route is not as easily identified.

On one hand, homolysis appears to be possible by directly lengthening the Co-S bond, which is consistent with Path A. On the other hand, the distinct minimum is also on Path B. Upon inspection of the S_1 PES based on vertical excitations (Figure 4.5a), there does not appear to be an energy barrier along Path A for Co-S photocleavage, yet there does appear to be one along Path B. Considering these observations, it would seem that the preferred path is Path A. However, this barrier does not appear to be significant based on the relaxed S_1 PES. That being said, the most intense absorption occurs for states S_3-S_5 (Table 4.2) meaning that the initial excitation is likely to one of these higher states. Plausibly, relaxation to the S_1 could be to any of the minima points on the S_1 PES. If the MLCT state is populated first (Point A I ($S_{1\ min}$), Figure 4.4), then the preferred direction of the photoreaction should be Path B. However, relaxation from the higher states to the S_1 state could lead directly to the LF region (Points B or C, Figure 4.4), which seems to be more in line with Path A. So, assuming that dissociation is possible from minimum B or C, then relaxation to point C and direct Co-S dissociation would be consistent with Path A,

but if the system is relaxed to point B, then the process direction would rather follow path B. For instance, as previously discussed, the S_2 state is the lowest energy PEC at longer Co-S distances and may be the likely candidate for direct relaxation to the LF region due to its particle σ* antibonding orbital character. Perhaps for NACCbl, multiple photolytic pathways are possible.

The dissociation energy associated with RP formation (Im-[CoII(corrin)]$^{\bullet+}{}_{LF}$ + $^{\bullet}$NAC) from point C on the S_1 PES was estimated to be approximately 20 kcal/mol. This barrier may have some error, because the LF state of the Im-[Co^{II}(corrin)]$^{\bullet+}{}_{LF}$ cannot be fully optimized. Unfortunately, due to the restrictions of a single determinant wave function approach, such as TD-DFT, the portion of the relaxed PES beyond 2.5 Å cannot be computed here. A multireference method would be required which is inherently very challenging in large transition metal containing systems. However, estimation of the PES beyond 2.5 Å can provide some insights. A fragment of the S_1 PES along the Co-S bond for a constant Co-N_{Im} = 2.3 Å distance (Appendix, Figure A.4.6) was used for the estimated curve. It seems that it would be possible to have a minimum and then an increase in energy to the dissociation limit, assuming that at about 3.5-4.0 Å the curve reaches that limit. This problem does not occur in the case of alkyl derivatives like CNCbl, but for HOCbl such a minimum on the S_1 PES, for the elongated Co-OH bond, is also visible. In the case of HOCbl, this part of the S_1 PES can lead to Co-OH dissociation from higher excited states. While this is what the PECs and PESs indicate for HOCbl, dissociation would require overcoming the barrier. Since the barrier is significant for NACCbl at point C, it maybe interpreted that a metastable photoproduct with a significantly elongated Co-S bond could be formed, which then, as a result of axial base detachment, would transform into an

intermediate capable of Co-S dissociation. Considering all of this and the features of the S_1 PES (Figure 4.4b or 4.5b), it is basically difficult to say for sure whether the photoreaction runs directly from A → B or A → C; it is even more difficult to say when exactly the photoreaction runs directly to point B or C from higher excited states. It can be argued that point C is reached first. This way a metastable product would be formed, which along the C → B path would then be transformed into a photodissociable form. Regardless, the conclusions that both paths are photoactive as shown in Figure 4.7 seems to be the most straightforward interpretation.

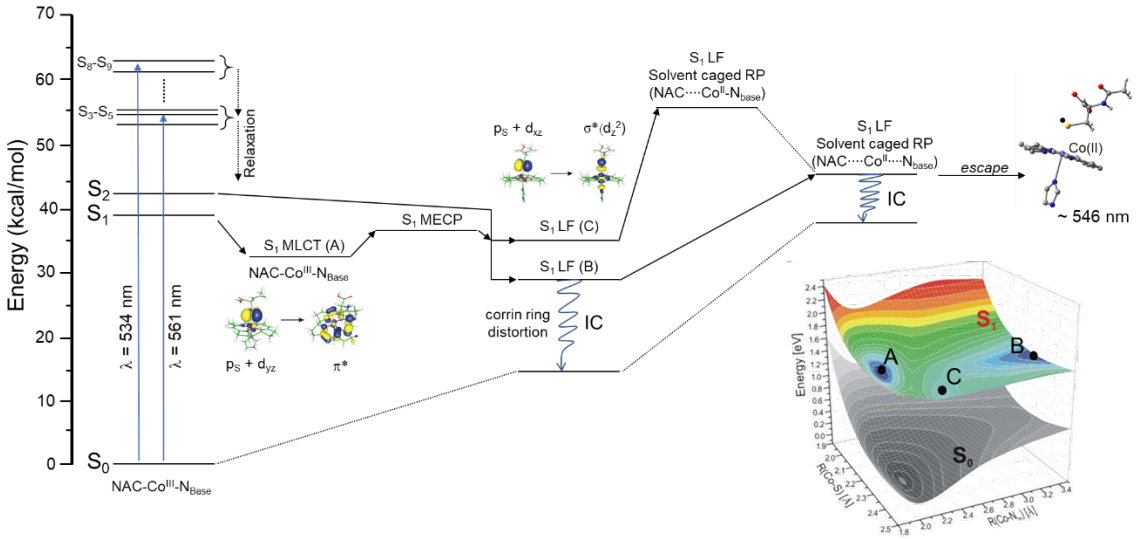

Figure 4.7. Scheme of photoreaction mechanisms for NACCbl. [a)]The energy of complex at indicated photoreaction point corresponds to energy at point C on S_1 PES presented in Figure 4.4. [b)] Corresponds to the structure of the model complex with a partially or fully detached axial base - point B on S_1 PES presented in Figure 4.4.

Figure 4.7 sums up the potential photoreaction mechanisms based on relative energetics. Initial excitation to S_3-S_5 or S_8-S_9 would correspond to experimental excitation of 561 or 534 nm, respectively. Relaxation of the system to the S_1 would result in population of the MLCT minimum, labeled NAC-Co^{III}-N_{Base} in Figure 4.7. In order to reach

the LF region from the S_1 MLCT minimum, the MECP would need to be crossed, leading to one of two minima regions in the LF, marked S_1 LF$^{a)}$ and S_1 LF$^{b)}$ in Figure 4.7. S_1 LF$^{a)}$ corresponds to point C on S_1 PES presented in Figure 4.4 where the Co-S bond is elongated (NAC$\cdots$Co^{III}-N$_{Base}$). S_1 LF$^{b)}$ corresponds to point B on the S_1 PES (Figure 7.4). Here, the Co-N$_{Base}$ bond is elongated (NAC-Co$^{III}\cdots$N$_{Base}$). Alternatively, relaxation from the upper excited states could result in relaxation to the S_2 state, wherefrom the LF can be accessed directly, i.e., without the need to cross the MECP. However, regardless of whether the LF is accessed via S_1 or S_2, either LF minima is a possibility for RP formation. From S_1 LF$^{a)}$, RP formation can occur via elongation of Co-S without any appreciable elongation of the Co-N$_{Base}$ bond (NAC$^{\bullet}$ + $^{\bullet}$Co^{II}-N$_{Base}$, Figure 4.7). From S_1 LF$^{b)}$, RP formation can occur via elongation of both axial bonds, where the axial base is potentially detached (NAC$^{\bullet}$ + $^{\bullet}$Co^{II} + N$_{Base}$, Figure 4.7). The relative energetics of these points were determined by the summation of the energies of the individual fragments, maintaining the methodology described in the Computational Details. Following RP formation that would occur from either LF minima, cage escape or IC conversion to the S_0 would follow.

To this point, the photolysis pathways correspond to experimental excitations from the α/β region of the Abs spectrum. However, photolysis of NACCbl was also investigated based on excitation from 360 nm. In order to analyze this photolysis pathway, excited states up to S_{45} were analyzed. These are included in Table A.4.1. Upon inspection, it appears that with excitation of 360 nm, the most likely states that can lead to the LF region are states S_{22} and S_{26}. The orbital contributions for S_{22} are 40% $d_{x2-y2} \rightarrow \sigma^*(d_{z2})$, 23% π_{NAC} + $\sigma(d_{z2}) \rightarrow \pi^*$, and 15% $\pi + (d_{z2}/p_S) \rightarrow \pi^*$. The orbital contributions for S_{26} are 65% π_{NAC} + $\sigma(d_{z2}) \rightarrow \sigma^*(d_{z2})$ and 19% $(d_{z2}/p_S) + \pi \rightarrow \sigma^*(d_{z2})$. S_{38} is also a possibility for accessing the

LF region with the character being 68% $\pi + d_{xz} \rightarrow \sigma^*(d_{z2})$, although S_{38} would correspond to excitation at 333 nm.

In the range 340-380 nm two calculated singlets, excited electronic transitions, S_{22} and S_{26}, contain a significant contribution of electronic excitation from the pure d and mixed π/σ occupied orbital to the $\sigma^*(d_{z2})$ antibonding orbital, mainly localized on axial bonds (Figure 4.8). The antibonding orbital, populated as a result of electronic excitation, contains linear combination of the cobalt d_{z2} orbital and p_z orbital of nitrogen and sulfur, respectively. Electron donation to $\sigma^*(d_{z2})$ orbital increases the electronic density along an axis perpendicular to the equatorial coordination sphere and weakens the Co-S and Co-N bonds with the axial ligands. Loosened axial bonds become susceptible to elongation and rupture; thus, by relaxation, it is possible to access the LF electronic state. Taking into account the character of the excitation and the significant value of the calculated oscillator strength for the S_{22} and S_{26} states, it is highly probable that both states can directly participate in the photolysis process after excitation by the wave at around 360 nm (Figure 4.8, Table A.4.1). Similar $\pi/d \rightarrow \sigma^*(d_{z2})$ character can be observed for S_{38}, corresponding to the excitation at the wavelength of 338 nm (Figure 4.8, Table A.4.1). Due to the higher excitation energy and the much lower value of oscillator strength, the participation of S_{38} in the photodissociation process is less likely.

3.7 Comparison with Experiment

3.6.1 Abs Spectroscopy

The photolysis of NACCbl was assessed using Abs spectroscopy at various wavelengths. LC-MS was used to confirm the identity of the photoproducts.[114] At 360, 405, and 546 nm, the photoproduct was identified to be HOCbl. For each wavelength, both the

Φ and the rate of photolysis for NACCbl were significantly lower than MeCbl. Nevertheless, the Co-S bond of NACCbl is photolabile. Interestingly, the Φ decreases with increasing wavelength for NACCbl. The Φ of NACCbl is approximately 4.4×10^{-4}, 1.3×10^{-4}, and 1.5×10^{-5} at 360, 405, and 546 nm, respectively. This appears to be distinctive of NACCbl. The Φ of alkylCbls tends to remain constant regardless of wavelength.[95] It is not surprising that the Φ for NACCbl at each wavelength is significantly lower than MeCbl. The methyl radical is much smaller than the NAC radical. Comparatively, it is easier for the methyl radical to diffuse from the solvent cage than for NACCbl. It would seem that it could be concluded that there is an increased likelihood of geminate recombination of the Co(II)/NAC• RP as compared to photolysis of MeCbl. At the same time, the NAC radical is comparable in size to the Ado ligand of AdoCbl, which is known to be efficiently photoactive regardless of its size. Clearly, ligand size is not the determining factor for the mild photoactivity of NACCbl. It would appear that NACCbl behaves more like the antivitamin B_{12} EtPhCbl, which also has a bulky upper ligand and is, similarly to NACCbl, a photoactive Cbl with a low Φ of photoproducts.[30, 112, 113] In EtPhCbl, there is branching between IC to the S_0 state and RP formation that are energetically comparable.[30] While geminate recombination is possible after RP formation, the more likely route for reversion to the S_0 state of EtPhCbl is IC. Likely, this is the same conclusion that can be drawn for NACCbl. The low Φ of photoproducts is likely due to the energetic favorability of the IC process over RP formation followed by geminate recombination.

3.6.2 EPR Spectroscopy

Photolysis via homolytic cleavage of the Co-R_{axial} bond is characteristic of Cbl photochemistry. Accordingly, it is not surprising that the photocleavage of the Co-S bond

of NACCbl is homolytic and results in the Co(II)/NAC• RP. This was shown via EPR spectroscopy.[114] NAC• was trapped after illumination at 546 nm. The results are consistent with the formation of NAC• which generates from the LF region. From a theoretical point of view, the Co(II)/NAC• RP could correspond to either point B or C on the S_1 PES (Figure 4.4). Orbital analysis further confirms this. The electronic transition associated with point B is characterized as $p_S + (d_{yz} + d_{xz}) \rightarrow \sigma^*(d_{z2})$ (Figure 4.6). The orbital characterization corresponding to point C is quite similar and is designated as $p_S + d_{xz} \rightarrow \sigma^*(d_{z2})$ (Figure 4.6).

3.8 Mechanism of Photodissociation

3.7.1 Photoreaction – from Photocleavage to Photodissociation

Based on the culmination of experimental data and the present calculations, the photoreaction of NACCbl is depicted in Figure 4.7. The first step in the process is excitation. Several excited states are good candidates for the initial excitation including S_3-S_5 and S_8-S_9, as these states can be assigned to absorption in the α/β region of the UV-vis spectrum (Table 4.2). An alternative is that photolysis can correspond to experimental excitation of 360 nm, with the most likely states that can lead to the S_1 LF region being S_{22} and S_{26}. Regardless of excitation wavelength, from any of these higher states, the relaxation to the lower states (S_2 and S_1) occurs. Knowing that photodissociation of Cbls occurs from the S_1 state, it is important to determine at which point on the S_1 PES the relaxation takes place. In other words, there are two options. Relaxation could lead to the MLCT minimum on the S_1 PES (Point A I $S_{1(min)}$, Figure 4.4) or to one of the LF minima (Point B or C, Figure 4.4). Should relaxation to the MLCT occur, the subsequent step would be to overcome the barrier (MECP) to reach the LF region. The barrier is less than 5.0 kcal/mol.

From here, Point C on the S_1 PES would be reached (labeled S_1 LF[a)], Figure 4.7). From S_1 LF[a)], RP formation occurs without detachment of the lower axial base. Homolytic cleavage of the Co-S bond was confirmed by the previously discussed EPR measurements. Alternatively, relaxation from the high energy states could lead to the S_2 state, which, theoretically, could result in population of the LF directly, thereby bypassing the MECP. The NTO analysis discussed previously confirms that this a possibility. Either LF minima, Point B (labeled S_1 LF[b)], Figure 4.7) or C, would be a candidate for this. From S_1 LF[b)], where the axial base is partially or perhaps fully detached, either RP formation or IC to the S_0 could occur. The most likely mechanism of IC would be distortion of the corrin ring (discussed in detail in ref 1). Regardless of whether photodissociation occurs from S_1 LF[a)] or S_1 LF[b)], the RP would be initially caged by solvent. The solvent caged RP can undergo geminate recombination and return to the octahedral geometry of the S_0 state. Additionally, the RP can escape the solvent cage. There is some experimental evidence for cage escape as evidenced by Φ measurements. However, significant diffusive loss of the NAC• radical is unlikely, especially in comparison to that of the methyl radical in photolysis of MeCbl. The reduction in Φ of NACCbl is more likely due to IC occurring from the LF region, which is also observed for the mildly photoresponsive antivitamin B_{12} EtPhCbl.

3.7.2 Deactivation

Accessing the LF region is a key component of photocleavage of the Co-S bond. This region of the S_1 PES is marked by elongated Co-N_{Im} bond length. If RP formation were to occur from the LF minima region containing point B, the Co-N_{Im} distance would need to be greater than 2.8 Å. In essence, the Co-N_{Im} bond would be broken or at least nearly broken and, recalling from the Computational Details, this is known as the base-off

form. From the LF region, essentially two options exist: either geminate recombination of the Co(II)/NAC• RP can occur or diffusive loss of NAC• from its solvent cage. Should the former occur, the base-off form of NACCbl, [Co^{III}(corrin)]-NAC^+, should be considered. The S_0 and S_1 PEC of [Co^{III}(corrin)]-NAC^+ is shown in Figure A.4.4. These curves can provide insight into the energetic feasibility of deactivation to the ground state minimum. As an example, CNCbl is photostable because the S_1 and S_0 PESs cross in the LF region preventing photolysis. For MeCbl and AdoCbl, there is a gap between the S_0 and S_1 PESs making the photolysis possible. The base-off PEC of NACCbl shows that the S_0 curve approaches the S_1 PEC at longer Co-S distances, representative of the LF. There is a small energetic difference between the two curves at Co-S distances greater than 2.8 Å. At Co-S 3.0 Å, the gap in energy between the S_0 and S_1 PEC is about 0.3 eV or ~7 kcal/mol. This perhaps explains the modest photoresponsiveness of NACCbl observed experimentally. The PECs do not cross, so photolysis is possible. At the same time, the gap is small, so it seems geminate recombination is likely. The deactivation mechanism of the LF state of NAC•···•Co^{II}_{LF}···Im system will be similar here to that in the case of photodissociation of Cbls alkyl derivatives.[1]

4.0 Summary and Conclusions

A theoretical analysis of the mechanism of photodissociation of NACCbl has been provided. It was determined by EPR spectroscopy that the Co-S bond of NACCbl is homolytically cleaved. This was confirmed by our calculations which indicate that the cleavage occurs in the LF region of the S_1 PES. The RP formation can occur from either Point B or C on the PES. Multiple possibilities appear to exist for the photodissociation mechanism including (1) relaxation to MLCT followed by crossing of the MECP to either

LF minima (Point B or C) or (2) relaxation directly to either Point B or C in the LF region. Regardless, while photodissociation can occur from either Point B or C, it seems that IC is the more likely photophysical event for NACCbl. However, should RP formation occur, cage effects will likely dominate and geminate recombination to the S_0 state will occur with a modest amount of NAC radicals escaping the cage due to the large ligand size; which may be another contributor to the modest Φ experimentally reported. NACCbl's photolytic properties are certainly distinctive of other previously studied Cbls. Overall, the photosensitive capability of NACCbl indicates that SCbls are good candidates for additional studies of light-based applications beyond cellular physiology.

CHAPTER 5

WHY IS CARH PHOTOLYTICALLY ACTIVE?

Synopsis

The discovery of naturally occurring B_{12}-depedent photoreceptors has allowed for applications of Cbls in optogenetics and synthetic biology to emerge. However, theoretical investigations of the complex mechanisms of these systems have been lacking. Adenosylcobalamin (AdoCbl)-dependent photoreceptor, CarH, is one example and it relies on daylight to perform its catalytic function. Typically, in enzymes employing AdoCbl as their cofactor, the Co-$C_{5'}$ bond activation and cleavage is triggered by substrate binding. The cleavage of the Co-$C_{5'}$ bond is homolytic resulting in radical pair formation. However, in CarH, this bond is instead activated by light. To explore this peculiarity, the ground and first excited state PESs were constructed using the quantum mechanics/molecular mechanics (QM/MM) framework and compared with other AdoCbl-dependent enzymes. QM/MM results indicate that CarH is photolytically active as a result of the AdoCbl dual role, acting as a radical generator and as a substrate. Photo-cleavage of the Co-$C_{5'}$ bond and subsequent H-atom abstraction is possible because of the specific orientation of the H-$C_{4'}$ bond with respect to the Co(II) center. Comparison with other AdoCbl-dependent enzymes indicate that the protein environment in the CarH active center alters the photochemistry of AdoCbl by controlling the stereochemistry of the ribose moiety.

1.0 Introduction [***]

While the light sensitivity of the cobalt-carbon (Co-$C_{5'}$) bond in coenzyme B_{12} (AdoCbl = coenzyme B_{12}, Figure 5.1) has been known for nearly five decades, only until recently has this been associated with light controlled reactivity, namely optogenetic regulation and light-activated drug delivery.[1, 22] In particular, the CarH photoreceptor, uses AdoCbl as a photoactive cofactor capable of inducing significant structural changes of the photoreceptor's protein chains to regulate DNA transcription.[23, 33, 224] Coenzyme B_{12} contains a Co(III) ion that is equatorially coordinated to four nitrogens of a corrin ring and perpendicularly to upper and lower ligands. The upper ligand is variable and used to distinguish Cbls from one another in B_{12} nomenclature.[3] In CarH, the upper axial ligand is a 5′-deoxy-5′-adenosyl (Ado, Figure 5.1) and is covalently bound to the Co via the $C_{5'}$ of the ribose moiety. The photolytic scission of the Co-$C_{5'}$ bond of AdoCbl is a key feature of CarH's mechanism of action.[32, 34] In B_{12}-dependent enzymes, the lower ligand is the dimethylbenzimidazole (DBI) base from the nucleotide loop or a histidine (His) residue.[3, 5, 6] In the CarH photoreceptor, the DBI base is replaced with His177, forming the base-off/His-on conformation of the cofactor.[33]

[***] *Chapter 5 adopted from:* Toda, M. J., Mamun, A. A., Lodowski, P. Kozlowski, P. M. Why is CarH Photolytically Active in Comparison to other B_{12}-dependent Enzymes? *J. Photochem. Photobiol. B: Biol.* **2020**, 111919.

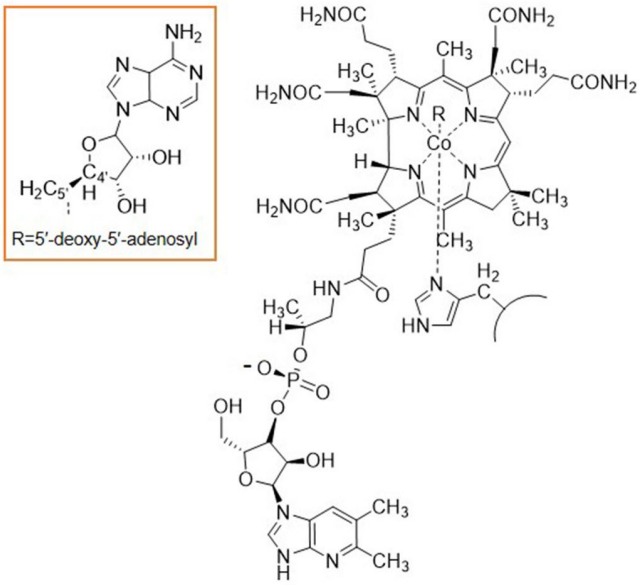

Figure 5.1. General molecular structure of base-off/His-on cobalamins. R represents the upper axial ligand and in CarH, *R* = 5′-deoxy-5′-adenosyl (Ado). Molecular structure of Ado group is presented in the orange box.

The CarH photoreceptor regulates DNA transcription in bacteria which results in the expression of genes responsible for biosynthesis of carotenoids.[23, 33, 224] This involves significant structural changes to the photoreceptor as well as local, molecular level processes in the Cbl binding domain. The overall mode of action for CarH is depicted in Figure 5.2. In the dark, CarH-DS (DS = Dark State), forms a tetramer upon AdoCbl binding. Transcription of carotenoid biosynthetic genes is repressed in the absence of daylight, where CarH-DS binds to DNA. In the presence of light, the Co-$C_{5'}$ bond is ruptured, and the Ado ligand is converted to the photoproduct, 4′,5′-anhydroadenosine (anhAdo).[32] As a result, His132 will take the place of the Ado ligand, forming a stable adduct with the cofactor.[33] This photoinitiated process induces a large-scale structural change in the protein's conformation and the tetramer dissociates into monomers forming CarH-LS (LS = Light State). In CarH-LS, the cofactor retains His132 and His177 as upper

and lower axial ligands, respectively, and this is denoted as bis-HisCbl.[23] Ultimately, this cascade of events initiates the transcription of carotenoid biosynthetic genes.

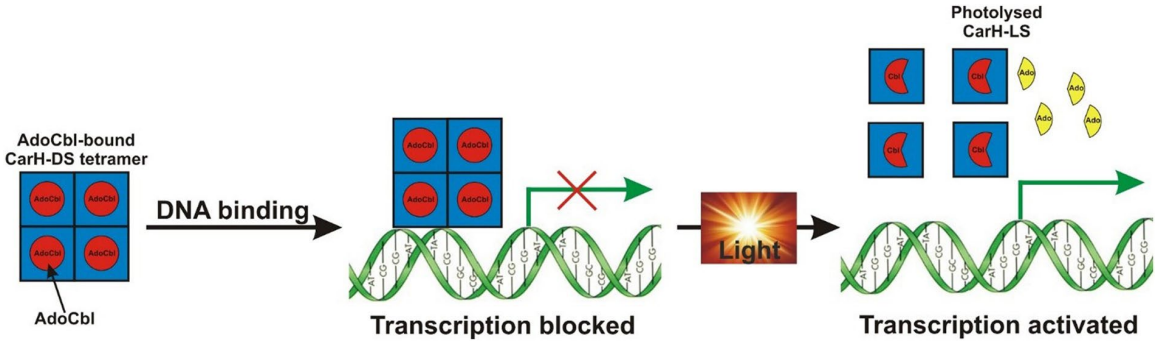

Figure 5.2. Overall scheme of the CarH mode of action. The CarH-DS is a dimer-of-dimers where monomers form head-to-tail dimers which form the tetramer. Each monomer contains a DNA binding domain, a helical bundle, and an AdoCbl binding domain. The "Ado" depicted in the color yellow is the product of photolysis formally referred to as 4′,5′-anhydroadenosine (anhAdo).

Although the 'big picture' mode of action for CarH seems to be generally understood, there are many issues and questions about the photo-catalytic mechanism that have not been explored to date. One important question has arisen: "how is the Co-$C_{5'}$ bond activated and cleaved in CarH-DS?" This seemingly simple question has in fact been quite perplexing because AdoCbl is known for its radical chemistry and, in terms of photochemistry, the cleavage of the Co-$C_{5'}$ bond of AdoCbl is homolytic.[3-6, 47, 92, 94, 95] It came as quite a surprise that a proposed mechanism for CarH, implicated heterolytic cleavage of the Co-$C_{5'}$ bond over homolytic cleavage.[34]

Even more intriguing is a second question: "what specifically makes CarH photolytically active in comparison to other AdoCbl-dependent enzymes?" Photolytic properties of AdoCbl-dependent enzymes, including glutamate mutase (GLM) and ethanolamine ammonia-lyase (EAL), have been thoroughly investigated both experimentally[25, 40, 41, 106, 225] [16–20] and computationally.[24, 122, 182] It was found that photo-

cleavage of the Co-$C_{5'}$ in GLM and EAL enzymes is suppressed and only a small portion of the Co-$C_{5'}$ bonds undergoes photodissociation. In stark contrast to CarH, excited state dynamics and photolytic studies of GLM and EAL revealed that these enzymes were essentially photostable. Intuitively, it is reasonable to suppose that there must be some aspect at the molecular level that is responsible for the different photo-reactivities of these enzymes especially considering that coenzyme B_{12} is utilized in each system mentioned above.

The purpose of this work presented in this chapter is to answer these two questions. QM/MM calculations were employed to probe the photolytic properties of CarH-DS and to determine what structural features of the AdoCbl cofactor contribute to these properties. When comparing the excited state properties, exemplified by the S_1 state PES, of CarH to the previously studied GLM and EAL, there are not any major differences. However, based on theoretical insights, it is apparent that the conformation of the Ado group of the cofactor significantly contributes to CarH's efficiency as a photoreceptor. Present calculations do not indicate that the protein environment in the CarH active center alters the photochemistry of AdoCbl, rather it appears that CarH alters the stereochemistry of the ribose moiety to allow for its photolytic activity. This will undoubtedly have implications for elucidating the entire CarH mechanism at the molecular level and in analyses of other similar photoreceptors.

2.0 Computational Details

The CarH model used in the QM/MM calculations was generated from the crystal structure of *Thermus thermophilus* CarH-DS bound to DNA (PDB ID: 5C8E).[33] The computational details for QM/MM results of GLM and EAL are included in Appendix 5.

Additionally, Tables A.5.1 and A.5.2 summarize the differences in the crystal structures and model structures of CarH, GLM, and EAL. CarH-DS is a tetramer, more specifically, it is a dimer-of-dimers type tetramer. In this study, the primary focus is the molecular activity in the active site containing the cofactor. The model system that was used for QM/MM calculations was constructed to effectively home in on the active site. The crystal structure that contained DNA (5C8E) was selected because Co-$C_{5'}$ bond activation via light occurs after DNA binding. First, the crystal structure was reduced to a single monomer with the DNA strand removed to ensure computational efficiency. The monomer was then protonated using PropKa 3.0[226] and minimized using the AMBER force field in UCSF Chimera.[227] This monomer comprised the model system that was the basis for the QM/MM calculations. Geometric parameters of QM/MM optimized CarH, GLM, and EAL, are listed in Table A.5.3 along with the corresponding values from the crystal structure. The QM/MM optimized geometries of AdoCbl bound to CarH, GLM, and EAL are depicted in Figure A.5.1.

The QM/MM calculations were performed using Gaussian 09 software with Revision B.[228] The minimized structure was divided into two layers, known as the high and low layer. The high layer was treated with QM using DFT/BP86 and the low layer was treated with MM. A truncated form of the cofactor was included in the high layer while the remaining portion of the cofactor, which is not critical in the catalytic process, was included in the low layer. The high layer contained a total of 68 atoms including the corrin ring, the Im part of His177, Co, and the Ado moiety. It is important to recall that, in CarH-DS, AdoCbl binds in the base-off/His-on conformation and His177 takes the place of the DBI base. Accordingly, the Im portion of His177 was included in the high layer and the notation

'Co-N_{Im}' refers to the lower axial bond. The lower axial ligand in CarH is His177 and for GLM the lower axial ligand is His16. Both His are protonated at the Nδ1 position and are formally described as HID in the input. In the ligand pocket (Figure A.5.2), the protonation states of His142 and Glu141 are as follows. For His142 of CarH, the ε-nitrogen is protonated and is formally HIE for the calculations. $NH3^+$ and COO^- are bound to the α-carbon of Glu141.The low layer contained a total of 4398 atoms including the remaining portion of the cofactor (the methyl, acetamide, and propionamide side chains attached to the corrin ring, the nucleotide loop, and DBI), as well as all the protein residues. Atoms within 20 A of the Co center were kept unfrozen and the rest of the protein was frozen. In total, the model contained 4466 atoms.

For the QM calculations, the pure GGA-type functional BP86 was employed within DFT and TD-DFT frameworks. This is consistent with other QM/MM studies of B_{12}-dependent enzymes.[24, 122, 182, 221] The TZVP basis set was used for H and TZVPP was used for Co, C, N, and O.[191, 192] The low layer was treated with the AMBER force field (FF99SB) with the AMBER parameters for the cofactor, including the Co ion, obtained from Marques *et al*.[229] Mechanical embedding was used for the ONIOM calculation. In sum, the model was optimized using QM(DFT)/MM(AMBER). The charge was one and the multiplicity singlet for the QM region. '

To study photo-induced Co-$C_{5'}$ bond cleavage, first a S_0 PEC was constructed as a function of Co-$C_{5'}$ bond distance. This PEC was generated by systematically elongating the Co-$C_{5'}$ bond distance with a step size of 0.1 A. The optimized geometries along the S_0 PEC were used to construct the entire S_0 PES, which is a function of Co-$C_{5'}$ and Co-N_{Im}, i.e. the axial bonds. The optimized ground state geometries were used to construct the S_1

PES . Single point QM(TD-DFT)/MM calculations were performed based on the optimized geometries for each point on the S_0 PES. The S_1 PES was not relaxed as the model size is far too large to perform these calculations within a reasonable amount of time. Thorough orbital analysis was performed to ensure that none of the selected transitions of the S_1 PES were the result of LRCT. The presented S_1 PES does not suffer from this issue.

3.0 Results and Discussion

3.1 Activation and Photolytic Co-$C_{5'}$ Bond Cleavage

To understand how CarH operates at the molecular level it is paramount to analyze the PESs associated with the ground state (S_0) and the lowest electronically excited state (S_1). The S_1 state is particularly important because photocleavage of the Co-$C_{5'}$ bond and the subsequent RP formation occurs from here.[1] DFT/MM and TD-DFT/MM were employed for generating the S_0 and S_1 PESs, respectively. The S_0 and S_1 PESs were constructed as a function of axial bond lengths, Co-$C_{5'}$ and Co-N_{Im} (Figure 5.3). Similar methodology was used for other AdoCbl-dependent enzymes including GLM and EAL as well as methylcobalamin (MeCbl)-dependent methionine synthase (MetH).[122, 182, 221]

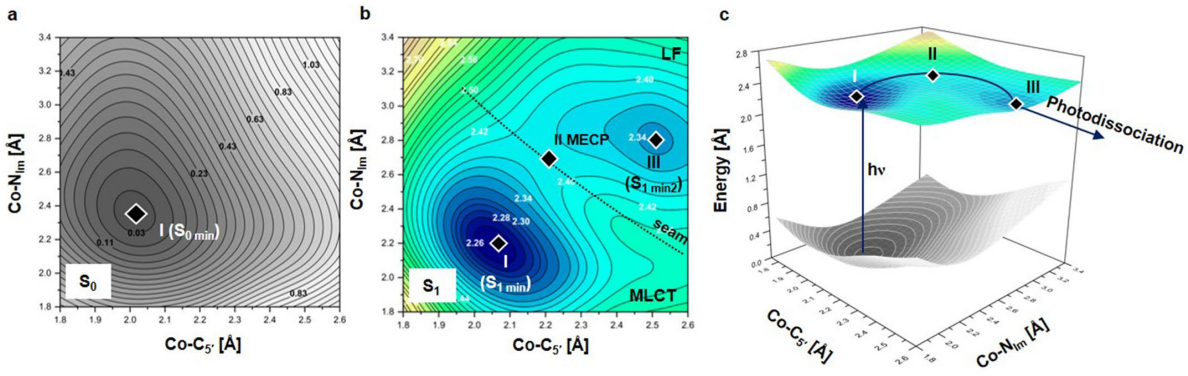

Figure 5.3. PESs for CarH-DS for the **a)** ground state (S_0), **b)** first excited state (S_1), and **c)** overlay of S_0 and S_1 PES with photodissociation pathway depicted.

The PES representing the S_1 state of CarH-DS contains two energy minima, MLCT and LF regions (Figure 5.3b). The crossing of these two electronic states forms a seam (dotted line, Figure 5.3b), approximately along the diagonal of the S_1 PES. The MECP between the MLCT and LF states is denoted as II MECP in Figure 5.3b. The MLCT minimum, denoted as I ($S_{1\ min}$) on Figure 5.3b, corresponds to the excited state geometry with axial bond lengths of approximately 2.1 Å and 2.2 Å for Co-$C_{5'}$ and Co-N_{Im}, respectively. The excitation from the S_0 state to the MLCT minimum (I $S_{0\ min} \rightarrow$ I $S_{1\ min}$, Figure 5.3) can be primarily associated with transition from metal d orbitals to corrin π^* orbitals. The MLCT can be characterized as mixture of d $\rightarrow \pi^*$ excitations from different d orbitals of Co. Specifically, the MLCT can be characterized as 23% $d_{xz} \rightarrow \pi^*$, 36% $d_{z2} + \pi \rightarrow \pi^*$, and 39% $d_{yz} + \pi \rightarrow \pi^*$ (Figure 5.4). The MECP is a mixture of both MLCT and LF type excitations, with the HOMO to LUMO+1 transition being dominant. Specifically, at the MECP, the excitations can be characterized as 18% $d_{yz} + \pi \rightarrow \pi^*$ and 73% $d_{yz} + \pi \rightarrow \sigma^*(d_{z2})$ (Figure 5.5). The LF minimum III ($S_{1\ min2}$) is 0.08 eV (1.8 kcal/mol) higher than the MLCT minimum (I $S_{1\ min}$) and the electronic excitations associated with the LF state, in about 99%, is a $d_{yz} + \pi \rightarrow \sigma^*(d_{z2})$ transition (Figure 5.6).

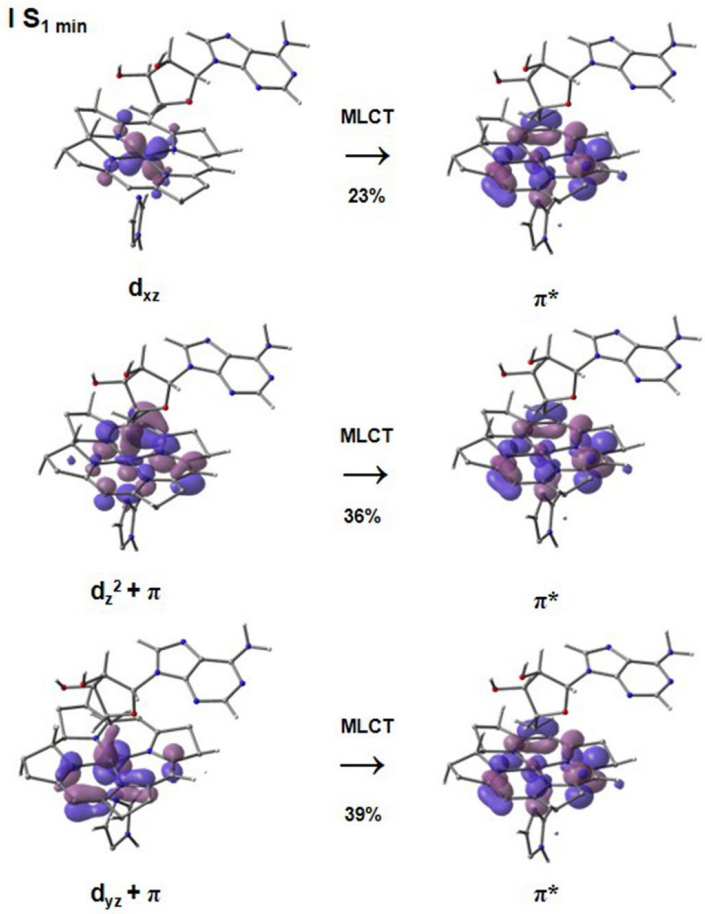

Figure 5.4. Kohn-Sham orbitals involved in excitations from the S_0 to the MLCT region minimum, I $S_{1\ min}$, of the S_1 PES (Figure 3).

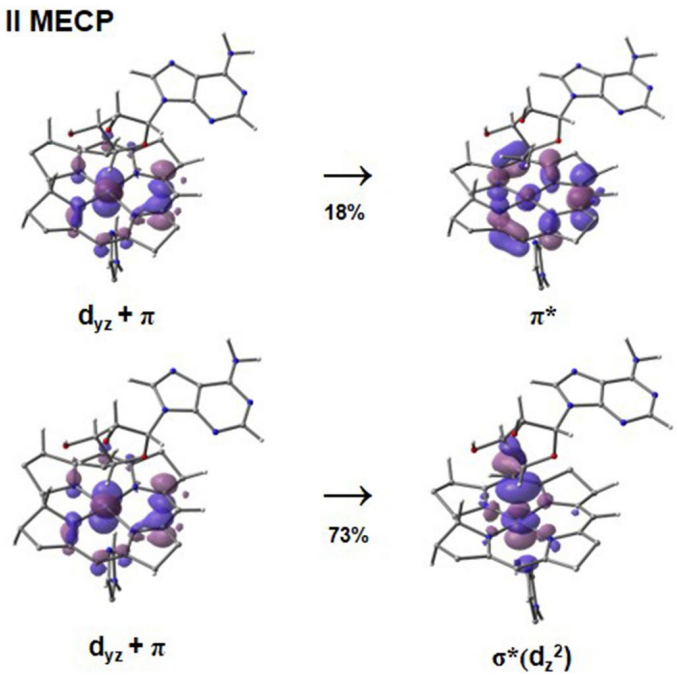

Figure 5.5. Kohn-Sham orbitals involved in excitations from the S_0 to the MECP, II MECP on the S_1 PES (Figure 5.3).

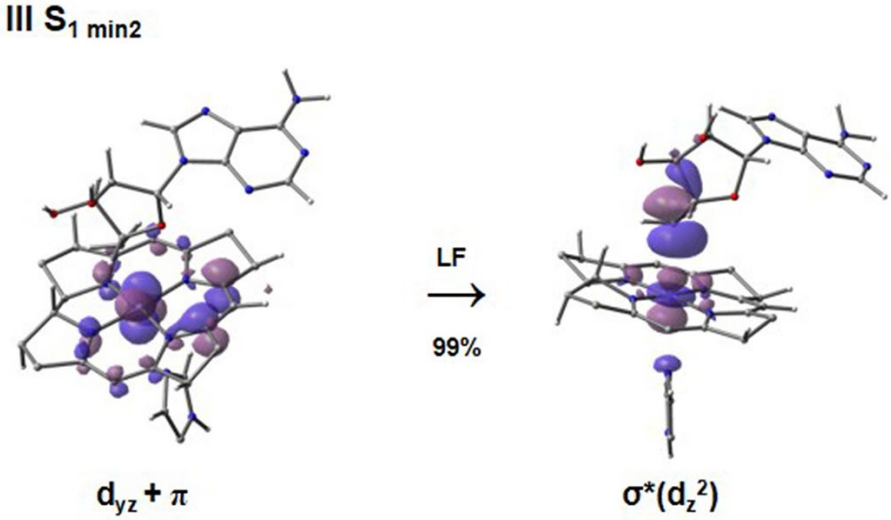

Figure 5.6. Kohn-Sham orbitals involved in excitations from the S_0 to the LF region minimum, III $S_{1\ min2}$, of the S_1 PES (Figure 5.3).

Previous studies of coenzyme B_{12}-depedent enzymes demonstrate that the S_1 PES involves a crossing of two electronic states, the MLCT and the LF.[122, 182] The seam in the PES can be attributed to this crossing and an MECP at the seam can be computed. In order to calculate the MECP we used the computed S_1 PES (See Figures 5.7 and 5.8). The topology of the S_1 PES in all three enzymes are similar, there is a MLCT region at equilibrium bond distances and LF region at the extended bond distances. The MLCT and LF are separated by a seam. In order to connect these MLCT and LF states, we used the following formula (Equation 1) to calculate the minimum energy pathway in this transition. Based on this analysis we identified the MECP point in this transition. The energy barriers were computed as a function of energy vs. Q value where

$$Q = \sqrt{R^2_{Co-C_5{}'} + R^2_{Co-N_{Im}}} \tag{5.1}$$

It is important to note that the features on the S_1 PES are not unique to CarH-DS. There would seem to be no reason to expect that the topology of the S_1 PES of CarH-DS would be markedly different than those of AdoCbl-dependent GLM or EAL, as both are based on the geometrical and electronic changes associated with the same cofactor, namely AdoCbl. Indeed, the S_1 PES of CarH-DS is quite like those of GLM and EAL in terms of topology, although, there are slight differences in terms of energetics (Figure 5.7) based on QM/MM calculations. For GLM and EAL, the LF region on the S_1 PES, is energetically more stabilized in comparison to the MLCT region. However, in CarH-DS, the LF region is not lower in energy than the MLCT region. This is not necessarily unexpected. Previous theoretical investigations as well as experimental insights have spurred on the hypothesis

that the role of the enzyme is to modulate the energetics associated with photo-catalytic pathways in B_{12}-dependent enzymes.[94, 103, 122, 182]

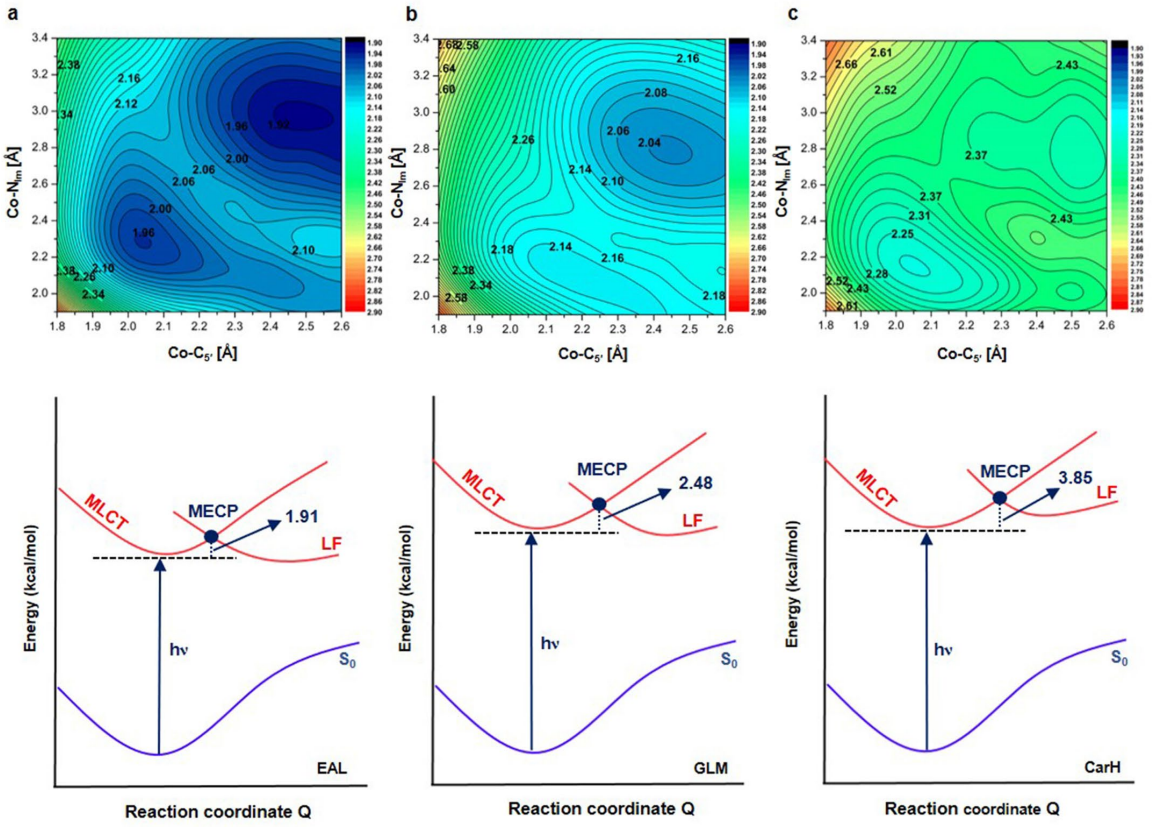

Figure 5.7. Topologies of the S_1 excited states, using the same color scale for the grid point energies in eV (upper panels) and schemes of energetic profiles for photoactive paths (lower panels) for AdoCbl-dependent **a)** EAL, **b)** GLM, and **c)** CarH.

In a recent QM/MM study of MetH, a MeCbl-dependent enzyme, a similar situation was observed for the S_1 PES.[221] It is known from crystallographic data that the AdoCbl binding domain of CarH-DS is markedly similar to the MeCbl-binding module in MetH.[23, 33] Consequently, it is not surprising that the relative energies on the S_1 PES of CarH are more similar to those which were observed in MetH (Figure 5.8), owing to the nearly identical enzymatic environment of the cofactor. Here, for both enzymes, the MLCT state is stabilized in relation to LF. On the other hand, it is also not surprising that the S_1 PES of

CarH-DS is very similar in terms of topology to GLM and EAL as these three involve the same cofactor (Figure 5.7). When comparing the energetic barriers on the possible photoreaction paths, it is apparent that the energy difference from the MLCT minimum of MetH to the MECP is nearly 10 kcal/mol while in CarH-DS the MECP is only 3.5 kcal/mol higher in energy than the MLCT minimum (Figure 5.8). MetH is not a photoreceptor, so it is reasonable that the barrier to the LF region is larger in comparison to CarH-DS. However, for CarH-DS, or really any coenzyme B_{12}-dependent photoreceptor to be photolytically active, it would be only logical that the barrier to the LF is not insurmountable.

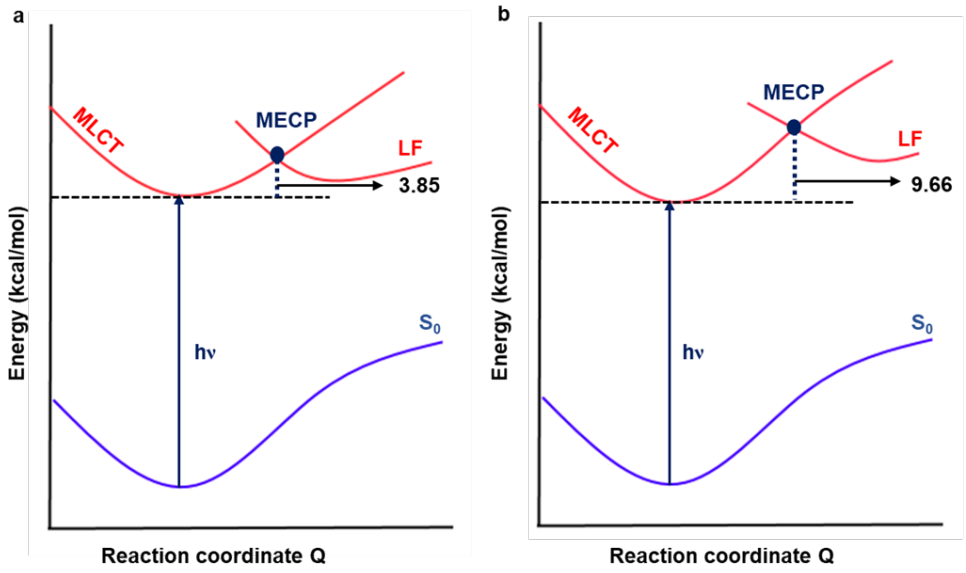

Figure 5.8. Schemes of photoreactions as a function of energy versus Q for **a)** AdoCbl-dependent CarH and **b)** MeCbl-dependent MetH.

The S_1 PES for CarH-DS clearly shows an energetically feasible route for cleaving the Co-$C_{5'}$ bond. Presumably, the light-sensing function of CarH can be initially associated with excitation to an upper singlet excited state which is followed by the rapid IC to the S_1 state. There are very little geometrical changes after excitation and relaxation, because the

topology of the energy minima associated with S_0 and MLCT states are very similar. As previously stated, photodissociation of the Co-$C_{5'}$ bond of AdoCbl occurs from LF region of the S_1 state. As such, the corresponding reaction pathway along the S_1 PES should involve the most favorable route from the MLCT region to the LF region. Present calculations indicate that the most energetically feasible path to photolysis in CarH-DS involves the initial elongation of the Co-N_{Im} bond followed by the elongation of the Co-$C_{5'}$ bond up to the complete cleavage (Figure 5.3c).

3.2 Considering Structural Factors Associated with Enzyme Bound AdoCbl

To understand what characteristic of CarH contributes to its role as a photoactive catalyst, it is important to explore what structural aspects of AdoCbl-dependent enzymes set them apart. In terms of geometry, the important difference between EAL, GLM, and CarH is related to the orientation of the ribose portion of the upper axial ligand of the cofactor. Specifically, the orientation of the -$C_{5'}$ of the Ado moiety bound to Co and the orientation of the -$C_{4'}$-H plays a critical role. In B_{12}-dependent enzymatic catalysis the ribose part of Ado ligand can undergo various conformational changes including pseudorotation or rotation around the glycosyl angle.[5, 6, 52, 230] Interestingly, the ribose conformations have been shown to control the radical trajectories in AdoCbl-dependent enzymes including diol dehydratase (DDH) and GLM.[6] There are two implications for the conformational change of the ribose portion of the Ado radical for both examples. One orientation favors radical recombination while the other position promotes H-atom abstraction from the substrate. For the native enzymatic reaction of GLM, the pseudorotation of the ribose ring moves the $C_{5'}$ radical in such a way to generate a substrate radical instead of recombining with the Co(II). For DDH or EAL, the $C_{5'}$ radical is moved

over an approximately 7 Å distance towards the substrate via rotation around the N-glycosidic bond to facilitate H-atom abstraction.[50]

However, there is a key difference between CarH and the two other previously mentioned AdoCbl-dependent enzymes, EAL and GLM. The ribose portion of the Ado group is flexible and can be found in either the 2′-endo or 3′-endo conformations.[6] For the optimized structures of EAL, GLM, and CarH, the initial conformation of the ribose ring is 3′-endo. The structural analysis of the AdoCbl cofactor in these three enzymes reveals a crucial difference related to stereochemistry, considering the various conformations that may arise based on rotation around the $C_{5'}$-$C_{4'}$ single bond of AdoCbl (Figure 5.9). In the case of CarH-DS, the hydrogen bound to the $C_{4'}$ in the equilibrium structure is oriented in such a way that would be suitable for H-atom abstraction. On the other hand, in EAL and GLM, the -$C_{4'}$-H projects in a different orientation that is not favorable for H-atom abstraction from the $C_{4'}$ atom. Furthermore, after photocleavage of the Co-$C_{5'}$ bond, present calculations indicate that the -$C_{4'}$-H is in perfect position to participate in β-H elimination and form the Co-hydride (HCbl). This species, having the Co-H bond, has been implicated to be a potential intermediate in proposed mechanisms for CarH-DS.[32, 36]

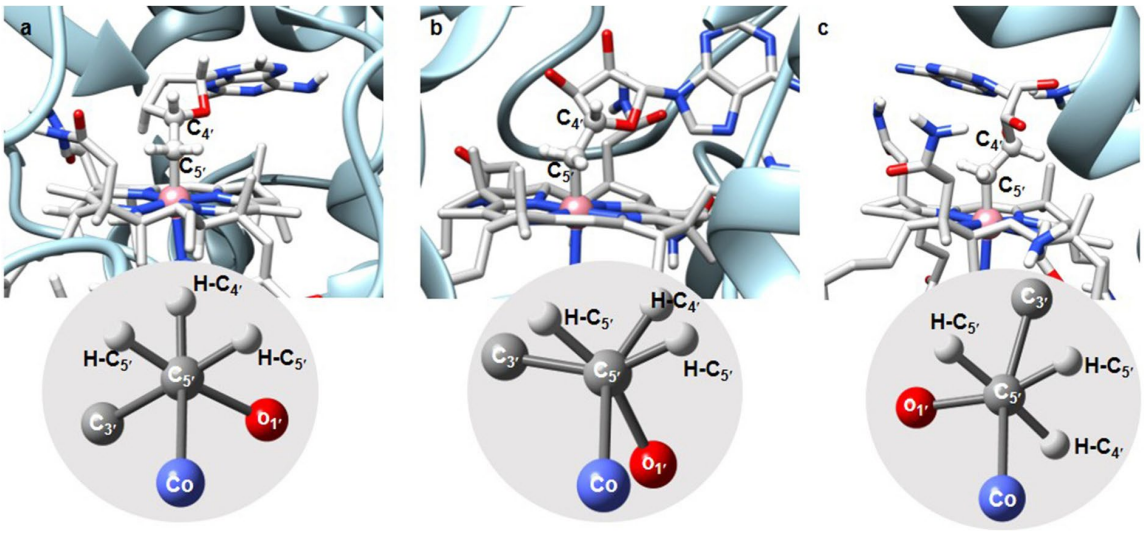

Figure 5.9. Optimized ground state equilibrium structures of AdoCbl bound to **a)** EAL, **b)** GLM, and **c)** CarH. $C_{5'}$ and $C_{4'}$ carbons and their corresponding hydrogens are represented in ball and stick form. The stereochemistry of β-lactam system along $C_{5'}$-$C_{4'}$ bond is presented in gray circle. See Table A.5.4 for complete listing of atom labeling for the truncated Ado ligand in the inset.

Here it is important to further comment on the geometric parameters of the crystal structures and QM/MM optimized AdoCbl structures bound to CarH, EAL, and GLM (Table A.5.3). There are not any significant differences in the Co-$C_{5'}$ bond length or of the bonds from Co to the nitrogens of the corrin ring (N_{21}-N_{24}). The only major difference is between the Co-N_{Im} bond. For CarH and GLM the Co-N_{Im} bond is 2.28 Å and 2.27 Å, respectively and is 2.37 Å for EAL. The similarity of the Co-N_{Im} bond of AdoCbl bound to CarH and GLM is to be expected as both of these are in the base-off/His-on binding mode. The Co-N_{Im} bond is longer for EAL because the cofactor is in the base-on binding mode. His is more basic than DBI so the Co-N_{Im} bond of AdoCbl is longer than for CarH and GLM. The differences in the bond and torsion angles of AdoCbl shown in Table S3 are best understood upon visualization. Figure A.5.1 shows the optimized molecular structure of the cofactor and further depicts the differences in the orientation of the Ado ligand across the three enzymes under comparison. With the short bond of the corrin ring

in the foreground, the adenine of Ado is directed directly away from the short bond of the corrin ring in CarH. In GLM, the adenine portion of Ado is bent forward and to the left of the corrin ring, when the short C-C bond is in the foreground. For EAL, the adenine is pointed back, but the ribose is rotated in comparison to CarH. Upon additional comparison, it would appear that the enzymatic environment serves to orient the cofactor in a particular position and thus keep the -$C_{4'}$-H in a particular position.

Table A.5.4 lists the geometric parameters related to ribose conformation of the Ado ligand for the QM/MM optimized AdoCbl structure bound to CarH, EAL, and GLM with the corresponding values from the crystal structures included. After computing the pseudorotation phase from the endocyclic angles of the ribose moiety, it was determined that the ribose is in the 3′-endo conformation for each case. That being said, exocyclic and endocyclic angles are markedly different when comparing the three cases. While the orientation and directionality of the Ado ligand is different in CarH, GLM, and EAL, the conformation of the ribose is the same in each and is 3′-endo. In the context of this discussion it is natural to consider if the enzymatic environment aids in keeping the Ado ligand in a particular location in the active site.

The residues contained in the AdoCbl ligand pocket, which are within hydrogen bonding distance and/or hydrophobic contact with the cofactor or other residues in the active site, are listed in Table A.5.5. The selected residues are based on the crystal structure data obtainable from the PDB. For CarH (PDB ID: 5C8E), GLM (PDB ID: 1I9C), and EAL (PDB ID: 3ABS), there are 7, 12, and 13 residues in the ligand pocket, respectively. Upon visualization of these residues, from both the crystal structure and the optimized model structure, it is apparent that these residues play a key role in keeping the Ado ligand

in a specific orientation. Based on the CarH crystal structure, there is a hydrogen bond between a $C_{5'}$-H and corrin ring. There is also a hydrogen bond between E141 and the O2 of the ribose (See Table A.5.4, inset for atom numbering). Based on the GLM crystal structure, there is a hydrogen bond between N2 of the adenine portion of Ado and a side chain of the corrin ring. There is also a hydrogen bond between a side chain of the corrin ring and the O2 of the ribose. For EAL (3ABS) the cofactor is adeninylpentylcobalamin (AdePeCbl) instead of AdoCbl. AdePeCbl does not contain a ribose ring, accordingly hydrogen bonding to the ribose ring is not a factor here but it is apparent based on visualization that the residues contained in the active site sterically prevent the Ado from significant rotation. This is apparent based on Figures A.5.3 - A.5.5 where the cofactor is shown embedded in the ribbon structure of the protein.

The residues of the active site, listed in Table A.5.5, are depicted in Figure A.5.2. This shows the molecular structures contained in the ligand pocket of a) CarH, b) GLM, and c) EAL. The structures were taken directly from crystallographic data, prior to any calculations. In each case, the amino acid residues flank the Ado ligand and appear to sterically hinder significant rotation around the glycosyl rotation angle. Additionally, the optimized molecular structures of the cofactor were compared. These are shown in Figures A.5.3 – A.5.5. Again, these figures show that the role of the active site residues is to keep the Ado ligand in a particular orientation which likely prevents significant free rotation around the glycosyl rotation angle or the $C_{4'}$-$C_{5'}$ single bond. To sum up this structural analysis, the residues of the active site of each enzyme under comparison affect the orientation and directionality of the Ado ligand thus contributing to the specific orientation of the -$C_{4'}$-H.

4.0 Summary and Conclusions

Present QM/MM calculations clearly indicate that role of light in the mechanism of CarH-DS is simply to generate the Co(II)/Ado• RP, in a similar fashion that has been observed for EAL and GLM . This is evident based on the similar topologies of the S_1 PESs of CarH, EAL, and GLM. In addition, unlike some B_{12}-dependent enzymes like MetH, an energetically feasible route for photodissociation can be identified on the S_1 PES of CarH-DS. It is also apparent that AdoCbl plays a unique dual role in CarH-DS as compared to other AdoCbl-dependent enzymes which require substrate binding for the activation of the Co-$C_{5'}$ bond. Upon photo-cleavage of the Co-$C_{5'}$ bond in CarH-DS, the specific orientation of the H-$C_{4'}$ bond with respect to the Co(II) center, allows for H-atom abstraction and, by analogy, the free Ado group can act like a substrate. While preliminary results from experiments have suggested that CarH alters the photochemistry of AdoCbl,[34] our theoretical investigation does not support this conclusion. Rather, CarH appears to alter the stereochemistry of AdoCbl in order to facilitate photoproduct formation. CarH is truly unique as a light-sensor especially in comparison to other AdoCbl-dependent enzymes that are not efficiently photoactive.

CHAPTER 6

ELECTRONIC AND PHOTOLYTIC PROPERTIES OF HYDRIDOCOBALAMIN

Synopsis:

HCbl, is a known member of the B_{12} family of molecules yet unlike other well-studied Cbls, little is known of the electronic and photolytic properties of this species. Interest in HCbl has increased significantly in recent years when at least three experimentally proposed mechanisms implicate HCbl as an intermediary in the photoreaction of coenzyme B_{12}-dependent photoreceptor CarH. Specifically, cleavage of the Co-$C_{5'}$ bond of coenzyme B_{12} could lead to β-hydride or β-hydrogen elimination reaction to form HCbl. HCbl is known to be a transient species where the oxidation state of the Co is variable; Co^{I}-H^{+} ⇋ Co^{II}-H ⇋ Co^{III}-H^{-}. Further, HCbl is a very unstable with a pKa of ~ 1. This complicates experimental studies and there are no available crystal structures of HCbl – either for the isolated molecule or bound to an enzyme. In this study, the electronic structure, photolytic properties, and reactivity of HCbl were explored to determine the preferred oxidation state as well as its potential role in the formation of the photoproduct in CarH. NBO analysis was performed to determine the oxidation state of Co in isolated HCbl. Based on the NBO analysis of HCbl, Co clearly had excess negative charge, which is in stark contrast to other alkylCbls where the Co ion is marked by significant positive charge. In sum, NBO results indicate that the Co-H bond is strongly polarized and almost ionic. It can be described as protonated Co(I). In addition, DFT was used to explore the BDE of HCbl based on

homolytic cleavage of the Co-H bond. TD-DFT calculations were used to compare theoretically computed electronic transitions to the experimentally determined Abs spectrum. The photoreaction of CarH was explored using an isolated model system and a pathway for hydrogen transfer was found. QM/MM calculations were employed to investigate the formation of HCbl in CarH.

1.0 Introduction †††

Reports of the reactivity of HCbl date back to the 1960's yet little is known of the electronic and photolytic properties of this species.[231-237] This intermediary has been implicated in several Cbl-dependent reactions including the B_{12}-dependent photoreceptor CarH.[32, 34, 37, 238] HCbls are members of the Cbl family of molecules, also known as B_{12} derivatives, where the parent molecule is vitamin B_{12} (CNCbl).[3, 5] HCbl shares the typical features of Cbls including the corrin macrocycle which is centrally bound to a Co ion and that is adorned with methyl, acetamide, and propionamide groups (Figure 6.1). As underscored throughout this dissertation, what distinguishes Cbls from each other is their axial ligation. Cbls with upper and lower ligands are octahedral where the Co^{III} metal center has d^6 electronic configuration. In the case of HCbl, the oxidation state of Co is Co^{I}, Co^{II}, or Co^{III} dependent upon whether a proton, hydrogen, or hydride is the upper ligand (Figure 1b), respectively. The nature of the upper ligand in HCbl is a topic of debate (Figure 6.1b).[36, 239]

---

†††*Chapter 6 adopted from:* Toda, M. J., Lodowski, P., Mamun, A. A., Kozlowski, P. M. Electronic and Photolytic Properties of Hydridocobalamin. *J. Photochem. Photobio. B* **2021**, https://doi.org/10.1016/j.jphotobiol.2021.112295.

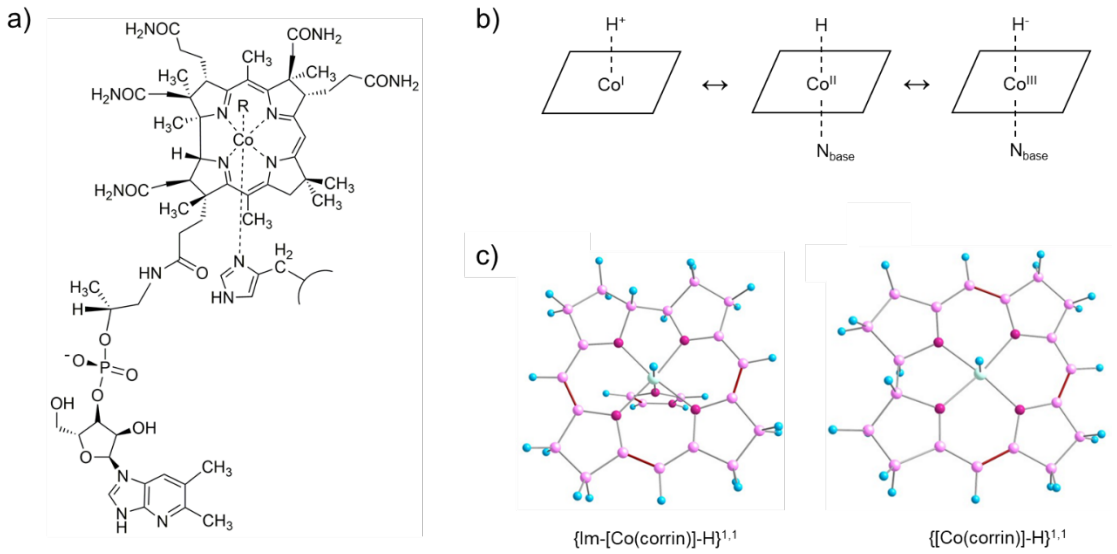

Figure 6.1: a) General molecular structure of base-off/His-on cobalamins (Cbls), such as CarH, where R represents the upper axial ligand. Various ligands (R) are described in the introduction. b) Oxidation states of Co for HCbl molecule based on whether a proton, hydrogen, or hydride is the upper ligand. Base = nitrogen from histidine residue or DBI from nucleotide loop (base-on Cbl). c) Truncated model structures used for DFT and TD-DFT calculations for base-on (left) and base-off (right) HCbl.

Several early studies reported the formation and the reactivity of HCbl. In 1971, Schrauzer and Holland demonstrated the instability of HCbl in anaerobic conditions and when HCbl is formed in an acidic medium, it rapidly decomposes to Co^{II} and molecular hydrogen (H_2).[231, 232] In 1975, Lexa and Savant expanded on this work and used cyclic voltammetry (CV) to determine that the pKa of HCbl ~ 1 and that the Co and DBI base is protonated.[234] HCbl can be considered as a protonated Co^{I} which can act as a Brönsted acid.[36] These studies provided foundational insights into the nature of HCbl Co corrinoids, yet few studies have explored the HCbl molecule for its potential role in enzymatic catalysis. Recently, the need for computational investigations of HCbl have become necessary as it has been implicated as a key intermediary in the mechanism of the coenzyme B_{12}-dependent photoreceptor CarH.[32-34, 36, 37] These proposals are described in Chapter 7.

While at least three experimental studies[32, 34, 37] have highlighted the potential of HCbl in the CarH mechanism, little is known about the electronic structure, properties, and reactivity of HCbl in the photoreceptor. In fact, there is no crystallographic data of isolated HCbl or HCbl in the enzymatic environment. Notably, HCbl is a transient species that can be described as Co^{I}-H^{+} ↔ Co^{II}-H ↔ Co^{III}-H^{-} where the electronic configuration of Co^{I} is d^8, Co^{II} is d^7, and Co^{III} is d^6.[36] The transient nature of HCbl and the assignment of the oxidation state of Co in the HCbl species, add a level of complexity to the study and analysis of these species. This brings into the forefront a fundamental question, what is the oxidation and ligation of the HCbl intermediary in the CarH mechanism? Herein, we seek to answer this question by determining the electronic and structural properties of isolated HCbl using DFT and TD-DFT. The excited state properties of HCbl are also included and compared to relevant experimental data. In addition, the formation of HCbl in CarH is explored using combined QM/MM calculations.

2.0 Computational Details

All reported DFT and TD-DFT calculations in this study were carried out using the BP86 functional.[138, 190, 240] For consistency with our previous studies of Cbls in solution as well as inside enzymes, the TZVP basis set for H and TZVPP basis set for Co, N, C and O was applied.[191, 241] The Turbomole[195] suite of programs was used for ground state geometry optimizations using DFT and the excited state calculations using TD-DFT using the COSMO solvation model. Turbomole was also used for the NBO calculations. For the COSMO calculations, the dielectric constant was ε= 78.39 and the radius of the rigid sphere solvent molecules was r_{Solv} = 1.98 Å. The definition of atomic vdW radii (in Å) was H=1.30, C=2.00, N=1.83, O=1.72, and Co=2.223. The ε and r_{Solv} were taken from the

solvents parameters of the COSMO model implemented in the ADF package. Gaussian 09, revision B[228] was used for the pKa calculations with the polarized continuum model (PCM) solvent model. The PCM model was used in the calculations with the Gaussian program and the default solvation model parameter values were used. Additionally, the RI approximation[189] was used in all calculations where the BP86 functional was applied and the identity approach for computing the electronic coulomb interaction (RI-J) was applied with the corresponding auxiliary basis sets for RI-DFT.[192]

The initial model system for the HCbl molecule was prepared based on the previously optimized structure of AdoCbl.[242] The upper axial ligand Ado was replaced with H and the side chains of the corrin ring were also truncated and replaced with H atoms. Two different model system were considered namely base-on HCbl denoted as {Im-[Co(corrin)]-H}^{1,1} and base-off HCbl denoted as {[Co^{III}(corrin)]-H}^{1,1} (Figure 6.1). DFT was applied to optimize the ground state geometries of the model systems and to construct the ground state S_0 PEC to calculate BDE. The BDE PEC was also computed using dispersion corrections (D3) and overall, there was very little difference in the energetics of the PECs, whether BP86 or BP86-D3 was used (Figure A.6.1).

3.0 Results and Discussion:

3.1 Geometry Optimization of Isolated HCbl:

The initial ground state geometry of the base-off and base-on HCbl were optimized using DFT whereas the excited state geometry was optimized using TD-DFT level of theory. Further information about the optimization protocols can be found in the *Computation Details* section. It is important to mention that there is no available crystal structure for the HCbl molecule so, calculations must be relied upon. The optimized model

structures of the base-on, {Im-[Co(corrin)]-H}^{1,1}, and the base-off, {[Co(corrin)]-H}^{1,1}, forms are shown in Figure 6.1c. The 1,1 superscript refers to the charge and multiplicity, respectively. The nucleotide loop of Cbls ends in a DBI group.[3] Generally speaking, the DBI can be bound to the Co on the lower face of the corrin ring in what is known as the base-on form. Alternatively, the DBI can be detached when the pH is highly acidic and in this case an H_2O molecule would bind to the Co as the lower ligand. In an enzymatic environment, the DBI can also be detached and when this occurs, the δ nitrogen of a His residue from the protein environment binds to the Co, making the His residue the lower ligand.[4-6] This is known as a base-off/His-on Cbl. The Cbls in CarH, AdoCbl and *bis*-HisCbl, are examples of base-off/His-on.[33] The base-on model contains a DBI group that is truncated to an Im group. The base-off model does not contain a lower ligand.

Geometric parameters around the coordination sphere of Co for the optimized S_0 and S_1 states for base-off and base-on isolated HCbl and HCbl bound to CarH are included in Table 6.1. For the optimized ground state model of base-on HCbl, the length of the upper axial Co-H bond was found to be 1.451 Å and the lower axial Co-N_{Im} was 2.155 Å. While comparisons to experiment can't be made for the Co-H bond, the S_0 Co-N_{Im} bond length reported here is typical for Cbls.[13, 168, 170, 242] For the optimized structure of the first excited state S_1 of the base-on model, the Co-H bond length is 1.455 Å and the Co-N_{Im} bond length is 2.048 Å. There appears to be a lengthening of the Co-H bond when comparing the base-on case to the base-off and the Co-H bond for {Co(corrin)-H}^{1,1} is 1.663 Å. Also, both the base-off and base-on model systems have minor differences in the bond angles and torsional angles (Table 6.1). In context of differences between S_0 and S_1 geometries, overall, the optimized geometries for both the ground and excited state reveal only minor

differences in the structure. This is consistent with previous studies for different Cbl systems such as MeCbl24-27[117, 118, 123, 126] and AdoCbl.22, 28-30[1, 110, 116, 119]

Table 6.1. Selected structural parameters of coordination sphere for singlet states of {Im-[Co(corrin)]-H}^{1,1} and {[Co(corrin)]-H}^{1,1} model complexes as well as HCbl in CarH.

	{Im-[Co(corrin)]-H}^{1,1}		**{[Co(corrin)]-H}^{1,1}**		**HCbl-CarH**
	S_0	S_1	S_0	S_1	S_0
Bond Distances, Å					
Co-H	1.451	1.455	1.429	1.663	1.445
Co-N_{Im}	2.155	2.048			2.152
Co-N_{21}	1.879	1.877	1.861	1.855	1.911
Co-N_{22}	1.936	1.979	1.913	1.923	1.919
Co-N_{23}	1.936	1.975	1.913	1.935	1.931
Co-N_{24}	1.877	1.875	1.859	1.849	1.888
Bond Angles, °					
N_{Im}-Co-H	178.7	161.4			175.7
N_{21}-Co-N_{23}	173.7	172.5	169.4	163.1	171.0
N_{22}-Co-N_{24}	170.8	167.6	173.6	174.0	169.4
Torsion Angles, °					
N_{21}-N_{22}-N_{23}-N_{24}	-4.7	-4.8	-6.2	-9.3	-2.0
N_{21}-N_{22}-N_{23}-Co	-0.02	2.4	-6.1	-11.0	3.9

3.2 Abs Spectra

The Abs spectra of Cbls have been studied extensively, resulting in several reviews.[2, 197, 198] The general features of a Cbl Abs spectra arise from the oxidation state and the nature of the axial ligands bound to the central Co ion. Accordingly, the Abs spectra of base-off and base-on Cbls as well as Co^{II} and Co^{I} are markedly different. Notably, the various bands of the Abs spectra of Cbls are designated by α, β, D/E, γ, and δ. The α and β bands are located in the visible region and are collectively referred to as the α/β region. The α/β region is broad in shape with moderate intensity (ε ~ 8,000 – 10,000 M^{-1} cm^{-1}) and spans a range between about 590 nm to 450 nm. Sometimes in experimental Abs spectra of Cbls a considerably weaker band, termed D/E, is observed between the α/β and γ bands

whose origin remains controversial.[2] In particular, CNCbl and H_2OCbl^+ Abs spectra are categorized as normal whereas Abs spectra of MeCbl and AdoCbl are anomalous.

The Abs spectrum of HCbl was reported by Chemaly and Pratt.[236] The HCbl species was obtained by the reduction of H_2OCbl^+ with glacial acetic acid and zinc dust In the HCbl experimental Abs spectrum, four peaks were present including at 470, 442, 384 and 303 nm. It was further concluded that the HCbl had a formal oxidation state of less than Co^{II}. After comparison with the Abs spectrum of base-off MeCbl and ethylCbl (EtCbl), it was noticed that there was a remarkable similarity between the 303, 380, and 440-460 nm band positions between the five-coordinate alkylCbls and HCbl. The major difference noted between the Abs spectrum of HCbl was in regard to the band observed at 470 nm which was slightly red-shifted compared to other base-off alkylCbls. Considering all of these factors, the major conclusion from Chemaly and Pratt's Abs spectrum was that the HCbl species was the five-coordinate, protonated, base-off HCbl. Present results are consistent with this study and a similar Abs spectrum of the HCbl molecule is reported here, based on TD-DFT calculations. The Abs spectra of alkylCbls including MeCbl and AdoCbl have been studied extensively both experimentally and theoretically.[2] Regardless of whether the comparison is to an experimental or computationally determined Abs spectrum, the α/β and γ band of HCbl is red shifted compared to the spectra of MeCbl and AdoCbl.

TD-DFT calculations were used to obtain the electronic transitions and simulate the corresponding Abs spectra for the base-off and base-on models (Figure 6.2). It is important to include electronic excited states for the base-off case here as axial ligation is known to affect both the features of an Abs spectrum as well as its photolytic properties. The

experimental Abs spectrum for the base-on model is included in Figure 6.2a. Fifty singlet excited states were calculated up to 4.0 eV based on vertical excitations from the ground state geometry and the first 20 vertical singlet electronic transitions are included in Table 6.2. A detailed orbital analysis for the low-lying excited states (S_1-S_{20}) and the vertical de-excitation for optimized S_1 state are also shown in Table 6.2. The triplet electronic transitions were not included in the analysis since they had zero transition dipole moment.

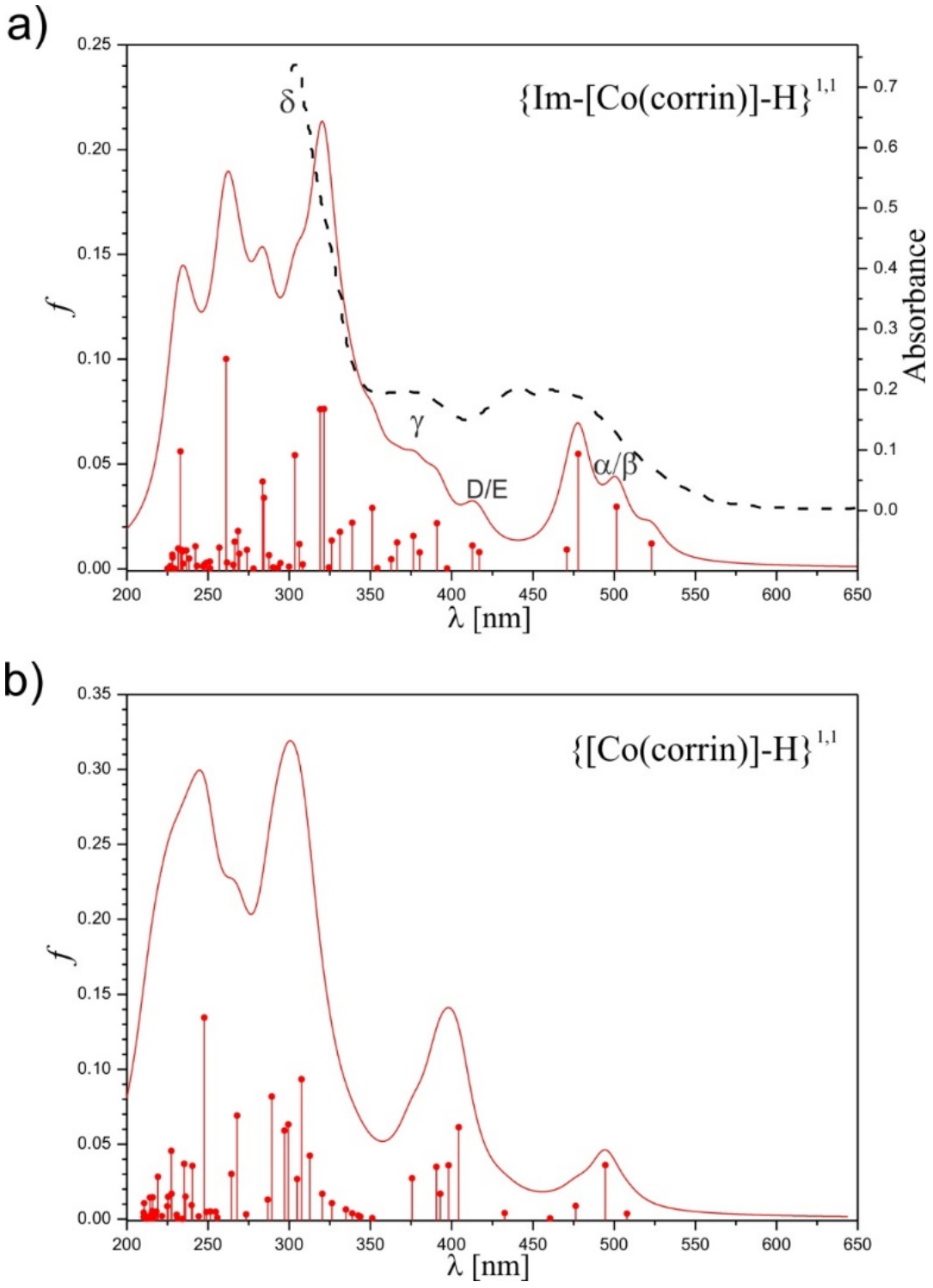

Figure 6.2: Calculated electronic transitions and simulated Abs spectra for a) model complexes. Vertical red lines – calculated electronic transitions at TD-DFT/BP86 level of theory, red solid lines – simulated Abs spectra based on TD-DFT results, dashed black line on panel a) – experimental electronic Abs spectrum HCbl. Experimental spectrum was digitalized from reference: S. M. Chemaly, J. M. Pratt, The Chemistry of Vitamin B_{12}. Part 24. Evidence for Hydride Complexes of Cobalt(III) Corrinoids, *J. Chem. Soc., Dalton Trans.,* 1984, 595-599.

Table 6.2. The twenty vertical singlet electronic transitions and value of $S_1 \rightarrow S_0$ transition for {Im-[Co(corrin)]-H}^{1,1} model complex based on the TD-DFT calculations.

	E(eV)	λ(nm)	*f*	%	Character			Exp. λ (eV)
S_1	2.37	523.0	0.0121	68	112 → 114	H-1 → L	$\pi+d_{z2}/n_{Im} \rightarrow \pi^*$	
				30	111 → 114	H-2 → L	$d_{xz}+\pi \rightarrow \pi^*$	
S_2	2.47	501.5	0.0296	85	113 → 114	H → L	$d_{yz}+\pi \rightarrow \pi^*$	470 (2.64)
S_3	2.59	477.9	0.0548	57	111 → 114	H-2 → L	$d_{xz}+\pi \rightarrow \pi^*$	442 (2.81)
				24	112 → 114	H-1 → L	$\pi+d_{z2}/n_{Im} \rightarrow \pi^*$	
				11	110 → 114	H-3 → L	$d_{x2-y2} \rightarrow \pi^*$	
S_4	2.63	470.8	0.0092	88	110 → 114	H-3 → L	$d_{x2-y2} \rightarrow \pi^*$	
S_5	2.97	416.9	0.0080	52	112 → 115	H-1 → L+1	$\pi+d_{z2}/n_{Im} \rightarrow d_{xy}$-n	
				25	113 → 115	H → L+1	$d_{yz}+\pi \rightarrow d_{xy}$-n	
				15	112 → 116	H-1 → L+2	$\pi+d_{z2}/n_{Im} \rightarrow \pi^*+[d_{xy}$-n]	
S_6	3.00	412.7	0.0111	62	113 → 115	H → L+1	$d_{yz}+\pi \rightarrow d_{xy}$-n	
				26	112 → 115	H-1 → L+1	$\pi+d_{z2}/n_{Im} \rightarrow d_{xy}$-n	
S_7	3.12	397.1	0.0002	84	109 → 114	H-4 → L	$\pi_{Im} \rightarrow \pi^*$	
				12	113 → 116	H → L+2	$d_{yz}+\pi \rightarrow \pi^*+[d_{xy}$-n]	
S_8	3.17	390.9	0.0218	68	113 → 116	H → L+2	$d_{yz}+\pi \rightarrow \pi^*+[d_{xy}$-n]	384 (3.23)
				14	109 → 114	H-4 → L	$\pi_{Im} \rightarrow \pi^*$	
S_9	3.26	380.2	0.0079	56	113 → 117	H → L+3	$d_{yz}+\pi \rightarrow \sigma^*(d_{z2})$-n	
				17	111 → 115	H-2 → L+1	$d_{xz}+\pi \rightarrow d_{xy}$-n	
				15	112 → 116	H-1 → L+2	$\pi+d_{z2}/n_{Im} \rightarrow \pi^*+[d_{xy}$-n]	
S_{10}	3.29	376.3	0.0157	32	112 → 116	H-1 → L+2	$\pi+d_{z2}/n_{Im} \rightarrow \pi^*+(d_{xy}$-n)	
				24	113 → 117	H → L+3	$d_{yz}+\pi \rightarrow \sigma^*(d_{z2})$-n	
				23	108 → 114	H-5 → L	$\pi+d_{yz} \rightarrow \pi^*$	
S_{11}	3.38	366.4	0.0126	68	112 → 117	H-1 → L+3	$\pi+d_{z2}/n_{Im} \rightarrow$	
				15	110 → 115	H-3 → L+1	$d_{x2-y2} \rightarrow d_{xy}$-n	
S_{12}	3.42	362.7	0.0046	62	110 → 115	H-3 → L+1	$d_{x2-y2} \rightarrow d_{xy}$-n	
S_{13}	3.50	354.1	0.0003	83	110 → 116	H-3 → L+2	$d_{x2-y2} \rightarrow \pi^*+(d_{xy}$-n)	
S_{14}	3.53	351.0	0.0290	39	111 → 115	H-2 → L+1	$d_{xz}+\pi \rightarrow d_{xy}$-n	
				10	112 → 116	H-1 → L+2	$\pi+d_{z2}/n_{Im} \rightarrow \pi^*+[d_{xy}$-n]	
S_{15}	3.66	338.7	0.0220	38	111 → 116	H-2 → L+2	$d_{xz}+\pi \rightarrow \pi^*+[d_{xy}$-n]	
				16	111 → 115	H-2 → L+1	$d_{xz}+\pi \rightarrow d_{xy}$-n	
				12	108 → 114	H-5 → L	$\pi+d_{yz} \rightarrow \pi^*$	
S_{16}	3.74	331.2	0.0177	47	111 → 117	H-2 → L+3	$d_{xz}+\pi \rightarrow \sigma^*(d_{z2})$-n	
				19	113 → 118	H → L+4	$d_{yz}+\pi \rightarrow \pi^*$	
S_{17}	3.80	326.0	0.0135	44	113 → 118	H → L+4	$d_{yz}+\pi \rightarrow \pi^*$	
				15	111 → 117	H-2 → L+3	$d_{xz}+\pi \rightarrow \sigma^*(d_{z2})$-n	
				14	111 → 116	H-2 → L+2	$d_{xz}+\pi \rightarrow \pi^*+[d_{xy}$-n]	
S_{18}	3.82	324.4	0.0007	58	112 → 118	H-1 → L+4	$\pi+d_{z2}/n_{Im} \rightarrow \pi^*$	
				38	107 → 114	H-6 → L	$\pi+d_{xz} \rightarrow \pi^*$	
S_{19}	3.86	321.4	0.0763	58	109 → 115	H-4 → L+1	$\pi_{Im} \rightarrow d_{xy}$-n	303 (4.09)
				14	113 → 118	H → L+4	$d_{yz}+\pi \rightarrow \pi^*$	
				12	108 → 114	H-5 → L	$\pi+d_{yz} \rightarrow \pi^*$	
S_{20}	3.89	319.0	0.0762	34	109 → 115	H-4 → L+1	$\pi_{Im} \rightarrow d_{xy}$-n	
				21	108 → 114	H-5 → L	$\pi+d_{yz} \rightarrow \pi^*$	
				12	111 → 116	H-2 → L+2	$d_{xz}+\pi \rightarrow \pi^*+[d_{xy}$-n]	
S_1	1.67	740.7	0.0041	97	113 →114	H → L	$\pi+d_{z2}/n_{Im} \rightarrow \pi^*$ ($\pi\pi^*$/MLCT)	

The relevant frontier MOs are depicted in Figure 6.3 for {Im-[Co(corrin)]-H}^{1,1}. In the range of experimental α/β band, between 460 nm and 490 nm, radiation absorption and electronic excitations are possible up to four low lying singlet states (S_1-S_4), Table 6.2 and Figure 6.3. Overall, it seems that the individual electronic states have a rather slightly underestimated energy based on the TD-DFT calculations and the simulated spectrum is slightly red shifted in relation to the experimental line. All the electronic excitations in the α/β region take place to a LUMO orbital which is a pure corrin π* orbital. The lowest, singlet electronic transition S_1 is combination of two excitations, i.e. $\pi + d_z^2/n_{Im} \rightarrow \pi^*$ and $d_{xz} + \pi \rightarrow \pi^*$ transitions with weight of participation 68% and 30%, respectively. The second electronic state (S_2) is almost completely the result of excitation of the $d_{yz} + \pi \rightarrow \pi^*$ character. The S_3 electronic transitions include 57% $d_{xz} + \pi \rightarrow \pi^*$ and 24% $\pi + d_z^2/n_{Im} \rightarrow \pi^*$. The S_4 state in 88% has $d_{x2-y2} \rightarrow \pi^*$ character. Among all four S_1-S_4 states forming the α/β band, excitation to the S_3 state, with the calculated oscillator strength 0.0548, is characterized by the highest intensity.

In general, with regard to the electronic structure of the above characterized electronic states, it can be concluded that all of these states are the result of charge-transfer transitions and can be described as MLCT-type states. At this point, it is also worth emphasizing, that the characters of the low-lying singlet excited states of HCbl are almost completely the same as the characters of the low-lying electronic states of previously studied alkyl derivatives of Cbl.[124, 125, 243] With regard to the energetics of these states a great similarity can also be noticed, but in the case of HCbl, the relevant excitations have a slightly higher energy. This is associated with stronger stabilization and destabilization

of the HOMO and LUMO orbitals, respectively, which are involved in the electronic excitation of HCbl molecule.

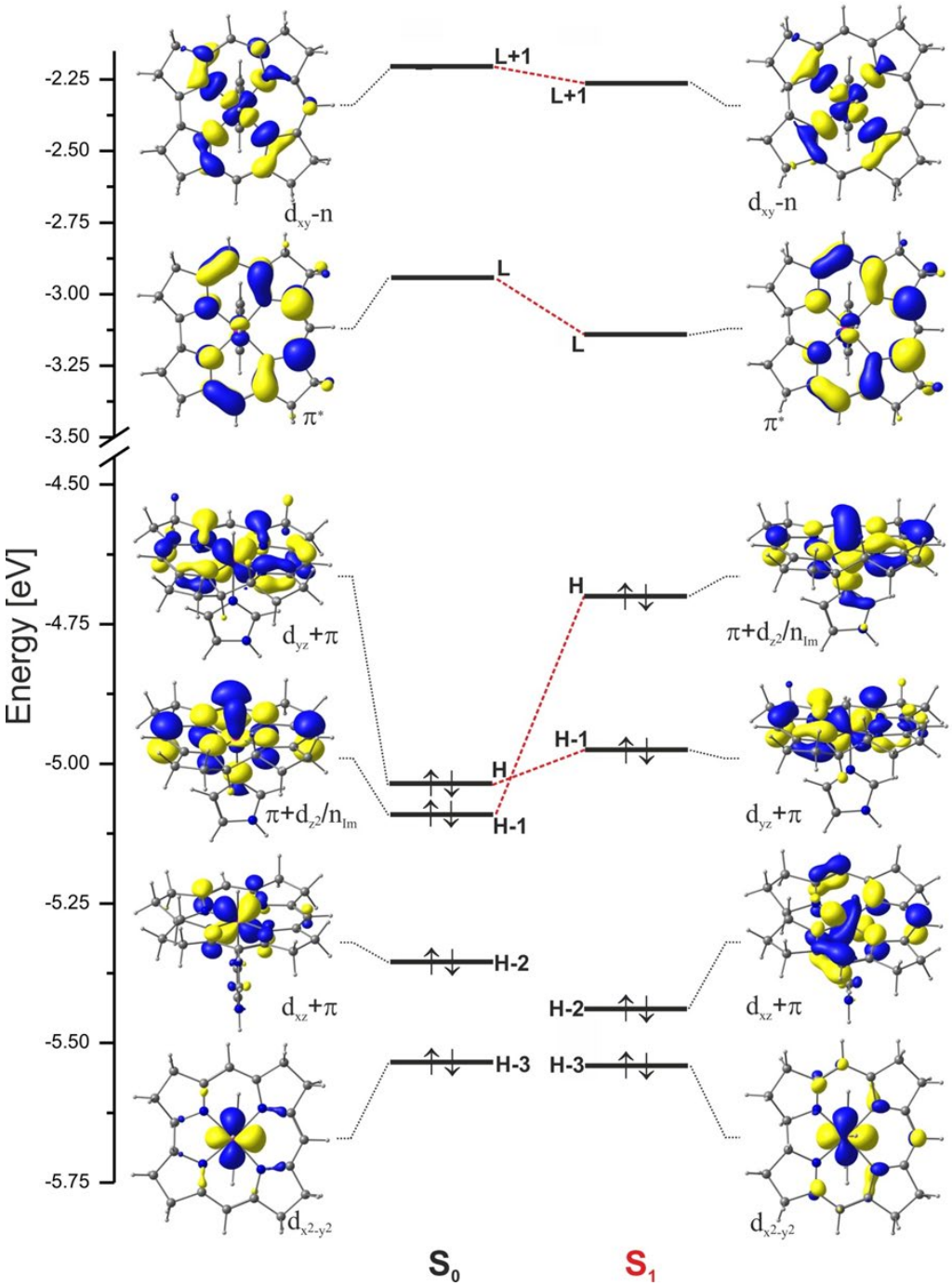

Figure 6.3. Kohn-Sham (KS) orbitals involved in lowest electronic excitations for equilibrium geometry of ground state (S_0) and first excited state (S_1) of {Im-[Co(corrin)]-H}^{1,1} model complex. The occupied KS orbitals are marked by pair of electrons.

The next two electronic states with the mean value of the oscillator strength in the calculated spectrum, S_5 and S_6, are the result of electronic transitions of a mixed nature $d/\pi \rightarrow d/\pi^*$. The electronic excitations involve occupied d orbitals and unoccupied d_{xy} orbital of Co. Due to the excitation energy, these transitions form a slightly separate group of electronic excitations. Most likely due to the low intensity and similar energy of excitation in relation to the higher states, these excitations are not visible in the experimental spectrum in the form of a separate and expressive band and accordingly could be interpreted as the so-called D/E band.

In the range from ~400 nm to ~325 nm, starting from the S_7 state, the next dozen or so electronic transitions are included in the simulated Abs band, which can be assigned to the experimental band with a maximum at 380 nm. In this group of electronic states, excitations are basically of a diverse and mixed character. In most cases, these are excitations of the $d/\pi \rightarrow d/\pi^*$, $d \rightarrow d/\pi^*$ and $d/\pi \rightarrow d$ types, which engage both occupied and unoccupied d Co orbitals and the bonding and antibonding π orbitals localized on the corrin ring. Of these electronic states, one of them, S_9 (380 nm), requires attention. The electronic structure of the S_9 state is the result of excitation between the occupied d orbital of Co and σ^* antibonding orbital of Co-H bond, with some contribution from the π orbital of the macrocyclic ligand. So, this state can be essentially characterized as a LF state. The calculated value of the oscillator strength for this state is relatively small so, it can be assumed that the participation of this state is limited in the process of light absorption. On the other hand, this state may play an important role in the photophysical process of Co-H bond rupture at excitation in the range of about 400 nm, similarly to the case of Co-C bond dissociation in the photolysis of alkyl Cbls.

The Abs spectrum of the base-off analogue of HCbl was also computed using the same level of theory (Figure 6.2). The relevant frontier MOs are depicted in Figure 6.4 for $\{[Co(corrin)]\text{-}H\}^{1,1}$. The twenty lowest, vertical singlet electronic transitions and value of $S_1 \rightarrow S_0$ transition for $\{[Co(corrin)]\text{-}H\}^{1,1}$ model complex based on the TD-DFT calculations are listed in Table A.6.1. The KS MOs involved in lowest electronic excitations for equilibrium geometry of ground state S_0 and S_1 excited state of the base-off model complex are depicted in Figure 6.4 The simulated Abs spectrum of the base-off form is to some extent similar to the simulated spectrum of the base-on form, although differences are also visible, mainly in the shape and intensity of individual bands of the simulated spectral line. However, as in the case of the base-on form, three bands can be indicated, respectively in the range 525 nm - 450 nm, 450 nm - 350 nm and below 350 nm. Basically, the shape of the simulated spectral line reflects the position of three distinct groups of calculated electronic excitations: S_1-S_4, S_6-S_{10} and a series of successive states starting from S_{11}. In the case of the base-off form, some of the calculated electronic states with similar character to the states for the base-on form are characterized by slightly different value of the excitation energy and the value of the oscillator strength. Thus, compared to the base-on form, there is a partial change in the order of the states and ultimately a change in both the shape and intensity of the individual simulated bands. One of the noticeable differences is the presence of a distinct and intense band in the range 450 nm - 350 nm. The analysis of the character of the states included in this band reveals that in the composition of electronic excitations, next to the $d/\pi \rightarrow d/\pi^*$ transitions, a large number of $d/\pi \rightarrow$ □* transitions appear.

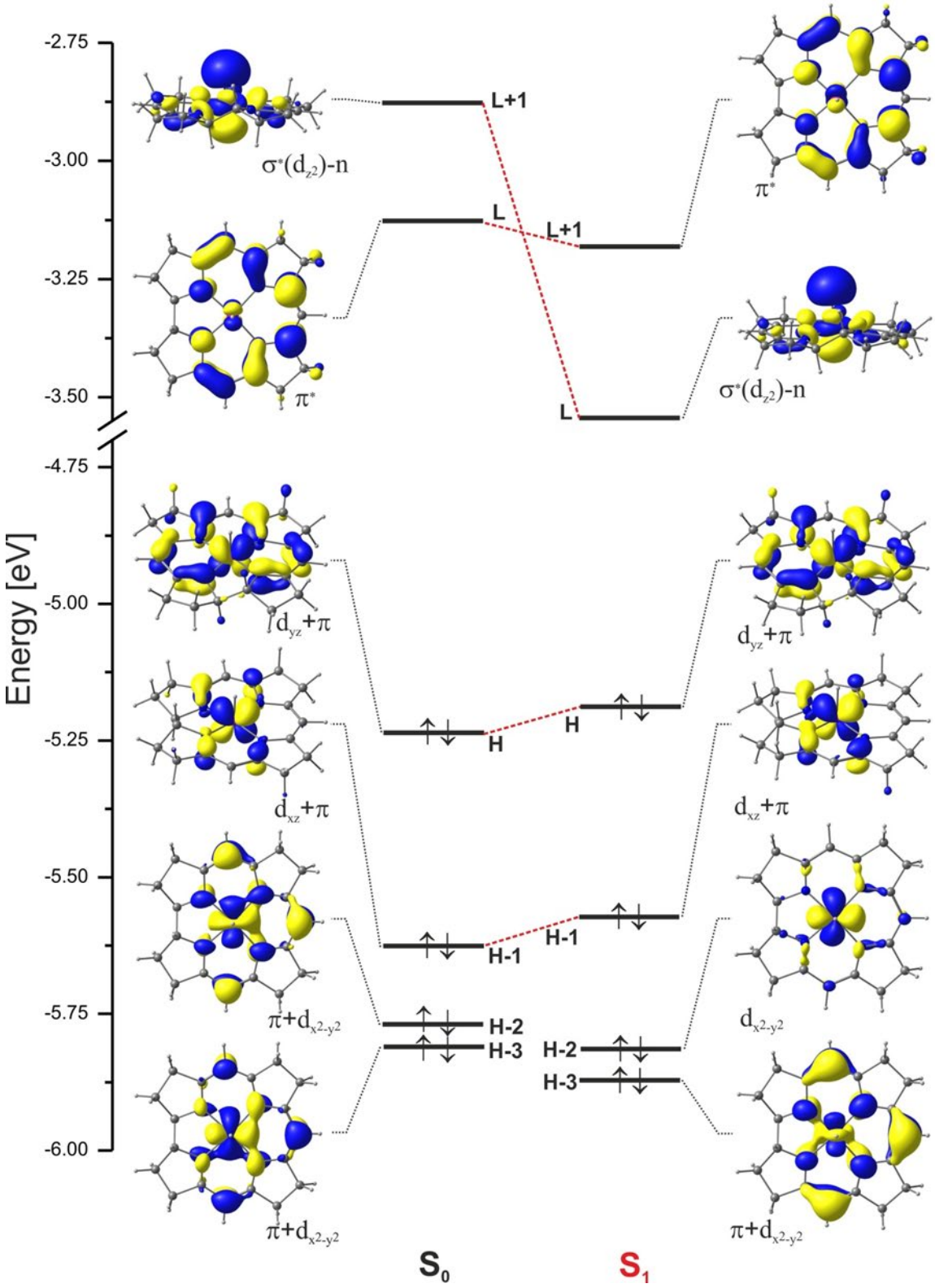

Figure 6.4. Kohn-Sham (KS) orbitals involved in lowest electronic excitations for equilibrium geometry of ground state (S_0) and first excited state (S_1) of {[Co(corrin)]-H}^{1,1} model complex. The occupied KS orbitals are marked by pair of electrons.

Moreover, as mentioned above for some of the electronic excitations, it is possible to observe a change in the excitation energy with respect to similar transitions identified for the base-on form, this change taking place both towards higher and lower energies. The second difference in respect to the electronic states is not as visible, but it should be given special attention. Namely, in the case of the base-off form, the S_1 state is LF type with the $d/\pi \rightarrow \sigma^*$ character. S_1 states characterized as LF are characteristic of base-off alkyl Cbls and participate directly in the photolysis of the Co-C bond. For base-off HCbl, the $d \rightarrow \sigma^*$ state lying in the γ band for the base-on form, lowers in energy when the axial base is disconnected and becomes the lowest electronic state. It is worth noting, that in the case of base-on form of HCbl, the σ^* orbital lies above two π^* orbitals with energy gap to HOMO equal about 3.24 eV, whereas the disconnection of the axial base results in an energy lowering of the σ^* orbital in relation to the occupied HOMO orbital by some 0.9 eV. This effect can be observed whether the ground state or relaxed S_1 is considered (Figure 6.4). The effective energy reduction of the σ^* orbital shows that lowering the LF state energy to the level of the lowest electronic state for the base-off form is a natural consequence of disconnecting the axial base. Likely, this state would play a similar key role in the photolytic mechanism of HCbl.

The KS orbitals involved in the lowest electronic excitations for equilibrium geometry of ground state S_0 and first excited state S_1 of $\{Im\text{-}[Co(corrin)]\text{-}H\}^{1,1}$ and $\{[Co(corrin)]\text{-}H\}^{1,1}$ model complexes, depicted in Figure 6.3 and 6.4 respectively, reveal an interesting similarity to alkylCbls. The H and H-1 energies switch from S_0 to S_1 for the base-on case and the L and L+1 switch energies for the base-off case. Overall, the change of the order of the orbitals as a result of the relaxation of the S_1 state is not in and of itself

very important and it should also be noted that the character of the lowest state does not change as a result of the relaxation of the vertical state. On the other hand, the changing of the order of the orbitals is very characteristic and is also observed for various alkylCbls. Further, the electronic structure of HCbl is more similar to that of alkyl derivatives than that of non-alkyl derivatives. The disconnection of the axial base results in an effective energy lowering of the σ* orbital, and the relaxation process itself exacerbates this effect. For base-on HCbl the $S_1 \rightarrow S_0$ transition is $\pi + d_{z2}/n_{Im} \rightarrow \pi^*$ whereas for base-off HCbl this transition is $d_{yz}+\pi \rightarrow [\sigma^*(d_z^2)\text{-n}]$. Put simply, the $S_1 \rightarrow S_0$ transition is MLCT for the base-on case and LF for the base-off case.

3.3 Analysis of Axial Bonding in HCbl

The major concern of this study is to investigate the unusual reactivity of the HCbl molecule. In order to investigate this central issue, it is crucial to focus on the upper axial bond, Co-H. The equilibrium bond distance of the Co-H is 1.451 Å for base-on HCbl and for the base-off HCbl it is 1.429 Å (see Table 6.1). This is relatively short bond distance for the upper axial ligand in comparison to other Cbls where the Co-R bond is typically ~2.00 Å. [1, 110, 163] It was proposed that the HCbl decomposed into Co^{II} and molecular H_2 through the cleavage of the upper axial Co-H bond. However, the BDE of Co-H bond was not explicitly shown for HCbl. Herein, the bond dissociation energy of the Co-H bond in HCbl was calculated using a PEC. The Co-H bond was constrained and optimized at each step along 1.20 Å to 3.20 Å, with a step size of 0.1 Å (Figure 6.5). For bond distances greater than 2.8 A, the unrestricted Kohn-Sham (UKS) broken symmetry (BS) wavefunctions were used.

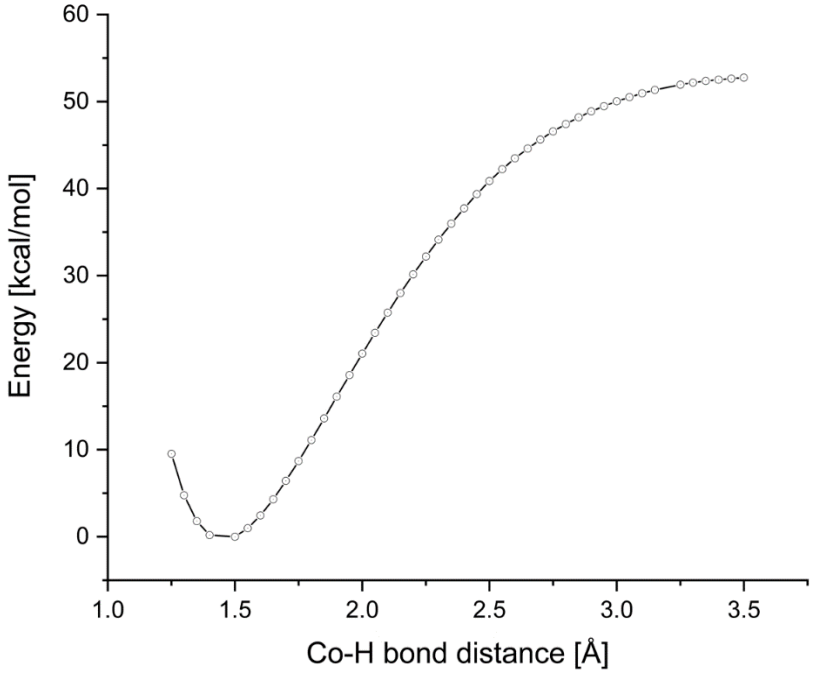

Figure 6.5. PEC for singlet ground state of {Im-[Co(corrin)]-H}^{1,1}, base-on HCbl model to determine the BDE.

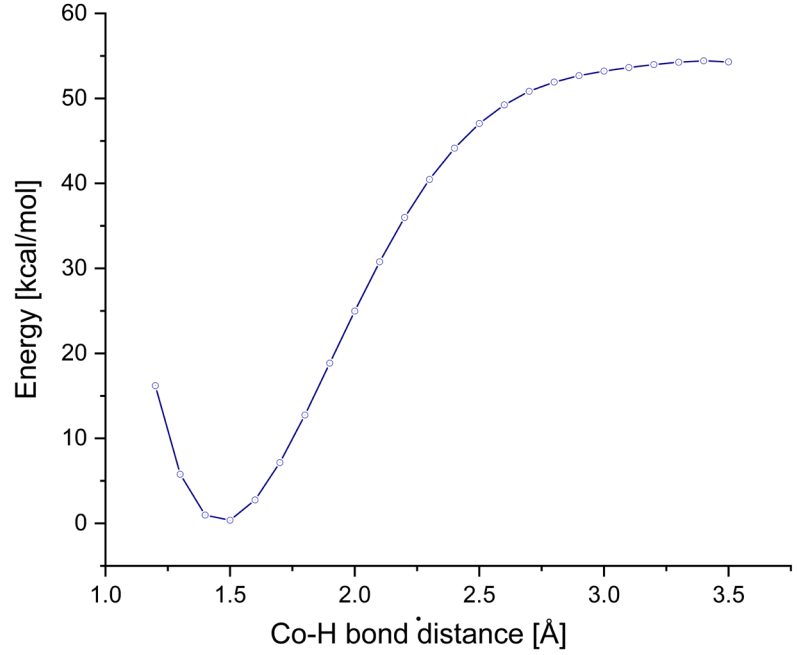

Figure 6.6. PEC for singlet ground state of {[Co(corrin)]-H}^{1,1}, base-off HCbl model to determine the BDE.

As depicted in Figure 6.5, it appears that the BDE of Co-H in base-on HCbl is 52.0 kcal/mol whereas for the base-off model it is 54.2 kcal/mol (Figure 6.6). Because BS

calculations were used in the construction of the PEC, the dissociation corresponds to homolytic cleavage of the Co-H bond which would lead to formation of the Co^{II}. The BDE of Co-H in HCbl was further compared with the BDE of Co-H computed in various studies using DFT[244-247] and high-level *ab initio* calculations.[248] The dissociation energy of diatomic Co-H ranges from 46 to 55 kcal/mol in these studies. Specifically, for the previous study involving *ab initio* calculations,[248] the BDE for the diatomic species including Co-H^+, Co-H, and Co-H^- was theoretically determined to be 46.4, 49.6, and 45.6 kcal/mol, respectively. So, the BDE of diatomic Co-H of 49.6 kcal/mol is in line with the homolytic BDE PEC depicted in Figure 6.5. However, it should be noted that these calculations were for the diatomic species not HCbl. To date, the experimental BDE of HCbl has not been reported. While comparing the Co-H BDE it is also important to mention that in HCbl the central Co atom is hexa coordinated and surrounded by a corrin ring. The presence of a corrin ring did not influence the Co-H BDE. Moreover, the BDE of Co-H in HCbl calculated in this method is much higher than the Co-C BDE for other alkylCbls. For example, the experimental range for BDE is 32-40 kcal/mol for MeCbl[156, 158] and 24-35 kcal/mol for AdoCbl.[249-253] While the Co-H BDE of HCbl appears to be higher than the other alkylCbls, the reason behind this can be further scrutinized using NBO analysis.

3.4 NBO Analysis

NBO analysis has proven to be very instrumental and effective method to describe the nature of chemical bonding and the reactivity in a variety of chemical systems.[254-258] Herein, NBO calculations were employed to further investigate the chemical bonding phenomena of the base-on and base-off models of HCbl. The results of the NBO analysis for the coordination sphere of Co in HCbl are gathered in Table 6.3. As was described in

the *Introduction*, the coordination of the Co ion is transient and can be described as Co(I), Co(II), or Co(III). Thus, it is important to understand the nature of the oxidation state of Co in HCbl. Based on the NBO analysis of the base-on model, the Co ion carries a -0.50 charge whereas the charge of the upper axial H is +0.54. For base-off model, the NBO charge of the Co ion is -0.27 while the upper axial H is +0.56. In HCbl, Co clearly has excess negative charge. This is in stark contrast to other alkylCbls where the Co has significant positive charge. The NBO analysis also indicates that the population of the Co 3d orbitals is ~8. Taken together, NBO results indicate that HCbl is the protonated form where the Co is more in line with Co(I). The Co-H bond is very strongly polarized, almost ionic.

The occupation and description of the six bonds coordinated to the Co ion the base-on model and the five bonds of the base-off model are also listed in Table 6.3. For the base-on model, the Co-H bond is formed between hybridized Co *spd* orbitals and the H *s* orbital. The occupation number is reported as 1.73 with a description of 74.4% Co($s^{24\%}p^{49\%}d^{27\%}$) + 25.6% H ($s^{100\%}$). The Co-N_{Im} bond has occupation number 1.93 and it is described as combination of hybridized orbitals 14.5% Co($s^{18\%}p^{51\%}d^{31\%}$) + 85.5% N($s^{32\%}p^{68\%}$). The occupation and description of the four equatorial bonds to the innermost nitrogens of the corrin ring ($N_{21\text{-}24}$) are also listed in Table 6.3 and these bonds arise from hybridized Co *spd* orbitals and hybridized *sp* orbitals of $N_{21\text{-}24}$ atoms. For the equatorial Co-$N_{21\text{-}24}$ bonds, the polarization is directed towards the N atoms. The Co-$N_{21\text{-}24}$ NBOs contain anywhere from 21% to 23% of Co hybridized *spd* orbitals and approximately 77% - 79% of hybridized *sp* N orbitals. All bonds have polarized character, whereby for Co-H bond, this polarization is in the Co direction while for Co-N bonds it is in the reverse direction.

Similar trends in regard to occupation and description were observed for the base-off model and are also listed in Table 6.3.

Table 6.3. NBO charges and bond analysis for coordination sphere of Co.

{Im-[Co(corrin)]-H^+}^{1,1}		
Atom	Charge	
Co	-0.50	
H	0.54	
Bond	Occupation	Description
Co – H	1.73	(74.4%) 0.8623·Co($s^{24\%}p^{49\%}d^{27\%}$) + (25.6%) 0.5064·H ($s^{100\%}$)
	0.02	(25.6%) 0.5064·Co($s^{24\%}p^{49\%}d^{27\%}$) - (74.4%) 0.8623·H ($s^{100\%}$)
Co – N_{21}	1.88	(22.7%) 0.4761·Co($s^{14\%}p^{49\%}d^{37\%}$) + (77.3%) 0.8794·N($s^{33\%}p^{67\%}$)
	0.13	(77.3%) 0.8794·Co($s^{14\%}p^{49\%}d^{37\%}$) - (22.7%) 0.4761·N($s^{33\%}p^{67\%}$)
Co – N_{22}	1.89	(20.6%) 0.4539·Co($s^{15\%}p^{51\%}d^{35\%}$) + (79.4%) 0.8910·N($s^{32\%}p^{68\%}$)
	0.13	(79.4%) 0.8910·Co($s^{15\%}p^{51\%}d^{35\%}$) - (20.6%) 0.4539·N($s^{32\%}p^{68\%}$)
Co – N_{23}	1.89	(20.6%) 0.4544·Co($s^{15\%}p^{51\%}d^{34\%}$) + (79.4%) 0.8908·N($s^{32\%}p^{68\%}$)
	0.13	(79.4%) 0.8908·Co($s^{15\%}p^{51\%}d^{34\%}$) - (20.6%) 0.4544·N($s^{32\%}p^{68\%}$)
Co – N_{24}	1.88	(22.7%) 0.4762·Co($s^{14\%}p^{49\%}d^{37\%}$) + (77.3%) 0.8794·N($s^{33\%}p^{67\%}$)
	0.14	(77.3%) 0.8794·Co($s^{14\%}p^{49\%}d^{37\%}$) - (22.7%) 0.4762·N($s^{33\%}p^{67\%}$)
Co – N_{Im}	1.93	(14.5%) 0.3814·Co($s^{18\%}p^{51\%}d^{31\%}$) + (85.5%) 0.9244·N($s^{32\%}p^{68\%}$)
	0.18	(85.5%) 0.9244·Co($s^{18\%}p^{51\%}d^{31\%}$) - (14.5%) 0.3814·N($s^{32\%}p^{68\%}$)
{[Co(corrin)]-H^+}^{1,1}		
Atom	Charge	
Co	-0.27	
H	0.56	
Bond	Occupation	Description
Co – H	1.82	(77.8%) 0.8819·Co($s^{41\%}p^{15\%}d^{45\%}$) + (22.2%) 0.4715·H($s^{100\%}$)
	0.04	(22.2%) 0.4715·Co($s^{41\%}p^{15\%}d^{45\%}$) - (77.8%) 0.8819·H($s^{100\%}$)
Co – N_{21}	1.88	(21.4%) 0.4629·Co($s^{12\%}p^{49\%}d^{39\%}$) + (78.6%) 0.8864·N($s^{32\%}p^{68\%}$)
	0.14	(78.6%) 0.8864·Co($s^{12\%}p^{49\%}d^{39\%}$) - (21.4%) 0.4629·N($s^{32\%}p^{68\%}$)
Co – N_{22}	1.89	(19.3%) 0.4398·Co($s^{13\%}p^{51\%}d^{36\%}$) + (80.7%) 0.8981·N($s^{32\%}p^{68\%}$)
	0.15	(80.7%) 0.8981·Co($s^{13\%}p^{51\%}d^{36\%}$) - (19.3%) 0.4398·N($s^{32\%}p^{68\%}$)
Co – N_{23}	1.89	(19.3%) 0.4397·Co($s^{14\%}p^{51\%}d^{36\%}$) + (80.7%) 0.8982·N($s^{32\%}p^{68\%}$)
	0.14	(80.7%) 0.8982·Co($s^{14\%}p^{51\%}d^{36\%}$) - (19.3%) 0.4397·N($s^{32\%}p^{68\%}$)
Co – N_{24}	1.88	(21.4%) 0.4621·Co($s^{13\%}p^{49\%}d^{38\%}$) + (78.6%) 0.8868·N($s^{32\%}p^{68\%}$)
	0.15	(78.6%) 0.8868·Co($s^{13\%}p^{49\%}d^{38\%}$) - (21.4%) 0.4621·N($s^{32\%}p^{68\%}$)

Further comparison indicates that the bonding nature of the Co-H bond is distinct in contrast to the Co-R bond for other Cbls. This can be seen in comparisons of HCbl to

MeCbl, where the Co-C_{CH3} bond of MeCbl can be described as 38.3% Co and 61.7% C. The participation of Co orbitals is largely increased in the case of Co-H bond in HCbl complex. The electronic density is more so concentrated on central Co ion while the H atom adopts a positive net charge which indicates the formation of a protonated Cbl. Additionally, the electrostatic potential (ESP) around the entire HCbl molecule, for both the base-on and base-off models is positive (Appendix, Figure A.6.2).

3.5 pK_a of the Co-H Bond

It is apparent from early experimental work that the pK_a of the Co-H bond can provide insight into the instability of the HCbl molecule.[234] The electrochemical nature of the Cbl derivatives have been extensively characterized using CV studies.[235] For HCbl, Lexa and Savant showed that the Bronsted basicity is very weak and thus, it can act as powerful nucleophile in a large pH range. Further, it was proposed that the pK_a of HCbl is ~1.0. First, it should be noted that HCBl is formed in an acidic medium and decomposes according to the following equation:[234]

$$Co(I) + H^+ \leftrightarrow Co(II) + ½\ H_2$$

This decomposition reaction is the major reason why the determination of the pKa of HCbl was so difficult. Nevertheless, Lexa and Saveant were able to determine the pKa for H_2O-[Co(II)Cbl] (historically referred to as B_{12r}) and H_2O-[Co(I)Cbl] (historically referred to as B_{12s}). For B_{12r} and B_{12s}, the pKa's were determined to be 2.9 and 1.0, respectively. It was also concluded that HCbl has a proton bound to Co and that the nitrogen of the DBI group, which is bound to Co in the base-on form, is protonated.

Here, the pK_a value was also determined computationally. As described in the previous paragraph, the pK_a of the Co-H bond was determined from H_2O-[Co(I)Cbl] (B_{12s}). Accordingly, truncated H_2OCbl^+ species were used as the models for predicting the pK_a. It also should be pointed out that the DBI lower ligand is replaced by a water molecule in low pH environments. The theoretical prediction of the pKa of the Co-H bond (aka the dissociation of the proton) corresponds to the following reaction;

$$\{H_2O\text{-}Co(corrin)\text{-}H\}^{1,1} \leftrightarrow \{H_2O\text{-}Co(corrin)\}^{0,1} + H^+$$

where the protonated model is denoted as $\{H_2O\text{-}Co(corrin)\text{-}H\}^{1,1}$ and the deprotonated as $\{H_2O\text{-}Co(corrin)\}^{0,1}$. These models are depicted in Figure A.6.3. The pK_a obtained with BP86 functional was -1.06. Additional details concerning pKa determination can be found in the footnote to A.6.3.

3.6 Connection Between HCbl and CarH

3.6.1 CarH and Previously Proposed Mechanisms

While studies of HCbl have taken place primarily in the 1960s-1980s, interest in HCbl has been renewed when it was implicated as a potential intermediary in the mechanism of coenzyme-B_{12} dependent photoreceptor CarH. The role of this photoreceptor is to regulate transcription of carotenoid biosynthetic genes in various bacteria in a complex mechanism that involves large-scale structural changes as well as less understood molecular transformations occurring in the active site.[22, 23, 32-35, 37]In the absence of daylight, CarH is a dimer-of-dimers type tetramer known as CarH-Dark State (CarH-DS).[33] Each monomeric subunit contains a DNA binding domain, a helical bundle, and a Cbl binding domain. The monomers form head-to-tail dimers, which form the tetramer. DNA binds to CarH-DS and from this conformation, the presence of daylight

initiates the cleavage of the Co-$C_{5'}$ bond of AdoCbl which in turn triggers the formation of the photoproduct, anhAdo the dissociation of DNA from the tetramer, and the splitting of the tetramer into monomers. These monomers are referred to as CarH-Light State (CarH-LS). Specifically, when the Co-$C_{5'}$ bond of AdoCbl is cleaved with light in *Thermus Thermophiles* CarH-DS, a His residue from the protein (His132) will take the place of the Ado ligand and form a covalent bond with the Co ion of the cofactor (Figure 6.1a). This forms a stable adduct known as *bis*-HisCbl in the Cbl binding domain of CarH-LS. Of note, transcription is repressed in CarH-DS but is activated in CarH-LS. Much of the details of the mechanism have come from the crystal structures of CarH-DS, DNA bound CarH-DS, and CarH-LS. Additionally, photolytic and photochemical studies have sought to look into the mechanism occurring in the active site, where the Co-$C_{5'}$ bond of AdoCbl is cleaved photolytically.[34, 37] Several mechanisms have thus been proposed which comment on the formation of the photoproduct and the formation of the *bis*-HisCbl stable adduct. Each of these shares a different take on the mechanism. However, each mechanism implicates or at least hypothesizes that HCbl is a viable intermediate between Co-$C_{5'}$ bond cleavage and the *bis*-HisCbl formation. Theoretically, the formation could occur through homolytic or heterolytic cleavage of the Co-$C_{5'}$ bond. For the case involving homolytic cleavage, β-hydrogen elimination (involving the $C_{4'}$-H) would lead to HCbl formation. For heterolytic cleavage, β-hydride elimination would result in formation of HCbl. There is some debate as to whether the Co-$C_{5'}$ bond cleaves homolytically or heterolytically in CarH-DS because AdoCbl is known for its radical chemistry and prior to the Kutta *et al*[34] TAS study, instance of heterolytic cleavage of the Co-$C_{5'}$ was unprecedented.[36] The hurdle for experimental studies is the instability and short-lived nature of HCbl so there is a need for a

computational analysis of this key step in the mechanism. Herein, the target is not to espouse on one proposed mechanism or another, rather we seek to determine the efficacy of one key and elusive portion of the mechanism – the role of HCbl.

3.6.2 Modeling Hydrogen Transfer Reaction

To model the hydrogen transfer reaction (i.e. the $C_{4'}$-H to Co(II)) that may occur in AdoCbl-dependent CarH, first the PECs for the S_0 and S_1 excited were computed along Co-$C_{5'}$ bond distance of {[Co(corrin)]-Ado}^{1,1} model complex with the Co-$C_{4'}$ bond distance frozen at 3.1 Å. These are shown in Figure 6.7. First the ground state (GS or S_0) was computed at the restricted Kohn-Sham (RKS) level and the UKS level. The UKS calculations used a BS wavefunction. For the S_1 excited state, three different curves are shown based on changes to the computational set-up and include the PECs based on vertical excitations, optimization of the S_1 state, and the vertical S_1 based on UTD-DFT with a BS wavefunction. Taking into consideration vertical excitations as an approximation of the relaxed excited state, the UTD-DFT curve appears to be a strong candidate for participation in IC and deactivation of the excited state from which the photodissociation of the Co-$C_{5'}$ bond occurs.

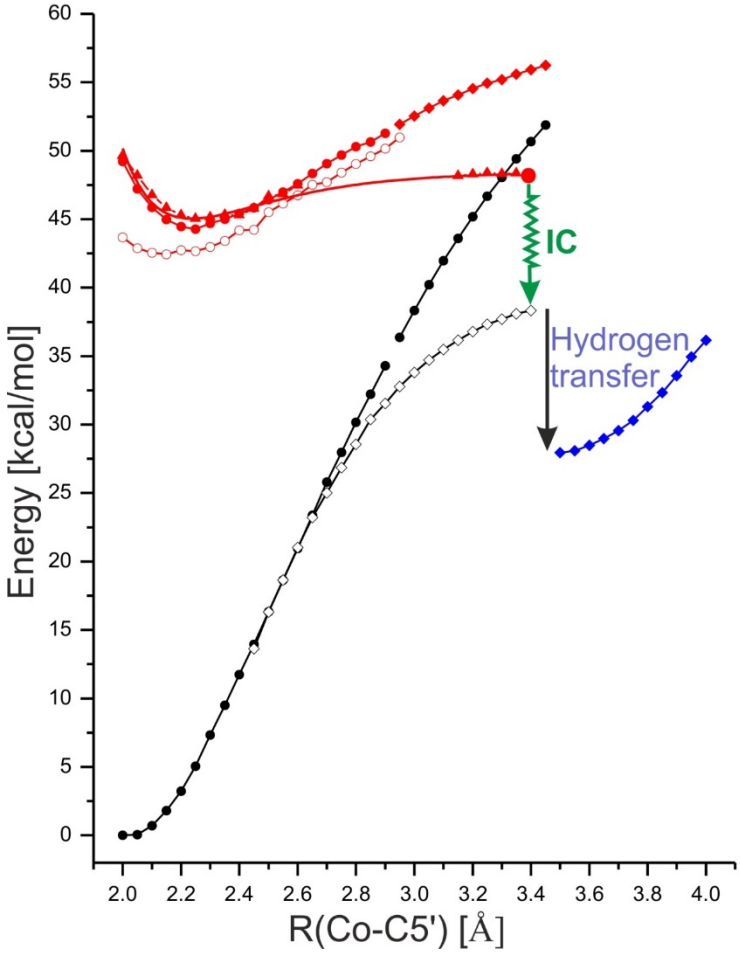

Figure 6.7. S_0 and S_1 PECs as function of Co-$C_{5'}$ distance for {[Co(corrin)]-Ado}^{1,1} model complex. Co-$C_{4'}$ distance was frozen at 3.1 Å. Black filled circle – GS at RKS level, black filled diamond - GS at UKS level, black open diamond – GS at UKS level for BS wave function, blue filled diamond – GS at UKS level for {[Co(corrin)]-H + anhAdo}^{1,1} system, red filled circle – vertical S_1 state, red open circle – optimized S_1 state, red filled triangle – vertical S_1 state based on UTD-DFT calculations with BS wave function.

The electronic excited state from which this process takes place, is LF type. As a result of the elongation of the Co-$C_{5'}$ bond and the formation of Co(II)/$^{\bullet}$Ado RP, the excited state is formally located on the Co(corr) fragment with the $d_{yz}^1 d_{z2}^2$ electronic configuration. As shown in Figure 6.8, $d_{yz} \rightarrow d_{z2}$ electronic excitation, followed by photo-ionization of the Co-$C_{5'}$ bond, leads to a double occupancy of the d_{z2} orbital and the electron hole on the d_{yz} orbital. In the case of larger Co-$C_{5'}$ distances, the Co(corr) fragment could be considered as an isolated system. For an isolated system, the electronic configuration $d_{yz}^1 d_{z2}^2$

corresponds to the configuration of the first, doublet excited state and differs from the configuration of the ground state only by the occupancy of the d orbitals. Due to the small energy gap between the mentioned excited state and the ground state, the excited state undergoes an effective non-radiative quenching. This process involves the transfer of an electron between the d orbitals of cobalt and leads to the $d_{yz}^2 d_{z2}^1$ configuration. The singly occupied d_{z2} orbital is now able to form a bond in the axial position of the Co(corr) system. After deactivation of the LF electronic state, where the Co-$C_{5'}$ bond is significantly elongated from its equilibrium geometry, it would seem feasible that there are two possibilities. The first being reformation of the Co-$C_{5'}$ bond and the second being hydrogen transfer. The curve representative of hydrogen transfer is depicted in blue on Figure 6.7. This PEC uses the $\{[Co(corrin)]\text{-}H \cdots anhAdo\}^{1,1}$ model system. The hydrogen transfer reduces the energy of the dissociated and deactivated $\{[Co(corrin)]^{\bullet} \cdots {}^{\bullet}Ado\}^{1,1}$ system by about 10 kcal/mol.

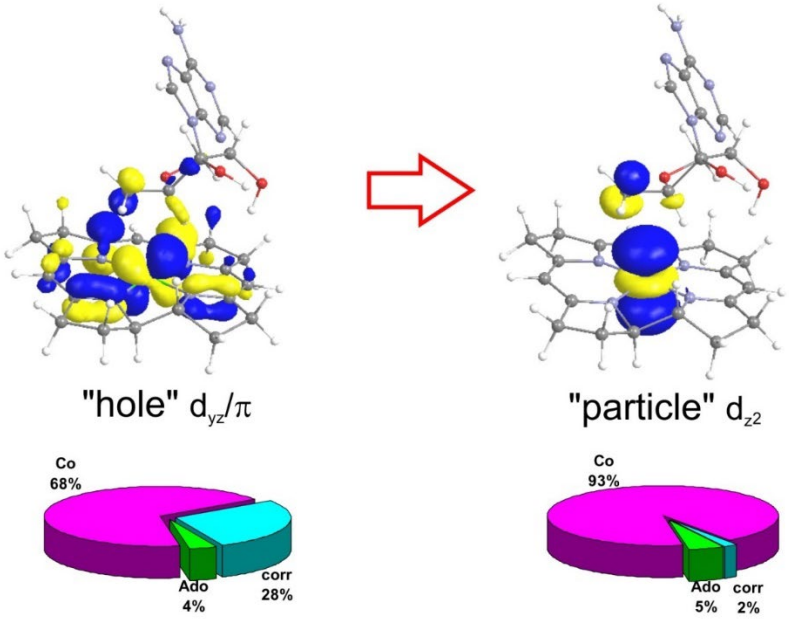

Figure 6.8. NTOs orbitals involved in S_1 electronic state for partially dissociated Ado group at Co-$C_{5'}$ and Co-$C_{4'}$ distances equal to 3.35 Å and 3.10 Å, respectively. (Corr = corrin ring)

3.6.3 Hydrogen Transfer and QM/MM Optimization of HCbl in CarH

The major implication of the analysis of the HCbl model is related to its role in the reactivity of CarH. The IC process resulting from RP formation in the S_1 state appears to involve the BS PEC for S_0 BDE of the isolated model (black curve, open diamond points, Figure 6.7) where the $S_1 \rightarrow S_0$ deactivation would lead to the S_0 geometry where the Co-$C_{5'}$ bond distance is significantly elongated. It is difficult to say at exactly which Co-$C_{5'}$ distance IC occurs, it cannot be calculated. The only condition that must be satisfied is that the energy gap between the states should be relatively small. It is usually assumed that up to about 10 kcal/mol, so-called hot states, a nonradiative transition between such states is possible. The distance of approx. 3.4 Å marked in Figure 6.7 results from the fact, that at the distance of 3.45 Å for the ground state, there is a spontaneous transition of hydrogen from Ado to Co (II). It should be noted that the exact Co-$C_{5'}$ distance for which hydrogen transfer occurs is not necessarily important for the qualitative description of the mechanism. Based on the experimental analysis of CarH,[33] after the anhAdo is formed, it leaves the reaction environment. In other words, the Co-$C_{5'}$ and Co-$C_{4'}$ distances should only increase indeterminately in the native catalytic cycle.

With this picture in mind, the Co-$C_{5'}$ BDE PEC for AdoCbl bound to CarH was computed using ONIOM calculations. Starting from the previously reported optimized AdoCbl-CarH geometry, the Co-$C_{5'}$ bond of the cofactor was stretched systematically with a step size of 0.1 Å up to 3.7 Å (Figure 6.9) with the optimizations completed using the same QM/MM protocol described in Chapter 5. The wavefunction was restricted from 1.8-2.7 Å and for bond lengths greater than 2.8 Å, the BS solution was used and the wavefunction was unrestricted. As shown in Figure 6.7, the IC from the S_1 state in AdoCbl

involves $S_1 \rightarrow S_0$ at Co-$C_{5'}$ distances possibly greater than ~3.2 Å. From here, hydrogen transfer is possible. The Co-$C_{5'}$ bond in AdoCbl-CarH was stretched to distances greater than 3.2 Å to fully explore the possibility of hydrogen transfer. The PEC revealed a leveling off of the S_0 PEC in CarH and the species corresponding to this point was optimized revealing a stable diradical (Figure 6.9b and c). Figure 6.9b shows the spin density profile of singlet diradical where Co spin = -0.97 and $C_{5'}$ spin = 1.05. The triplet diradical was also optimized. The energy difference between the singlet and triplet diradical was small, with the triplet diradical being 0.05 kcal/mol less than the singlet. The spin density values for the triplet were Co = 0.98 and $C_{5'}$ = 1.05.

The BS S_0 PEC for AdoCbl bound to CarH (Figure 6.9) connects the corresponding S_0 PEC of the isolated model to the enzymatic environment. Both PECs show a leveling-off in energy after Co-$C_{5'}$ distances of 3.0 Å. For the BS S_0 PEC of the isolated system, $\{[Co(corrin)]\text{-}H + anhAdo\}^{1,1}$, the energy at the point of IC is ~37 kcal/mol (Co-$C_{5'}$ = 3.40 Å). This is consistent with the experimental BDE values of Co-$C_{5'}$ bond cleavage. On the other hand, for the PEC from AdoCbl bound to CarH, this energy is lower and is ~31 kcal/mol. This is to be expected as the enzymatic environment lowers the barrier for Co-$C_{5'}$ bond cleavage. The PECs depicted in Figure 6.7 indicate that the transfer of the $C_{4'}$-H would occur at a Co-$C_{5'}$ bond distance of approximately 3.4 Å. So, the BDE curve for AdoCbl bound to CarH was extended beyond this point (up to 3.7 Å). There is an ~5.0 kcal/mol reduction in energy from 3.5 Å to 3.7 Å. Further, the energies associated with Co-$C_{5'}$ bond distance of 3.6 Å and 3.7 Å are nearly identical. Using the 3.7 Å constrained geometry as a starting point, the species was optimized without any constraints revealing a stable diradical (Co(II)/Ado$^{\bullet}$ RP) in the CarH enzymatic environment (Figure 6.9b and

c). The $C_{4'}$-H of the diradical species is oriented in such a way as to facilitate hydrogen transfer and subsequently form the Co-H bond of HCbl and the photoproduct. The diradical species appears to connect the IC process to the HCbl formation.

CarH-DS has previously been studied using a combined QM/MM approach where it was found that the orientation of the Ado ligand was a key player in CarH's efficient photolytic abilities.[136] The geometry of the diradical species, with particular emphasis on the orientation of the $C_{4'}$-H, underscore this previously determined conclusion. The HCbl enzyme bound model system was generated from QM/MM optimized structures from the crystal structure of full-length *Thermus thermophilus* CarH-DS bound to AdoCbl with PDB ID: 5C8D. There is no crystal structure for HCbl bound to CarH or isolated HCbl so calculations must be relied upon. The coordinates of the previously optimized AdoCbl in CarH were used to generate a HCbl species.[136] From the diradical species, the hydrogen of $C_{4'}$-H was manually shifted to form a Co-H bond. This species was optimized and revealed the HCbl species and the anhAdo product that is shown in Figure 8. The coordinates for the optimized diradical were used as a starting point to explore the formation of HCbl in CarH. The QM/MM optimized HCbl, with the photoproduct anhAdo, is depicted in Figure 6.10. No imaginary frequencies were present after QM/MM optimization. Additionally, structural parameters around the coordination sphere of Co are listed in Table 6.1 and reveal strong similarity to isolated base-on HCbl especially in terms of axial bonding. Other structural parameters are such as Co-$N_{21\text{-}24}$ bind distance, bond angles, and torsion angles are consistent with the base-on and base-off isolated models. Based on QM/MM optimization, it would seem that the HCbl species is a viable intermediate for the CarH mechanism.

4.0 Conclusion

Based on this study it is clear that the HCbl molecule exhibits distinct geometric and spectroscopic properties in comparison to other alkylCbls. The calculated Abs spectra of HCbl exhibits properties consistent with the experiment conducted by Chemaly *et al*.[36] Describing the nature of the upper axial Co-H bond was explored using NBO analysis and it was shown that the electron density of the Co-H bond is mostly concentrated on the Co atom with the H atom possessing positive charge. The polarization of the Co-H bond occurs in the Co direction. Thus, it appears that the HCbl species possess a unique character which can be identified as protonated Co(I)-complex. In addition, DFT calculations with the BP86 functional estimate that the pK_a of the Co-H bond in HCbl is -1.06, which is qualitative agreement with the experimentally determined pK_a that was previously reported by Lexa and Savant.[234]

The historical significance of HCbl is evident but only until recently was this species found to play a potential role in nature. In the proposed photochemical mechanism of AdoCbl-dependent enzyme CarH, it was suggested that the photolysis of Co-$C_{5'}$ bond in CarH generates Co(II) and Ado radical species. Subsequently the Ado radical could undergo β-hydride elimination to yield anhAdo and the HCbl complex. It was further suggested that HCbl will undergo further decomposition to Co(II) and H_2 in aerobic conditions.[32] It is apparent, based on current QM/MM calculations, that HCbl is a viable intermediate in CarH. There is a need to expand this work to include the enzymatic environment to determine the role of HCbl in CarH as well as to determine if the transient nature of the HCbl species observed in solution has any implication on the mechanism of CarH.

CHAPTER 7

PHOTOPRODUCT FORMATION IN CARH VIA A SINGLET PATHWAY

Synopsis

The CarH photoreceptor takes advantage of the light-sensing ability of coenzyme B_{12} (aka adenosylcobalamin = AdoCbl) to perform its catalytic function which includes large-scale structural changes to regulate transcription. In daylight, transcription is activated in CarH via the photo-cleavage of the Co-$C_{5'}$ bond of coenzyme B_{12}. Subsequently, the photoproduct, 4′,5′-anhydroadenosine (anhAdo) is formed inducing dissociation of the CarH tetramer from DNA. Several experimental works have proposed that hydridocoblamin (HCbl) may be formed in process with anhAdo. The photolytic cleavage of the Co-$C_{5'}$ bond of AdoCbl was previously investigated using photochemical experiments and the involvement of both singlet and triplet excited states were explored. Herein, QM/MM calculations are employed to probe (1) the photolytic processes which may involve singlet excited states, (2) the mechanism of anhAdo formation, and (3) whether HCbl is a viable intermediate in CarH. Time-dependent density functional theory (TD-DFT) calculations indicate that the mechanism of photodissociation of the Ado ligand is via the ligand field (LF) portion of the lowest singlet excited state (S_1). This is followed by deactivation to a point on the S_0 potential energy surface (PES) where the Co-$C_{5'}$ bond remains broken. This species is characterized as a singlet diradical intermediate. From this point anhAdo formation is explored using the active coordinates, Co-$C_{5'}$ and Co-$C_{4'}$ bond

distances. These coordinates were used to construct a PES where a local minimum representing anhAdo and HCbl formation was found. The transition state (TS) for the formation of the Co-H bond of HCbl was computed and contained a single imaginary frequency of *i*1592 cm^{-1}. Comparisons to experimental works and the potential role of rotation around the *N*-glycosidic bond of the Ado ligand are discussed.

1.0 Introduction

Photoreceptors are ubiquitous in nature.[23] Together with their chromophores, these light responsive enzymes participate in a variety of biological processes including catalysis. Recently, this class of enzymes expanded with the discovery of a new family of photoreceptors whose chromophore is AdoCbl, or coenzyme B_{12}, Figure 7.1a.[23] Notable in this group of photoreceptors is CarH, which has been the subject of significant interest from structural biology,[33] biochemistry,[32] spectroscopy,[34, 37] and computational chemistry.[136] CarH's light driven mechanism at the molecular level leads to enormous conformational changes in the protein's secondary structure.[33] At the heart of this process is the AdoCbl cofactor, which initiates the molecular transformation events by cleavage of the Co-$C_{5'}$ bond via daylight.

The CarH photoreceptor, uses light and coenzyme B_{12} to regulate the transcription of carotenoid biosynthetic genes in a complex catalytic cycle. In the absence of daylight, AdoCbl bound CarH is a dimer-of-dimers type tetramer.[33] Each monomeric subunit contains a DNA binding domain, a helical bundle, and a Cbl binding domain. The monomers form head-to-tail dimers, which form the tetramer. In this state, CarH-DS, DNA binds to the tetramer (Figure 7.1b, left). The transcription of the gene responsible for the synthesis of carotenoids is repressed in CarH-DS but is activated in CarH-Light State

(CarH-LS). From the DS conformation, the photoproduct, anhAdo, the dissociation of the tetramer from DNA, and the splitting of the tetramer into monomers.[32] These monomers are referred to as CarH-LS. Specifically, when the Co-$C_{5'}$ bond of AdoCbl is cleaved with light, a His residue from the protein (His132) will form a covalent bond with the Co ion of the cofactor.[34] This forms a stable adduct known as *bis*-HisCbl in the Cbl binding domain of CarH-LS. Additionally, transcription is repressed in CarH-DS but is activated in CarH-LS.

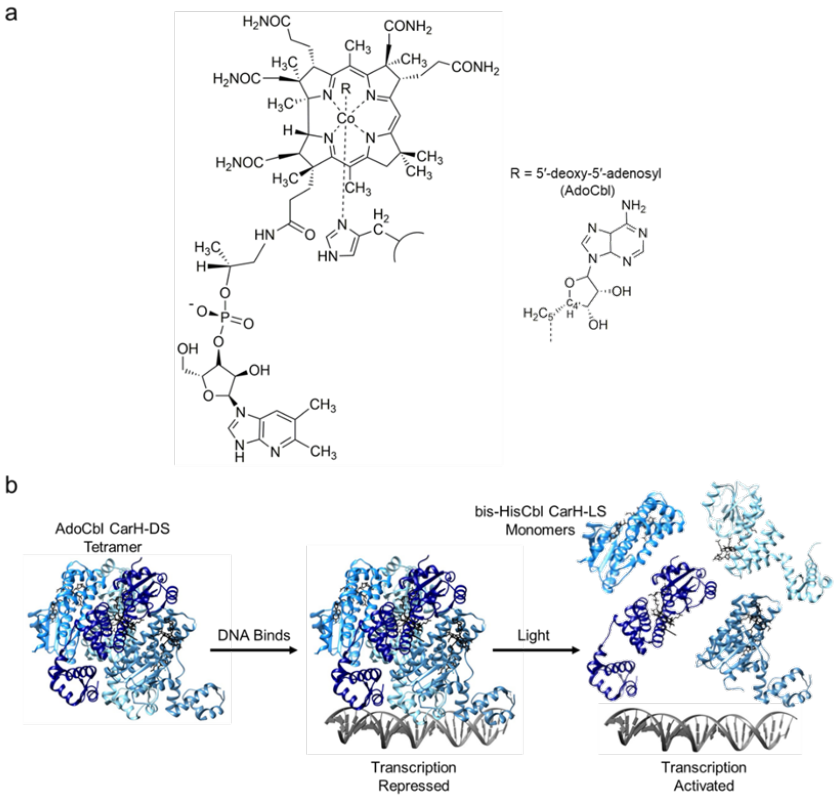

Figure 7.1: a) General molecular structure of base-off/His-on cobalamins where the dimethylbenzimidazole (DBI) from the nucleotide loop is detached and replaced with a histidine (His) residue from the protein. R represents the upper axial ligand. In CarH, R=5′-deoxy-5′-adenosyl (Ado) (Inset) and the lower axial ligand is the Im moiety from the His177 residue. In addition to the $C_{5'}$ of Ado, the Co(III) ion of coenzyme B_{12} is bound to the four nitrogens of the corrin ring and to the nitrogen of a lower axial ligand. **b)** Overall scheme of the CarH mode of action, described in detail in the Introduction.

While there are several components of CarH's mechanism of action, the key aspect to the entire catalytic cycle is the light-induced cleavage of the Co-$C_{5'}$ bond of AdoCbl. In AdoCbl-dependent enzymatic catalysis, the cleavage of the Co-$C_{5'}$ bond is triggered by substrate binding and is homolytic, forming the Co(II)/Ado• RP.[6] While CarH is in fact a coenzyme B_{12}-dependent enzyme, it is distinct from other enzymes in this category because it does not require a substrate to initiate molecular transformations. Rather, CarH utilizes light to photolytically cleave the Co-$C_{5'}$ bond. In Chapter 5, it was demonstrated that the orientation of the $C_{4'}$-H plays a key role and the orientation of $C_{4'}$-H throughout the catalytic cycle is a key contributor to the formation of anhAdo.

While at least three proposals have been put forth describing the potential mechanism of CarH used to form anhAdo and *bis*-HisCbl, none have undergone scrutiny with a theoretical lens.[32, 34, 37] The first proposal came from Drennan, *et al* who used liquid chromatography-mass spectrometry (LC-MS) and UV-vis experiments, to present a mechanism for CarH, which had two possible routes.[32] These were referred to as 'path 1' and 'path 2'. In path 1, the Co-$C_{5'}$ bond is cleaved homolytically and subsequently, β-H elimination from the -$C_{4'}$-H forms the products anhAdo and, potentially, HCbl. The formation of anhAdo was confirmed by LC-MS and NMR measurements. The second route that was proposed, path 2, is essentially the same as path 1, except the cleavage of the Co-$C_{5'}$ bond would be heterolytic. Photolysis via heterolytic cleavage would result in the formation of Ado anion and Co(III)Cbl. β-H elimination would still occur in this path, which would also result in the formation of the photoproduct anhAdo and HCbl. The experimental results appear to favor 'path 1'. The third possibility is concerted pathway, path 3 (Figure 7.2), but taking into consideration distance between Co, $C_{4'}$, and $C_{5'}$-H the

concerted mechanism seems unlikely. The target of the work presented in this Chapter is to further explore the 'path 1' mechanism (Figure 7.2) using QM/MM calculations.

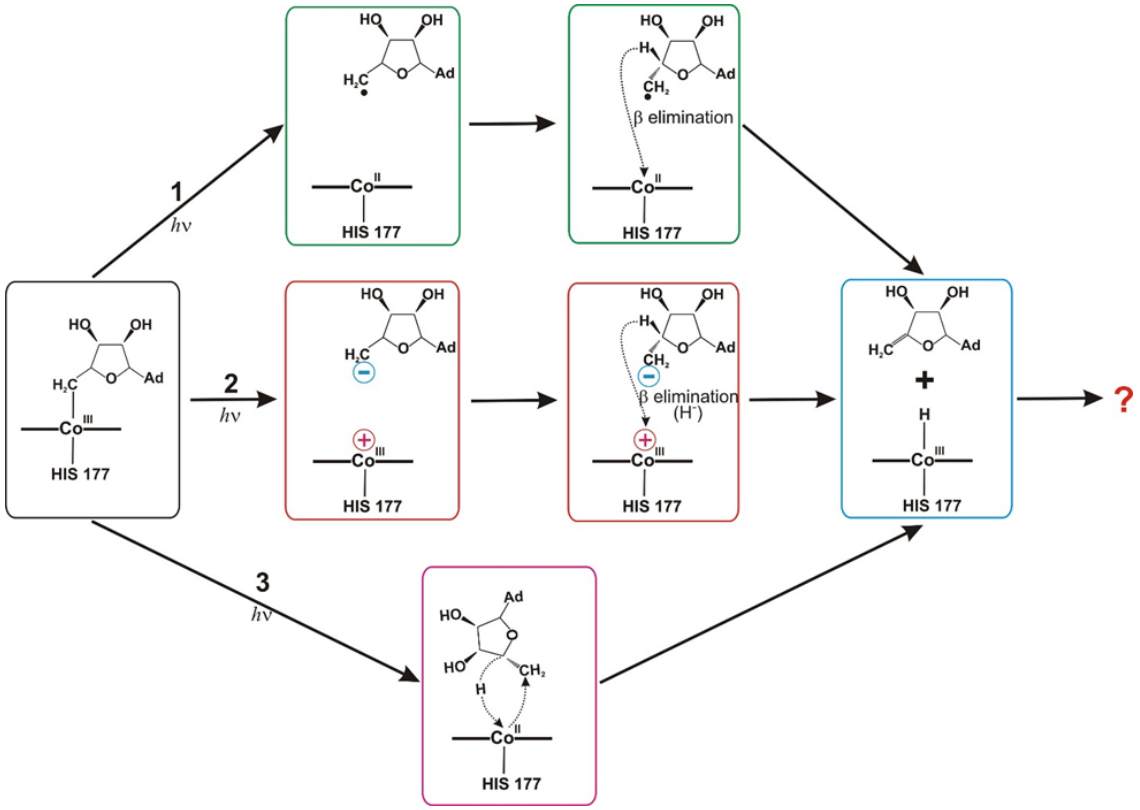

Figure 7.2. Drennan, *et al*[32] proposal for light-induced cleavage of the Co-$C_{5'}$ bond of AdoCbl in CarH-DS.

In Chapter 6, it was shown that HCbl appears to be a viable intermediate in the CarH mechanism. The results presented here provide a more in-depth analysis of the mechanism of CarH-DS to determine how the anhAdo photoproduct is formed and how HCl may be involved. To accomplish this, first the PESs associated with the low-lying excited states of CarH-DS, were constructed to characterize the nature of the singlet excited states, respectively. Second, analysis of both ground and excited state PESs indicated that the mechanism of deactivation involves a stable ground state diradical intermediate. As will be discussed throughout, the diradical species appears to be a key intermediate in the

formation of anhAdo and HCbl. A PES based on the $C_{4'}$-H and Co-$C_{5'}$ distances of the cofactor was constructed to explore the involvement of the diradical intermediate in the mechanism. Excitingly, this led to the location of the TS for formation of the anhAdo photoproduct.

2.0 Computational Details

The QM/MM set-up is based on previous studies of CarH-DS that was described in Chapter 5.[136] The CarH-DS model was generated from the crystal structure of *Thermus thermophilus* CarH bound to DNA (PDB ID: 5C8E).[33] DFT was used for ground state optimizations while TD-DFT was employed for the excited states. The pure GGA functional, BP86 was used in the QM layer with the TZVP basis set was used for H and TZVPP was used for Co, C, N, and O. The low layer was treated with MM using the ff99sb AMBER force field. A truncated AdoCbl occupied the high-layer (QM layer). The construction of PESs based on axial ligation are in line with our previous studies of Cbls and this procedure has been discussed in Chapter 2.

3.0 Results and Discussion

3.1 S_1 PES

It has been demonstrated that the S_1 PES constructed as a function of axial bond distances provide reliable tool to explore underlying mechanism of photodissociation in B_{12}-dependent systems. Also, previous TD-DFT calculations revealed that RP generation occurs from the ligand field (LF) region of the S_1 PES.[1, 2, 40, 41, 92, 94-98, 102, 111] Thus, in the case of CarH photoreceptor, the S_1 PES can be used as a tool to understand the underlying mechanism of photodissociation.[1, 110] It is reasonable to expect that the S_1 state of CarH-

DS would play a role in the photolytic processes of this coenzyme B_{12}-dependent enzyme. In Chapter 5, the S_1 state of CarH was reported based on QM/MM calculations and compared with the S_1 states of EAL, GLM, and MetH. As is typical for B_{12}-dependent systems, the S_1 states for each of these enzymes, including CarH-DS, arise from a crossing of two electronic states, namely MLCT and LF.[122, 136, 182, 221] While the character of the MLCT and LF minima regions are consistent, there are some differences in the relative energetics of these regions. For EAL and GLM, consistent with experiment, the LF region is stabilized in comparison to the MLCT region.[40, 41, 106, 122, 182] The reverse is true for CarH-DS and, like unto MetH, the MLCT region for the photoreceptor is stabilized in comparison to the LF region.[221] Put another way, the energetics associated with the photolytic properties of AdoCbl in CarH-DS are more in-line with those of MeCbl in MetH.

The S_1 PES for CarH-DS has an energetically feasible route for cleaving the Co-$C_{5'}$ bond. The light-sensing function of CarH can be initially associated with $S_0 \rightarrow S_3$ electronic excitation resulting in the rapid IC to the S_1 state. There are very little geometrical changes upon excitation because the topology of the energy minima associated with S_0 and MLCT states are very similar. Typically, photodissociation of the Co-$C_{5'}$ bond of AdoCbl bound to enzyme, as well as in solution for that matter, occurs from LF region of the S_1 state. According to previous studies there are two possible pathways for photodissociation of the Ado ligand called path A and B. These paths connect the MLCT minimum to the LF minimum. Path A involves elongation of the Co-$C_{5'}$ bond followed by the elongation of the Co-N_{Im} bond. Path B involves elongation of the Co-N_{Im} bond followed by the elongation of the Co-$C_{5'}$ bond. Based on QM/MM calculations the most energetically feasible is path B. Both the Co-N_{Im} and Co-$C_{5'}$ bond elongate in the formation

of the RP, with the full cleavage of the Co-$C_{5'}$ bond occurring from the LF region. However, the LF region can only be explored up to a certain point (Co-$C_{5'}$ distances of ~ 2.6 Å) when using a single reference method such as TD-DFT and for longer distance the results need to be extrapolated.

Interestingly, the S_1 PES based on QM/MM calculations of CarH-DS is consistent with the experimental observation that there are modest changes in the axial bond lengths in the enzymatic environment when compared to solution cases (Table 7.1). For isolated AdoCbl and MeCbl, the LF minimum is located at Co-C bond distances of ~2.5 Å and ~2.3 Å, respectively. For the AdoCbl-dependent enzymes, EAL, GLM, and CarH-DS the LF minimum is found at Co-$C_{5'}$ bond distances of 2.5 Å and for 2.9, 2.7. The Co-$C_{5'}$ equilibrium bond distance is ~2.0 Å for the S_1 MLCT minimum so there is only an ~0.5 Å increase from the equilibrium to the LF region. However, the Co-$C_{5'}$ bond distance for the LF minimum is essentially unchanged when comparing the solution case to the enzyme bound cases. The equilibrium Co-N_{Im} bond distances is typically ~2.2 Å. For isolated MeCbl and AdoCbl, this bond length is increased significantly when comparing the equilibrium distance to the LF minimum distance of 3.4 Å. The Co-N_{Im} bond, is not so significantly increased in the LF region of the enzymatic environment.

Table 7.1. Axial bond lengths for the LF minimum region of the S_1 PES of various B_{12} systems.

	LF min Co-C (Å)	LF min Co-N_{Im} (Å)
Isolated AdoCbl[116]	2.50	3.40
Isolated MeCbl[117]	2.30	3.40
AdoCbl-dependent EAL[182]	2.50	2.90
AdoCbl-dependent GLM[122]	2.50	2.70
AdoCbl-dependent CarH[136]	2.50	2.80
MeCbl-dependent MetH[221]	2.40	3.40

Generally speaking, in the LF state, the position of the base is influenced by structural factors, i.e. the ability of the nucleotide loop to undergo conformational changes under given environmental conditions (presence of a protein or solvent) as well as local interactions with side chains of the corrin ligand and/or solvent or protein. In the case of the solvent or protein environment, a certain equilibrium is established which causes the axial base to remain in a certain proximity to the cobalt ion. When AdoCbl is in an environment of solvent particles, it is generally more susceptible to changes related to geometric relaxation. For the isolated cofactor the base group has a greater freedom of movement and consequently the distance between cobalt and nitrogen may be greater, than in the case of the bound cofactor. In the protein environment, significant elongation of the Co-N_{Im} bond is prevented and this was evidenced by recent XANES measurements of CarH. Here, the QM/MM calculations also confirm that significant elongation of the axial bonds is reduced in the enzyme case in comparison to the solution environment.

3.2 Manifold of Singlet Excited States

The manifold of twenty vertical singlet excited states is characterized in Table 7.2. There are various transitions represented in the list of singlet excited states. States $S_{1\text{-}4}$ are of MLCT character namely, $d_{xz} \rightarrow \pi^*$ and $d_{yz} + \pi \rightarrow \pi^*$. States $S_{5\text{-}8}$ involve so called d-d transitions namely, $d_{xz} \rightarrow d_{z2}/d_{xy}+n$ and $d_{yz} + \pi \rightarrow d_{z2}/d_{xy}+n$. States $S_{9\text{-}20}$ involve MCLT and d-d transitions but also involve some LF type transitions ($S_{9\text{-}12}$, $S_{14\text{-}15}$, $S_{17\text{-}20}$). The vertical excitations are key to interpret the experimental Abs spectrum which is a historically important tool for the analysis of the photolytic properties as well as the oxidation and ligation of the metal center of Cbls.[2, 197, 198] Sension and coworkers pointed

out that the experimental Abs spectrum of AdoCbl-dependent CarH has distinct similarities to isolated MeCbl.[37] Specifically, the α/β band of both is similar in shape and is located at ~500 nm. The γ band is located at 338 nm for both as well. It was further concluded that the spectrum of CarH and isolated MeCbl is also very similar to AdoCbl-dependent GLM.[40, 41, 91, 93] For CarH, the α/β band at 500 nm most likely corresponds to the $S_{1\text{-}4}$ states where the excitations are MLCT in character (Table 7.2). The experimental band of 527 nm for isolated MeCbl is a H → L transition described as $d_{yz} + \pi \rightarrow \pi^*$. The γ band is located at 338 nm for MeCbl was previously identified as arising from the S_{19} state which is comprised of 18% $\pi_{Im}+\pi + d_{xy} \rightarrow \pi^*$, 12% $d_{xz} + \pi \rightarrow \pi^* + d_{xy}$, and 20% $d_{yz} + \pi \rightarrow \pi^*$.[124] Based on these insights from vertical excitations calculated from TD-DFT with the BP86 functional, we can corroborate the conclusion that MeCbl and CarH are similar in Abs spectrum. While the qualitative similarity between the Abs spectrum of CarH and isolated MeCbl is evident, it is also clear that there are some similarities between the Abs spectrum of isolated AdoCbl that should be mentioned.[125] The experimental Abs spectrum indicates an α/β band at 528 nm and a γ band at 338 nm. The α/β band was previously identified as a MLCT transition from the S_3 state, namely 66% $\pi + d_{yz} \rightarrow \pi^*$. The γ band was identified as arising from the S_{35} state with a character of 24% $\pi + d_{yz} \rightarrow \pi^*$ and $\pi + d_{yz} \rightarrow$ Ado(π^*). Put another way, the transitions for the α/β band and γ band for CarH and isolated MeCbl and AdoCbl are primarily MLCT in nature.

Present QM/MM calculations are also consistent with the experimental observation that the excited state of CarH is similar to that of GLM. A previous theoretical study of AdoCbl-dependent GLM model indicated that the initial excitation is associated with S_2 state which is followed by IC to the S_1 MLCT minimum.[122] The S_2 state is consistent with

the MLCT assignment based on TAS measurements and also corresponds well with the excitation energy for the α/β band maximum. The dominant contributions to the S_2 state are 44% $d_{xz} + \pi \rightarrow \pi^*$ and 34% $d_{xz}/d_{z2} \rightarrow \pi^*$. For CarH, the α/β band is likely comprised of the $S_{1\text{-}4}$ states. The Abs maximum is most closely associated with the S_3 state, which has the highest oscillator strength of the first four lowest excitations (Table 7.2). Like the S_2 state of GLM, the dominant contributions to the S_3 state of CarH are MLCT in character, namely 35% $d_{xy} \rightarrow \pi^*$ and 42% $d_{yz} + \pi \rightarrow \pi^*$.

Table 7.2. Twenty lowest singlet electronic transitions and orbital characterization of AdoCbl bound to CarH based on single point TD-DFT/MM calculations.

	E [eV]	λ [nm]	f	%	Character		Exp.
1	2.2403	553	0.0046	40	175 → 179	$d_{xz} \rightarrow \pi^*$	α/β region
				24	177 → 179	$d_{yz} + \pi \rightarrow \pi^*$	
				26	178 → 179	$d_{yz} + \pi \rightarrow \pi^*$	
2	2.3237	534	0.0188	19	175 → 179	$d_{xz} \rightarrow \pi^*$	α/β region
				60	178 → 179	$d_{yz} + \pi \rightarrow \pi^*$	
3	2.4636	504	0.0610	35	175 → 179	$d_{xz} \rightarrow \pi^*$	α/β region
				42	177 → 179	$d_{yz} + \pi \rightarrow \pi^*$	
4	2.5213	492	0.0074	89	173 → 179	$d_{xy} \rightarrow \pi^*$	α/β region
5	2.7934	444	0.0002	22	177 → 180	$d_{yz} + \pi \rightarrow d_{z2}/d_{xy}+n$	
6	2.8187	440	0.0121	11	175 → 180	$d_{xz} \rightarrow d_{z2}/d_{xy}+n$	
				65	178 → 180	$d_{yz} + \pi \rightarrow d_{z2}/d_{xy}+n$	
7	2.9104	426	0.0043	60	177 → 180	$d_{yz} + \pi \rightarrow d_{z2}/d_{xy}+n$	
8	2.9576	419	0.0002	20	177 → 181	$d_{yz} + \pi \rightarrow d_{xy}+n$	
9	2.9679	418	0.0083	64	178 → 181	$d_{yz} + \pi \rightarrow d_{xy}+n$	
				14	178 → 182	$d_{yz} + \pi \rightarrow \sigma(d_{z2}) + \pi^*$	
10	3.0507	406	0.0087	15	175 → 180	$d_{xz} \rightarrow d_{z2}/d_{xy}+n$	
				60	178 → 182	$d_{yz} + \pi \rightarrow \sigma(d_{z2}) + \pi^*$	
11	3.1084	399	0.0002	23	177 → 182	$d_{yz} + \pi \rightarrow \sigma(d_{z2}) + \pi^*$	
12	3.1339	396	0.0109	15	175 → 181	$d_{xz} \rightarrow d_{xy}+n$	
				29	177 → 181	$d_{yz} + \pi \rightarrow d_{xy}+n$	
				11	177 → 182	$d_{yz} + \pi \rightarrow \sigma(d_{z2}) + \pi^*$	
13	3.1485	394	0.0007	17	171 → 179	$d_{yz} + \pi \rightarrow \pi^*$	
14	3.157	393	0.0093	38	171 → 179	$d_{yz} + \pi \rightarrow \pi^*$	
				19	177 → 182	$d_{yz} + \pi \rightarrow \sigma(d_{z2}) + \pi^*$	
15	3.1736	391	0.0048	18	173 → 180	$d_{xy} \rightarrow d_{z2}/d_{xy}+n$	
				28	175 → 180	$d_{xz} \rightarrow d_{z2}/d_{xy}+n$	
				11	175 → 182	$d_{xz} \rightarrow \sigma(d_{z2}) + \pi^*$	
				11	177 → 181	$d_{yz} + \pi \rightarrow d_{xy}+n$	
16	3.2871	377	0.0019	52	173 → 180	$d_{xy} \rightarrow d_{z2}/d_{xy}+n$	

				26	173 → 181	$d_{xy} \rightarrow d_{xy}+n$
17	3.3378	371	0.0178	57	167 → 179	$d_{yz} + \pi \rightarrow \pi^*$
				9	177 → 182	$d_{yz} + \pi \rightarrow \sigma(d_{z2}) + \pi^*$
18	3.4203	362	0.0023	39	173 → 181	$d_{xy} \rightarrow d_{xy}+n$
				19	173 → 182	$d_{xy} \rightarrow \sigma(d_{z2}) + \pi^*$
19	3.4793	356	0.0256	9	173 → 181	$d_{xy} \rightarrow d_{xy}+n$
				30	175 → 181	$d_{xz} \rightarrow d_{xy}+n$
				12	175 → 182	$d_{xz} \rightarrow \sigma(d_{z2}) + \pi^*$
				10	177 → 181	$d_{yz} + \pi \rightarrow d_{xy}+n$
20	3.5303	351	0.0154	9	167 → 179	$d_{yz} + \pi \rightarrow \pi^*$
				16	175 → 181	$d_{xz} \rightarrow d_{xy}+n$
				17	175 → 182	$d_{xz} \rightarrow \sigma(d_{z2}) + \pi^*$

3.3 Formation of Singlet Diradical Intermediate

The most important issue related to CarH mechanism is the question related to how the anhAdo is formed in CarH-DS. To date, a consensus has not been reached as to whether the formation of anhAdo as well as potentially HCbl, occurs in the excited state or the ground state.[32, 34, 37] Present calculations explore the formation in the ground state, after photocleavage of the Co-$C_{5'}$ bond. Analysis of the S_0 and S_1 PESs associated with AdoCbl inside CarH-DS (Figure 7.3) indicate that the role of light is only to generate the Co(II)/Ado• RP in the electronically excited state. From an energetic point of view, it is much easier to generate RP on the in the excited state rather than on the S_0 PES. In fact, the barrier for RP formation on the S_0 PES is ~25 kcal/mol, while in the S_1 state the barrier between the MLCT minimum (I S_{1min}) to the MECP (IIB) is ~4 kcal/mol.

The initial excitation $S_0 \rightarrow S_3$ results in fast decay to the S_1 state where geometry of AdoCbl remains essentially intact. Previously it was shown that the most energetically feasible path to photolysis on the S_1 PES in CarH-DS involves path B where the initial elongation of the Co-N_{Im} bond is followed by the elongation of the Co-$C_{5'}$ bond.[136] This energy path, which connects the MLCT and LF regions, involves crossing the seam at the minimum energy crossing point (MECP), Figure 7.3. The final stage of the Co-$C_{5'}$ bond

cleavage involves only Co-$C_{5'}$ bond elongation and it can be expected that once the LF minimum (IIIB S_{1min}) is reached, either RP formation or geminate recombination is possible. Further, it is expected that RP formation would occur at distances beyond the limit of TD-DFT. Nevertheless, the RP formation process can be described by extrapolation to the dissociation limit which was demonstrated in previous studies of isolated AdoCbl.[110, 116] The reaction to form anhAdo requires that geminate recombination be prevented. So the formation of the Co(II)/Ado• RP from the LF region should be considered next.

On Figure 7.3, the point where RP formation would occur is marked IVB S_1. From here, IC to the S_0 PES would occur, marked V S_0. There are two possibilities from V S_0 but the key component to note is that the IC is to a point on the S_{0ax} PES where the axial bonds are elongated and the Co(II)/Ado• RP is intact. The S_{0ax} PES depicted in Figure 7.3 was extended to Co-$C_{5'}$ distances of 4.3 Å to explore the region of the PES where IC would occur. From 1.8-2.6 Å the wavefunction was restricted and for Co-$C_{5'}$ distances beyond 2.6 Å an unrestricted wavefunction was used. There are two minima regions on the S_{0ax} PES. The minimum energy points for each region are denoted I $S_{0ax\ min}$ and II $S_{0ax\ min2}$. The optimized geometries corresponding to these points are depicted in Figure 7.3 and 7.4 with relevant structural details included. Point V S_0, corresponds to a geometry where the Co-N_{Im} bond is ~ 3.30 Å and the Co-$C_{5'}$ bond is ~ 3.20 Å. The first possibility from V S_0 is that the Co(II) and Ado• dissociate from each other solely along the Co-$C_{5'}$ coordinate, approaching VI S_0. The second possibility is that the Co-N_{Im} bond contracts back to a length closer to the equilibrium, while the Co-$C_{5'}$ bond remains elongated. This possibility corresponds to the second minima region on the S_{0ax} PES, marked II $S_{0ax\ min\ 2}$ corresponds

to a diradical species where the Co-N_{Im} bond is 2.15 Å and the Co-$C_{5'}$ bond is 3.62 Å (Figure 7.3). The energetics associated with this minima region are depicted in Figure A.7.1. The $C_{5'}$ and the Co of the diradical have electronic spins of +1 and -1, respectively and this would indicate that the Co-$C_{5'}$ bond is broken in this minima region of the S_{0ax} PES.

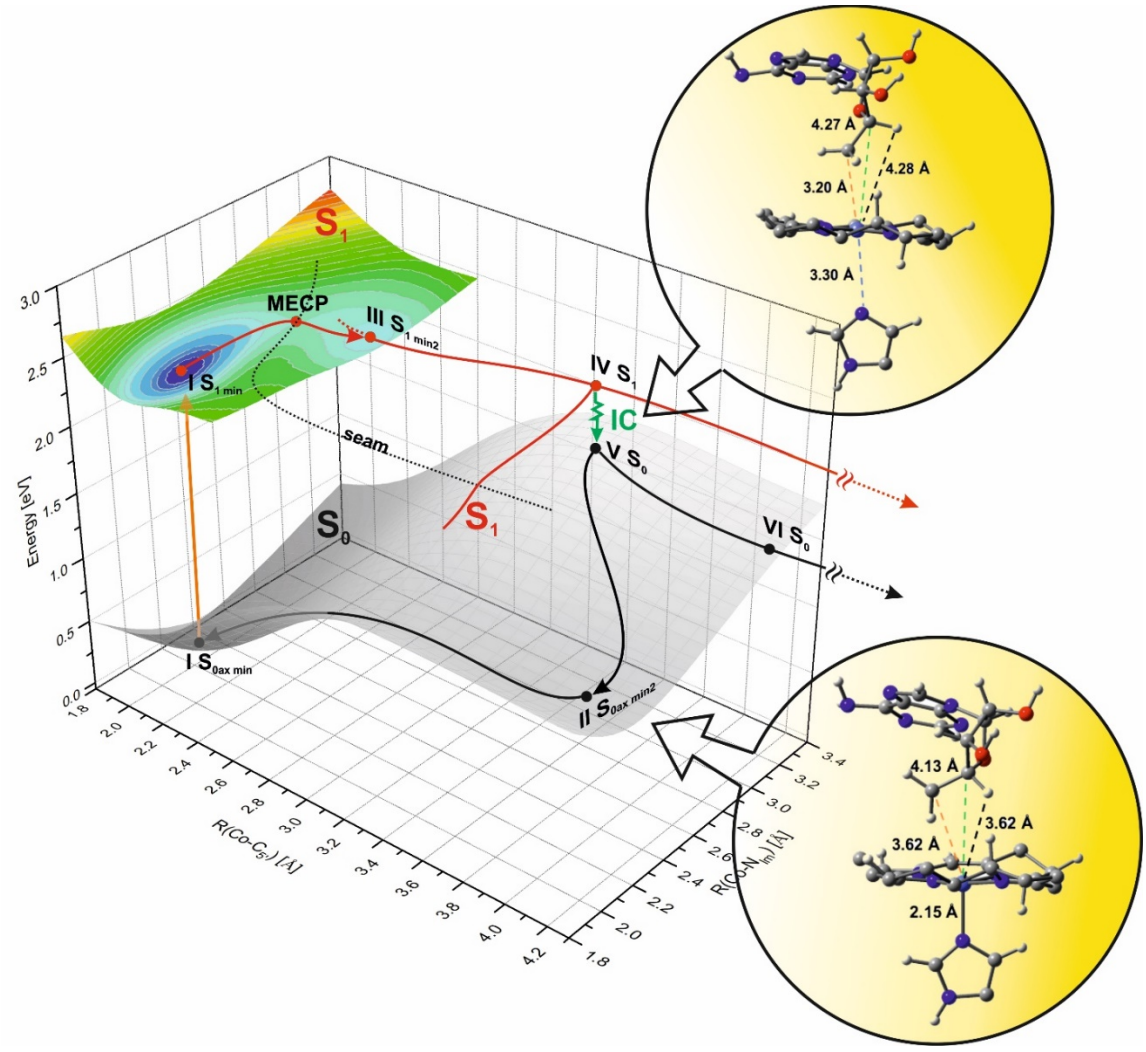

Figure 7.3. S_0 and S_1 PESs of CarH-DS as a function of axial (ax) bond lengths. The S_1 PES is based on vertical excitations from QM/MM optimized S_0 geometries. The wavefunction is restricted up to Co-$C_{5'}$ bond distances of 2.6 Å and for Co-$C_{5'}$ bond distances greater than 2.6 Å, the wavefunction is unrestricted. The geometries of key ground state points highlight in the insets with QM/MM bond lengths depicted. The S_0 geometry (V S_0) involved in the $S_1 \rightarrow S_0$ IC process depicted in the top inset. The geometry corresponding to II $S_{0ax\ min2}$ depicted in bottom inset.

There are several implications of the presence of the diradical species on the S_{0ax} PES. Intuitively, the first to consider is the possibility to reform the Co-$C_{5'}$ bond of the AdoCbl cofactor which would result in the return to I $S_{0ax\ min}$. This could be described as the geminate recombination pathway and also ineffective for the formation of anhAdo. This possibility would only be in play for a singlet diradical. Regardless, there isn't experimental evidence corroborating this geminate recombination pathway.[37] Alternatively, a second possibility should be considered; one that would involve the formation of the anhAdo product from the singlet diradical. A probable way to form the anhAdo is for the hydrogen of the $C_{4'}$ to be transferred to the Co(II), forming HCbl. To test the hypothesis that HCbl is formed together with anhAdo, it is important to construct a PES with the active coordinates. The Co-N_{Im} bond is no longer an active coordinate in the formation of HCbl/anhAdo, for two reasons. First, the Co-N_{Im} bond reforms in the de-activation process (see insets Figure 7.3) and secondly, the Co-N_{Im} is essentially unchanged in plateau-like region of the S_{0ax} PES where the second minima is located (II$S_{0ax\ min2}$, Figure A.7.1).

Rather, the more appropriate set of coordinates for the second option are the Co-$C_{5'}$ and Co-$C_{4'}$ distances (See Figure 7.1a inset for location of $C_{4'}$). This is evident based on the relaxed geometry of the singlet diradical at point II $S_{0ax\ min2}$ (Figure 7.4 and 7.5). At the equilibrium geometry (I $S_{0ax\ min}$), the Co-$C_{5'}$ and Co-$C_{4'}$ bond lengths are 2.00 Å and 3.21 Å, respectively (Figure 7.4). For the optimized singlet diradical, the Co-$C_{5'}$ and Co-$C_{4'}$ bond lengths are 3.62 Å and 4.13 Å, respectively (Figure 7.4). Also, of note, when comparing the equilibrium geometry to the optimized singlet diradical, the $C_{4'}$ shifted directly above the Co ion. At the equilibrium, the $C_{5'}$ is directly above the Co ion as

evidenced by the 175° N_{Im}-Co-$C_{5'}$ angle (Figure 7.5). For the optimized diradical, the N_{Im}-Co-$C_{5'}$ angle shifted and is 161° and the $C_{4'}$ is almost directly above the Co and this angle, N_{Im}-Co-$C_{4'}$, is 177° (Figure 7.5).

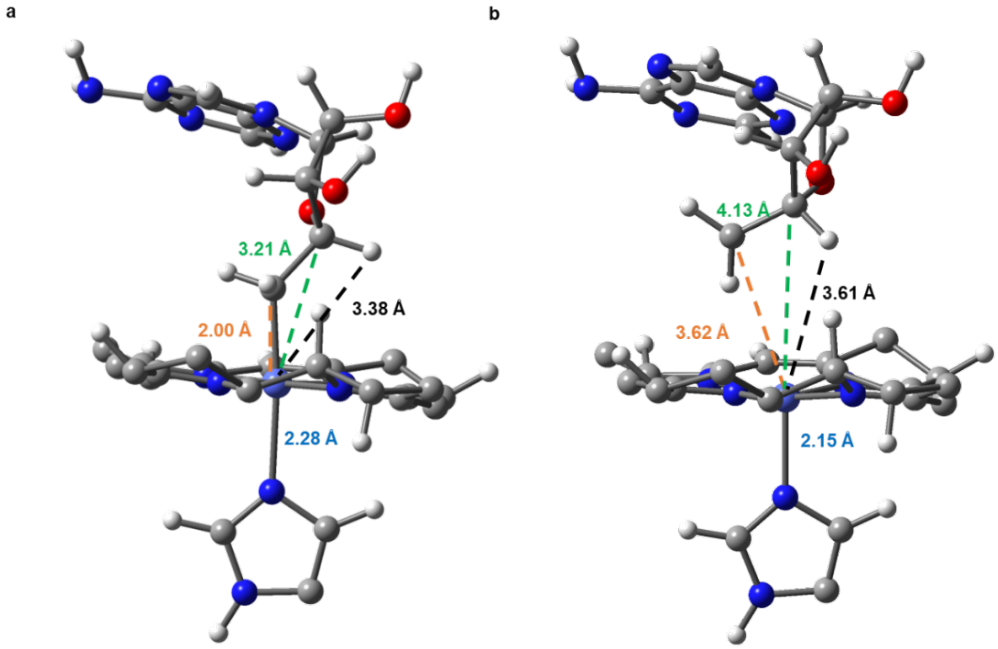

Figure 7.4. Optimized geometries with bond lengths depicted for **a)** AdoCbl equilibrium structure corresponding to I $S_{0ax\ min}$ (Figure 3 and S3) and **b)** the optimized Co(II)/Ado diradical corresponding to II $S_{0ax\ min2}$ (Figure 3 and S3). The bond distance colors are Co-$C_{5'}$ = orange, Co-$C_{4'}$ = green, and Co-H = black.

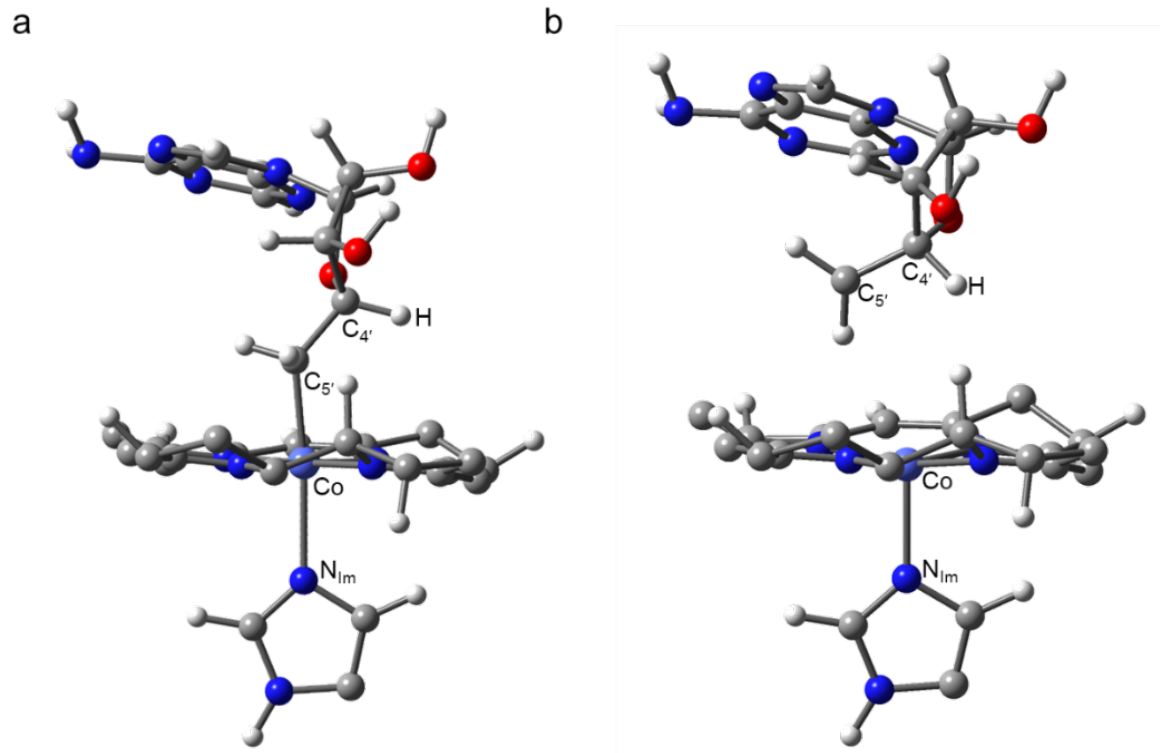

Angle	a) AdoCbl	b) {Co(II)/Ado•}^{1,1}
N_{Im} – Co – $C_{5'}$	175°	161°
N_{Im} – Co – $C_{4'}$	162°	177°
N_{Im} – Co – H	146°	164°

Figure 7.5. Optimized geometries with bond angles listed for **a)** AdoCbl equilibrium structure corresponding to I $S_{0ax\ min}$ (Figure 3 and S3) and **b)** the optimized Co(II)/Ado diradical corresponding to II $S_{0ax\ min2}$ (Figure 3 and S3). The bond angle colors are Co-$C_{5'}$ = orange, Co-$C_{4'}$ = green, and Co-H = black.

3.4 Formation of anhAdo

Based on these geometric changes, attention can be turned to the PESs computed as a function of Co-$C_{5'}$ and Co-$C_{4'}$ distances which, in essence, explore the role of the ribose portion of the Ado ligand in the formation of the photoproduct. This PES will be referred to as $[S_{0rib}]^{1,1}$, where the superscript represents charge, multiplicity. The $[S_{0rib}]^{1,1}$ PES (Figure 7.6) contains several characteristic features including two minima regions. The minimum localized around short Co-$C_{4'}$ and Co-$C_{5'}$ bond distances corresponds to the equilibrium geometry of CarH-DS where the AdoCbl cofactor is intact. Accordingly, this

region is analogous to point I $S_{0ax\ min}$ on the S_{0ax} PES from Figure 7.3 and Figure A.7.1. The S_{0ax} PES also has Co-$C_{5'}$ as a coordinate. The other minimum on the $[S_{0rib}]^{1,1}$ PES, marked with the label, HCbl + anhAdo, corresponds to the formation of the Co-H bond and the photoproduct. The geometry corresponding to this point was successfully optimized without any constraints. There is also a plateau-like region on the $[S_{0rib}]^{1,1}$ PES which extends from distances of 3.0-4.2 Å and 3.5-4.2 Å for the Co-$C_{5'}$ and Co-$C_{4'}$ bonds, respectively. The relaxation of the geometry of this point, also results in a diradical species, labeled $\{Co(II)/Ado\bullet\}^{1,1}$, this point is analogous to the region II $S_{0\ min2}$ (Figure 7.3). A spin density of approximately -1 and +1 is observed on the Co and $C_{5'}$, respectively, on the section of the $[S_{0rib}]^{1,1}$ PES from Co-$C_{5'}$ distances of 3.0-4.8 Å and Co-$C_{4'}$ distances of 3.1-5.1 Å. The spin density profiles for the Co and $C_{5'}$ across the entire $[S_{0rib}]^{1,1}$ PES are depicted in Figure 7.6.

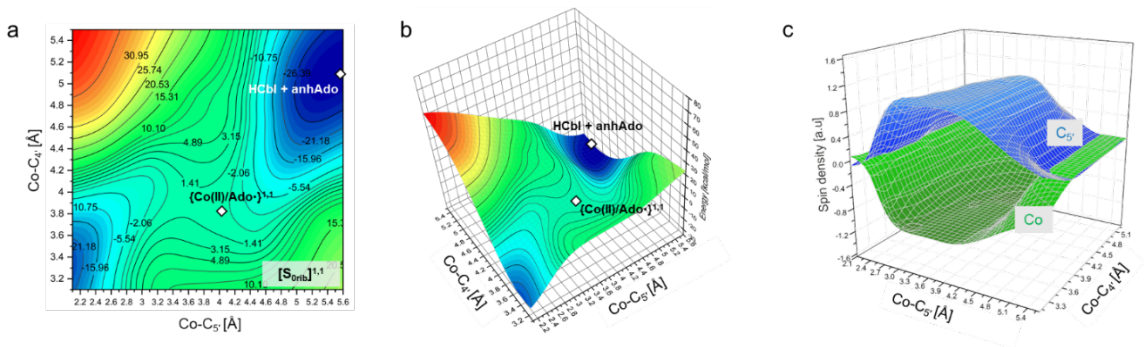

Figure 7.6. a) Contour plot of ground state PESs of CarH-DS ($[S_{0rib}]^{1,1}$) as function of Co-$C_{5'}$ and Co-$C_{4'}$ bond lengths with singlet multiplicity and the b) corresponding 3D representation. Points corresponding to the optimized singlet diradical species are labeled $\{Co(II)/Ado\cdot\}^{1,1}$. The superscript refers to the charge and multiplicity of the QM region for the QM/MM calculations. Panel c), spin densities on Co and $C_{5'}$ atoms, plotted as function of Co-$C_{5'}$ and Co-$C_{4'}$ distances.

The topology of the $[S_{0rib}]^{1,1}$ PES implies that the Co(II)/Ado• RP can recombine, by the re-formation the Co-$C_{5'}$ bond. This energetically feasible route would result in the

return to the energy minimum of the S_{0ax} PES (I $S_{0ax\ min}$, Figure 7.3, A.7.1). This would potentially explain the rather low QY that was observed in the TAS study of CarH. The second possibility from $\{Co(II)/Ado\bullet\}^{1,1}$ is to reach the other minimum, denoted HCbl + anhAdo, by further elongation of the Co-$C_{5'}$ bond and Co-$C_{4'}$. Again, this local minimum region corresponds to the formation of HCbl and anhAdo. Before detailed discussion will be presented, it needs to be pointed out that although in the LF state the Co can be associated with Co(II) because of Co---$C_{5'}$ separation, electronically it somehow resembles Co(I) because the d_z^2 orbital is doubly occupied due to $d_{xx} \rightarrow d_{xx}$ excitation. Consequently, the Co center has noticeable electron density oriented perpendicularly to the corrin ring and this can be considered as the initial driving force for the Co---H interaction. Further, it was previously demonstrated that the HCbl metal center is more in-line with Co(I)-H^+ than other electronic configurations such as Co(II) or Co(III). While it is evident that there is a feasible connection from the Co(II)/Ado• RP to the initial cofactor (AdoCbl) as well as to the products HCbl and anhAdo, the location of the TS is not immediately apparent based solely on inspection of the $[S_{0rib}]^{1,1}$ PES. However, analysis of the $[S_{0rib}]^{1,1}$ PES reveals that the two key coordinates involved in the formation of the photoproducts were Co-$C_{4'}$ and Co-H. The optimized geometry of $\{Co(II)/Ado\bullet\}^{1,1}$ is the same as that depicted in Figure 7.4 and shows that the $C_{4'}$-H is oriented towards the macrocycle and in position to form HCbl.

3.5 Transition State Associated with Co-H Formation

To search for the TS between the singlet diradical and the formation of the photoproducts, a PES as a function of Co-$C_{4'}$ and Co-H distances (Figure 7.7) was constructed. The energy reference for the $[S_{0TS}]^{1,1}$ is the singlet diradical, $\{Co(II)/Ado\bullet\}^{1,1}$

from the $[S_{0rib}]^{1,1}$ PES, and this was also the starting geometry for the constructions of the $[S_{0TS}]^{1,1}$ PES. From the optimized singlet diradical, the Co-$C_{4'}$ and Co-H bond distances were systematically stretched/contracted with a step size of 0.1 Å to span distances of 3.0-5.0 Å and 3.5-1.4 Å, respectively. There are four key regions on the $[S_{0TS}]^{1,1}$ PES. The first, marked $\{Co(II)/Ado\bullet\}^{1,1}$ on Figure 7.7, corresponds to the optimized diradical. The two broad minima regions marked in deep blue color in Figure 7.7 correspond to intact AdoCbl and HCbl + anhAdo. The AdoCbl minimum region is found at Co-$C_{4'}$ and Co-H bond distances greater than 3.2 A. The photoproduct region, labeled HCbl + anhAdo, is at the opposite side of the $[S_{0TS}]^{1,1}$ PES where the Co-$C_{4'}$ bond is greater than ~4.6 Å and the Co-H bond is ~1.5 Å. Finally, the TS is clearly depicted on the $[S_{0TS}]^{1,1}$ PES. According to the computed PES, the formation of the Co-H bond of HCbl is associated with a TS containing partially elongated $C_{4'}$-H and Co-H bonds. The corresponding TS lies approximately at Co-$C_{4'}$ and Co-H bond distances of 3.2 Å and 1.8 Å, respectively (Figure 7.7). This has been taken as an intuitive guess for the TS search. There is a single imaginary frequency of *i*1592 cm^{-1} from the geometry at point TS on $[S_{0TS}]^{1,1}$. The vectors associated with the motions of this frequency are depicted in Figure 7.8. Based on the computed PES we can propose that the energy barrier associated with $C_{4'}$---H---Co TS is ~15.0 kcal/mol from the diradical state.

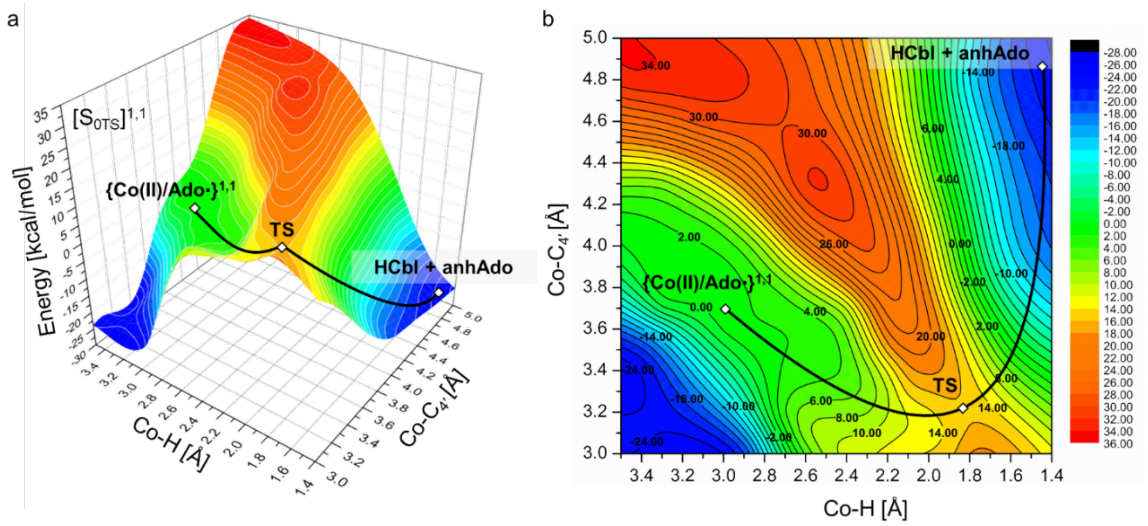

Figure 7.7. Ground state PESs ($[S_{0TS}]^{1,1}$) corresponding to the singlet QM/MM optimized geometries with Co-$C_{4'}$ and Co-H bond of AdoCbl in CarH-DS constrained. **a)** 3D representation and **b)** contour plot where the yellow line connects the TS between the singlet diradical and photoproducts HCbl + anhAdo. The energy reference is the optimized singlet diradical species (with no constraints) depicted in Figure 7.4 The PESs use the color scale depicted on the right-hand side with energies in kcal/mol.

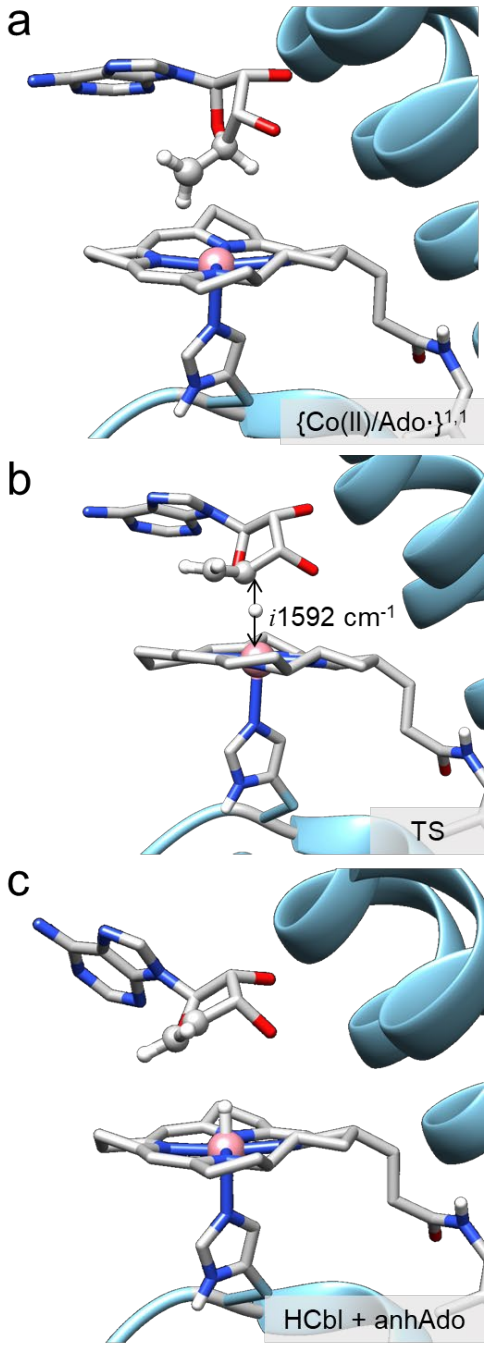

Figure 7.8. QM/MM optimized molecular structures corresponding to points on $[S_{0TS}]^{1,1}$ PES including **a)** singlet diradical species **b)** TS connecting diradical to photoreaction products with the vectors associated with the single imaginary frequency of *i*1592 cm^{-1} and **c)** the photoreaction product, HCbl and anhAdo.

3.6 Viability of HCbl

The role of the Co-H species requires further exploration. In the 1960's, despite lack of experimental evidence at the time, it was hypothesized that HCbl played role in B_{12}-dependent enzymatic catalysis.[3] Although the only basis for this supposition was theoretical and chemical intuition, it seems that the hypothesis of the 1960's may be confirmed with CarH. One of the challenges to probing this hypothesis is that the HCbl molecule is difficult to characterize due to its transient nature. The pKa of Co-H is reported to be approximately ~1.0, and thus it is remarkably unstable.[236] Chemaly posited on the possibility of HCbl in the CarH mechanism from a literature-based point of view.[36] First, the HCbl intermediate can be described as follows:

$$\text{Co(I)-H}^+ \leftrightarrow \text{Co(II)-H} \leftrightarrow \text{Co(III)-H}^-$$

Second, when HCbl is considered as protonated Co(I), it can act as a Brönsted acid to protonate water (or potentially an amino acid side chain of the protein) in a reaction described below:

$$\text{Co(I)-H}^+ + \text{H}_2\text{O} \rightarrow \text{Co(I)} + \text{H}_3\text{O}^+$$

The transient nature of HCbl as well as its experimental instability provide major challenges for investigators. However, the instability of the HCbl intermediary can perhaps be the driving force for the formation of the *bis*-HisCbl CarH-LS species. Based on the X-ray crystal structure, His132 forms the *bis*-HisCbl after photoproduct formation. Should HCbl be formed, it is reasonable to suppose that His132 would replace the proton/hydrogen/hydride to make a much more stable adduct. In a recent computational study, it was demonstrated that HCbl is best described as protonated Co(I).[135]

3.7 Key Considerations in AdoCbl-dependent Catalysis

3.7.1 Considering Cage Effects

In AdoCbl-dependent radical mediated catalysis, whether the activation of the Co-$C_{5'}$ is via light or substrate binding, it is important to consider how the trajectory of the radical is controlled.[6] For solution-based photochemical studies in general, cage effects significantly contribute to this. In simplest terms, if the RPs remain in the solvent cage, geminate recombination is the likely route for deactivation to the ground state. If the radicals can escape the cage, possibilities for true photochemical reactions can be explored. These cage effects have been observed and studied via TAS and it is well known that the photolysis of AdoCbl in solution is affected by environment, with solvent viscosity playing a role.

But what of enzymes? It has been shown that the enzymatic environment can provide a sort of cage controlling photolytic activity, analogous to a solvent cage.[259] In particular, cage effects have been observed for AdoCbl-dependent GLM and MeCbl-dependent MetH.[40, 41, 259] In TAS studies of MetH, it was shown the active site of the MeCbl cofactor contains several hydrophobic residues from the α-helical domain which cage the methyl radical from diffusive loss.[259] This, in turn, promotes recombination with the corresponding Co(II)/Me• RP which formed upon cleavage via light. This is an important point to be aware of in terms of analyzing CarH photochemistry, especially considering the previously described similarities of the CarH, GLM, and MeCbl excited states. Of the other B_{12}-dependent enzymes, the AdoCbl binding domain of CarH is most like the MeCbl binding domain of MetH with a few exceptions.[23, 35] Due to the structural similarities with MetH, Drennan, *et al.* hypothesized that cage effects may be active in CarH as well,

although, with a different purpose than geminate recombination which is observed in GLM and MetH.[32] Cage effects in CarH may be necessary to prevent diffusion of Co(II)/Ado• RP immediately after Co-$C_{5'}$ bond activation in order to favor β-H elimination.

In the early 1990's Garr and Finke observed radical cage effects in coenzyme-B_{12} in solution.[260] In particular, they observed that, in the viscous solvent glycerol, the Co(II)/Ado• RP is caged. The implication of this is that anhAdo is formed because the solvent cage orients the Ado radical in such a way that β-H elimination is feasible. Not only is the photoproduct anhAdo formed, but HCbl is formed as well. In addition, this study showed that β-H elimination does not occur in a concerted fashion. In fact, β-H elimination in AdoCbl photolysis occurs through the caged Co(II)/Ado• RP. It is possible that cage effects in CarH allow for the formation of anhAdo, similar to what was observed in glycerol. If this is the case, it seems that in CarH-DS, the photoproduct could be formed via a similar mechanism as in glycerol which would also imply that HCbl was formed along with anhAdo after β-H elimination. Our results provide evidence that the formation of anhAdo and HCbl is possible based on the relative orientations of the $C_{5'}$• and -$C_{4'}$-H in CarH-DS along the reaction pathway visualized on both the $[S_{0rib}]^{1,1}$ and $[S_{0TS}]^{1,1}$ PESs.

3.7.2 Considering Structural Factors Associated with Enzyme Bound AdoCbl

It is important to note the aspects of AdoCbl-dependent enzymes that set them apart, in terms of geometry, to understand what aspect of CarH contributes to its photolability. As discussed in a previously, the contribution of cage effects in CarH-DS is to favor β-H elimination. The optimized geometries and the corresponding crystal structures of CarH-DS were compared with EAL and GLM. It was observed that the orientation of the -$C_{5'}$ of the Ado moiety bound to Co and the orientation of the -$C_{4'}$-H play

a critical role in why CarH is able to operate without a substrate. In EAL and GLM, the -$C_{4'}$-H is directed towards the substrate while in CarH the -$C_{4'}$-H is directed towards the Co metal center.[6] It is well understood that the ribose part of Ado ligand can undergo various conformational changes including pseudorotation or rotation around the glycosyl angle. Interestingly, the ribose conformations have been shown to control the radical trajectories in AdoCbl-dependent enzymes including diol dehydratase (DDH) and GLM.[6] There are two different implications for the conformational change of the ribose portion of the Ado radical for both of these examples. One orientation favors radical recombination while the other position promotes H-atom abstraction from the substrate. For the native enzymatic reaction of GLM, the pseudorotation of the ribose ring moves the $C_{5'}$ radical in such a way to generate a substrate radical instead of recombining with the Co(II). For DDH, the $C_{5'}$ radical is moved over an approximately 7Å distance via rotation around the N-glycosidic bond in order to facilitate H-atom abstraction from the substrate. So, what are the implications of these observations for CarH?

There is a key difference between CarH and the two other previously mentioned AdoCbl-dependent enzymes, EAL and GLM. Notably, EAL and GLM are essentially photostable.[24, 122, 182] As was previously demonstrated, after, photocleavage of the Co-$C_{5'}$ bond, QM/MM calculations, as well as the corresponding crystal structures, indicate that the -$C_{4'}$-H is in perfect position to participate in β-H elimination and form the Co-hydride, HCbl; which would be in-line with the Drennan and coworkers proposal.[32]

3.7.3 Comparison with AdoCbl-dependent Catalysis

Generally speaking, AdoCbl-dependent catalysis can be summed up in three steps, with the Ado radical playing a major part.[261] The key initial step involves homolytic

cleavage of the Co-$C_{5'}$ bond and the formation of the RP. The primary Ado• has not been detected experimentally until recently.[262] Its formation is coupled with the hydrogen abstraction from a substrate. The $C_{5'}$• repositions itself 5-10 Å away from the Co(II) and the propagation of the radical toward the substrate is a highly controlled process regardless of which AdoCbl-dependent enzyme is under consideration. Lastly, with the reorientation of the $C_{5'}$•, the Ado moiety is perfectly positioned participate in H-atom abstraction from the substrate.

While this three-step summary is generally observed in coenzyme B_{12}-dependent catalysis, there are some notable differences in CarH. Because the CarH photoreceptor operates without the presence of a substrate and the Co-$C_{5'}$ activation is via light, the Ado• plays dual role, as a radical and substrate. It is also known that there are two key motions that aid in the control of radical trajectories in coenzyme B_{12}-dependent enzymes and these include conformational changes associated with the ribose portion of the Ado ligand and rotation around the N-glycosidic bond.[6] Sugars, including the ribose portion of Ado, are notably flexible and in AdoCbl the ribose may be found in either the 2′-endo or 3′endo conformation.[230] Typically, intact AdoCbl is in the 2′-endo conformation while after Co-$C_{5'}$ bond cleavage, the ribose is found in the 3′-endo conformation. Further the conformation of the ribose after homolytic cleavage of the Co-$C_{5'}$ bond is indicative of whether the $C_{5'}$• is oriented towards recombination with the Co(II)Cbl or hydrogen atom abstraction from the substrate. When ribose is in the 2′-endo conformation the $C_{5'}$ is oriented towards the metal center whereas if the ribose is in the 3′-endo conformation, the $C_{5'}$ is oriented towards the substrate. Nature takes advantage of this in the catalytic cycle and, at some point after or perhaps during Co-$C_{5'}$ cleavage, there is typically a switch from

2′-endo to 3′-endo. This pseudorotation ensures that the Co-$C_{5'}$ bond won't be reformed and that H-atom abstraction from the substrate occurs. While this is exhibited in AdoCbl-dependent enzymes such as MCM, in CarH-DS, this conformational switch is not observed. Instead, the crystal structure and the QM/MM optimized intact AdoCbl in CarH-DS shows that the conformation of the ribose is 3′-endo. After photolytic cleavage of the Co-$C_{5'}$ bond, the conformation of the ribose of the diradical is also 3′-endo. This is perhaps a driving force for photoproduct formation. Additionally, the $C_{4'}$-H bond, is in perfect position for the Co(II) to abstract H.

The other motion to consider in AdoCbl-dependent catalysis is the rotation around the N-glycosidic bond between the ribose and the adenine of the Ado ligand.[6, 230] This angle is also known as the glycosyl rotation angle where $\chi = O_{1'}\text{-}C_{1'}\text{-}N_{1'}\text{-}C_{5'}$. After Co-$C_{5'}$ bond cleavage the ribose portion of the Ado ligand is able to rotate around the N-glycosidic bond. In DDH, this motion is dominant and the $C_{5'}$• is moved ~7 Å toward the substrate via rotation around the χ angle. In DDH, the ribose moiety rotates counterclockwise by 94°, the $C_{5'}$• moves to 2.0 Å away from the C_1 of the substrate. This is within van der Waal's distance and the $C_{5'}$• can abstract the H from substrate atom C1. This rotation also prevents re-formation of the Co-$C_{5'}$ bond or Co(II) abstraction of the $C_{4'}$-H of ribose which would both be unwanted side-reactions in AdoCbl-dependent catalysis involving H-atom abstraction with a substrate. In CarH, a similar rotation around the N-glycosidic bond is observed, although with a lesser degree of rotation. In the QM/MM optimized CarH-DS model (Figure 7.8a), the χ angle between the ribose and adenine groups of intact AdoCbl is 87.44°. At the TS point (Figure 7.8b), the same χ angle is 74.62°, which is an ~13° degree difference compared to the equilibrium geometry where the Co-$C_{5'}$ bond is intact. For the

QM/MM optimized structure with HCbl and anhAdo (Figure 7.8c), the χ angle is 73.29°. It would seem that CarH exhibits similarities to DDH in that there is a counterclockwise rotation leading to H-atom abstraction. However, the major difference between the two is that in CarH the H of $C_{4'}$ is transferred to the Co(II)Cbl and in DDH the $C_{5'}$• abstracts the pro(*S*) H from the substrate.[263] It appears the enzymatic environment housing the AdoCbl cofactor in CarH-DS prevents the significant rotation around the N-glycosidic bond that is observed in DDH to instead aid in the formation of HCbl.

4.0 Conclusion

It would seem that the role of light in the mechanism of CarH-DS is simply to generate the Co(II)/Ado• RP. It is also apparent that AdoCbl plays a unique dual role in CarH-DS as compared to other coenzyme-B_{12} dependent enzymes which require substrate binding as the activation source for the Co-$C_{5'}$ bond. Upon cleavage of the Co-$C_{5'}$ bond in CarH-DS, AdoCbl becomes the electronic trigger for the next steps of the catalytic cycle while simultaneously acting, by analogy, as a substrate. Once the RP are formed in the LF region of the S_1 PES, de-excitation to the ground state leads to several possibilities, including an energetically feasible route to the anhAdo product which would involve the formation of HCbl via a singlet pathway.

In sum, the initial excitation in CarH-DS is likely to the S_3 state. This is followed by relaxation to the S_1 MLCT minimum. From here, the axial bonds elongate toward the LF region, with the enzymatic environment preventing the significant elongation that is observed in the photodissociation of isolated AdoCbl. Co(II)/Ado• RP is formed in the LF region. From here IC from the S_1 state occurs to a high energy region on the S_0 PES where both axial bonds are elongated. The Co-N_{Im} bond reforms to the equilibrium distance and

a stable diradical intermediate is formed. From here, there are two possibilities. The first is the reversion to the S_0 equilibrium geometry where the AdoCbl is intact, which is ineffective for photoproduct formation. The second is that the Co-$C_{5'}$ and Co-$C_{4'}$ bond continue to elongate until the point where anhAdo and HCbl are formed. The barrier between the diradical and the TS is ~14 kcal/mol. It also appears that rotation around the N-glycosidic bond is active in the formation of anhAdo and HCbl albeit to a lesser extent than other enzymes such as DDH. The QM/MM calculations appear to corroborate the Drennan, *et al* 'path 1' proposal. However, this finding does not preclude that other mechanistic possibilities, including intersystem crossing, are possible. Further theoretical studies will be required to explore all the possibilities that have been put forth based on experimental studies. Regardless, it is reasonable to predict that other recently discovered B_{12}-photoreceptors would operate in similar ways as what has been presented for CarH.

CONCLUDING REMARKS

While Cbls are perhaps best known for their role as cofactors, the light-sensing function of these species continues to rise in significance as synthetic and natural applications for this capability continue to emerge. The antivitamins B_{12} understudy in Chapter 3 are promising examples for how to design Cbls that could be used as scaffolds in drug delivery. PhEtyCbl is photostable while EtPhCbl is minimally photoactive. These two xamples are not themselves sufficiently photolabile for application purposes but their axial ligation can be modified in future studies which target development of photolabile Cbls. In contrast to the antivitamins, NACCbl is a photolabile nonalkyCbl whose axial ligation is a suitable candidate for photochemical applications which require cleavage of the bond to the upper ligand. In the dissertation's example of a naturally occurring photosensitive Cbl-depdendent system, CarH, it is clear that Nature has sufficiently harvested the light-sensing function of the photoreceptor for transcription regulation. This photoreceptor promises to become a prototypical example for the development of biomimetic catalysts that use light to initiate complex molecular transformations.

In the immediate future computational studies are underway to explore the role of ISC in the CarH excited state mechanism. This analysis involves the coupling of Landau Zener theory and El-Sayad rules. In this preliminary theoretical investigation, TD-DFT was employed and several triplet excited states have been identified as promising candidates for ISC with the lowest singlet excited state. Additionally, future computational studies

which target the formation of bis-HisCbl are underway. These projects have two targets, first to determine how the Co-N_{His629} bond is formed after anhAdo and second, to determine the mechanism by which this initiates the dissociation of the tetramer into monomers.

As applications for the photochemistry of bioinorganic systems continue to emerge, there will be a significant need for theoretical studies to elucidate reaction mechanisms. These studies may include the use of multi-reference calculations such as CASSCF in the modeling of excited state processes.

REFERENCES

1. Toda, M. J.; Lodowski, P.; Mamun, A. A.; Jaworska, M.; Kozlowski, P. M., Photolytic Properties of the Biologically Active Forms of Vitamin B_{12}. *Coord. Chem. Rev.* **2019,** *385*, 20-43.
2. Toda, M. J.; Kozlowski, P. M.; Andruniów, T., Assessing Electronically Excited States of Cobalamins Via Absorption Spectroscopy and Time-Dependent Density Functional Theory. In *Transition Metals in Coordination Environments: Computational Chemistry and Catalysis Viewpoints*, Broclawik, E.; Borowski, T.; Radoń, M., Eds. Springer International Publishing: Cham, 2019; pp 219-258.
3. Dolphin, D., *B_{12} Volume 1: Chemistry*. John Wiley & Sons, N. Y.: 1982; Vol. 1.
4. Banerjee, R., The Yin-Yang of Cobalamin Biochemistry. *Chem. Biol.* **1997,** *4*, 175-186.
5. Banerjee, R., *Chemistry and Biochemistry of B_{12}*. Wiley: New York, 1999.
6. Banerjee, R.; Ragsdale, S. W., The Many Faces of Vitamin B_{12}: Catalysis by Cobalamin-Dependent Enzymes. *Annu. Rev. Biochem.* **2003,** *72*, 209-247.
7. Brown, K. L., Chemistry and Enzymology of Vitamin B_{12}. *Chem. Rev.* **2005,** *105*, 2075-2150.
8. Halpern, J., Mechanisms of Coenzyme B_{12}-Dependent Rearrangements. *Science* **1985,** *227*, 869.
9. Ludwig, M. L.; Matthews, R. G., Structure-Based Perspectives on B_{12}-Dependent Enzymes. *Annu. Rev. Biochem.* **1997,** *66*, 269-313.
10. Krautler, B. A., D., Golding, B. T., *Vitamin B_{12} and B_{12}-Proteins*. Wiley-VCH: Weinheim, 1998.
11. Reedijk, J.; Bouwman, E., *Bioinorganic Catalysis*. 2nd ed., rev. and expanded. ed.; Marcel Dekker, Inc.: New York, 1999.
12. Toraya, T., Radical Catalysis of B_{12} Enzymes: Structure, Mechanism, Inactivation, and Reactivation of Diol and Glycerol Dehydratases. *Cellular and Molecular Life Sciences CMLS* **2000,** *57*, 106-127.
13. Randaccio, L.; Geremia, S.; Demitri, N.; Wuerges, J., Vitamin B_{12}: Unique Metalorganic Compounds and the Most Complex Vitamins. *Molecules* **2010,** *15*.
14. Randaccio, L. G., S. Demitri, N. Wuerges, J. , *Trends in Inorganic Chemistry* **2009,** *11*.
15. Matthews, R. G., Cobalamin- and Corrinoid-Dependent Enzymes. *Met. Ions Life Sci.* **2009,** *6*, 53-114.

16. Zelder, F., Recent Trends in the Development of Vitamin B_{12} Derivatives for Medicinal Applications. *Chem. Commun. (Camb)* **2015,** *51*, 14004-14017.

17. Jones, A. R., The Photochemistry and Photobiology of Vitamin B_{12}. *Photochem. Photobiol. Sci.* **2017,** *16*, 820-834.

18. Shell, T. A.; Lawrence, D. S., A New Trick (Hydroxyl Radical Generation) for an Old Vitamin (B_{12}). *J. Am. Chem. Soc.* **2011,** *133*, 2148-2150.

19. Shell, T. A.; Shell, J. R.; Rodgers, Z. L.; Lawrence, D. S., Tunable Visible and near-IR Photoactivation of Light-Responsive Compounds by Using Fluorophores as Light-Capturing Antennas. *Angew. Chem. Int. Ed.* **2014,** *53*, 875-878.

20. Shell, T. A.; Lawrence, D. S., Vitamin B_{12}: A Tunable, Long Wavelength, Light-Responsive Platform for Launching Therapeutic Agents. *Acc. Chem. Res.* **2015,** *48*, 2866-2874.

21. Zelder, F.; Sonnay, M.; Prieto, L., Antivitamins for Medicinal Applications. *ChemBioChem* **2015,** *16*, 1264-1278.

22. Padmanabhan, S.; Pérez-Castaño, R.; Elías-Arnanz, M., B_{12}-Based Photoreceptors: From Structure and Function to Applications in Optogenetics and Synthetic Biology. *Curr. Opin. Struct. Biol.* **2019,** *57*, 47-55.

23. Padmanabhan, S.; Jost, M.; Drennan, C. L.; Elías-Arnanz, M., A New Facet of Vitamin B_{12}: Gene Regulation by Cobalamin-Based Photoreceptors. *Annu. Rev. Biochem.* **2017,** *86*, 485-514.

24. Mamun, A. A.; Toda, M. J.; Kozlowski, P. M., Can Photolysis of the Co-C Bond in Coenzyme B_{12}-Dependent Enzymes Be Used to Mimic the Native Reaction? *J. Photochem. Photobiol. B: Biol.* **2019,** *191*, 175-184.

25. Robertson, W. D.; Wang, M.; Warncke, K., Characterization of Protein Contributions to Cobalt-Carbon Bond Cleavage Catalysis in Adenosylcobalamin-Dependent Ethanolamine Ammonia-Lyase by Using Photolysis in the Ternary Complex. *J. Am. Chem. Soc.* **2011,** *133*, 6968-6977.

26. Ruetz, M.; Gherasim, C.; Gruber, K.; Fedosov, S.; Banerjee, R.; Krautler, B., Access to Organometallic Arylcobaltcorrins through Radical Synthesis: 4-Ethylphenylcobalamin, a Potential "Antivitamin B_{12}". *Angew. Chem. Int. Ed. Engl.* **2013,** *52*, 2606-2610.

27. Mutti, E.; Ruetz, M.; Birn, H.; Kräutler, B.; Nexo, E., 4-Ethylphenyl-Cobalamin Impairs Tissue Uptake of Vitamin B_{12} and Causes Vitamin B_{12} Deficiency in Mice. *PLOS ONE* **2013,** *8*, e75312.

28. Ruetz, M.; Salchner, R.; Wurst, K.; Fedosov, S.; Kräutler, B., Phenylethynylcobalamin: A Light - Stable and Thermolysis - Resistant Organometallic Vitamin B_{12} Derivative Prepared by Radical Synthesis. *Angew. Chem. Int. Ed.* **2013,** *52*, 11406-11409.

29. Krautler, B., Antivitamins B_{12}--a Structure- and Reactivity-Based Concept. *Chemistry* **2015,** *21*, 11280-11287.

30. Miller, N. A.; Wiley, T. E.; Spears, K. G.; Ruetz, M.; Kieninger, C.; Krautler, B.; Sension, R. J., Toward the Design of Photoresponsive Conditional Antivitamins

B_{12}: A Transient Absorption Study of an Arylcobalamin and an Alkynylcobalamin. *J. Am. Chem. Soc.* **2016,** *138*, 14250-14256.

31. Salerno, E. V.; Miller, N. A.; Konar, A.; Salchner, R.; Kieninger, C.; Wurst, K.; Spears, K. G.; Kräutler, B.; Sension, R. J., Exceptional Photochemical Stability of the Co-C Bond of Alkynyl Cobalamins, Potential Antivitamins B_{12} and Core Elements of B_{12}-Based Biological Vectors. *Inorg. Chem.* **2020,** *59*, 6422-6431.
32. Jost, M.; Simpson, J. H.; Drennan, C. L., The Transcription Factor Carh Safeguards Use of Adenosylcobalamin as a Light Sensor by Altering the Photolysis Products. *Biochemistry* **2015,** *54*, 3231-3234.
33. Jost, M.; Fernandez-Zapata, J.; Polanco, M. C.; Ortiz-Guerrero, J. M.; Chen, P. Y.; Kang, G.; Padmanabhan, S.; Elias-Arnanz, M.; Drennan, C. L., Structural Basis for Gene Regulation by a B_{12}-Dependent Photoreceptor. *Nature* **2015,** *526*, 536-541.
34. Kutta, R. J.; Hardman, S. J.; Johannissen, L. O.; Bellina, B.; Messiha, H. L.; Ortiz-Guerrero, J. M.; Elias-Arnanz, M.; Padmanabhan, S.; Barran, P.; Scrutton, N. S.; Jones, A. R., The Photochemical Mechanism of a B_{12}-Dependent Photoreceptor Protein. *Nat. Commun.* **2015,** *6*, 7907.
35. Bridwell-Rabb, J.; Drennan, C. L., Vitamin B_{12} in the Spotlight Again. *Curr. Opin. Chem. Biol.* **2017,** *37*, 63-70.
36. Chemaly, S. M., New Light on Vitamin B_{12}: The Adenosylcobalamin-Dependent Photoreceptor Protein Carh. *S. Afr. J. Sci.* **2016,** *112*.
37. Miller, N. A.; Kaneshiro, A. K.; Konar, A.; Alonso-Mori, R.; Britz, A.; Deb, A.; Glownia, J. M.; Koralek, J. D.; Mallik, L.; Meadows, J. H.; Michocki, L. B.; van Driel, T. B.; Koutmos, M.; Padmanabhan, S.; Elías-Arnanz, M.; Kubarych, K. J.; Marsh, E. N. G.; Penner-Hahn, J. E.; Sension, R. J., The Photoactive Excited State of the B_{12}-Based Photoreceptor Carh. *J. Phys. Chem. B* **2020,** *124*, 10732-10738.
38. Marsh, E. N.; Melendez, G. D., Adenosylcobalamin Enzymes: Theory and Experiment Begin to Converge. *Biochim. Biophys. Acta* **2012,** *1824*, 1154-1164.
39. Roman-Melendez, G. D.; von Glehn, P.; Harvey, J. N.; Mulholland, A. J.; Marsh, E. N., Role of Active Site Residues in Promoting Cobalt-Carbon Bond Homolysis in Adenosylcobalamin-Dependent Mutases Revealed through Experiment and Computation. *Biochemistry* **2014,** *53*, 169-177.
40. Sension, R. J.; Cole, A. G.; Harris, A. D.; Fox, C. C.; Woodbury, N. W.; Lin, S.; Marsh, E. N., Photolysis and Recombination of Adenosylcobalamin Bound to Glutamate Mutase. *J. Am. Chem. Soc.* **2004,** *126*, 1598-1599.
41. Sension, R. J.; Harris, D. A.; Stickrath, A.; Cole, A. G.; Fox, C. C.; Marsh, E. N., Time-Resolved Measurements of the Photolysis and Recombination of Adenosylcobalamin Bound to Glutamate Mutase. *J. Phys. Chem. B* **2005,** *109*, 18146-18152.
42. Matthews, R. G., Cobalamin-Dependent Methyltransferases. *Acc. Chem. Res.* **2001,** *34*, 681-689.

43. Matthews, R. G.; Koutmos, M.; Datta, S., Cobalamin-Dependent and Cobamide-Dependent Methyltransferases. *Curr. Opin. Struct. Biol.* **2008,** *18*, 658-666.

44. Toraya, T., Radical Catalysis in Coenzyme B_{12}-Dependent Isomerization (Eliminating) Reactions. *Chem. Rev.* **2003,** *103*, 2095-2128.

45. Banerjee, R., Radical Peregrinations Catalyzed by Coenzyme B_{12}-Dependent Enzymes. *Biochemistry* **2001,** *40*, 6191-6198.

46. Toraya, T., Enzymatic Radical Catalysis: Coenzyme B_{12}-Dependent Diol Dehydratase. *Chem. Rec.* **2002,** *2*, 352-366.

47. Marsh, E. N.; Patterson, D. P.; Li, L., Adenosyl Radical: Reagent and Catalyst in Enzyme Reactions. *ChemBioChem* **2010,** *11*, 604-621.

48. Frey, P. A.; Reed, G. H., Radical Mechanisms in Adenosylmethionine- and Adenosylcobalamin-Dependent Enzymatic Reactions. *Arch. Biochem. Biophys.* **2000,** *382*, 6-14.

49. Frey, P. A., Radical Mechanisms of Enzymatic Catalysis. *Annu. Rev. Biochem.* **2001,** *70*, 121-148.

50. Reed, G. H., Radical Mechanisms in Adenosylcobalamin-Dependent Enzymes. *Curr. Opin. Chem. Biol.* **2004,** *8*, 477-483.

51. Buckel, W.; Golding, B. T., Radical Enzymes in Anaerobes. *Annu. Rev. Microbiol.* **2006,** *60*, 27-49.

52. Gruber, K.; Reitzer, R.; Kratky, C., Radical Shuttling in a Protein: Ribose Pseudorotation Controls Alkyl-Radical Transfer in the Coenzyme B_{12} Dependent Enzyme Glutamate Mutase. *Angew. Chem. Int. Ed.* **2001,** *40*, 3377-3380.

53. Marsh, E. N.; Ballou, D. P., Coupling of Cobalt-Carbon Bond Homolysis and Hydrogen Atom Abstraction in Adenosylcobalamin-Dependent Glutamate Mutase. *Biochemistry* **1998,** *37*, 11864-11872.

54. Marsh, E. N., Review Article Coenzyme-B_{12}-Dependent Glutamate Mutase. *Bioorg. Chem.* **2000,** *28*, 176-189.

55. Huhta, M. S.; Ciceri, D.; Golding, B. T.; Marsh, E. N., A Novel Reaction between Adenosylcobalamin and 2-Methyleneglutarate Catalyzed by Glutamate Mutase. *Biochemistry* **2002,** *41*, 3200-3206.

56. Buckel, W.; Kratky, C.; Golding, B. T., Stabilisation of Methylene Radicals by Cob(II)alamin in Coenzyme B_{12} Dependent Mutases. *Chemistry* **2005,** *12*, 352-362.

57. Banerjee, R., Radical Carbon Skeleton Rearrangements: Catalysis by Coenzyme B_{12}-Dependent Mutases. *Chem. Rev.* **2003,** *103*, 2083.

58. Banerjee, R., Radical Carbon Skeleton Rearrangements: Catalysis by Coenzyme B_{12}-Dependent Mutases. *Chem. Rev.* **2003,** *103*, 2083-2094.

59. Gruber, K.; Kratky, C., Coenzyme B_{12} Dependent Glutamate Mutase. *Curr. Opin. Chem. Biol.* **2002,** *6*, 598-603.

60. Wetmore, S. D.; Smith, D. M.; Bennett, J. T.; Radom, L., Understanding the Mechanism of Action of B_{12}-Dependent Ethanolamine Ammonia-Lyase: Synergistic Interactions at Play. *J. Am. Chem. Soc.* **2002,** *124*, 14054-14065.

61. Minot, G. R.; Murphy, W. P., Treatment of Pernicious Anemia by a Special Diet. *J. Am. Med. Assoc.* **1926,** *87*, 470-476.

62. Stevenson, L. G., *Nobel Prize Winners in Medicine and Physiology, 1901-1950*. Henry Schuman: New York, 1953; Vol. 29.

63. Rickes, E. L.; Brink, N. G.; Koniuszy, F. R.; Wood, T. R.; Folkers, K., Crystalline Vitamin B_{12}. *Science* **1948,** *107*, 396.

64. Shorb, M. S., Activity of Vitamin B_{12} for the Growth of Lactobacillus Lactis. *Science* **1948,** *107*, 397.

65. Smith, E. L., Purification of Anti-Pernicious Anæmia Factors from Liver. *Nature* **1948,** *161*, 638-639.

66. Smith, E. L., Presence of Cobalt in the Anti-Pernicious Anæmia Factor. *Nature* **1948,** *162*, 144-145.

67. Rickes, E. L.; Brink, N. G.; Koniuszy, F. R.; Wood, T. R.; Folkers, K., Vitamin B_{12}; a Cobalt Complex. *Science* **1948,** *108*, 134.

68. Dorothy Crowfoot Hodgkin, F. R. S., June Lindsey, Maureen Mackay, K. N. Trueblood, The Structure of Vitamin B_{12} - Iv. The X-Ray Analysis of Air-Dried Crystals of B_{12}. *Proceedings of the Royal Society of London. Series A. Mathematical and Physical Sciences* **1962,** *266*, 475.

69. Brink, C.; Hodgkin, D. C.; Lindsey, J.; Pickworth, J.; Robertson, J. H.; White, J. G., Structure of Vitamin B_{12}: X-Ray Crystallographic Evidence on the Structure of Vitamin B_{12}. *Nature* **1954,** *174*, 1169-1171.

70. Hodgkin, D. C.; Kamper, J.; Mackay, M.; Pickworth, J.; Trueblood, K. N.; White, J. G., Structure of Vitamin B_{12}. *Nature* **1956,** *178*, 64-66.

71. James, L. K., *Nobel Laureates in Chemistry, 1901-1992*. American Chemical Society : Chemical Heritage Foundation: [Washington, D.C.], 1993.

72. Howard, J. A. K., Dorothy Hodgkin and Her Contributions to Biochemistry. *Nat. Rev. Mol. Cell Biol.* **2003,** *4*, 891-896.

73. Firth, R. A.; Hill, H. A. O.; Pratt, J. M.; Williams, R. J. P.; Jackson, W. R., The Circular Dichroism and Absorption Spectra of Some Vitamin B_{12} Derivatives. *Biochemistry* **1967,** *6*, 2178-2189.

74. Pratt, J. M., 988. The Chemistry of Vitamin B_{12}. Part Ii. Photochemical Reactions. *J. Chem. Soc. (Resumed)* **1964**, 5154-5160.

75. Pratt, J. M.; Whitear, B. R. D., Photolysis of Methylcobalamin. *J. Chem. Soc. A: Inorg. Phys. Theo.* **1971**, 252-255.

76. Taylor, R. T.; Smucker, L.; Hanna, M. L.; Gill, J., Aerobic Photoiysis of Alkylcobalamins: Quantum Yields and Light-Action Spectra. *Arch. Biochem. Biophys.* **1973,** *156*, 521-533.

77. Barker, H. A.; Weissbach, H.; Smyth, R. D., A Coenzyme Containing Pseudovitamin B_{12} *Proc. Natl. Acad. Sci. U. S. A.* **1958,** *44*, 1093-1097.

78. Barker, H. A.; Smyth, R. D.; Weissbach, H.; Toohey, J. I.; Ladd, J. N.; Volcani, B. E., Isolation and Properties of Crystalline Cobamide Coenzymes Containing Benzimidazole or 5,6-dimethylbenzimidazole. *J. Biol. Chem.* **1960,** *235*, 480-488.

79. Weissbach, H.; Ladd, J. N.; Volcani, B. E.; Smyth, R. D.; Barker, H. A., Structure of the Adenylcobamide Coenzyme: Degradation by Cyanide, Acid, and Light. *J. Biol. Chem.* **1960,** *235*, 1462-1473.

80. Johnson, A. W.; Shaw, N., 888. Some Reactions of the Vitamin B_{12} Coenzyme. *J. Chem. Soc. (Resumed)* **1962**, 4608-4614.

81. Johnson, A. W.; Mervyn, L.; Shaw, N.; Smith, E. L., 785. A Partial Synthesis of the Vitamin B_{12} Coenzyme and Some of Its Analogues. *J. Chem. Soc. (Resumed)* **1963**, 4146-4156.

82. Hogenkamp, H. P. C.; Barker, H. A., The Identification of a Sugar Derived from Coenzyme B_{12}. *J. Biol. Chem.* **1961,** *236*, 3097 3101.

83. Hogenkamp, H. P. C.; Ladd, J. N.; Barker, H. A., The Identification of a Nucleoside Derived from a Coenzyme B_{12}. *J. Biol. Chem.* **1962,** *237*, 1950-1952.

84. Hogenkamp, H. P. C., A Cyclic Nucleoside Derived from Coenzyme B_{12}. *J. Biol. Chem.* **1963,** *238*, 477-480.

85. Schrauzer, G. N.; Sibert, J. W.; Windgassen, R. J., Photochemical and Thermal Cobalt-Carbon Bond Cleavage in Alkylcobalamins and Related Organometallic Compounds. Comparative Study. *J. Am. Chem. Soc.* **1968,** *90*, 6681-6688.

86. Schrauzer, G. N.; Lee, L. P.; Sibert, J. W., Alkylcobalamins and Alkylcobaloximes. Electronic Structure, Spectra, and Mechanism of Photodealkylation. *J. Am. Chem. Soc.* **1970,** *92*, 2997-3005.

87. Dolphin, D.; Johnson, A. W.; Rodrigo, R., 606. Reactions of the Alkylcobalamins. *J. Chem. Soc. (Resumed)* **1964**, 3186-3193.

88. Day, P., The Electronic Structure and Spectrum of Vitamin B_{12}. *Coord. Chem. Rev.* **1967,** *2*, 99-108.

89. Chen, E.; Chance, M. R., Nanosecond Transient Absorption Spectroscopy of Coenzyme B_{12}. Quantum Yields and Spectral Dynamics. *J. Biol. Chem.* **1990,** *265*, 12987-12994.

90. Chen, E.; Chance, M. R., Continuous-Wave Quantum Yields of Various Cobalamins Are Influenced by Competition between Geminate Recombination and Cage Escape. *Biochemistry* **1993,** *32*, 1480-1487.

91. Walker, L. A.; Jarrett, J. T.; Anderson, N. A.; Pullen, S. H.; Matthews, R. G.; Sension, R. J., Time-Resolved Spectroscopic Studies of B_{12} Coenzymes: The Identification of a Metastable Cob(III)alamin Photoproduct in the Photolysis of Methylcobalamin. *J. Am. Chem. Soc.* **1998,** *120*, 3597-3603.

92. Walker, L. A.; Shiang, J. J.; Anderson, N. A.; Pullen, S. H.; Sension, R. J., Time-Resolved Spectroscopic Studies of B_{12} Coenzymes: The Photolysis and Geminate Recombination of Adenosylcobalamin. *J. Am. Chem. Soc.* **1998,** *120*, 7286-7292.

93. Shiang, J. J.; Walker, L. A.; Anderson, N. A.; Cole, A. G.; Sension, R. J., Time-Resolved Spectroscopic Studies of B_{12} Coenzymes: The Photolysis of Methylcobalamin Is Wavelength Dependent. *J. Phys. Chem. B* **1999,** *103*, 10532-10539.

94. Yoder, L. M.; Cole, A. G.; Walker, L. A.; Sension, R. J., Time-Resolved Spectroscopic Studies of B_{12} Coenzymes: Influence of Solvent on the Photolysis of Adenosylcobalamin. *J. Phys. Chem. B* **2001,** *105*, 12180-12188.

95. Cole, A. G.; Yoder, L. M.; Shiang, J. J.; Anderson, N. A.; Walker, L. A.; Banaszak Holl, M. M.; Sension, R. J., Time-Resolved Spectroscopic Studies of B_{12} Coenzymes: A Comparison of the Primary Photolysis Mechanism in Methyl-, Ethyl-, N-Propyl-, and 5'-Deoxyadenosylcobalamin. *J. Am. Chem. Soc.* **2002,** *124*, 434-441.

96. Andrew B. Stickrath, E. C. C., Xiaochuan Dai, D. Ahmasi Harris, Aaron Rury, Broc Smith, Kuo-Chun Tang, Jonathan Wert, and Roseanne J. Sension, Solvent-Dependent Cage Dynamics of Small Nonpolar Radicals: Lessons from the Photodissociation and Geminate Recombination of Alkylcobalamins. *J. Phys. Chem. A* **2009,** *113*, 8513-8522.

97. Sension, R. J.; Harris, D. A.; Cole, A. G., Time-Resolved Spectroscopic Studies of B_{12} Coenzymes: Comparison of the Influence of Solvent on the Primary Photolysis Mechanism and Geminate Recombination of Methyl-, Ethyl-, N-Propyl-, and 5′-deoxyadenosylcobalamin. *J. Phys. Chem. B* **2005,** *109*, 21954-21962.

98. Joseph J. Shiang, A. G. C., Roseanne J. Sension, Kun Hang, Yuxiang Weng, Jenna S. Trommel, Luigi G. Marzilli, and Tianquan Lian, Ultrafast Excited-State Dynamics in Vitamin B_{12} and Related Cob(III)alamins. *J. Am. Chem. Soc.* **2006,** *128*, 801-808.

99. Peng, J.; Tang, K.-C.; McLoughlin, K.; Yang, Y.; Forgach, D.; Sension, R. J., Ultrafast Excited-State Dynamics and Photolysis in Base-Off B_{12} Coenzymes and Analogues: Absence of the Trans-Nitrogenous Ligand Opens a Channel for Rapid Nonradiative Decay. *J. Phys. Chem. B* **2010,** *114*, 12398-12405.

100. Wiley, T. E.; Arruda, B. C.; Miller, N. A.; Lenard, M.; Sension, R. J., Excited Electronic States and Internal Conversion in Cyanocobalamin. *Chin. Chem. Lett.* **2015,** *26*, 439-443.

101. Wiley, T. E.; Miller, W. R.; Miller, N. A.; Sension, R. J.; Lodowski, P.; Jaworska, M.; Kozlowski, P. M., Photostability of Hydroxocobalamin: Ultrafast Excited State Dynamics and Computational Studies. *J. Phys. Chem. Lett.* **2016,** *7*, 143-147.

102. Harris, D. A.; Stickrath, A. B.; Carroll, E. C.; Sension, R. J., Influence of Environment on the Electronic Structure of Cob(III)alamins: Time-Resolved Absorption Studies of the S1 State Spectrum and Dynamics. *J. Am. Chem. Soc.* **2007,** *129*, 7578-7585.

103. Rury, A. S.; Wiley, T. E.; Sension, R. J., Energy Cascades, Excited State Dynamics, and Photochemistry in Cob(III)alamins and Ferric Porphyrins. *Acc. Chem. Res.* **2015,** *48*, 860-867.

104. Warncke, K., Characterization of the Product Radical Structure in the Co^{ii}-Product Radical Pair State of Coenzyme B_{12}-Dependent Ethanolamine Deaminase by Using Three-Pulse ^{2}H Eseem Spectroscopy. *Biochemistry* **2005,** *44*, 3184-3193.

105. Canfield, J. M.; Warncke, K., Active Site Reactant Center Geometry in the Co(II)-Product Radical Pair State of Coenzyme B_{12}-Dependent Ethanolamine Deaminase

Determined by Using Orientation-Selection Electron Spin-Echo Envelope Modulation Spectroscopy. *J. Phys. Chem. B* **2005,** *109*, 3053-3064.

106. Robertson, W. D.; Warncke, K., Photolysis of Adenosylcobalamin and Radical Pair Recombination in Ethanolamine Ammonia-Lyase Probed on the Micro- to Millisecond Time Scale by Using Time-Resolved Optical Absorption Spectroscopy. *Biochemistry* **2009,** *48*, 140-147.
107. Jones, A. R.; Hardman, S. J. O.; Hay, S.; Scrutton, N. S., Is There a Dynamic Protein Contribution to the Substrate Trigger in Coenzyme B_{12}-Dependent Ethanolamine Ammonia Lyase? *Angew. Chem. Int. Ed.* **2011,** *50*, 10843-10846.
108. Jones, A. R.; Russell, H. J.; Greetham, G. M.; Towrie, M.; Hay, S.; Scrutton, N. S., Ultrafast Infrared Spectral Fingerprints of Vitamin B_{12} and Related Cobalamins. *J. Phys. Chem. A* **2012,** *116*, 5586-5594.
109. Alex R. Jones, C. L., Sam Hay, and Nigel S. Scrutton, Relating Localized Protein Motions to the Reaction Coordinate in Coenzyme B_{12}-Dependent Enzymes. *FEBS J.* **2013,** *280*, 2997-3008.
110. Kozlowski, P. M.; Garabato, B. D.; Lodowski, P.; Jaworska, M., Photolytic Properties of Cobalamins: A Theoretical Perspective. *Dalton Trans* **2016,** *45*, 4457-4470.
111. Wiley, T. E.; Miller, N. A.; Miller, W. R.; Sofferman, D. L.; Lodowski, P.; Toda, M. J.; Jaworska, M.; Kozlowski, P. M.; Sension, R. J., Off to the Races: Comparison of Excited State Dynamics in Vitamin B_{12} Derivatives Hydroxocobalamin and Aquocobalamin. *J. Phys. Chem. A* **2018,** *122*, 6693-6703.
112. Lodowski, P.; Ciura, K.; Toda, M. J.; Jaworska, M.; Kozlowski, P. M., Photodissociation of Ethylphenylcobalamin Antivitamin B_{12}. *Phys. Chem. Chem. Phys.* **2017,** *19*, 30310-30315.
113. Lodowski, P.; Toda, M. J.; Ciura, K.; Jaworska, M.; Kozlowski, P. M., Photolytic Properties of Antivitamins B_{12}. *Inorg. Chem.* **2018,** *57*, 7838-7850.
114. Rodgers, Z. L.; Shell, T. A.; Brugh, A. M.; Nowotarski, H. L.; Forbes, M. D. E.; Lawrence, D. S., Fluorophore Assisted Photolysis of Thiolato-Cob(III)alamins. *Inorg. Chem.* **2016,** *55*, 1962-1969.
115. Toda, M. J.; Lodowski, P.; Thurman, T. M.; Kozlowski, P. M., Light Mediated Properties of a Thiolato-Derivative of Vitamin B_{12}. *Inorg. Chem.* **2020,** *59*, 17200-17212.
116. Garabato, B. D.; Lodowski, P.; Jaworska, M.; Kozlowski, P. M., Mechanism of Co-C Photodissociation in Adenosylcobalamin. *Phys. Chem. Chem. Phys.* **2016,** *18*, 19070-19082.
117. Lodowski, P.; Jaworska, M.; Andruniow, T.; Garabato, B. D.; Kozlowski, P. M., Mechanism of Co-C Bond Photolysis in the Base-on Form of Methylcobalamin. *J. Phys. Chem. A* **2014,** *118*, 11718-11734.
118. Lodowski, P.; Jaworska, M.; Garabato, B. D.; Kozlowski, P. M., Mechanism of Co-C Bond Photolysis in Methylcobalamin: Influence of Axial Base. *J. Phys. Chem. A* **2015,** *119*, 3913-3928.

119. Liu, H.; Kornobis, K.; Lodowski, P.; Jaworska, M.; Kozlowski, P. M., TD-DFT Insight into Photodissociation of the Co-C Bond in Coenzyme B_{12}. *Front. Chem.* **2014,** *1*, 1-12.

120. Lodowski, P.; Jaworska, M.; Andruniow, T.; Garabato, B. D.; Kozlowski, P. M., Mechanism of the S_1 Excited State Internal Conversion in Vitamin B_{12}. *Phys. Chem. Chem. Phys.* **2014,** *16*, 18675-18679.

121. Sension, R., Following Photoexcited Electrons in Reactions. *Science* **2017,** *356*, 31.

122. Mamun, A. A.; Toda, M. J.; Lodowski, P.; Kozlowski, P. M., Photolytic Cleavage of Co-C Bond in Coenzyme B_{12}-Dependent Glutamate Mutase. *J. Phys. Chem. B* **2019,** *123*, 2585-2598.

123. Jaworska, M.; Lodowski, P.; Andruniów, T.; Kozlowski, P. M., Photolysis of Methylcobalamin: Identification of the Relevant Excited States Involved in Co-C Bond Scission. *J. Phys. Chem. B* **2007,** *111*, 2419-2422.

124. Andruniów, T.; Jaworska, M.; Lodowski, P.; Zgierski, M. Z.; Dreos, R.; Randaccio, L.; Kozlowski, P. M., Time-Dependent Density Functional Theory Study of Cobalt Corrinoids: Electronically Excited States of Methylcobalamin. *J. Chem. Phys.* **2008,** *129*, 085101.

125. Andruniów, T.; Jaworska, M.; Lodowski, P.; Zgierski, M. Z.; Dreos, R.; Randaccio, L.; Kozlowski, P. M., Time-Dependent Density Functional Theory Study of Cobalt Corrinoids: Electronically Excited States of Coenzyme B_{12}. *J. Chem. Phys.* **2009,** *131*, 105105.

126. Lodowski, P.; Jaworska, M.; Andruniów, T.; Kumar, M.; Kozlowski, P. M., Photodissociation of Co-C Bond in Methyl- and Ethylcobalamin: An Insight from TD-DFT Calculations. *J. Phys. Chem. B* **2009,** *113*, 6898-6909.

127. Grissom, C. B. C., Alexander M., Magnetic Field Effects in Model B_{12} Enzymatic Reactions. The Photolysis of Methylcob(III)alamin. *Z. Phys. Chem.* **1992,** *1*, 181-188.

128. Chagovetz, A. M.; Grissom, C. B., Magnetic Field Effects in Adenosylcob(III)alamin Photolysis: Relevance to B_{12} Enzymes. *J. Am. Chem. Soc.* **1993,** *115*, 12152-12157.

129. Harkins, T. T.; Grissom, C. B., Magnetic Field Effects on B_{12} Ethanolamine Ammonia Lyase: Evidence for a Radical Mechanism. *Science* **1994,** *263*, 958-960.

130. Harkins, T. T.; Grissom, C. B., The Magnetic Field Dependent Step in B_{12} Ethanolamine Ammonia Lyase Is Radical-Pair Recombination. *J. Am. Chem. Soc.* **1995,** *117*, 566-567.

131. Jones, A. R.; Hay, S.; Woodward, J. R.; Scrutton, N. S., Magnetic Field Effect Studies Indicate Reduced Geminate Recombination of the Radical Pair in Substrate-Bound Adenosylcobalamin-Dependent Ethanolamine Ammonia Lyase. *J. Am. Chem. Soc.* **2007,** *129*, 15718-15727.

132. Jones, A. R.; Woodward, J. R.; Scrutton, N. S., Continuous Wave Photolysis Magnetic Field Effect Investigations with Free and Protein-Bound Alkylcobalamins. *J. Am. Chem. Soc.* **2009,** *131*, 17246-17253.

133. Chen, J.-R.; Ke, S.-C., Magnetic Field Effects on Coenzyme B_{12}- and B_6-Dependent Lysine 5,6-Aminomutase: Switching of the J-Resonance through a Kinetically Competent Radical-Pair Intermediate. *Phys. Chem. Chem. Phys.* **2018,** *20*, 13068-13074.

134. Schwartz, P. A.; Frey, P. A., 5′-peroyadenosine and 5′-peroxyadenosylcobalamin as Intermediates in the Aerobic Photolysis of Adenosylcobalamin. *Biochemistry* **2007,** *46*, 7284-7292.

135. Toda, M. J.; Lodowski, P.; Mamun, A. A.; Kozlowski Pawel, M., Elelctronic and Photolytic Properties of Hydridocobalamin. *J. Photochem. Photobiol. B: Biol.* **2021**.

136. Toda, M. J.; Mamun, A. A.; Lodowski, P.; Kozlowski, P. M., Why Is Carh Photolytically Active in Comparison to Other B_{12}-Dependent Enzymes? *J. Photochem. Photobiol. B: Biol.* **2020,** *209*, 111919.

137. Kohn, W.; Sham, L. J., Self-Consistent Equations Including Exchange and Correlation Effects. *Phys. Rev.* **1965,** *140*, A1133-A1138.

138. Runge, E.; Gross, E. K. U., Density-Functional Theory for Time-Dependent Systems. *Phys. Rev. Lett.* **1984,** *52*, 997-1000.

139. Kornobis, K.; Kumar, N.; Lodowski, P.; Jaworska, M.; Piecuch, P.; Lutz, J. J.; Wong, B. M.; Kozlowski, P. M., Electronic Structure of the S_1 State in Methylcobalamin: Insight from CASSCF/MC-XQDPT2, EOM-CCSD, and TD-DFT Calculations. *J. Comput. Chem.* **2013,** *34*, 987-1004.

140. Jensen, K. P.; Ryde, U., Theoretical Prediction of the Co-C Bond Strength in Cobalamins. *J. Phys. Chem. A* **2003,** *107*, 7539-7545.

141. Jensen, K. P., Electronic Structure of Cob(I)alamin: The Story of an Unusual Nucleophile. *J. Phys. Chem. B* **2005,** *109*, 10505-10512.

142. Wick, C. R.; Smith, D. M., Modelling the Reactions Catalyzed by Coenzyme B_{12} Dependent Enzymes: Accuracy and Cost-Quality Balance. *J. Phys. Chem. A* **2018**.

143. Kepp, K. P., Co-C Dissociation of Adenosylcobalamin (Coenzyme B_{12}): Role of Dispersion, Induction Effects, Solvent Polarity, and Relativistic and Thermal Corrections. *J. Phys. Chem. A* **2014,** *118*, 7104-7117.

144. Kuta, J.; Patchkovskii, S.; Zgierski Marek, Z.; Kozlowski Pawel, M., Performance of DFT in Modeling Electronic and Structural Properties of Cobalamins. *J. Comput. Chem.* **2006,** *27*, 1429-1437.

145. Kornobis, K.; Kumar, N.; Wong, B. M.; Lodowski, P.; Jaworska, M.; Andruniow, T.; Ruud, K.; Kozlowski, P. M., Electronically Excited States of Vitamin B_{12}: Benchmark Calculations Including Time-Dependent Density Functional Theory and Correlated *Ab Initio* Methods. *J. Phys. Chem. A* **2011,** *115*, 1280-1292.

146. Lodowski, P.; Jaworska, M.; Kornobis, K.; Andruniow, T.; Kozlowski, P. M., Electronic and Structural Properties of Low-Lying Excited States of Vitamin B_{12}. *J. Phys. Chem. B* **2011,** *115*, 13304-13319.

147. Solheim, H.; Kornobis, K.; Ruud, K.; Kozlowski, P. M., Electronically Excited States of Vitamin B_{12} and Methylcobalamin: Theoretical Analysis of Absorption, CD, and MCD Data. *J. Phys. Chem. B* **2011,** *115*, 737-748.

148. Garabato, B. D.; Kumar, N.; Lodowski, P.; Jaworska, M.; Kozlowski, P. M., Electronically Excited States of Cob(II)alamin: Insights from CASSCF/XMCQDPT2 and TD-DFT Calculations. *Phys. Chem. Chem. Phys.* **2016,** *18*, 4513-4526.

149. Ghosh, A. P.; Lodowski, P.; Bazarganpour, A.; Leks, M.; Kozlowski, P. M., Aerobic Photolysis of Methylcobalamin: Structural and Electronic Properties of the Cbl–O-O-CH_3 Intermediate. *Dalton Trans.* **2020,** *49*, 4114-4124.

150. Roos, B. O.; Taylor, P. R.; Siögbahn, P. E. M., A Complete Active Space Scf Method (CASSCF) Using a Density Matrix Formulated Super-CI Approach. *Chem. Phys.* **1980,** *48*, 157-173.

151. Andersson, K.; Malmqvist, P. A.; Roos, B. O.; Sadlej, A. J.; Wolinski, K., Second-Order Perturbation Theory with a CASSCF Reference Function. *J. Phys. Chem.* **1990,** *94*, 5483-5488.

152. Andersson, K.; Malmqvist, P. Å.; Roos, B. O., Second‐Order Perturbation Theory with a Complete Active Space Self‐Consistent Field Reference Function. *J. Chem. Phys.* **1992,** *96*, 1218-1226.

153. Perdew, J. P., Density-Functional Approximation for the Correlation Energy of the Inhomogeneous Electron Gas. *Phys. Rev. B* **1986,** *33*, 8822-8824.

154. Burke, K.; Werschnik, J.; Gross, E. K. U., Time-Dependent Density Functional Theory: Past, Present, and Future. *J. Chem. Phys.* **2005,** *123*, 062206.

155. Peach, M. J.; Benfield, P.; Helgaker, T.; Tozer, D. J., Excitation Energies in Density Functional Theory: An Evaluation and a Diagnostic Test. *J. Chem. Phys.* **2008,** *128*, 044118.

156. Martin, B. D.; Finke, R. G., Cobalt-Carbon Homolysis and Bond Dissociation Energy Studies of Biological Alkylcobalamins: Methylcobalamin, Including $\geq 10^{15}$ Co-CH_3 Homolysis Rate Enhancement at 25°C Following One-Electron Reduction. *J. Am. Chem. Soc.* **1990,** *112*, 2419-2420.

157. Martin, B. D.; Finke, R. G., Methylcobalamin's Full- Vs. Half-Strength Cobalt-Carbon Sigma Bonds and Bond Dissociation Enthalpies: A $>10^{15}$ Co-CH_3 Homolysis Rate Enhancement Following One-Antibonding-Electron Reduction of Methlycobalamin. *J. Am. Chem. Soc.* **1992,** *114*, 585-592.

158. Hung, R. R.; Grabowski, J. J., Listening to Reactive Intermediates: Application of Photoacoustic Calorimetry to Vitamin B_{12} Compounds. *J. Am. Chem. Soc.* **1999,** *121*, 1359-1364.

159. Finke, R. G., Coenzyme B_{12}-Based Chemical Precedent for Co-C Bond Homolysis and Other Key Elementary Steps. In *Vitamin B_{12} and B_{12}-Proteins*, 1998; pp 383-402.

160. Hay, B. P.; Finke, R. G., Thermolysis of the Co-C Bond in Adenosylcobalamin (Coenzyme B_{12}) - IV. Products, Kinetics and Co-C Bond Dissociation Energy Studies in Ethylene Glycol. *Polyhedron* **1988,** *7*, 1469-1481.

161. Bin Luo, L.; Li, G.; Lan Chen, H.; Wei Fu, S.; Yi Zhang, S., Laser-Induced Photoacoustic Calorimetric Determination of Enthalpy and Volume Changes in Photolysis of 5'-Deoxyadenosylcobalamin and Methylcobalamin. *J. Chem. Soc., Dalton Trans.* **1998**, 2103-2108.

162. Kobylianskii, I. J.; Widner, F. J.; Krautler, B.; Chen, P., Co-C Bond Energies in Adenosylcobinamide and Methylcobinamide in the Gas Phase and in Silico. *J. Am. Chem. Soc.* **2013,** *135*, 13648-13651.

163. Kozlowski, P. M.; Kumar, M.; Piecuch, P.; Li, W.; Bauman, N. P.; Hansen, J. A.; Lodowski, P.; Jaworska, M., The Cobalt-Methyl Bond Dissociation in Methylcobalamin: New Benchmark Analysis Based on Density Functional Theory and Completely Renormalized Coupled-Cluster Calculations. *J. Chem. Theory Comput.* **2012,** *8*, 1870-1894.

164. Ryde, U.; Mata, R. A.; Grimme, S., Does Dft-D Estimate Accurate Energies for the Binding of Ligands to Metal Complexes? *Dalton Trans.* **2011,** *40*, 11176-11183.

165. Hirao, H., Which DFT Functional Performs Well in the Calculation of Methylcobalamin? Comparison of the B3LYP and BP86 Functionals and Evaluation of the Impact of Empirical Dispersion Correction. *J. Phys. Chem. A* **2011,** *115*, 9308-9313.

166. Liptak, M. D.; Brunold, T. C., Spectroscopic and Computational Studies of Co^{1+}cobalamin: Spectral and Electronic Properties of the "Superreduced" B_{12} Cofactor. *J. Am. Chem. Soc.* **2006,** *128*, 9144-9156.

167. Kornobis, K.; Ruud, K.; Kozlowski, P. M., Cob(I)Alamin: Insight into the Nature of Electronically Excited States Elucidated Via Quantum Chemical Computations and Analysis of Absorption, Cd and Mcd Data. *J. Phys. Chem. A* **2013,** *117*, 863-876.

168. Randaccio, L.; Geremia, S.; Nardin, G.; Wuerges, J., X-Ray Structural Chemistry of Cobalamins. *Coord. Chem. Rev.* **2006,** *250*, 1332-1350.

169. Randaccio, L.; Furlan, M.; Geremia, S.; Šlouf, M.; Srnova, I.; Toffoli, D., Similarities and Differences between Cobalamins and Cobaloximes. Accurate Structural Determination of Methylcobalamin and of LiCl- and KCl-Containing Cyanocobalamins by Synchrotron Radiation. *Inorg. Chem.* **2000,** *39*, 3403-3413.

170. Kurmaev, E. Z.; Moewes, A.; Ouyang, L.; Randaccio, L.; Rulis, P.; Ching, W. Y.; Bach, M.; Neumann, M., The Electronic Structure and Chemical Bonding of Vitamin B_{12}. *EPL (Europhysics Letters)* **2003,** *62*, 582.

171. Ouyang, L.; Rulis, P.; Ching, W.-Y.; Slouf, M.; Nardin, G.; Randaccio, L., Electronic Structure and Bonding in Hydroxocobalamin. *Spectrochim. Acta, Part A* **2005,** *61*, 1647-1652.

172. Miller, N. A.; Deb, A.; Alonso-Mori, R.; Garabato, B. D.; Glownia, J. M.; Kiefer, L. M.; Koralek, J.; Sikorski, M.; Spears, K. G.; Wiley, T. E.; Zhu, D.; Kozlowski,

P. M.; Kubarych, K. J.; Penner-Hahn, J. E.; Sension, R. J., Polarized Xanes Monitors Femtosecond Structural Evolution of Photoexcited Vitamin B_{12}. *J. Am. Chem. Soc.* **2017,** *139*, 1894-1899.

173. Dunietz, B. D.; Dreuw, A.; Head-Gordon, M., Initial Steps of the Photodissociation of the Co Ligated Heme Group. *J. Phys. Chem. B* **2003,** *107*, 5623-5629.

174. Goumans, T. P. M.; Ehlers, A. W.; van Hemert, M. C.; Rosa, A.; Baerends, E.-J.; Lammertsma, K., Photodissociation of the Phosphine-Substituted Transition Metal Carbonyl Complexes Cr(Co)5L and Fe(Co)4L: A Theoretical Study. *J. Am. Chem. Soc.* **2003,** *125*, 3558-3567.

175. Dreuw, A.; Dunietz, B. D.; Head-Gordon, M., Characterization of the Relevant Excited States in the Photodissociation of Co-Ligated Hemoglobin and Myoglobin. *J. Am. Chem. Soc.* **2002,** *124*, 12070-12071.

176. Dreuw, A.; Fleming, G. R.; Head-Gordon, M., Charge-Transfer State as a Possible Signature of a Zeaxanthin-Chlorophyll Dimer in the Non-Photochemical Quenching Process in Green Plants. *J. Phys. Chem. B* **2003,** *107*, 6500-6503.

177. De Angelis, F.; Car, R.; Spiro, T. G., Role of Ligand Bending in the Photodissociation of O_2 vs Co-Heme: A Time-Dependent Density Functional Study. *J. Am. Chem. Soc.* **2003,** *125*, 15710-15711.

178. Kepp, K. P., O_2 Binding to Heme Is Strongly Facilitated by near-Degeneracy of Electronic States. *Chemphyschem* **2013,** *14*, 3551-3558.

179. Galezowski, W.; Kuta, J.; Kozlowski, P. M., Dft Study of Co−C Bond Cleavage in the Neutral and One-Electron-Reduced Alkyl-Cobalt(III) Phthalocyanines. *J. Phys. Chem. B* **2008,** *112*, 3177-3183.

180. Kozlowski, P. M.; Kuta, J.; Galezowski, W., Reductive Cleavage Mechanism of Methylcobalamin: Elementary Steps of Co-C Bond Breaking. *J. Phys. Chem. B* **2007,** *111*, 7638-7645.

181. Alfonso-Prieto, M.; Biarnés, X.; Kumar, M.; Rovira, C.; Kozlowski, P. M., Reductive Cleavage Mechanism of Co-C Bond in Cobalamin-Dependent Methionine Synthase. *J. Phys. Chem. B* **2010,** *114*, 12965-12971.

182. Mamun, A. A.; Toda, M. J.; Lodowski, P.; Jaworska, M.; Kozlowski, P. M., Mechanism of Light Induced Radical Pair Formation in Coenzyme B_{12}-Dependent Ethanolamine Ammonia-Lyase. *ACS Catal.* **2018,** *8*, 7164-7178.

183. Somogyi, J. C., *Results of Basic Medical Research* 1956; Vol. 1.

184. Freedman, M. D., Warfarin and Other "Anti"-Vitamin K Anticoagulants: Pharmacodynamics and Clinical Use. *Am. J. Therapeut.* **1996,** *3*, 771-783.

185. Hirsh, J.; O'Donnell, M.; Eikelboom, J. W., Beyond Unfractionated Heparin and Warfarin. *Circulation* **2007,** *116*, 552.

186. Zhou, K.; Oetterli René, M.; Brandl, H.; Lyatuu Fredrick, E.; Buckel, W.; Zelder, F., Chemistry and Bioactivity of an Artificial Adenosylpeptide B_{12} Cofactor. *ChemBioChem* **2012,** *13*, 2052-2055.

187. Zhou, K.; Zelder, F., Vitamin B_{12} Mimics Having a Peptide Backbone and Tuneable Coordination and Redox Properties. *Angew. Chem. Int. Ed.* **2010,** *49*, 5178-5180.

188. Banerjee, R.; Gherasim, C.; Padovani, D., The Tinker, Tailor, Soldier in Intracellular B_{12} Trafficking. *Curr. Opin. Chem. Biol.* **2009,** *13*, 484-491.

189. Sierka, M.; Hogekamp, A.; Ahlrichs, R., Fast Evaluation of the Coulomb Potential for Electron Densities Using Multipole Accelerated Resolution of Identity Approximation. *J. Chem. Phys.* **2003,** *118*, 9136-9148.

190. Becke, A. D., Density-Functional Exchange-Energy Approximation with Correct Asymptotic Behavior. *Phys. Rev. A* **1988,** *38*, 3098-3100.

191. F. Weigend, M. H., H. Patzelt, and R. Ahlrichs, RI-MP2: Optimized Auxiliary Basis Sets and Demonstration of Efficiency. *Chem. Phys. Lett.* **1998,** *294*, 143-152.

192. Eichkorn, K.; Weigend, F.; Treutler, O.; Ahlrichs, R., Auxiliary Basis Sets for Main Row Atoms and Transition Metals and their use to Approximate Coulomb Potentials. *Theor. Chem. Acc.* **1997,** *97*, 119-124.

193. Klamt, A.; Schuurmann, G., Cosmo: A New Approach to Dielectric Screening in Solvents with Explicit Expressions for the Screening Energy and Its Gradient. *J. Chem. Soc., Perkin Trans. 2* **1993**, 799-805.

194. Klamt, A.; Jonas, V.; Bürger, T.; Lohrenz, J. C. W., Refinement and Parametrization of Cosmo-Rs. *J. Phys. Chem. A* **1998,** *102*, 5074-5085.

195. TURBOMOLE has been designed by the QuantumChemistry Group, University of Karlsruhe, Germany, since 1988. The following members of the group have made contributions: R. Ahlrichs, M. Ba¨r, H. P. Baron, R. Bauernschmitt, S. Bo¨cker, N. Crawford, P. Deglmann, M. Ehrig, K. Eichkorn, S. Elliott, F. Furche, F. Haase, M. Ha¨ser, C. Ha¨ttig, A. Hellweg, H. Horn, C. Huber, U. Huniar, M. Kattannek, A. Ko¨hn, C. Ko¨lmel, M. Kollwitz, K. S. May, P. Nava, C. Ochsenfeld, H. O¨hm, H. Patzelt, D. Rappoport, O. Rubner, A. Scha¨fer, U. Schneider, M. Sierka, O. Treutler, B. Unterreiner, M. von Arnim, F. Weigend, P. Weis and H. Weiss, http://www.turbomole.com.

196. Schmidt Michael, W.; Baldridge Kim, K.; Boatz Jerry, A.; Elbert Steven, T.; Gordon Mark, S.; Jensen Jan, H.; Koseki, S.; Matsunaga, N.; Nguyen Kiet, A.; Su, S.; Windus Theresa, L.; Dupuis, M.; Montgomery John, A., General Atomic and Molecular Electronic Structure System. *J. Comput. Chem.* **2004,** *14*, 1347-1363.

197. Gianotti, C., Electronic Spectra of B_{12} and Related Systems. In *B_{12}: Volume 1, Chemistry*, Dolphin, D., Ed. Wiley: New York, 1982; pp 393-430.

198. Pratt, J. M., Electronic Structure and Spectra of B_{12}: From Trans Effects to Protein Conformation I and Ii. In *Chemistry and Biochemistry of B_{12}*, Banerjee, R., Ed. Wiley: New York, 1999; pp 113-164.

199. Pratt, J. M., *Inorganic Chemistry of Vitamin B_{12}*. Academic Press: London, New York, 1972.

200. Stich, T. A.; Brooks, A. J.; Buan, N. R.; Brunold, T. C., Spectroscopic and Computational Studies of Co^{3+}-corrinoids: Spectral and Electronic Properties of

the B_{12} Cofactors and Biologically Relevant Precursors. *J. Am. Chem. Soc.* **2003,** *125*, 5897-5914.

201. Smith, W. J.; Oien, N. P.; Hughes, R. M.; Marvin, C. M.; Rodgers, Z. L.; Lee, J.; Lawrence, D. S., Cell-Mediated Assembly of Phototherapeutics. *Angew. Chem. Int. Ed.* **2014,** *53*, 10945-10948.

202. Miller, N. A.; Deb, A.; Alonso-Mori, R.; Glownia, J. M.; Kiefer, L. M.; Konar, A.; Michocki, L. B.; Sikorski, M.; Sofferman, D. L.; Song, S.; Toda, M. J.; Wiley, T. E.; Zhu, D.; Kozlowski, P. M.; Kubarych, K. J.; Penner-Hahn, J. E.; Sension, R. J., Ultrafast X-Ray Absorption near Edge Structure Reveals Ballistic Excited State Structural Dynamics. *J. Phys. Chem. A* **2018,** *122*, 4963-4971.

203. Michocki, L. B.; Miller, N. A.; Alonso-Mori, R.; Britz, A.; Deb, A.; Glownia, J. M.; Kaneshiro, A. K.; Konar, A.; Koralek, J.; Meadows, J. H.; Sofferman, D. L.; Song, S.; Toda, M. J.; van Driel, T. B.; Kozlowski, P. M.; Kubarych, K. J.; Penner-Hahn, J. E.; Sension, R. J., Probing the Excited State of Methylcobalamin Using Polarized Time-Resolved X-Ray Absorption Spectroscopy. *J. Phys. Chem. B* **2019,** *123*, 6042-6048.

204. Wagner, F. B., K.;, New Aspects of the Structure of Corrinoid Coenzymes. *Ann. N.Y. Acad. Sci.* **1964,** *112*, 580.

205. Adler, N.; Medwick, T.; Poznanski, T. J., Reaction of Hydroxocobalamin with Thiols. *J. Am. Chem. Soc.* **1966,** *88*, 5018-5020.

206. Pezacka, E. G., R.; Jacobsen, D. W. , Glutathionylcobalamin as an Intermediate in the Formation of Cobalamin Coenzymes. *Biochem. Biophys. Res. Commun.* **1990,** *169*, 443.

207. Pezacka, E. G., R.; Jacobsen, D. W., Intracellular Cobalamin Metabolism: A Thiolcobalamin Adduct as an Intermediate in Cobalamin Coenzyme Formation. *FASEB J.* **1990,** *4*.

208. Pezacka, E. H. J., D. W.; Luce, K.; Green, R., Glial Cells as a Model for the Role of Cobalamin in the Nervous System: Impaired Synthesis of Cobalamin Coenzymes in Cultured Human Astrocytes Following Short-Term Cobalamin-Deprivation. *Biochem. Biophys. Res. Commun.* **1992,** *184*, 832-839.

209. Pezacka, E. H., Identification and Characterization of Two Enzymes Involved in the Intracellular Metabolism of Cobalamin. Cyanocobalamin B-Ligand Transferase and Microsomal Cob(III)alamin Reductase. *Biochim. Biophys. Acta* **1993,** *1157*, 167-177.

210. Jacobsen, D. W. L.-D., C.; Luce, K.; Green, R., Glutathionylcobalamin (GS-Cbl) Is Found in Cultured and Ascites Leukemia L1210 Cells. . *Fed. Proc.* **1987,** *46*, 1005.

211. Tahara, K.; Matsuzaki, A.; Masuko, T.; Kikuchi, J.-i.; Hisaeda, Y., Synthesis, Characterization, Co–S Bond Reactivity of a Vitamin B_{12} Model Complex Having Pentafluorophenylthiolate as an Axial Ligand. *Dalton Transactions* **2013,** *42*, 6410-6416.

212. Scheuring, E. M.; Sagi, I.; Chance, M. R., Sulfur-Containing Cobalamins: X-Ray Absorption Spectroscopic Characterization. *Biochemistry* **1994,** *33*, 6310-6315.

213. Hannibal, L.; Smith, C. A.; Jacobsen, D. W., The X-Ray Crystal Structure of Glutathionylcobalamin Revealed. *Inorg. Chem.* **2010,** *49*, 9921-9927.

214. Xia, L.; Ballou, D. P.; Marsh, E. N. G., Role of Arg100 in the Active Site of Adenosylcobalamin-Dependent Glutamate Mutase. *Biochemistry* **2004,** *43*, 3238-3245.

215. Hannibal, L.; Axhemi, A.; Glushchenko, A. V.; Moreira, E. S.; Brasch, N. E.; Jacobsen, D. W., Accurate Assessment and Identification of Naturally Occurring Cellular Cobalamins. *Clin. Chem. Lab. Med.* **2008,** *46*, 1739-1746.

216. Suto, R. K.; Brasch, N. E.; Anderson, O. P.; Finke, R. G., Synthesis, Characterization, Solution Stability, and X-Ray Crystal Structure of the Thiolatocobalamin Γ-Glutamylcysteinylcobalamin, a Dipeptide Analogue of Glutathionylcobalamin: Insights into the Enhanced Co-S Bond Stability of the Natural Product Glutathionylcobalamin. *Inorg. Chem.* **2001,** *40*, 2686-2692.

217. Brasch, N. E.; Hsu, T.-L. C.; Doll, K. M.; Finke, R. G., Synthesis and Characterization of Isolable Thiolatocobalamin Complexes Relevant to Coenzyme B_{12}-Dependent Ribonucleoside Triphosphate Reductase. *J. Inorg. Biochem.* **1999,** *76*, 197-209.

218. Reig, A. J.; Conrad, K. S.; Brunold, T. C., Combined Spectroscopic/Computational Studies of Vitamin B_{12} Precursors: Geometric and Electronic Structures of Cobinamides. *Inorg. Chem.* **2012,** *51*, 2867-2879.

219. Eisenberg, A. S.; Likhtina, I. V.; Znamenskiy, V. S.; Birke, R. L., Electronic Spectroscopy and Computational Studies of Glutathionylco(III)balamin. *J. Phys. Chem. A* **2012,** *116*, 6851-6869.

220. Sajan, A.; Birke, R. L., The Reductive Cleavage Mechanism and Complex Stability of Glutathionyl-Cobalamin in Acidic Media. *Electroanalysis* **2016,** *28*, 2743-2753.

221. Ghosh, A. P.; Mamun, A. A.; Lodowski, P.; Jaworska, M.; Kozlowski, P. M., Mechanism of the Photo-Induced Activation of Co-C Bond in Methylcobalamin-Dependent Methionine Synthase. *J. Photochem. Photobiol. B: Biol.* **2018,** *189*, 306-317.

222. Suarez-Moreira, E.; Hannibal, L.; Smith, C. A.; Chavez, R. A.; Jacobsen, D. W.; Brasch, N. E., A Simple, Convenient Method to Synthesize Cobalamins: Synthesis of Homocysteinylcobalamin, N-Acetylcysteinylcobalamin, 2-N-Acetylamino-2-Carbomethoxyethanethiolatocobalamin, Sulfitocobalamin and Nitrocobalamin. *Dalton Trans.* **2006**, 5269.

223. Miller, N. A.; Michocki, L. B.; Konar, A.; Alonso-Mori, R.; Deb, A.; Glownia, J. M.; Sofferman, D. L.; Song, S.; Kozlowski, P. M.; Kubarych, K. J.; Penner-Hahn, J. E.; Sension, R. J., Ultrafast Xanes Monitors Femtosecond Sequential Structural Evolution in Photoexcited Coenzyme B_{12}. *J. Phys. Chem. B* **2020,** *124*, 199-209.

224. Ortiz-Guerrero, J. M.; Polanco, M. C.; Murillo, F. J.; Padmanabhan, S.; Elías-Arnanz, M., Light-Dependent Gene Regulation by a Coenzyme B_{12}-Based Photoreceptor. *Proc. Natl. Acad. Sci.* **2011,** *108*, 7565.

225. Ke, S. C.; Torrent, M.; Museav, D. G.; Morokuma, K.; Warncke, K., Identification of Dimethylbenzimidazole Axial Coordination and Characterization of (14)N Superhyperfine and Nuclear Quadrupole Coupling in Cob(II)alamin Bound to Ethanolamine Deaminase in a Catalytically-Engaged Substrate Radical-Cobalt(II) Biradical State. *Biochemistry* **1999,** *38*, 12681-12689.

226. Olsson, M. H. M.; Søndergaard, C. R.; Rostkowski, M.; Jensen, J. H., Propka3: Consistent Treatment of Internal and Surface Residues in Empirical Pka Predictions. *J. Chem. Theory Comput.* **2011,** *7*, 525-537.

227. Pettersen, E. F.; Goddard, T. D.; Huang, C. C.; Couch, G. S.; Greenblatt, D. M.; Meng, E. C.; Ferrin, T. E., Ucsf Chimera - A Visualization System for Exploratory Research and Analysis. *J. Comput. Chem.* **2004,** *25*, 1605-1612.

228. M. J. Frisch, G. W. T., H. B. Schlegel, G. E. Scuseria, M. A. Robb, J. R. Cheeseman, G. Scalmani, V. Barone, G. A. Petersson, H. Nakatsuji, X. Li, M. Caricato, A. Marenich, J. Bloino, B. G. Janesko, R. Gomperts, B. Mennucci, H. P. Hratchian, J. V. Ortiz, A. F. Izmaylov, J. L. Sonnenberg, D. Williams-Young, F. Ding, F. Lipparini, F. Egidi, J. Goings, B. Peng, A. Petrone, T. Henderson, D. Ranasinghe, V. G. Zakrzewski, J. Gao, N. Rega, G. Zheng, W. Liang, M. Hada, M. Ehara, K. Toyota, R. Fukuda, J. Hasegawa, M. Ishida, T. Nakajima, Y. Honda, O. Kitao, H. Nakai, T. Vreven, K. Throssell, J. A. Montgomery, Jr., J. E. Peralta, F. Ogliaro, M. Bearpark, J. J. Heyd, E. Brothers, K. N. Kudin, V. N. Staroverov, T. Keith, R. Kobayashi, J. Normand, K. Raghavachari, A. Rendell, J. C. Burant, S. S. Iyengar, J. Tomasi, M. Cossi, J. M. Millam, M. Klene, C. Adamo, R. Cammi, J. W. Ochterski, R. L. Martin, K. Morokuma, O. Farkas, J. B. Foresman, and D. J. Fox *Gaussian 09, Revision B*, Gaussian, Inc.: Wallingford CT, 2009.

229. Marques, H. M.; Ngoma, B.; Egan, T. J.; Brown, K. L., Parameters for the Amber Force Field for the Molecular Mechanics Modeling of the Cobalt Corrinoids. *J. Mol. Struct.* **2001,** *561*, 71-91.

230. Altona, C.; Sundaralingam, M., Conformational Analysis of the Sugar Ring in Nucleosides and Nucleotides. A New Description Using the Concept of Pseudorotation. *J. Am. Chem. Soc.* **1972,** *94*, 8205-8212.

231. Schrauzer, G. N.; Holland, R. J., Hydridocobaloximes. *J. Am. Chem. Soc.* **1971,** *93*, 1505-1506.

232. Schrauzer, G. N.; Holland, R. J., Hydridocobalamin and a New Synthesis of Organocobalt Derivatives of Vitamin B_{12}. *J. Am. Chem. Soc.* **1971,** *93*, 4060-4062.

233. Zingales, F., Canziani, F., Chiesa, A., A New Cobalt Hydride. *Inorg. Chem.* **1963,** *2*, 1303-1304.

234. Lexa, D.; Savéant, J.-M., Brönsted Basicity of Vitamin B_{12s}. *J. Chem. Soc., Chem. Commun.* **1975**, 872-874.

235. Lexa, D.; Saveant, J. M., The Electrochemistry of Vitamin B_{12}. *Acc. Chem. Res.* **1983,** *16*, 235-243.

236. Chemaly, S. M.; Pratt, J. M., The Chemistry of Vitamin B_{12}. Part 24. Evidence for Hydride Complexes of Cobalt(III) Corrinoids. *J. Chem. Soc., Dalton Trans.* **1984**, 595-599.

237. Baldwin, D. A.; Betterton, E. A.; Chemaly, S. M.; Pratt, J. M., The Chemistry of Vitamin B_{12}. Part 25. Mechanism of the B-Elimination of Olefins from Alkylcorrinoids; Evidence for an Initial Homolytic Fission of the Co-C Bond. *J. Chem. Soc., Dalton Trans.* **1985**, 1613-1618.

238. Estes, D. P.; Grills, D. C.; Norton, J. R., The Reaction of Cobaloximes with Hydrogen: Products and Thermodynamics. *J. Am. Chem. Soc.* **2014,** *136*, 17362-17365.

239. Lacy, D. C.; Roberts, G. M.; Peters, J. C., The Cobalt Hydride That Never Was: Revisiting Schrauzer's "Hydridocobaloxime". *J. Am. Chem. Soc.* **2015,** *137*, 4860-4864.

240. Casida, M. E., *Recent Developments and Application of Modern Density Functional Theory*. Elsvevier: Amsterdam, 1996.

241. Weigend, F. H., C.; Ahlrichs, R. , Fully Optimized Contracted Gaussian Basis Sets of Triple Zeta Valence Quality for Atoms Li to Kr. *The Journal of Chemical Physics* **1994,** *100*, 5829-5835.

242. Rovira, C.; Kozlowski, P. M., First Principles Study of Coenzyme B_{12}. Crystal Packing Forces Effect on Axial Bond Lengths. *J. Phys. Chem. B* **2007,** *111*, 3251-3257.

243. Andruniow, T.; Kozlowski, P. M.; Zgierski, M. Z., Theoretical Analysis of Electronic Absorption Spectra of Vitamin B_{12} Models. *J. Chem. Phys.* **2001,** *115*, 7522-7533.

244. Barone, V.; Adamo, C., First-Row Transition-Metal Hydrides: A Challenging Playground for New Theoretical Approaches. *Int. J. Quantum Chem* **1997,** *61*, 443-451.

245. Anglada, J.; Bruna, P. J.; Grein, F., Theoretical Study of Low‐Lying Electronic States of CoH^+. *J. Chem. Phys.* **1990,** *92*, 6732-6741.

246. Blomberg, M. R. A.; Siegbahn, P. E. M.; Svensson, M., Comparisons of Results from Parametrized Configuration Interaction (PCI‐80) and from Hybrid Density Functional Theory with Experiments for First Row Transition Metal Compounds. *J. Chem. Phys.* **1996,** *104*, 9546-9554.

247. Barone, V.; Adamo, C.; Mele, F., Comparison of Convetional and Hybrid Density Functional Approaches. Cationic Hydrides of First-Row Transition Metals as a Case Study. *Chem. Phys. Lett.* **1996,** *249*, 290-296.

248. Sakellaris, C. N.; Mavridis, A., First Principles Study of Cobalt Hydride, Coh, and its Ions CoH^+ and CoH^-. *J. Chem. Phys.* **2012,** *137*, 034309.

249. Halpern, J.; Kim, S. H.; Leung, T. W., Cobalt-Carbon Bond Dissociation Energy of Coenzyme B_{12}. *J. Am. Chem. Soc.* **1984,** *106*, 8317-8319.

250. Koenig, T. W.; Hay, B. P.; Finke, R. G., Cage Effects in Organotransition Metal Chemistry: Their Importance in the Kinetic Estimation of Bond Dissociation Energies in Solution. *Polyhedron* **1988,** *7*, 1499-1516.

251. Chen, H.; Yan, H.; Luo, L.; Cui, X.; Tang, W., Study of the Thermal Decomposition, Axial-Base Equilibrium, and Co-C Bond Dissociation Energy of

2′,5′-dideoxyadenosylcobalamin in Ethylene Glycol. *J. Inorg. Biochem.* **1997,** *66*, 219-225.

252. Li, G.; Zhang, F. F.; Chen, H.; Yin, H. F.; Chen, H. L.; Zhang, S. Y., Determination of Co-C Bond Dissociation Energies for Organocobalt Complexes Related to Coenzyme B_{12} Using Photoacoustic Calorimetry. *J. Chem. Soc., Dalton Trans.* **2002**, 105-110.

253. Chen, H.; Li, G.; Zhang, F. F.; Sun, L.; Chen, H. L.; Zhang, S. Y., Co C Bond Dissociation Energy and Reaction Volume Change of 2′,5′-dideoxyadenosylcobalamin Studied by Laser-Induced Time-Resolved Photoacoustic Calorimetry. *Spectrochim. Acta, Part A* **2003,** *59*, 2767-2774.

254. Weinhold, F.; Landis, C. R., *Valency and Bonding: A Natural Bond Orbital Donor-Acceptor Perspective*. Cambridge University Press: Cambridge, 2005.

255. Foster, J. P.; Weinhold, F., Natural Hybrid Orbitals. *J. Am. Chem. Soc.* **1980,** *102*, 7211-7218.

256. Reed, A. E.; Curtiss, L. A.; Weinhold, F., Intermolecular Interactions from a Natural Bond Orbital, Donor-Acceptor Viewpoint. *Chem. Rev.* **1988,** *88*, 899-926.

257. Reed, A. E.; Weinhold, F., Natural Localized Molecular Orbitals. *J. Chem. Phys.* **1985,** *83*, 1736-1740.

258. Glendening, E. D.; Landis, C. R.; Weinhold, F., Natural Bond Orbital Methods. *WIREs Comput. Mol. Sci.* **2012,** *2*, 1-42.

259. Jarrett, J. T.; Drennan, C. L.; Amaratunga, M.; Scholten, J. D.; Ludwig, M. L.; Matthews, R. G., A Protein Radical Cage Slows Photolysis of Methylcobalamin in Methionine Synthase from Escherichia Coli. *Biorg. Med. Chem.* **1996,** *4*, 1237-1246.

260. Garr, C. D.; Finke, R. G., Radical Cage Effects in Adocobinamide (Axial-Base-Off Coenzyme B_{12}: A Simple Method for Trapping [$Ado^{\cdot\cdot}Co^{II}$] Radical Pairs. A New β-H Elimination Product from the Radical Pair and Measurement of an Unprecedentedly Large Cage-Recombination Efficiency Factor, $Fc \geq 0.94$. *J. Am. Chem. Soc.* **1992,** *114*, 10440-10445.

261. Khoroshun, D. V.; Warncke, K.; Ke, S. C.; Musaev, D. G.; Morokuma, K., Internal Degrees of Freedom, Structural Motifs, and Conformational Energetics of the 5'-Deoxyadenosyl Radical: Implications for Function in Adenosylcobalamin-Dependent Enzymes. A Computational Study. *J. Am. Chem. Soc.* **2003,** *125*, 570-579.

262. Yang, H.; McDaniel, E. C.; Impano, S.; Byer, A. S.; Jodts, R. J.; Yokoyama, K.; Broderick, W. E.; Broderick, J. B.; Hoffman, B. M., The Elusive 5′-Deoxyadenosyl Radical: Captured and Characterized by Electron Paramagnetic Resonance and Electron Nuclear Double Resonance Spectroscopies. *J. Am. Chem. Soc.* **2019,** *141*, 12139-12146.

263. Masuda, J.; Shibata, N.; Morimoto, Y.; Toraya, T.; Yasuoka, N., How a Protein Generates a Catalytic Radical from Coenzyme B_{12}: X-Ray Structure of a Diol-Dehydratase-Adeninylpentylcobalamin Complex. *Structure* **2000,** *8*, 775-788.

APPENDIX

APPENDIX LIST OF TABLES

APPENDIX LIST OF FIGURES

Appendix [Chapter 2]

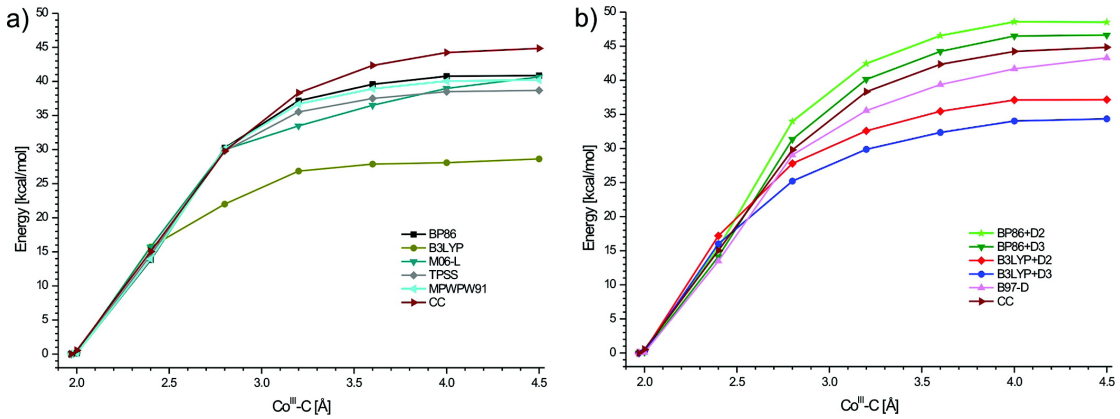

Figure A.2.1. Comparison of Co-C bond dissociation curves computed using selected DFT functionals without (a) and with(b) a dispersion correction with a reference coupled cluster (CR-CC(2,3)/CCSD method denoted as CC) curve for MeCbl model (Im-[Co^{III}-corrin]-Me+). 6-31G(d) basis set was used in all calculations. From: Kozlowski P.M., *et al*. The cobalt-methyl bond dissociation in methylcobalamin […] *J. Chem. Theo. Comput*. 2012, 8, 1870-1894.

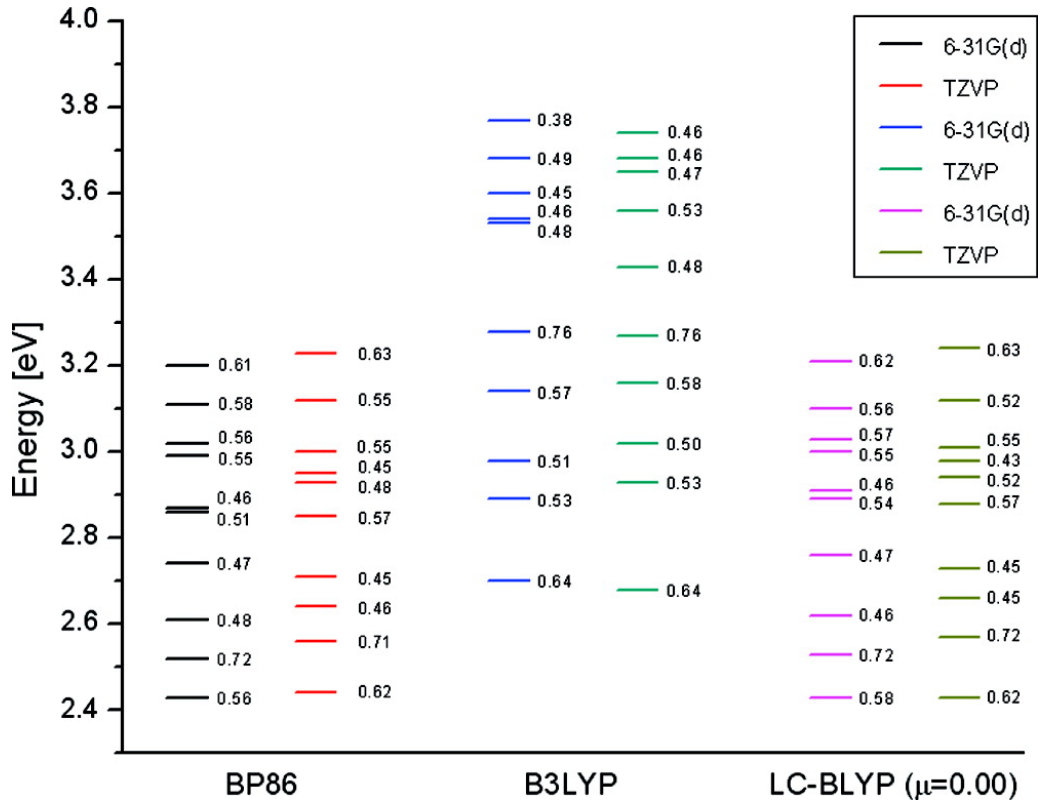

Figure A.2.2. TD-DFT based ten lowest electronic transitions of Im-[CoIII(corrin)]-CN+ calculated with three different density functionals and basis sets (see inset) together with the corresponding Λ diagnostic values (presented as numbers). From: Kornobis K., et al. Electronically excited states of vitamin B_{12} […] J. Phys. Chem. A 2011, 115, 1280-1292.

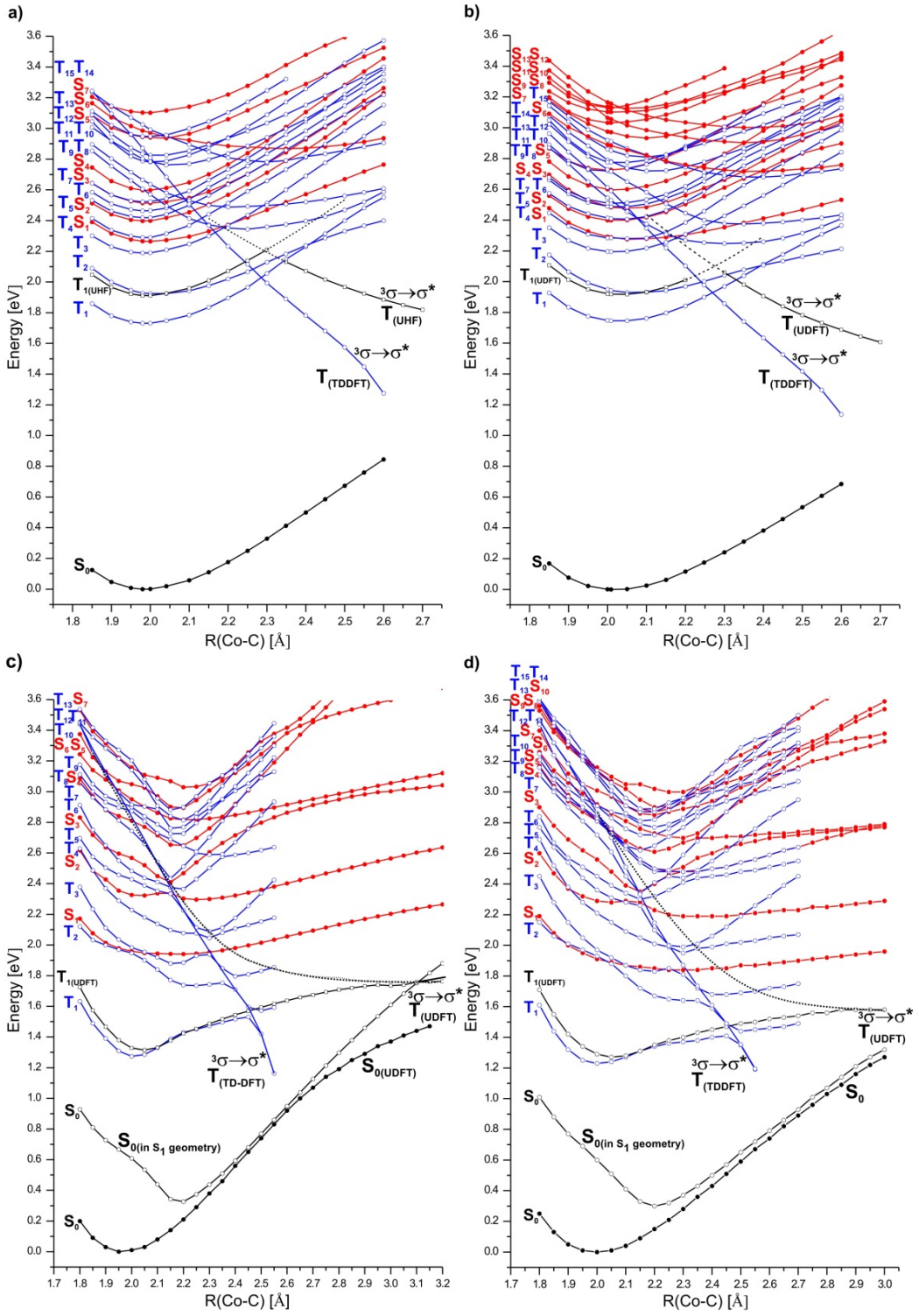

Figure A.2.3. Potential energy curves of the ground and lowest-excited states (singlet and triplet) of the (a) Im-[Co^{III}(corrin)]-Me^+, (b) Im-[Co^{III}(corrin)]-Ado^+, (c) [Co^{III}(corrin)]-Me^+ and (d) [Co^{III}(corrin)]-Ado^+ model complexes along the Co−C bond stretch computed at the ground-state optimized geometry (a, b) and at the S_1 state optimized geometry (c, d). The dotted line corresponds to the approximate course of the triplet excited state.

Appendix [Chapter 3]

Table A.3.1. Selected, optimized geometric parameters for Im-[Co^{III}(corrin)]-$EtPh^+$ model complex in *base-on* and *base-off* form, in the ground state S_0 and in the excited state S_1.

	Im-[Co^{III}(corrin)]-$EtPh^+$ *base-on*		[Co^{III}(corrin)]-$EtPh^+$ *base-off*			
Parameter	S_0	S_1	S_0	$S_{1(min1)}$	$S_{1(min2)}$	Exp.[a)]
r[Å]						
Co - C_{1Ph}	1.973	1.927	1.939	1.847	2.018	1.981
Co - N	2.197	2.107				2.230
Co - N_{21}	1.882	1.892	1.869	1.894	1.892	1.879
Co - N_{22}	1.942	1.980	1.927	1.943	1.929	1.923
Co - N_{23}	1.938	1.976	1.925	1.960	1.976	1.915
Co - N_{24}	1.880	1.887	1.866	1.894	1.883	1.886
Valence angle[^{O}]						
C_{1Ph} -Co - N	179.4	171.1				176.5
N_{21} – Co - C_{1Ph}	93.6	97.9	97.7	104.6	112.4	93.5
N_{22} – Co - C_{1Ph}	90.9	87.8	94.8	97.1	94.2	91.8
N_{23} – Co - C_{1Ph}	92.0	88.5	96.3	98.7	101.2	91.5
N_{24} – Co - C_{1Ph}	88.3	93.0	91.4	93.3	93.1	86.6
N_{21} – Co - N	87.0	89.0				89.8
N_{22} – Co - N	89.1	86.5				87.2
N_{23} - Co - N	87.4	85.2				85.4
N_{24} - Co - N	91.7	93.5				94.8
N_{21} – Co - N_{22}	91.1	90.7	90.6	89.5	90.5	90.0
N_{22} - Co - N_{23}	94.9	95.9	94.1	95.0	93.3	96.6
N_{23} – Co - N_{24}	91.7	91.2	91.6	89.9	90.3	90.3
N_{24} - Co - N_{21}	82.4	82.1	82.2	81.4	81.9	83.3
Co - N_{21} - C_1	116.5	116.4	117.5	118.0	117.7	116.4
Co - N_{22} - C_9	124.4	122.8	125.1	123.9	125.3	122.7
Co - N_{23} - C_{11}	124.6	123.0	125.3	123.1	123.5	123.6
Co - N_{24} - C_{19}	116.6	116.3	116.7	115.6	115.3	113.5
N_{21} - Co – N_{23}	171.7	170.9	164.7	155.6	145.8	172.9
N_{22} - Co – N_{24}	173.4	172.8	171.1	167.6	171.1	171.6
Dihedral angle [^{O}]						
C_{10} – Co - C_{1Ph} - C_{2Ph}	95.7	96.2	94.9	94.5	81.9	94.7
N_{21} – N_{22} – N_{23} - Co	-3.9	-4.3	-10.0	-16.6	-23.1	-3.6
N_{21} – N_{22} – N_{23} - N_{24}	-4.3	-3.9	-5.3	-8.7	-17.5	-4.6
Co - N_{22} - C_9 - C_{10}	1.3	2.2	4.1	6.8	7.6	-5.8
Co - N_{22} - C_6 - C_5	-4.3	-3.6	-7.4	-7.7	-9.9	-8.9
Co - N_{23} - C_{14} - C_{15}	-2.5	-2.5	1.4	4.8	2.8	-5.3
Co - N_{21} - C_1 - C_{19}	32.1	32.5	28.4	20.5	22.3	33.6
N_{21} – C_1 – C_{19} - N_{24}	-39.0	-39.8	-37.5	-35.4	-36.8	-44.1
N_{21} – Co - N_{24} - C_{19}	-14.4	-14.6	-17.6	-23.8	-23.6	-18.0
C_1 – C_2 – C_3 - C_4	-26.1	-26.7	-27.9	-28.0	-23.9	-32.3
C_6 – C_7 – C_8 - C_9	-7.3	-7.0	-6.9	-7.8	-6.8	-25.6
C_{11} – C_{12} – C_{13} - C_{14}	-2.8	-4.3	-3.0	-3.2	-9.6	-24.1
C_{16} – C_{17} - C_{18} - C_{19}	-24.6	-26.2	-24.4	-24.2	-18.7	-30.2

[a)] Ruetz, M.; Gherasim, C.; Gruber, K.; Fedosov, S.; Banerjee, R.; Kräutler, B. *Angew. Chem., Int. Ed.* 2013, 52, 2606–2610. Experimental data is for base-on form of EtPhCbl.

Table A.3.2. Selected, optimized geometric parameters for Im-[Co^{III}(corrin)]-$PhEty^+$ model complex in *base-on* and *base-off* form, in the S_0 and S_1 states.

	Im-[Co^{III}(corrin)]-$PhEty^+$ *(base-on)*		[Co^{III}(corrin)]-$PhEty^+$ (*base-off)*		
Parameter	S_0	S_1	S_0	S_{1min}	Exp.[28]
r[Å]					
Co - C_{1Ety}	1.860	1.775	1.820	1.857	1.861
C_{1Ety} - C_{2Ety}	1.229	1.256	1.227	1.256	1.209
Co - N	2.084	2.057	-	-	2.084
Co - N_{21}	1.890	1.914	1.871	1.912	1.881
Co - N_{22}	1.945	1.963	1.923	1.932	1.921
Co - N_{23}	1.946	1.971	1.923	1.984	1.914
Co - N_{24}	1.886	1.909	1.865	1.884	1.890
Valence angle[^{O}]					
C_{1Ph} -Co - N	179.6	179.3			176.5
C_{1Ety} - Co - N	179.2	178.7			178.6
Co – C_{1Ety} - C_{2Ety}	178.4	179.1	179.1	179.3	172.1
N_{21} – Co - C_{1Ph}	91.1	93.5	98.4	108.5	85.2
N_{22} – Co - C_{1Ph}	89.4	89.9	92.5	94.8	91.9
N_{23} – Co - C_{1Ph}	91.7	92.4	94.9	103.0	95.2
N_{24} – Co - C_{1Ph}	87.1	89.0	92.2	94.7	82.9
N_{21} – Co - N	88.5	87.2			92.1
N_{22} – Co - N	90.7	89.9			90.3
N_{23} - Co - N	88.7	87.0			87.2
N_{24} - Co - N	92.8	91.3			94.6
N_{21} – Co - N_{22}	91.4	91.2	90.7	89.8	90.1
N_{22} - Co - N_{23}	95.0	96.0	94.6	93.2	96.5
N_{23} – Co - N_{24}	91.5	91.3	91.4	90.4	90.0
N_{24} - Co - N_{21}	82.2	81.6	82.3	81.6	83.5
Co - N_{21} - C_1	116.7	116.8	117.5	117.7	116.8
Co - N_{22} - C_9	124.3	123.3	124.9	125.4	122.8
Co - N_{23} - C_{11}	124.2	122.8	124.9	124.1	123.7
Co - N_{24} - C_{19}	116.3	115.9	116.4	116.1	113.7
N_{21} - Co – N_{23}	173.0	170.7	165.5	148.0	173.4
N_{22} - Co – N_{24}	172.3	172.6	172.0	168.8	172.1
Dihedral angle [^{O}]					
C_{10} – Co - C_{1Ph} - C_{2Ph}	22.4	22.9	22.1	27.9	105.7
N_{21} – N_{22} – N_{23} - Co	-1.9	-4.0	-9.3	-21.9	-0.5
N_{21} – N_{22} – N_{23} - N_{24}	-4.2	-4.6	-5.7	-14.6	-3.7
Co - N_{22} - C_9 - C_{10}	1.6	0.4	5.5	7.5	-8.2
Co - N_{22} - C_6 - C_5	-6.9	-6.6	-10.0	-13.8	-10.9
Co - N_{23} - C_{14} - C_{15}	-0.7	-0.8	3.8	3.6	-4.1
Co - N_{21} - C_1 - C_{19}	32.5	30.2	28.1	23.2	32.9
N_{21} – C_1 – C_{19} - N_{24}	-39.1	-39.6	-37.5	-36.1	-41.9
N_{21} – Co - N_{24} - C_{19}	-13.7	-16.7	-17.6	-21.5	-15.8
C_1 – C_2 – C_3 - C_4	-24.4	-25.2	-26.9	-25.6	-30.1
C_6 – C_7 – C_8 - C_9	-7.3	-7.9	-7.2	-10.1	-28.3
C_{11} – C_{12} – C_{13} - C_{14}	-1.2	-0.9	-3.6	-7.4	-26.9
C_{16} – C_{17} - C_{18} - C_{19}	-26.5	-26.1	-25.3	-22.5	-32.8

Table A.3.3. The lowest twenty-five vertical singlet states for Im-[Co^{III}(corrin)]-$EtPh^+$ (*base-on*) from TD-DFT/TZVPP calculations with solvent COSMO/H_2O model.

	E [eV]	λ [nm]	*f*	%	Character	
S_1	2.22	557.5	0.0002	50.9	140 → 142 H-1 → L	$\pi + d_{xz} \rightarrow \pi^*$
				46.3	139 → 142 H-2 → L	$d_{xz} + \pi_{Ph} \rightarrow \pi^*$
S_2	2.44	506.9	0.0314	73.5	141 → 142 H → L	$d_{yz} + \pi \rightarrow \pi^*$
				11.8	140 → 142 H-1 → L	$\pi + d_{xz} \rightarrow \pi^*$
S_3	2.48	500.3	0.0462	46.4	139 → 142 H-2 → L	$d_{xz} + \pi_{Ph} \rightarrow \pi^*$
				34.6	140 → 142 H-1 → L	$\pi + d_{xz} \rightarrow \pi^*$
				11.3	141 → 142 H → L	$d_{yz} + \pi \rightarrow \pi^*$
S_4	2.66	466.6	0.0004	97.2	138 → 142 H-3 → L	$d_{x^2-y^2} \rightarrow \pi^*$
S_5	2.90	427.3	0.0002	48.6	141 → 143 H → L+1	$d_{yz} + \pi \rightarrow d_{xy}$ - n
				24.7	137 → 142 H-4 → L	$\pi_{Ph} + d_{xz} \rightarrow \pi^*$
				13.4	141 → 144 H → L+2	$d_{yz} + \pi \rightarrow d_{xy}$ - n + π^*
				11.0	139 → 143 H-2 → L+1	$d_{xz} + \pi_{Ph} \rightarrow d_{xy}$ - n
S_6	2.93	423.4	0.0033	75.7	140 → 143 H-1 → L+1	$\pi + d_{xz} \rightarrow d_{xy}$ - n
				12.6	140 → 144 H-1 → L+2	$\pi + d_{xz} \rightarrow d_{xy}$ - n + π^*
S_7	2.97	416.8	0.0071	45.5	137 → 142 H-4 → L	$\pi_{Ph} + d_{xz} \rightarrow \pi^*$
				19.5	139 → 143 H-2 → L+1	$d_{xz} + \pi_{Ph} \rightarrow d_{xy}$ - n
				12.4	141 → 143 H → L+1	$d_{yz} + \pi \rightarrow d_{xy}$ - n
S_8	3.03	409.1	0.0002	86.5	136 → 142 H-5 → L	$\pi_{Ph} + \pi_{Im} \rightarrow \pi^*$
S_9	3.05	407.1	0.0023	36.3	141 → 145 H → L+3	$d_{yz} + \pi \rightarrow \sigma^*(d_z^2)$ - n
				26.9	141 → 144 H → L+2	$d_{yz} + \pi \rightarrow d_{xy}$ - n + π^*
S_{10}	3.07	403.7	0.0008	81.1	135 → 142 H-6 → L	$\pi_{Ph} + \pi_{Im} \rightarrow \pi^*$
S_{11}	3.11	398.2	0.0128	29.3	139 → 143 H-2 → L+1	$d_{xz} + \pi_{Ph} \rightarrow d_{xy}$ - n
				23.0	139 → 144 H-2 → L+2	$d_{xz} + \pi_{Ph} \rightarrow d_{xy}$ - n + π^*
				12.6	141 → 143 H → L+1	$d_{yz} + \pi \rightarrow d_{xy}$ - n
S_{12}	3.16	392.5	0.0083	63.1	140 → 145 H-1 → L+3	$\pi + d_{xz} \rightarrow \sigma^*(d_z^2)$ - n

S_{13}	3.18	390.1	0.0178	32.9	141 → 145	H → L+3	$d_{yz} + \pi \rightarrow \sigma^*(d_z^2)$ - n
				22.7	141 → 144	H → L+2	$d_{yz} + \pi \rightarrow d_{xy}$ - n + π^*
				12.0	137 → 142	H-4 → L	$\pi_{Ph} + d_{xz} \rightarrow \pi^*$
S_{14}	3.22	384.8	0.0133	31.1	134 → 142	H-7 → L	$\pi + d_{yz} \rightarrow \pi^*$
				23.2	140 → 144	H-1 → L+2	$\pi + d_{xz} \rightarrow d_{xy}$ - n + π^*
				17.6	139 → 145	H-2 → L+3	$d_{xz} + \pi_{Ph} \rightarrow \sigma^*(d_z^2$ - n)
S_{15}	3.30	375.7	0.0046	42.4	139 → 144	H-2 → L+2	$d_{xz} + \pi_{Ph} \rightarrow d_{xy}$ - n + π^*
				14.1	140 → 144	H-1 → L+2	$\pi + d_{xz} \rightarrow d_{xy}$-n + π^*
S_{16}	3.35	370.5	0.0206	47.1	139 → 145	H-2 → L+3	$d_{xz} + \pi_{Ph} \rightarrow \sigma^*(d_z^2)$ - n
				20.7	140 → 144	H-1 → L+2	$\pi + d_{xz} \rightarrow d_{xy}$ - n + π^*
S_{17}	3.43	361.1	0.0011	59.2	138 → 143	H-3 → L+1	$d_{x^2-y^2} \rightarrow d_{xy}$ - n
				25.8	138 → 144	H-3 → L+2	$d_{x^2-y^2} \rightarrow d_{xy}$ - n + π^*
S_{18}	3.54	349.8	0.0010	57.1	138 → 144	H-3 → L+2	$d_{x^2-y^2} \rightarrow d_{xy}$ - n + π^*
				17.7	138 → 145	H-3 → L+3	$d_{x^2-y^2} \rightarrow \sigma^*(d_z^2)$ - n
				10.5	138 → 143	H-3 → L+1	$d_{x^2-y^2} \rightarrow d_{xy}$ - n
S_{19}	3.62	342.6	0.0784	43.1	134 → 142	H-7 → L	$\pi + d_{yz} \rightarrow \pi^*$
S_{20}	3.68	337.3	0.0088	66.9	133 → 142	H-8 → L	$\sigma (d_z^2) \rightarrow \pi^*$
				25.0	140 → 146	H-1 → L+4	$\pi + d_{xz} \rightarrow \pi^*$
S_{21}	3.71	334.4	0.0037	42.6	137 → 143	H-4 → L+1	$\pi_{Ph} + d_{xz} \rightarrow d_{xy}$ - n
				40.7	136 → 143	H-5 → L+1	$\pi_{Ph} + \pi_{Im} \rightarrow d_{xy}$ - n
S_{22}	3.75	330.5	0.0001	47.6	136 → 143	H-5 → L+1	$\pi_{Ph} + \pi_{Im} \rightarrow d_{xy}$ - n
				19.9	135 → 143	H-6 → L+1	$\pi_{Ph} + \pi_{Im} \rightarrow d_{xy}$ - n
				18.0	137 → 143	H-4 → L+1	$\pi_{Ph} + d_{xz} \rightarrow d_{xy}$ - n
S_{23}	3.77	328.4	0.0125	59.3	135 → 143	H-6 → L+1	$\pi_{Ph} + \pi_{Im} \rightarrow d_{xy}$ - n
				23.3	141 → 146	H → L+4	$d_{yz} + \pi \rightarrow \pi^*$
S_{24}	3.81	325.7	0.0318	32.4	141 → 146	H → L+4	$d_{yz} + \pi \rightarrow \pi^*$
				18.1	135 → 143	H-6 → L+1	$\pi_{Ph} + \pi_{Im} \rightarrow d_{xy}$ - n

S_{25}	3.82	324.4	0.0392	60.9	139 → 146 H-2 → L+4	$d_{xz} + \pi_{Ph} \rightarrow \pi^*$

Table A.3.4. The lowest twenty-five vertical singlet states and the first adiabatic excited state for Im-[Co^{III}(corrin)]-$PhEty^+$ (*base-on*) received from TD-DFT/TZVPP calculations with solvent COSMO/H_2O model.

	E [eV]	λ [nm]	*f*	%	Character	
S_1	2.05	603.1	0.0019	93.2	139 → 140 H → L	$\pi_{PhEty} + d_{yz} \rightarrow \pi^*$
S_2	2.33	531.1	0.0029	59.9	137 → 140 H-2 → L	$\pi_{Ety} + d_{yz} \rightarrow \pi^*$
				22.6	138 → 140 H-1 → L	$\pi + d_z^2 \rightarrow \pi^*$
				14.3	136 → 140 H-3 → L	$\pi_{Ety} + d_{yz} + \pi \rightarrow \pi^*$
S_3	2.51	493.6	0.0558	66.5	138 → 140 H-1 → L	$\pi + d_z^2 \rightarrow \pi^*$
				21.6	137 → 140 H-2 → L	$\pi_{Ety} + d_{yz} \rightarrow \pi^*$
S_4	2.56	483.9	0.0034	87.9	139 → 141 H → L+1	$\pi_{PhEty} + d_{yz} \rightarrow d_{xy}$ - n
S_5	2.69	460.1	0.0135	44.7	138 → 141 H-1 → L+1	$\pi + d_z^2 \rightarrow d_{xy}$ -n
				40.1	136 → 140 H-3 → L	$\pi_{Ety} + d_{yz} + \pi \rightarrow \pi^*$
S_6	2.75	450.5	0.0155	43.4	138 → 141 H-1 → L+1	$\pi + d_z^2 \rightarrow d_{xy}$ - n
				28.1	136 → 140 H-3 → L	$\pi_{Ety} + d_{yz} + \pi \rightarrow \pi^*$
S_7	2.78	445.1	0.0013	84.2	139 → 142 H → L+2	$\pi_{PhEty} + d_{yz} \rightarrow \sigma^*(d_z^2)$ - n
S_8	2.89	428.0	0.0040	40.0	137 → 141 H-2 → L+1	$\pi_{Ety} + d_{yz} \rightarrow d_{xy}$ - n
				35.6	135 → 140 H-4 → L	$d_x^2 - {}_y^2 \rightarrow \pi^*$
S_9	2.91	425.9	0.0015	77.2	139 → 143 H → L+3	$\pi_{PhEty} + d_{yz} \rightarrow \pi^* + d_{xz}$
S_{10}	2.95	420.1	0.0014	41.6	135 → 140 H-4 → L	$d_x^2 - {}_y^2 \rightarrow \pi^*$
				20.2	137 → 141 H-2 → L+1	$\pi_{Ety} + d_{yz} \rightarrow d_{xy}$ - n
				18.6	136 → 141 H-3 → L+1	$\pi_{Ety} + d_{yz} + \pi \rightarrow d_{xy}$ - n
S_{11}	2.99	414.7	0.0104	61.0	138 → 142 H-1 → L+2	$\pi + d_z^2 \rightarrow \sigma^*(d_z^2)$ - n
				14.7	138 → 143 H-1 → L+3	$\pi + d_z^2 \rightarrow \pi^*$
S_{12}	3.03	409.5	0.0031	77.3	137 → 142 H-2 → L+2	$\pi_{Ety} + d_{yz} \rightarrow \sigma^*(d_z^2)$ - n
				10.6	137 → 141 H-2 → L+1	$\pi_{Ety} + d_{yz} \rightarrow d_{xy}$ - n
S_{13}	3.09	401.4	0.0007	62.7	136 → 141 H-3 → L+1	$\pi_{Ety} + d_{yz} + \pi \rightarrow d_{xy}$ - n
				12.3	137 → 141 H-2 → L+1	$\pi_{Ety} + d_{yz} \rightarrow d_{xy}$ - n
S_{14}	3.10	399.4	0.0029	81.9	134 → 140 H-5 → L	$\pi_{Ety} + \pi_{Im} + d_{xz} \rightarrow \pi^*$
				12.0	133 → 140 H-6 → L	$\pi_{Ety} + \pi_{Im} + d_{xz} \rightarrow \pi^*$

S_{15}	3.21	386.7	0.0084	52.8	133 → 140 H-6 → L	$\pi_{Ety} + \pi_{Im} + d_{xz} \rightarrow \pi^*$
				25.7	137 → 143 H-2 → L+3	$\pi_{Ety} + d_{yz} \rightarrow \pi^*$
S_{16}	3.27	378.8	0.0003	49.0	136 → 142 H-3 → L+2	$\pi_{Ety} + d_{yz} + \pi \rightarrow \sigma^*(d_z^2)$ - n
				36.9	137 → 143 H-2 → L+3	$\pi_{Ety} + d_{yz} \rightarrow \pi^*$
S_{17}	3.34	371.4	0.0248	31.3	136 → 142 H-3 → L+2	$\pi_{Ety} + d_{yz} + \pi \rightarrow \sigma^*(d_z^2)$ - n
				22.8	137 → 143 H-2 → L+3	$\pi_{Ety} + d_{yz} \rightarrow \pi^*$
				14.9	133 → 140 H-6 → L	$\pi_{Ety} + \pi_{Im} + d_{xz} \rightarrow \pi^*$
S_{18}	3.36	368.6	0.0000	99.9	132 → 140 H-7 → L	$\pi_{Ph} \rightarrow \pi^*$
S_{19}	3.44	360.6	0.0742	44.8	138 → 143 H-1 → L+3	$\pi + d_z^2 \rightarrow \pi^*$
				11.3	131 → 140 H-8 → L	$\pi + d_{yz} \rightarrow \pi^*$
				11.3	135 → 141 H-4 → L+1	$d_{x^2-y^2} \rightarrow d_{xy}$ - n
S_{20}	3.46	357.7	0.0194	70.8	135 → 141 H-4 → L+1	$d_{x^2-y^2} \rightarrow d_{xy}$ - n
S_{21}	3.50	353.7	0.0099	74.3	136 → 143 H-3 → L+3	$\pi_{Ety} + d_{yz} + \pi \rightarrow \pi^*$
S_{22}	3.60	344.2	0.0019	75.9	134 → 141 H-5 → L+1	$\pi_{Ety} + \pi_{Im} + d_{xz} \rightarrow d_{xy}$ - n
				15.3	133 → 141 H-6 → L+1	$\pi_{Ety} + \pi_{Im} + d_{xz} \rightarrow d_{xy}$ - n
S_{23}	3.60	343.8	0.0173	73.4	139 → 145 H → L+5	$\pi_{PhEty} + d_{yz} \rightarrow \pi^*$
S_{24}	3.64	340.4	0.0041	88.4	138 → 144 H-1 → L+4	$\pi + d_z^2 \rightarrow \pi^*_{PhEty}$
S_{25}	3.69	335.6	0.0338	61.5	137 → 144 H-2 → L+4	$\pi_{Ety} + d_{yz} \rightarrow \pi^*_{PhEty}$

Table A.3.5. The lowest ten vertical singlet states and for [Co^{III}(corrin)]-$EtPh^+$ (*base-off*) received from TD-DFT/TZVPP calculations with solvent COSMO/H_2O model.

	E [eV]	λ [nm]	*f*	%	Character	
S_1	2.19	566.8	0.0006	81.8	122 → 124 H-1 → L	$\pi_{Ph} + d_{xz} \rightarrow \pi^*$
				14.8	123 → 125 H → L+1	$d_{yz} + \pi \rightarrow \sigma^*(z^2)$
S_2	2.22	558.5	0.0064	62.3	123 → 125 H → L+1	$d_{yz} + \pi \rightarrow \sigma^*(d_z^2)$
				13.6	122 → 124 H-1 → L	$\pi_{Ph} + d_{xz} \rightarrow \pi^*$
				13.5	123 → 124 H → L	$d_{yz} + \pi \rightarrow \pi^*$
S_3	2.33	531.3	0.0040	84.9	122 → 125 H-1 → L+1	$\pi_{Ph} + d_{xz} \rightarrow \sigma^*(d_z^2)$
S_4	2.42	512.7	0.0307	67.4	123 → 124 H → L	$d_{yz} + \pi \rightarrow \pi^*$
				13.4	123 → 125 H → L+1	$d_{yz} + \pi \rightarrow \sigma^*(d_z^2)$
S_5	2.69	461.26	0.0004	90.8	121 → 124 H-2 → L	$d_{xy} \rightarrow \pi^*$
S_6	2.94	420.9	0.0078	31.3	120 → 125 H-3 → L+1	$\pi + d_{yz} \rightarrow \sigma^*(d_z^2)$
				24.8	121 → 125 H-2 → L+1	$d_{xy} \rightarrow \sigma^*(d_z^2)$
				17.0	122 → 127 H-1 → L+3	$\pi_{Ph} + d_{xz} \rightarrow \pi^* + d_{xz}$
S_7	2.97	416.9	0.0047	26.9	123 → 127 H → L+3	$d_{yz} + \pi \rightarrow \pi^* + d_{xz}$
				24.4	123 → 126 H → L+2	$d_{yz} + \pi \rightarrow d_{xy}$ - n
				14.5	120 → 124 H-3 → L	$\pi_{Ph} + d_{yz} \rightarrow \pi^*$
				11.9	122 → 126 H-1 → L+2	$\pi_{Ph} + d_{xz} \rightarrow d_{xy}$ - n
				11.2	119 → 124 H-4 → L	$\pi_{Ph} + d_{xz} \rightarrow \pi^*$
S_8	3.01	412.0	0.0198	31.5	120 → 124 H-3 → L	$\pi_{Ph} + d_{yz} \rightarrow \pi^*$
				21.7	121 → 125 H-2 → L+1	$d_{xy} \rightarrow \sigma^*(d_z^2)$
				18.9	119 → 124 H-4 → L	$\pi_{Ph} + d_{xz} \rightarrow \pi^*$
S_9	3.03	408.5	0.0188	21.7	123 → 126 H → L+2	$d_{yz} + \pi \rightarrow d_{xy}$ - n
				20.9	120 → 124 H-3 → L	$\pi_{Ph} + d_{yz} \rightarrow \pi^*$
				18.8	123 → 127 H → L+3	$d_{yz} + \pi \rightarrow \pi^* + d_{xz}$
				12.5	120 → 125 H-3 → L+1	$\pi_{Ph} + d_{yz} \rightarrow \sigma^*(d_z^2)$
S_{10}	3.08	402.6	0.0019	77.0	118 → 124 H-5 → L	$\pi_{Ph} \rightarrow \pi^*$

Table A.3.6. The lowest ten vertical singlet states and the first adiabatic excited state for [Co^{III}(corrin)]-$PhEty^+$ (*base-off*) received from TD-DFT/TZVPP calculations with solvent COSMO/H_2O model.

	E [eV]	λ [nm]	*f*	%	Character	
S_1	1.64	756.9	0.0006	99.3	121 → 122 H→ L	$\pi_{PhEty}+ d_{yz} \rightarrow \sigma^*(d_z^2)$ - n
S_2	1.94	637.5	0.0017	93.0	121 → 123 H→ L+1	$\pi_{PhEty}+ d_{yz} \rightarrow \pi^*$
S_3	2.03	609.5	0.0022	96.3	120 → 122 H-1→ L	$\pi_{Ety}+ d_{yz} \rightarrow \sigma^*(d_z^2)$ - n
S_4	2.29	541.3	0.0021	74.9	120 → 123 H-1→ L+1	$\pi_{Ety}+ d_{yz} \rightarrow \pi^*$
				14.1	119 → 122 H-2→ L	$\pi_{Ety}+ \pi + d_{xz} \rightarrow \sigma^*(d_z^2)$ - n
S_5	2.32	535.4	0.0105	79.4	119 → 122 H-2→ L	$\pi_{Ety}+ \pi + d_{xz} \rightarrow \sigma^*(d_z^2)$ - n
				13.3	120 → 123 H-1→ L+1	$\pi_{Ety}+ d_{yz} \rightarrow \pi^*$
S_6	2.61	475.6	0.0005	92.2	121 → 124 H→ L+2	$\pi_{PhEty}+ d_{yz} \rightarrow d_{xy}$ -n
S_7	2.67	464.6	0.0053	53.7	118 → 122 H-3→ L	$\pi \rightarrow \sigma^*(d_z^2)$ - n
				36.7	119 → 123 H-2→ L+1	$\pi_{Ety}+ \pi + d_{xz} \rightarrow \pi^*$
S_8	2.76	449.7	0.0084	80.3	121 → 125 H→ L+3	$\pi_{PhEty}+ d_{yz} \rightarrow \pi + d_{xy}$
				10.0	119 → 123 H-2→ L+1	$\pi_{Ety}+ \pi + d_{xz} \rightarrow \pi^*$
S_9	2.85	435.5	0.0242	22.6	120 → 124 H-1→ L+2	$\pi_{Ety}+ d_{yz} \rightarrow d_{xy}$ -n
				19.0	118 → 122 H-3→ L	$\pi \rightarrow \sigma^*(d_z^2)$ - n
				17.4	119 → 123 H-2→ L+1	$\pi_{Ety}+ \pi + d_{xz} \rightarrow \pi^*$
				13.4	117 → 123 H-4→ L+1	$d_{x^2-y^2} \rightarrow \pi^*$
S_{10}	2.88	431.1	0.0000	100.0	116 → 122 H-5→ L	$\pi_{Ph} \rightarrow \sigma^*(d_z^2)$ - n

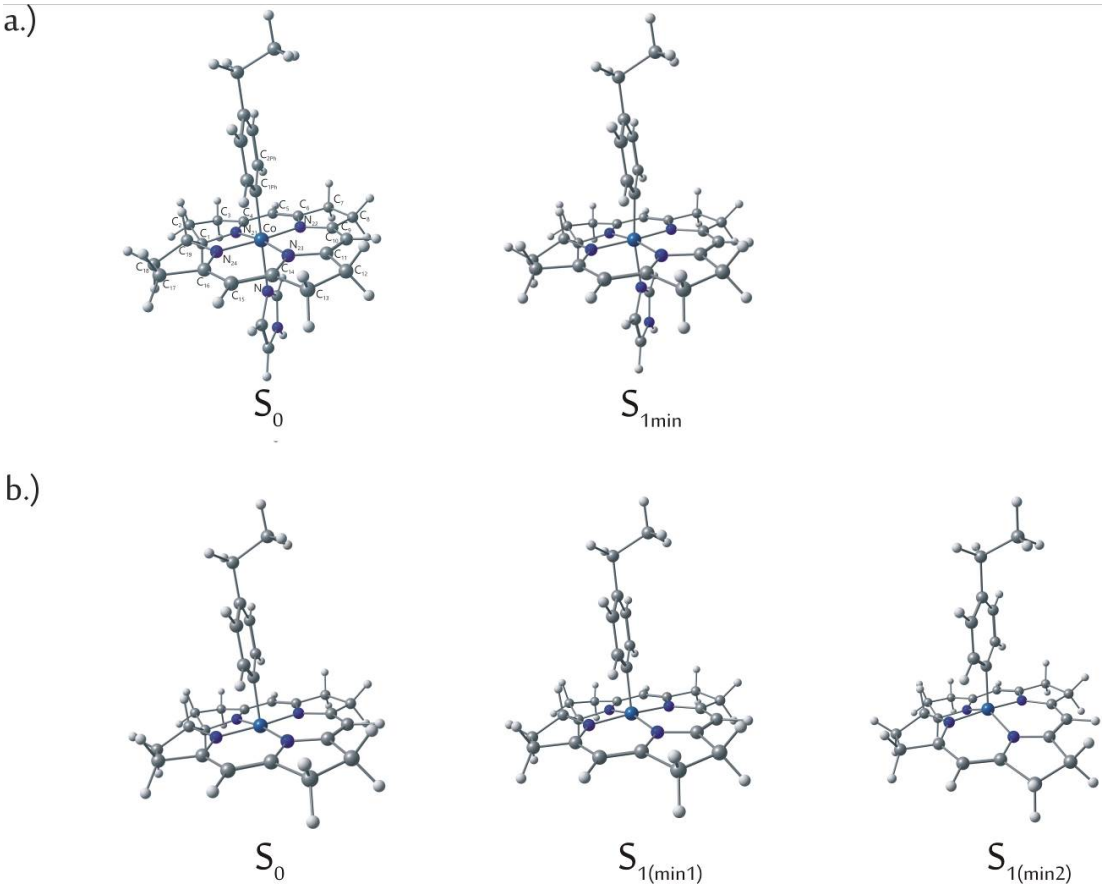

Figure A.3.1 The optimized geometry of model complexes in ground state S_0 and in excited state S_1, a) Im-[Co^{III}(corrin)]-$EtPh^+$ and b) [Co^{III}(corrin)]-$EtPh^+$.

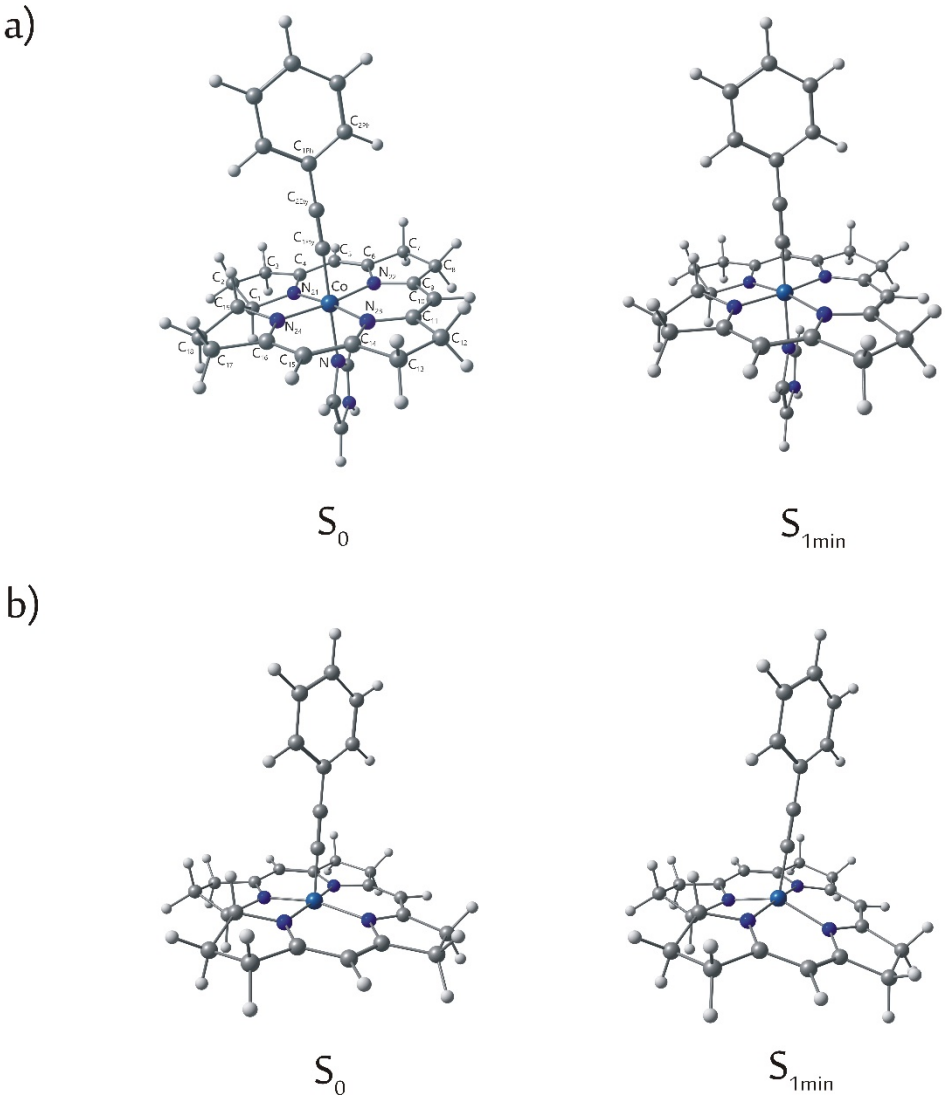

Figure A.3.2. The optimized geometry of model complexes in ground state S_0 and in excited state S_1, a) Im-[Co^{III}(corrin)]-$PhEty^+$ and b) [Co^{III}(corrin)]-$PhEty^+$.

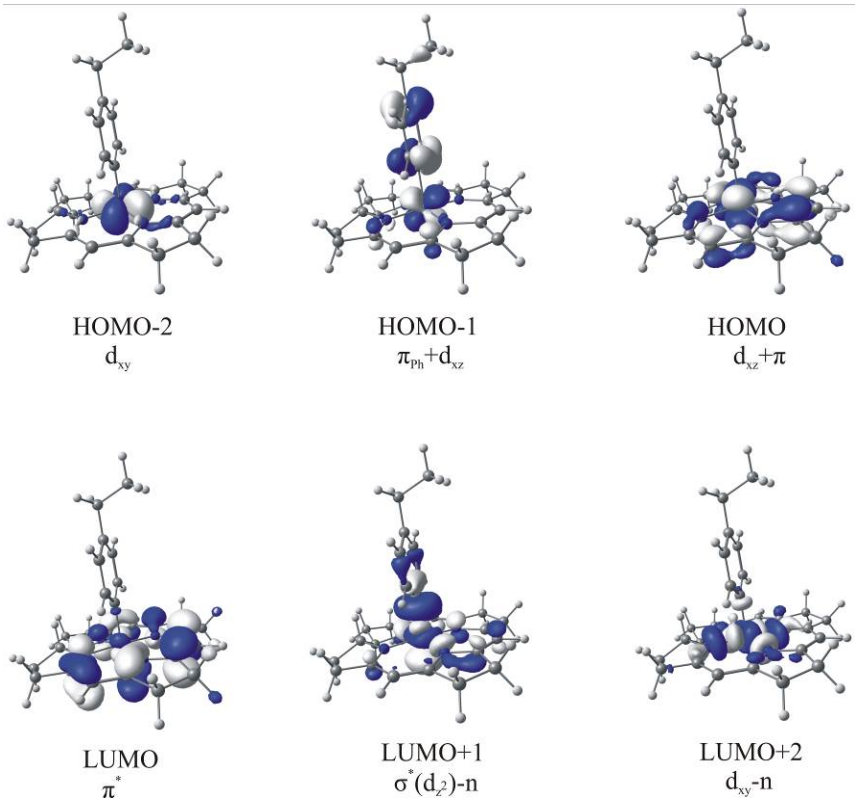

Figure A.3.3. Selected molecular orbitals involved in electronic excitations for $[Co^{III}(corrin)]$-$EtPh^+$ model complex.

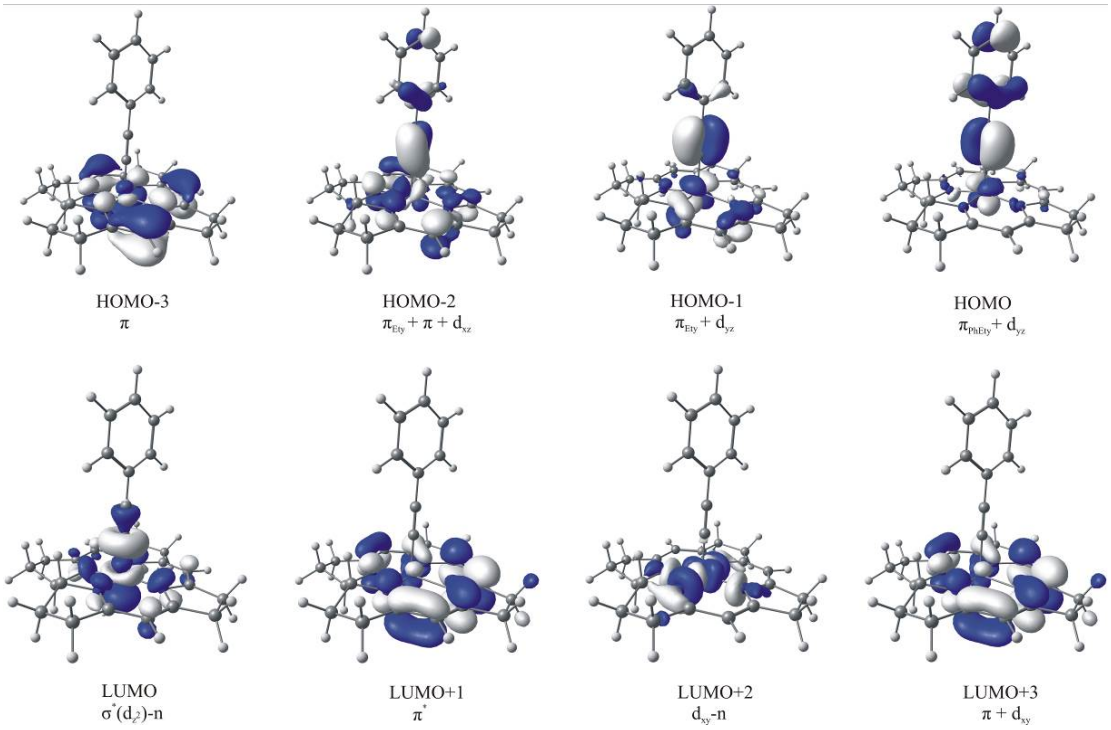

Figure A.3.4. Selected molecular orbitals involved in electronic excitations for $[Co^{III}(corrin)]$-$PhEty^+$ model complex.

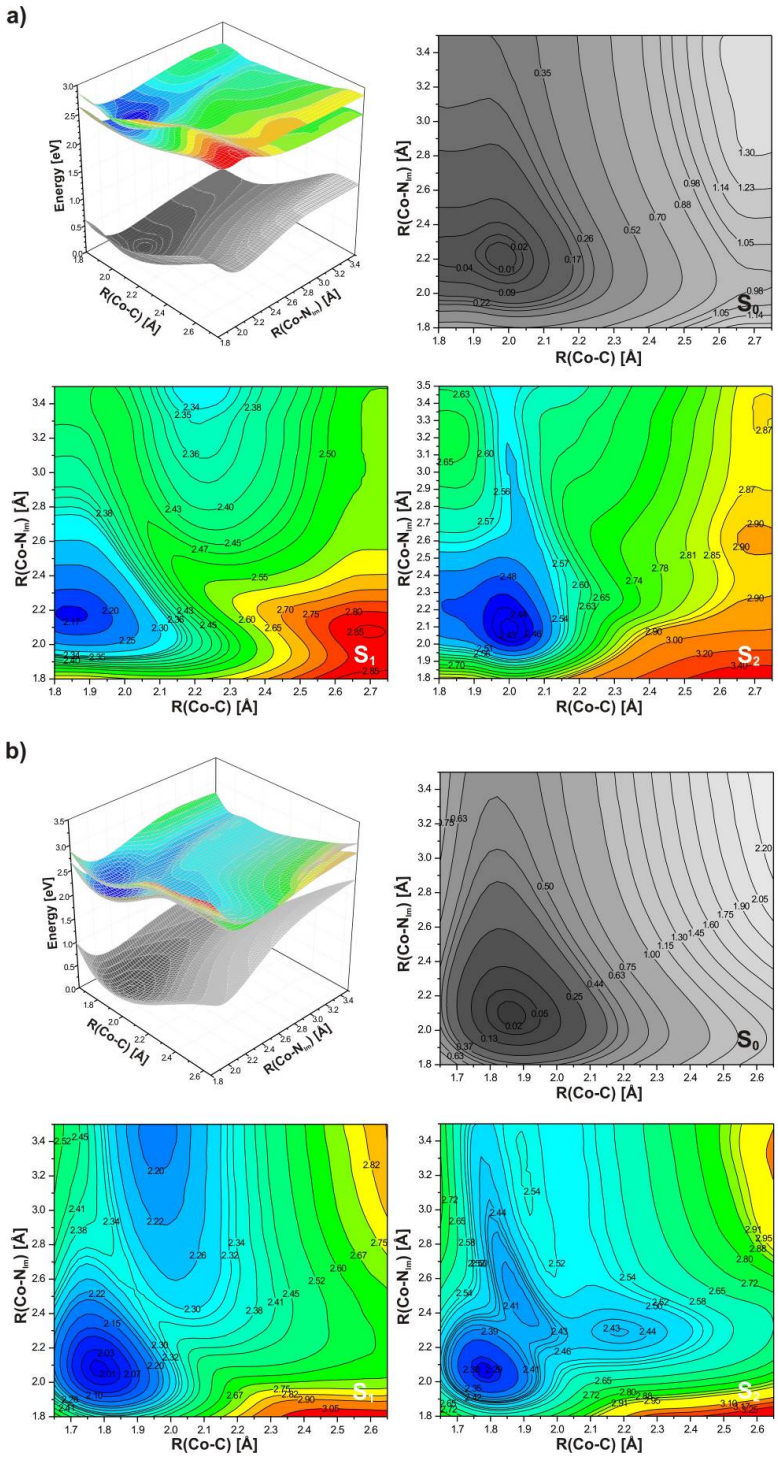

Figure A.3.5. Potential energy surfaces (PESs) for ground state and first excited state of a) Im-[Co^{III}(corrin)]-$EtPh^+$ and b) Im-[Co^{III}(corrin)]-$PhEty^+$ together with vertical projections of PES for S_0, S_1 and S_2 electronic state plotted as a function of axial bond lengths calculated in water solution (COSMO) with BP86/TZVPP. The vertical projections plots have separate color scales.

Appendix [Chapter 4]

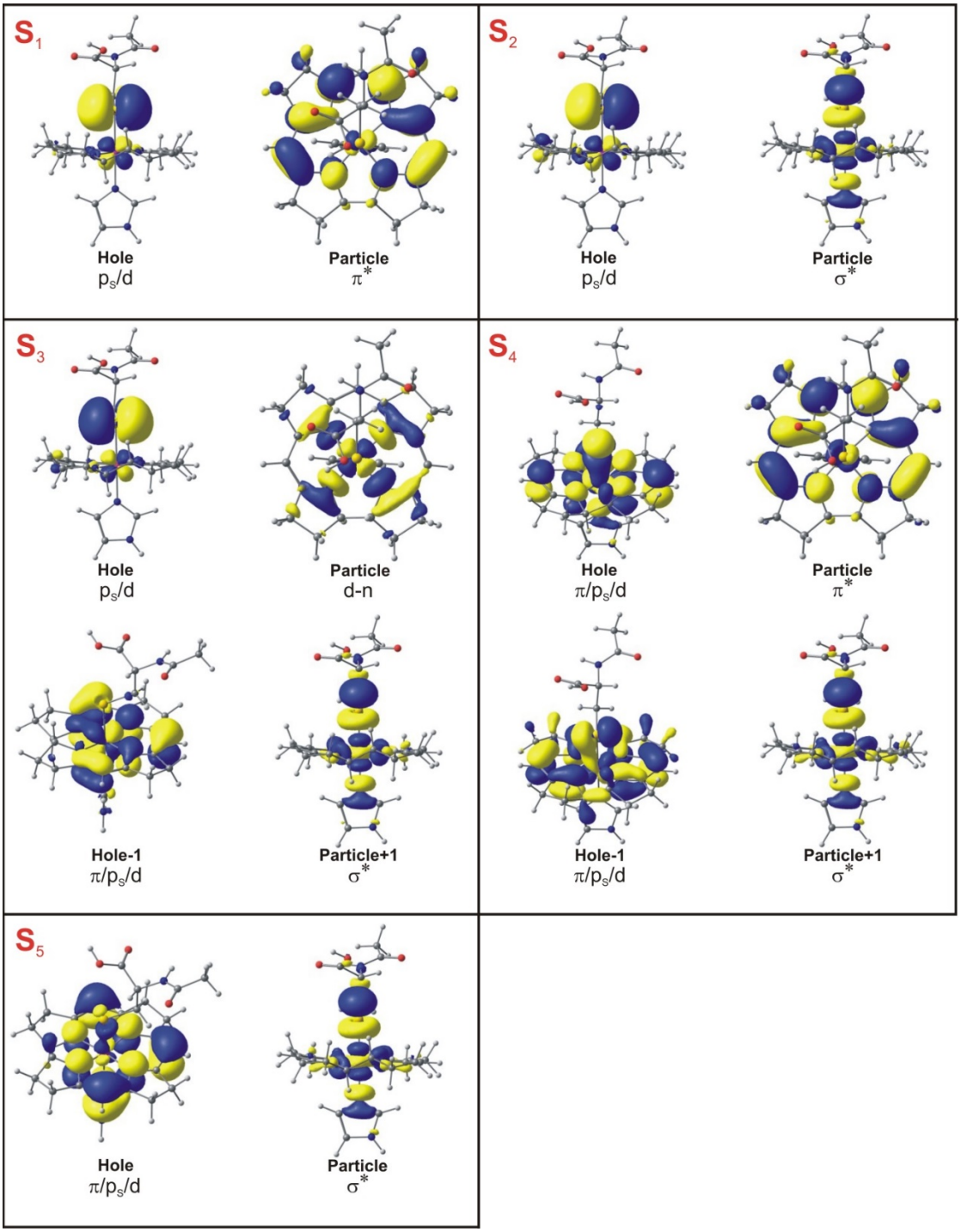

Figure A.4.1. Natural transition orbitals (NTO) describing singlet, lowest, excited electronic states S_1-S_5.

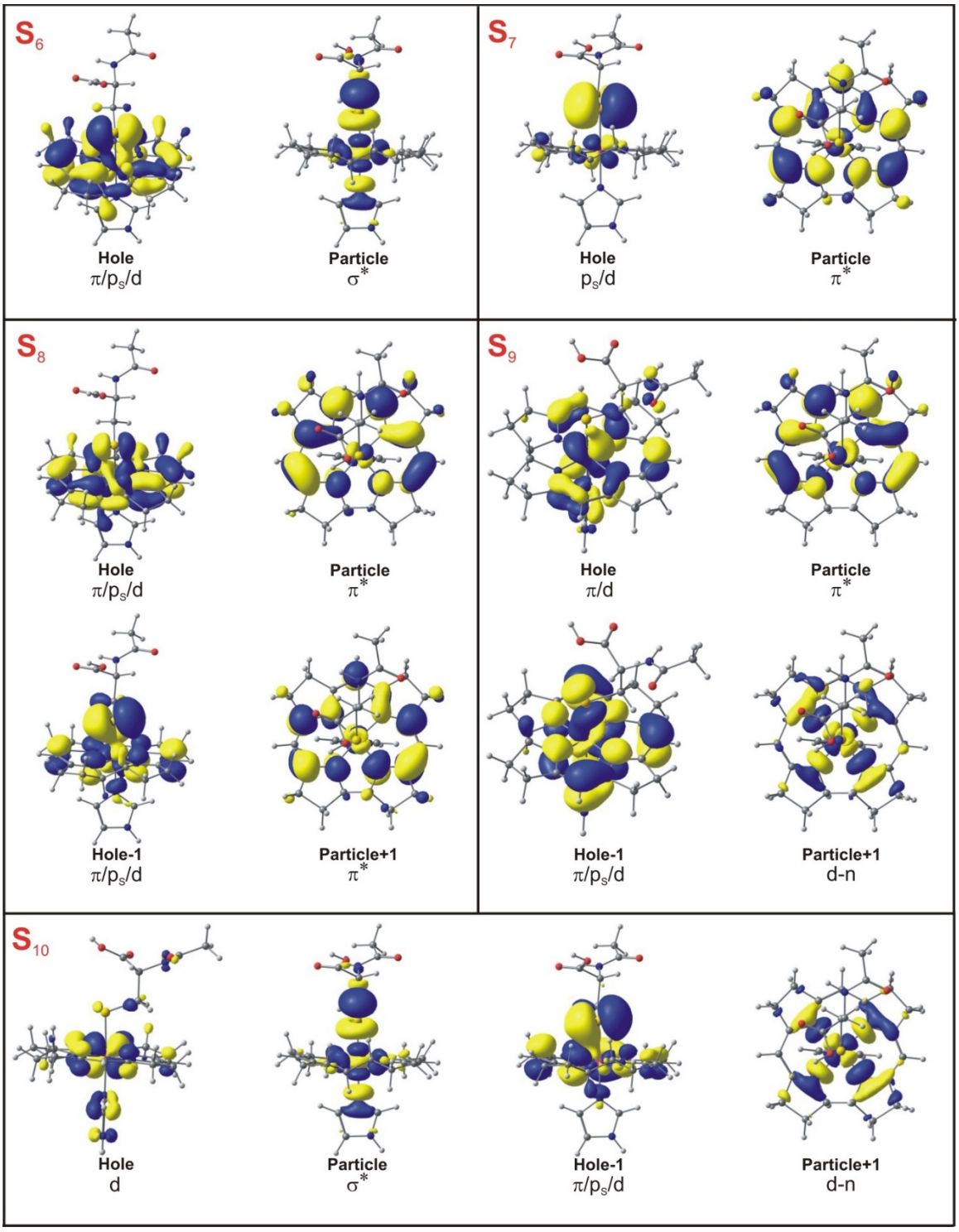

Figure A.4.2. Natural transition orbitals (NTO) describing singlet, lowest, excited electronic states S_6-S_{10}.

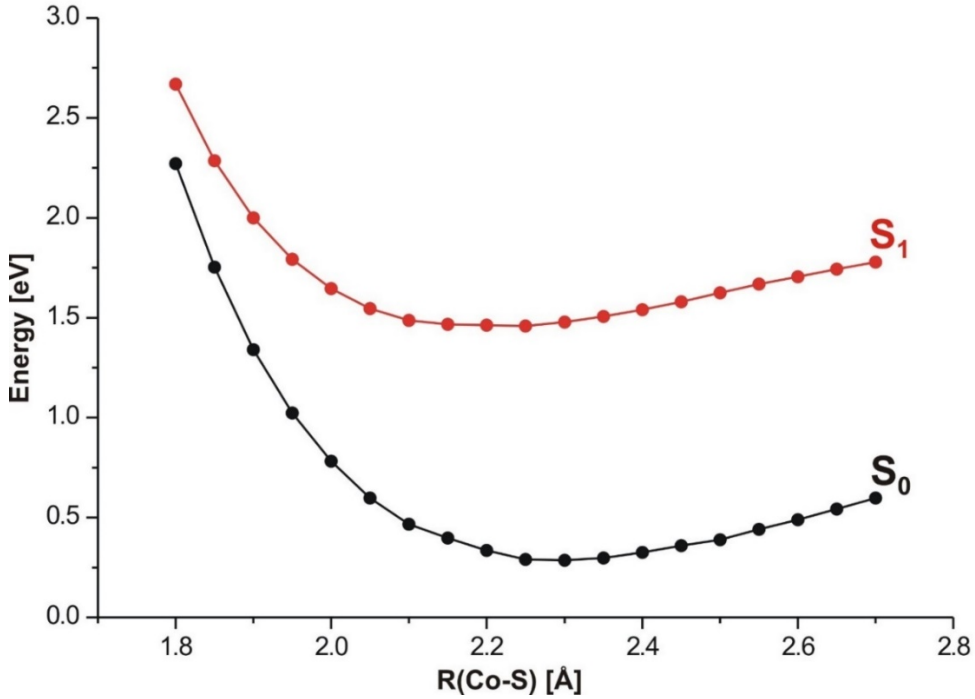

Figure A.4.3. Potential energy curves of the S_0 ground and S_1 excited states as function of Co-S axial bond length for optimized geometry S_1 state of Im-[Co^{III}(corrin)]-NAC^+ model complex.

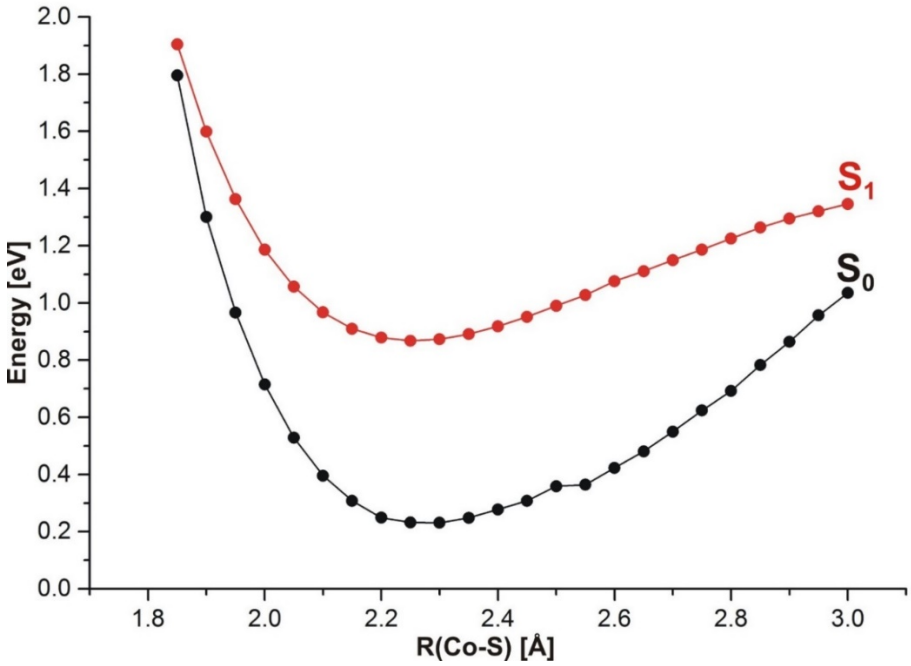

Figure A.4.4. Potential energy curves of the S_0 ground and S_1 excited states as function of Co-S axial bond length for optimized geometry S_1 state of $[Co^{III}(corrin)]$-NAC^+ model complex.

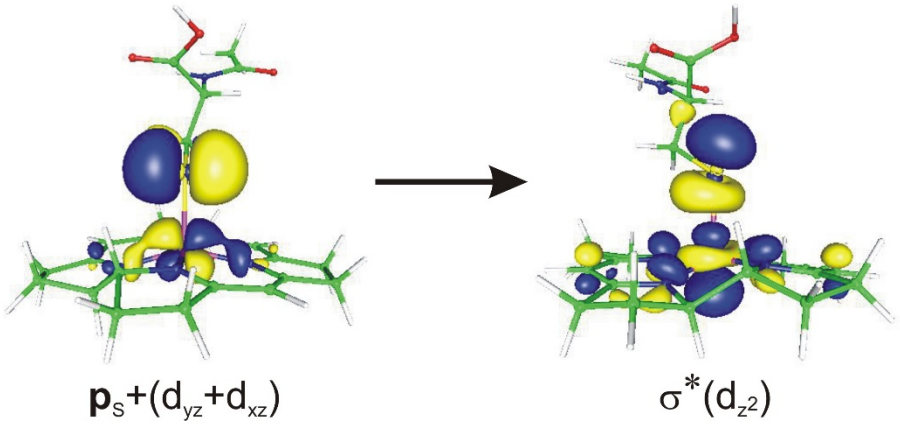

Figure A.4.5. Kohn-Sham orbitals involved in electronic excitation at minimum energy on S_1 PEC of $[Co^{III}(corrin)]$-NAC^+ model complex (Figure A.4.4).

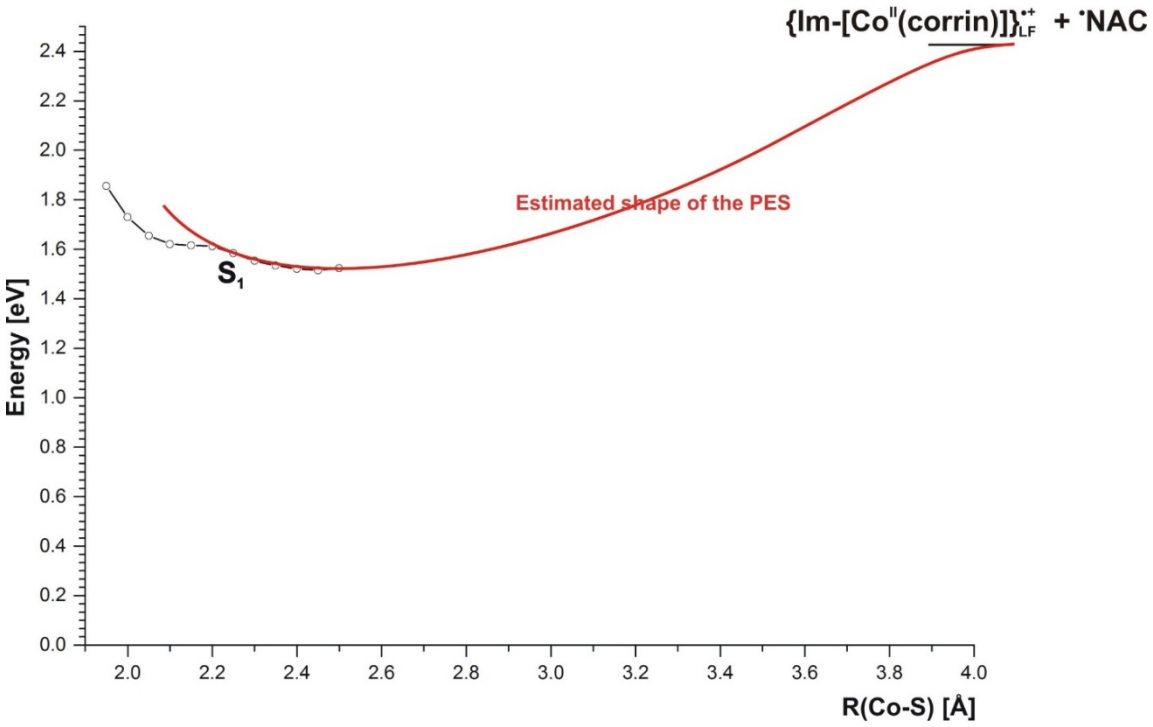

Figure A.4.6. The estimation of the PES beyond 2.5 Å based on a fragment of the S_1 PES along the Co-S bond for a constant Co-N_{Im} = 2.3 Å distance.

Table A.4.1. Forty-five, vertical singlet states for the Im-[Co^{III}(corrin)]-NAC^{+} model complex.

	E [eV]	λ [nm]	*f*	%	Character		Exp. λ[nm] (eV) [b)]
S_1	1.70	729.6	0.0012	95	H → L	$p_S + d_{yz} \rightarrow \pi^*$	615 sh
S_2	1.85	669.9	0.0002	96	H → L+1	$p_S + d_{yz} \rightarrow \sigma^*(d_z^2)$	(2.02)
S_3	2.30	538.1	0.0067	57	H → L+2	$p_S + d_{yz} \rightarrow d_{xz} - n$	
				26	H-1→ L+1	$\pi + (d_z^2/p_S) \rightarrow \sigma^*(d_z^2)$	
				12	H-1→ L	$\pi + (d_z^2/p_S) \rightarrow \pi^*$	
S_4	2.34	529.5	0.0180	43	H-1→ L	$\pi + (d_z^2/p_S) \rightarrow \pi^*$	561
				32	H → L+2	$p_S + d_{yz} \rightarrow d_{xz} - n$	(2.21)
				15	H-1→ L+1	$\pi + (d_z^2/p_S) \rightarrow \sigma^*(d_z^2)$	
S_5	2.38	521.4	0.0207	49	H-1→ L+1	$\pi + (d_z^2/p_S) \rightarrow \sigma^*(d_z^2)$	
				27	H-1→ L	$\pi + (d_z^2/p_S) \rightarrow \pi^*$	
S_6	2.47	502.3	0.0052	78	H-2 → L+1	$\pi + (d_{yz}/p_S) \rightarrow \sigma^*(d_z^2)$	
S_7	2.51	493.7	0.0004	97	H → L+3	$p_S + d_{yz} \rightarrow \pi^*$	
S_8	2.64	470.4	0.0216	69	H-2 → L	$\pi + (d_{yz}/p_S) \rightarrow \pi^*$	
				11	H-1→ L+3	$\pi + (d_z^2/p_S) \rightarrow \pi^*$	534
S_9	2.71	458.0	0.0233	69	H-3 → L	$d_{xz} \rightarrow \pi^*$	(2.32)
				20	H-1→ L+2	$\pi + (d_z^2/p_S) \rightarrow d_{xz} - n$	
S_{10}	2.77	446.9	0.0022	78	H-3 → L+1	$d_{xz} \rightarrow \sigma^*(d_z^2)$	
				10	H-2 → L+2	$\pi + (d_{yz}/p_S) \rightarrow d_{xz} - n$	
S_{11}	2.79	444.1	0.0139	67	H-1→ L+2	$\pi + (d_z^2/p_S) \rightarrow d_{xz} - n$	498
				16	H-3 → L	$d_{xz} \rightarrow \pi^*$	(2.49)
S_{12}	2.85	435.6	0.0039	91	H-4 → L	$d_x^2\text{-}_y^2 \rightarrow \pi^*$	
S_{13}	3.06	404.8	0.0006	82	H-2 → L+2	$\pi + (d_{yz}/p_S) \rightarrow d_{xz} - n$	
S_{14}	3.12	397.7	0.0003	100	H-5 → L	$p_{O(NAC)} \rightarrow \pi^*$	
S_{15}	3.18	390.3	0.0006	94	H-6 → L	$\pi_{Im} \rightarrow \pi^*$	433
S_{16}	3.18	389.8	0.0082	98	H → L+4	$p_S + d_{yz} \rightarrow \pi^*_{NAC}$	(2.86)
S_{17}	3.19	388.7	0.0005	93	H → L+5	$p_S + d_{yz} \rightarrow \pi^*$	
S_{18}	3.20	388.1	0.0019	96	H-5 → L+1	$p_{O(NAC)} \rightarrow \sigma^*(d_z^2)$	
S_{19}	3.25	381.2	0.0001	94	H-6 → L+1	$\pi_{Im} \rightarrow \sigma^*(d_z^2)$	
S_{20}	3.29	376.6	0.0398	51	H-1 → L+3	$\pi + (d_z^2/p_S) \rightarrow \pi^*$	
				12	H-4 → L+1	$d_x^2\text{-}_y^2 \rightarrow \sigma^*(d_z^2)$	
				12	H-8 → L	$(d_{yz}/p_S) + \pi \rightarrow \pi^*$	
S_{21}	3.32	373.2	0.0101	66	H-2 → L+3	$\pi + (d_{yz}/p_S) \rightarrow \pi^*$	
S_{22}	3.36	368.7	0.0277	40	H-4 → L+1	$d_x^2\text{-}_y^2 \rightarrow \sigma^*(d_z^2)$	
				23	H-7 → L	$\pi_{NAC} + \sigma(d_z^2) \rightarrow \pi^*$	
				15	H-1 → L+3	$\pi + (d_z^2/p_S) \rightarrow \pi^*$	372
S_{23}	3.38	367.2	0.0187	60	H-7 → L	$\pi_{NAC} + \sigma(d_z^2) \rightarrow \pi^*$	(3.33)
				12	H-2 → L+3	$\pi + (d_{yz}/p_S) \rightarrow \pi^*$	
				11	H-4 → L+1	$d_x^2\text{-}_y^2 \rightarrow \sigma^*(d_z^2)$	
S_{24}	3.46	358.4	0.0051	49	H-3 → L+2	$d_{xz} \rightarrow d_{xz} - n$	
				29	H-8 → L+1	$(d_{yz}/p_S) + \pi \rightarrow \sigma^*(d_z^2)$	
S_{25}	3.48	356.7	0.0028	83	H-4 → L+2	$d_x^2\text{-}_y^2 \rightarrow d_{xz} - n$	
S_{26}	3.49	355.4	0.0297	65	H-7 → L+1	$\pi_{NAC} + \sigma(d_z^2) \rightarrow \sigma^*(d_z^2)$	
				19	H-9 → L+1	$(d_z^2/p_S) + \pi \rightarrow \sigma^*(d_z^2)$	355
S_{27}	3.59	345.8	0.0050	63	H-9 → L	$(d_z^2/p_S) + \pi \rightarrow \pi^*$	(3.49)
				22	H-8 → L	$(d_{yz}/p_S) + \pi \rightarrow \pi^*$	

S_{28}	3.63	341.9	0.0004	95	H-1 → L+4	$\pi + (d_z^2/p_S) \rightarrow \pi^*_{NAC}$	
S_{29}	3.70	334.7	0.0013	88	H-4 → L+3	$d_x^2\text{-}_y^2 \rightarrow \pi^*$	
S_{30}	3.71	333.9	0.0030	51	H-5 → L+2	$p_{O(NAC)} \rightarrow d_{xz} - n$	
				15	H-8 → L+1	$(d_{yz}/p_S) + \pi \rightarrow \sigma^*(d_z^2)$	
S_{31}	3.72	333.2	0.0048	47	H-5 → L+2	$p_{O(NAC)} \rightarrow d_{xz} - n$	
S_{32}	3.73	332.2	0.0004	98	H → L+6	$p_S + d_{yz} \rightarrow \pi^*_{Im}$	
S_{33}	3.76	330.2	0.0137	26	H-6 → L+2	$\pi_{Im} \rightarrow d_{xz} - n$	333 (3.72)
				25	H-3 → L+3	$d_{xz} \rightarrow \pi^*$	
S_{34}	3.79	327.5	0.0023	45	H-1 → L+5	$\pi + (d_z^2/p_S) \rightarrow \pi^*$	
				33	H-10→ L	$\pi + d_{xz} \rightarrow \pi^*$	
S_{35}	3.80	326.0	0.0012	49	H-6 → L+2	$\pi_{Im} \rightarrow d_{xz} - n$	
				13	H-3 → L+2	$d_{xz} \rightarrow d_{xz} - n$	
S_{36}	3.82	324.2	0.0508	23	H-8 → L	$(d_{yz}/p_S) + \pi \rightarrow \pi^*$	
				16	H-9 → L	$(d_z^2/p_S) + \pi \rightarrow \pi^*$	
				14	H-3 → L+3	$d_{xz} \rightarrow \pi^*$	
S_{37}	3.84	322.5	0.0057	87	H-2 → L+4	$\pi + (d_{yz}/p_S) \rightarrow \pi^*_{NAC}$	
S_{38}	3.86	321.2	0.0034	68	H-10 → L+1	$\pi + d_{xz} \rightarrow \sigma^*(d_z^2)$	
S_{39}	3.96	313.1	0.0021	88	H-7 → L+2	$\pi_{NAC} + \sigma(d_z^2) \rightarrow d_{xz} - n$	
S_{40}	3.97	312.1	0.0034	72	H-11 → L	$p_{O(NAC)} \rightarrow \pi^*$	
				11	H-5 → L+3	$p_{O(NAC)} \rightarrow \pi^*$	
S_{41}	3.97	312.0	0.0011	87	H-5 → L+3	$p_{O(NAC)} \rightarrow \pi^*$	
				11	H-11→ L	$p_{O(NAC)} \rightarrow \pi^*$	
S_{42}	3.99	310.5	0.0005	99	H → L+7	$p_S + d_{yz} \rightarrow \pi^*_{NAC}$	
S_{43}	4.01	308.9	0.0113	57	H-2 → L+5	$\pi + (d_{yz}/p_S) \rightarrow \pi^*$	
				32	H-6 → L+3	$\pi_{Im} \rightarrow \pi^*$	
S_{44}	4.06	305.4	0.0121	59	H-6 → L+3	$\pi_{Im} \rightarrow \pi^*$	
				22	H-2 → L+5	$\pi + (d_{yz}/p_S) \rightarrow \pi^*$	
S_{45}	4.07	304.7	0.0018	89	H-11 → L+1	$p_{O(NAC)} \rightarrow \sigma^*(d_z^2)$	

[b] Experimentally observed peaks for Glutathionylco(III)balamin (GSCbl) from A. S. Eisenberg, I. V. Likhtina, V. S. Znamenskiy, R. L. Birke, Electronic Spectroscopy and Computational Studies of Glutathionylco(III)balamin, *J. Phys. Chem. A* 2012, 116, 6851−6869. dx.doi.org/10.1021/jp301294x

Appendix [Chapter 5]

Additional Computational Details Relevant to Chapter 5

For all of the reported QM/MM calculations, the model structures were first protonated with Propka 3.0 software and minimized using the AMBER force field in UCSF Chimera. The reported QM/MM calculations were performed using Gaussian 09. In the proceeding sections, information specific to the computational set-up of EAL and GLM, respectively, is explained. As a note, EAL was optimized using a three-layer model system. To improve computational efficiency over the initial EAL study, two-layers were used for the QM/MM calculations of GLM and CarH. Nevertheless, several details remain the same in the computational set-up and are summarized as follows. For each model structure, the high layer was treated with the BP86 functional with the TZVP basis set for H atoms and TZVPP for Co, C, N, and O atoms. The low layer was treated with the AMBER force field FF99SB. AMBER parameters for the AdoCbl cofactor were obtained from Marques *et al*, manuscript reference.[229] Mechanical embedding was used for the ONIOM calculation. Our previous studies have demonstrated that the use of mechanical embedding produces good agreement with the experiment. It was also noted by Morokuma and coworkers that the inclusion of electronic embedding has very negligible effect on the geometries of the system.[1] Considering this point and to maintain consistency with previous studies, electronic embedding was not included in this analysis of CarH.

Generation of EAL model complex *based on* Mamun, A. A., Toda, M.J., Lodowski, P., Jaworska, M., Kozlowski, P.M. *ACS Catal*., **2018**, *8*, 7164-7178.

The model structure for the AdoCbl-dependent EAL enzyme that was referred to in the main manuscript was generated from the crystal structure deposited in the Protein Data Bank (PDB ID 3ABS). The structure was crystallized at a resolution of 2.25 Å and contained two asymmetric units. The asymmetric units are identical, and the reactive parts, the cofactor and substrates, are independent to their respective subunits and do not interact. One asymmetric unit of EAL is

composed of α and β subunits with adeninylpentylcobalamin (AdePeCbl) instead of AdoCbl cofactor and ethanol amine (EA) as a substrate. The AdePeCbl binds in the base-on configuration where the lower axial ligand is DBI. The X-ray structure is available only for the substrate-bound AdoCbl-dependent EAL.

To generate the QM/MM input, only a single asymmetric unit was used in the calculations. The structure was protonated using PropKa 3.0 software, and the protonation states of the titratable residues were determined by manual inspection. The AdePeCbl was modified by adding a ribose moiety to the purine ring to restore the actual structure of AdoCbl cofactor. Substrate EA was removed from the structure, and two water molecules were added to fill the empty cavity. The substrate was removed in order to ensure that Co-C bond activation would be based on light and not substrate binding. The modified EAL structure was minimized with the MM level of theory using AMBER force field in UCSF Chimera.[227] The minimized structure was divided into three layers. The corrin ring, imidazole (Im) part of the DBI base with the side chain replaced by hydrogen, cobalt atom, and the Ado moiety were added to the high layer system. The remaining part of coenzyme B_{12} with the additional water molecules was placed into the middle layer, and the rest of the protein, including the crystal water, was placed into the low layer. Atoms within 20 Å from the Co center were kept unfrozen, and the rest of the protein was frozen. The model used in calculations contained a total of 11,988 atoms, with 3550 unfrozen and 8438 frozen.

The high layer was computed using DFT with BP86 functional. The middle layer of the system was computed using semi empirical (PM6) level of theory while the protein part of the system was treated with the AMBER force field (FF99SB). QM(DFT)/PM6/MM(AMBER) calculations were performed to optimize the structure of the EAL.

Generation of GLM model complex *based on* Mamun, A. A., Toda, M.J., Lodowski, P., Kozlowski, P.M. *J. Phys. Chem. B* **2019**, *123*, 2585−2598.

The crystal structure of AdoCbl-dependent GLM was obtained from the PDB (PDB ID: 1I9C) and contains two identical asymmetric units, which are independent and at a distance from each other. One asymmetric unit contains two subunits (α and β). Only one unit was used for the calculations. In the crystal structure, two conformations of the ribose ring of the upper axial ligand were reported and are denoted as 2′-endo and 3′-endo. The 2′-endo structure was used to model the photolytic reaction because this conformation was reported to be present prior to the hydrogen-atom abstraction step in the native reaction. The crystal structure also contained the substrate molecule (S)-glutamate. To represent photophysical processes, which do not require substrate binding to activate the Co-C bond, the substrate was removed. Six water molecules were used to occupy the cavity left by the removal of the substrate. The structure was then protonated using the PropKa program. The axially coordinated His16 residue was protonated at Nδ1 position. The model system was at the MM level of theory using the AMBER force field. The minimized structure was used to initiate the QM/MM calculations.

The GLM model system was partitioned into two layers. The truncated cofactor without the side chains of the corrin and the Im base from His16 were placed into the high layer. The rest of the atoms were placed into the low layer and included the remaining components of the cofactor, including the side chains of the corrin ring and the nucleotide loop, the protein residues, and the six water molecules. Consistent with the EAL calculations, atoms within 20 Å from the Co center were kept unfrozen, and the rest of the protein was frozen. The GLM model for QM/MM calculations contained a total of 10,981 atoms, with 3,542 unfrozen and 7,439 frozen.

Enzyme	PDB ID	Classification	Resolution	Non-water atom count in asymmetric subunit in crystal structure	QM/MM input atom count, including protonation
CarH	5C8E	Transcription regulator/DNA	3.89 Å	17,492	4,466
EAL	3ABS	Lyase	2.25 Å	11,060	11,988
GLM	1I9C	Isomerase	1.90 Å	10,032	10,981

Table A.5.1. Characteristics of the crystal structure and corresponding QM/MM model structures for CarH, EAL, and GLM.

Enzyme	PDB ID	Binding mode of cofactor	Lower axial ligand	Upper ligand of cofactor	Notes for cofactor in QM/MM input
CarH	5C8E	Base-off/His-on	His177 in crystal structure, HID in calculations	AdoCbl	AdoCbl intact from crystal structure
EAL	3ABS	Base-on	DBI Base of nucleotide loop	AdePeCbl	AdePeCbl modified by adding ribose moiety to purine ring to generate AdoCbl cofactor
GLM	1I9C	Base-off/His-on	His16 in crystal structure, HID in calculations	Mixture of 2′-endo and 3′-endo ribose conformation	2′-endo conformation selected

Table A.5.2. Summary of the cofactor from crystal structure and the corresponding QM/MM model structures for CarH, EAL, and GLM.

	Optimized Structure			Crystal Structure		
	CarH	EAL	GLM	CarH 5C8E	EAL 3ABS	GLM 1I9C
Bond Length (Å)						
$Co\text{-}C_{5'}$	2.00	2.05	2.08	2.03	2.01	3.17
$Co\text{-}N_{Im}$	2.28	2.37	2.27	2.25	2.61	2.22
$Co\text{-}N_{21}$	1.92	1.93	1.92	1.88	1.82	1.88
$Co\text{-}N_{22}$	1.93	1.96	1.94	1.92	1.85	2.02
$Co\text{-}N_{23}$	1.94	1.94	1.94	1.92	1.83	1.93
$Co\text{-}N_{24}$	1.89	1.91	1.90	1.89	1.83	1.90
Bond Angle (°)						
$C_{5'}\text{-}Co\text{-}N_{Im}$	174.8	171.5	163.8	166.7	177.1	170.5
$N_{21}\text{-}Co\text{-}C_{5'}$	82.6	92.3	101.9	94.5	89.4	90.8
$N_{22}\text{-}Co\text{-}C_{5'}$	87.8	94.7	88.3	88.9	90.4	80.4
$N_{23}\text{-}Co\text{-}C_{5'}$	97.7	93.1	81.8	86.6	95.1	82.5
$N_{24}\text{-}Co\text{-}C_{5'}$	89.9	84.4	92.0	83.7	84.7	92.4
Torsional Angle (°)						
$N_{21}\text{-}N_{22}\text{-}N_{23}\text{-}Co$	-0.1	-4.4	-2.5	-0.7	-3.2	5.3
$N_{21}\text{-}N_{22}\text{-}N_{23}\text{-}N_{24}$	-1.1	-3.3	-3.1	-6.1	-6.2	-0.1
$Co\text{-}N_{22}\text{-}C_{9}\text{-}C_{10}$	-11.9	-3.9	-10.2	-6.4	-11.5	-9.4
$Co\text{-}N_{22}\text{-}C_{6}\text{-}C_{5}$	-5.9	-1.0	3.3	-12.6	-2.1	8.7
$Co\text{-}N_{23}\text{-}C_{14}\text{-}C_{15}$	-2.4	-9.8	-3.4	-8.8	-19.0	-28.3

Table A.5.3. Geometric parameters for QM/MM optimized AdoCbl structure bound to CarH, EAL, and GLM. Corresponding values from the crystal structures are also included.

		Optimized Structure			Crystal Structure		
		CarH	EAL	GLM	CarH 5C8E	EAL 3ABS	GLM 1I9C
Exocyclic Angle (°)							
Φ_2	$C_{1'}$-$C_{2'}$-$O_{2'}$-$O_{2'}H$	88.11	-30.25	167.33	175.17	N/A	170.80
Φ_3	$C_{2'}$-$C_{3'}$-$O_{3'}$-$O_{3'}H$	1.00	9.11	-6.68	63.00	N/A	173.50
χ_{CN}	$O_{1'}$-$C_{1'}$-$N_{1'}$-$C_{5'}$	87.44	-72.46	-11.57	75.85	N/A	17.04
Endocyclic Angle (°)							
θ_0	$C_{1'}$-$C_{2'}$-$C_{3'}$-$C_{4'}$	30.49	9.87	1.64	15.85	N/A	-45.21
θ_1	$C_{2'}$-$C_{3'}$-$C_{4'}$-$O_{1'}$	-35.99	-35.86	-27.05	-33.99	N/A	29.28
θ_2	$C_{3'}$-$C_{4'}$-$O_{1'}$-$C_{1'}$	26.53	49.72	44.01	40.15	N/A	0.73
θ_3	$C_{4'}$-$O_{1'}$-$C_{1'}$-$C_{2'}$	-6.53	-43.30	-42.76	-29.91	N/A	-29.83
θ_4	$O_{1'}$-$C_{1'}$-$C_{2'}$-$C_{3'}$	-15.98	19.54	23.88	7.58	N/A	46.65
P	Pseudorotation Phase	-8.13	78.48	87.91	2.29	N/A	152.7
θ_m	Pseudorotation Amplitude	30.80	49.42	52.9	15.86	N/A	51.37
	Ribose Conformation	3′-endo	3′-endo	3′-endo	3′-endo	N/A	2′-endo

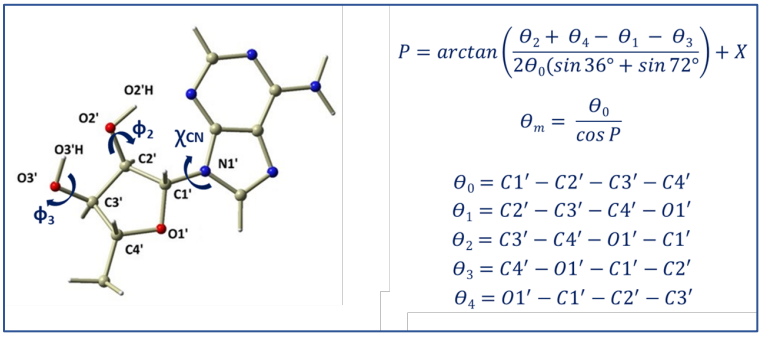

Table A.5.4. Geometric parameters related to ribose conformation of the Ado ligand for QM/MM optimized AdoCbl structure bound to CarH, EAL, and GLM. Corresponding values from the crystal structures are also included. Note: for EAL (3ABS) the cofactor is adeninylpentylcobalamin (AdePeCbl) instead of AdoCbl. AdePeCbl does not contain a ribose ring. Inset: Structure of Ado ligand with glycosyl rotation angle χ_{CN}=O1′-C1′-N1′-C5′, exocyclic ribose angle Φ_2=C1′-C2′-O2′-O2′H, and exocyclic ribose angle Φ_3=C2′-C3′-O3′-O3′H. **(b)** Definition of psuedorotation phase (P), pseudorotation amplitude (Θ_m) and endocyclic ribose angles ($\Theta_{0\text{-}4}$).[1] If $\Theta_0 > 0$ and $\Theta_2+\Theta_4-\Theta_1-\Theta_3 > 0$, X=0°. If $\Theta_0 > 0$ and $\Theta_2+\Theta_4-\Theta_1-\Theta_3 < 0$, then X=360°. If $\Theta_0 < 0$ then X =180°.

[1]Altona, C., Sundaralingam, M. Conformational Analysis of the Sugar Ring in Nucleosides and Nucleotides. A New Description using the Concept of Pseudorotation. *J. Am. Chem. Soc.* **1972,** *94*, 8205-8212.

Ligand Pocket of CarH		Ligand Pocket of GLM		Ligand Pocket of EAL	
Valine	V127	Arginine	R66	Arginine	R160
Glycine	G128	Alanine	A67	Glutamine	Q162
Valine	V138	Glycine	G68	Asparagine	N193
Glutamate	E141	Valine	V69	Leucine	L225
Histidine	H142	Asparagine	N123	Tyrosine	Y285
Aspartate	D201	Glycine	G124	Glutamate	E287
Proline	P203	Methionine	M294	Asparagine	N324
		Lysine	K326	Valine	V236
		Glutamate	E330	Phenylalanine	F329
		Isoleucine	I334	Aspartate	D362
		Proline	P335	Methionine	M392
		Asparagine	N340	Leucine	L402
				Tyrosine	Y404

Table A.5.5. Residues contained in the AdoCbl ligand pocket which are within hydrogen bonding distance and/or hydrophobic contact with the cofactor or other residues in the pocket. Selected residues based on crystal structure data obtainable from the PDB.

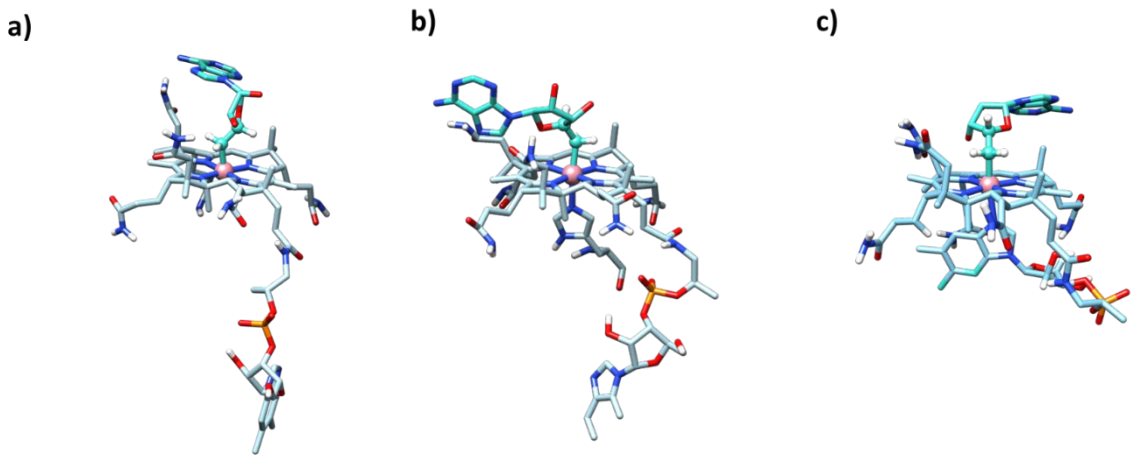

Figure A.5.1. Optimized molecular structures of AdoCbl bound to a) CarH, b) GLM, and c) EAL. For each panel, the orientation of the cofactor is based on the corrin macrocycle and the C-C bond of the corrin ring is in the foreground. Hydrogens of the cofactor computed via Propka software are not depicted for visualization purposes. The $C_{4'}$, $C_{4'}$-H, and $C_{5'}$ of the ribose moiety of the Ado ligand are depicted in the ball and stick format. The bonds of the corrin macrocycle are depicted in white. The bonds of the adenosyl (Ado) ligand are depicted in turquois.

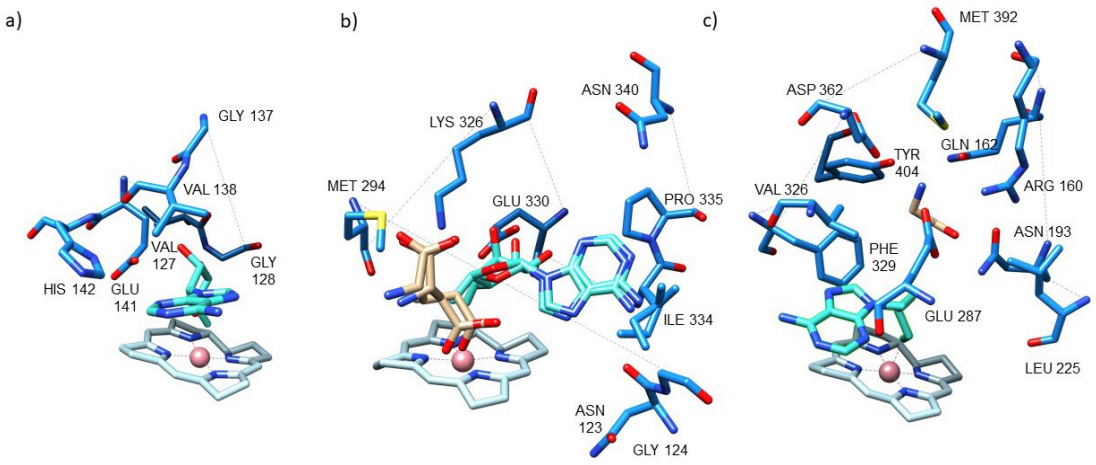

Figure A.5.2. Molecular structures contained in the ligand pocket of a) CarH (PDB ID: 5C8E), b) GLM (PDB ID: 1I9C), and c) EAL (PDB ID: 3ABS). Structures taken directly from crystallographic data, prior to any calculations, however the side chains, nucleotide loop, and lower axial ligands of the cofactors were removed simply for visualization purposes. Residues depicted are those within range of weak interactions with the cofactor via hydrogen bonding or hydrophobic contacts. The bonds of the corrin macrocycle are depicted in white. The bonds of the Ado ligand and the amino acid residues are depicted in turquois and blue, respectively. The bonds of substrate molecules are depicted in tan. In the GLM crystal structure (b), both the 2′-endo and 3′-endo conformations were reported and both are depicted here. The crystal structure also contained the corresponding two conformations of the substrate molecule (S)-glutamate. In the EAL crystal structure (c), the upper axial ligand is adeninylpentylcobalamin (AdePeCbl) instead of Ado and ethanolamine (EA) is the substrate molecule.

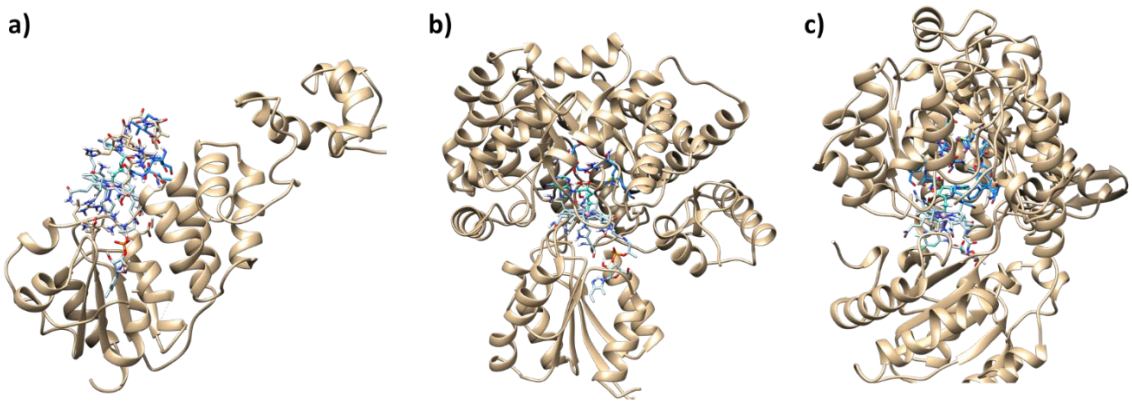

Figure A.5.3. Optimized model structures of a) CarH, b) GLM, and c) EAL. For each panel, the orientation of the cofactor is based on the corrin macrocycle and the short C-C bond of the corrin ring is in the foreground. Residues depicted are those in the ligand pocket, as designated by the PDB, within range of weak interactions with the cofactor via hydrogen bonding or hydrophobic contacts. Hydrogens of the cofactor computed via Propka software are not depicted for visualization purposes. The $C_{4'}$, $C_{4'}$-H, and $C_{5'}$ of the ribose moiety of the Ado ligand are depicted in the ball and stick format. The bonds of the corrin macrocycle are depicted in white. The bonds of the adenosyl (Ado) ligand and the amino acid residues are depicted in turquois and blue, respectively. Amino acid residues of the protein are depicted in tan. GLM and EAL do not contain substrate molecules.

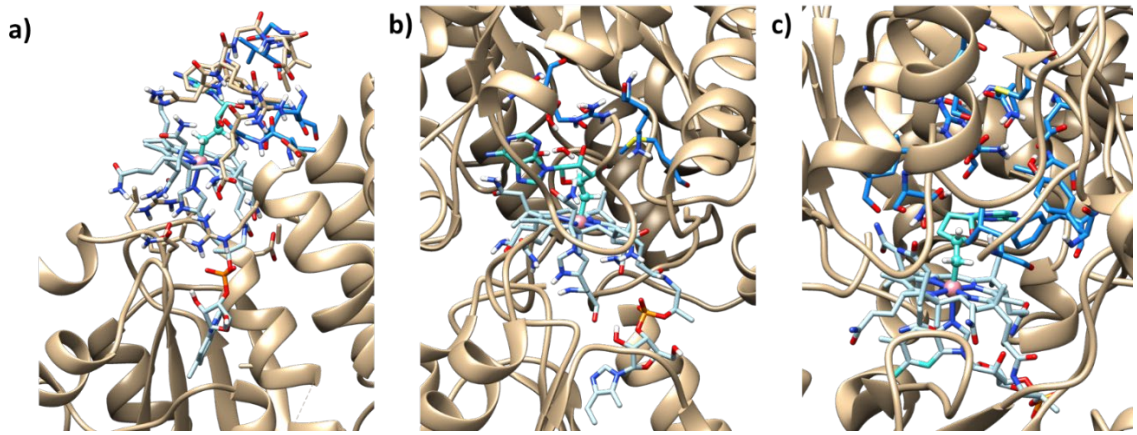

Figure A.5.4. Optimized molecular structures of a) CarH, b) GLM, and c) EAL. For each panel, the orientation of the cofactor is based on the corrin macrocycle and the short C-C bond of the corrin ring is in the foreground. Residues depicted are those in the ligand pocket, as designated by the PDB, within range of weak interactions with the cofactor via hydrogen bonding or hydrophobic contacts. Hydrogens of the cofactor computed via Propka software are not depicted for visualization purposes. The $C_{4'}$, $C_{4'}$-H, and $C_{5'}$ of the ribose moiety of the Ado ligand are depicted in the ball and stick format. The bonds of the corrin macrocycle are depicted in white. The bonds of the adenosyl (Ado) ligand and the amino acid residues are depicted in turquois and blue, respectively. Amino acid residues of the protein are depicted in tan. GLM and EAL do not contain substrate molecules.

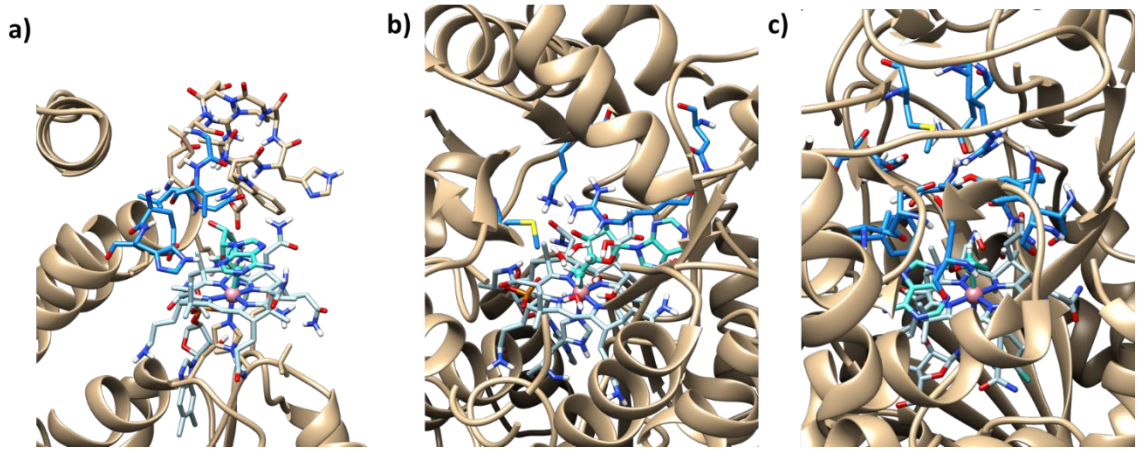

Figure A.5.5. Optimized molecular structures of a) CarH, b) GLM, and c) EAL. For each panel, the orientation of the cofactor is based on the corrin macrocycle and the short C-C bond of the corrin ring is in the background. Residues depicted are those in the ligand pocket, as designated by the PDB, within range of weak interactions with the cofactor via hydrogen bonding or hydrophobic contacts. Hydrogens of the cofactor computed via Propka software are not depicted for visualization purposes. The $C_{4'}$, $C_{4'}$-H, and $C_{5'}$ of the ribose moiety of the Ado ligand are depicted in the ball and stick format. The bonds of the corrin macrocycle are depicted in white. The bonds of the adenosyl (Ado) ligand and the amino acid residues are depicted in turquois and blue, respectively. Amino acid residues of the protein are depicted in tan. GLM and EAL do not contain substrate molecules but instead contain water molecules in their place.

Appendix [Chapter 6]

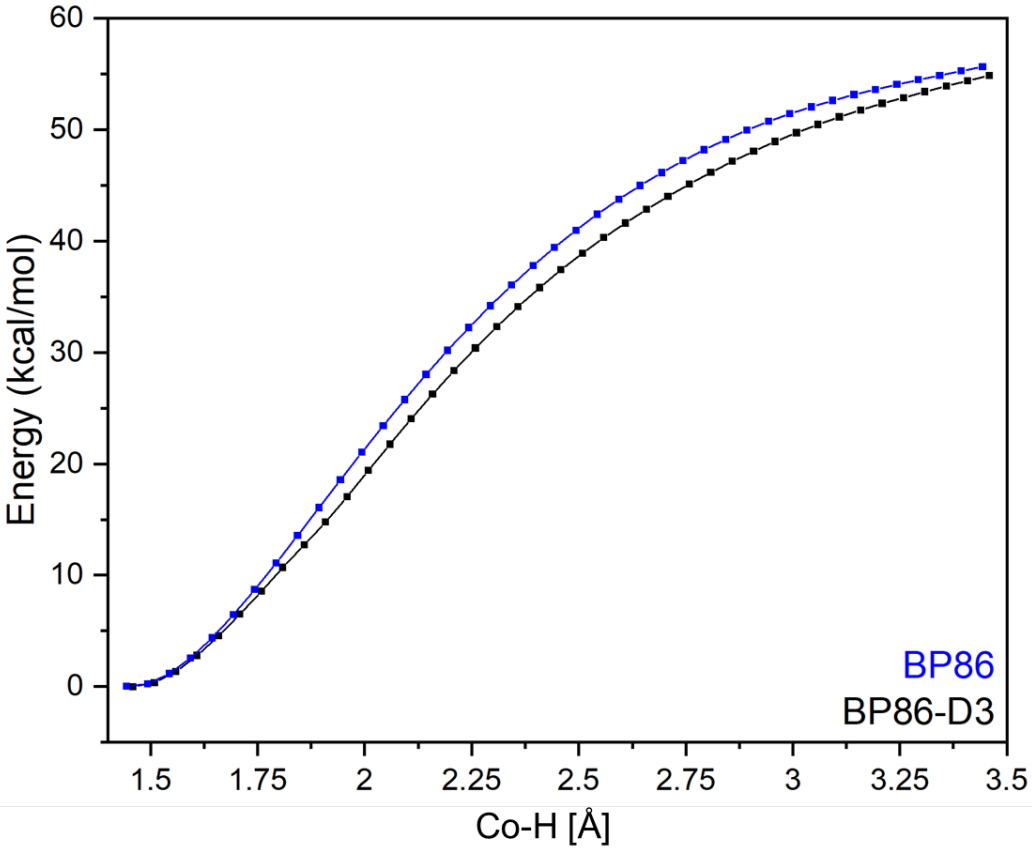

Figure A.6.1. Potential energy curves for singlet ground state of {Im-[Co(corrin)]-H}1,1, base-on HCbl model, to determine the bond dissociation energy (BDE). The blue curve was generated using the BP86 functional while the black curve was generated from the BP86 functional with D3 corrections.

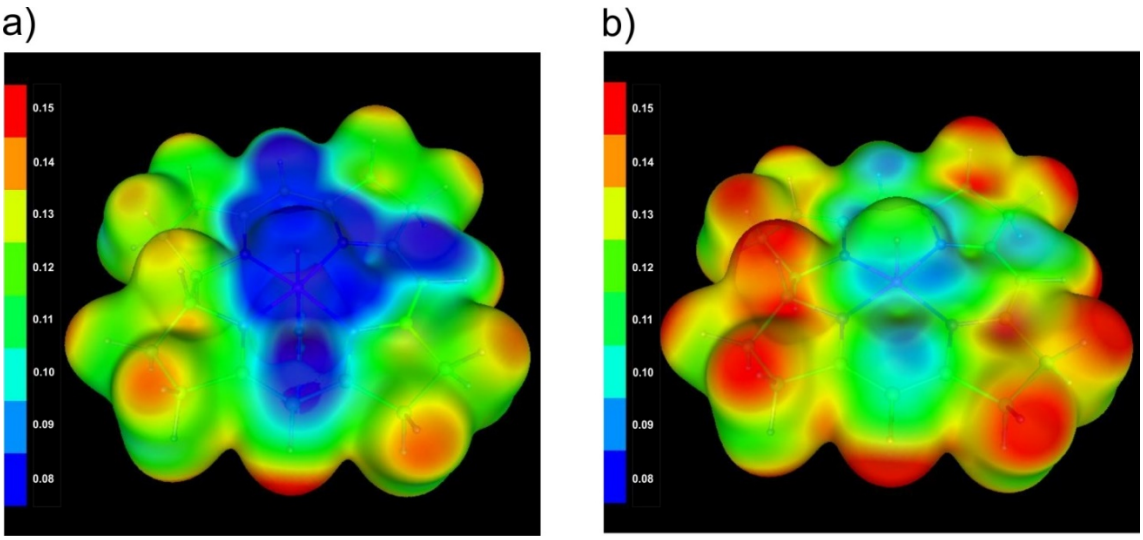

Figure A.6.2. Electrostatic potential in range from 0.08 to 0.15 a.u. mapped on isosurface of electronic density with value 0.005 a.u. for model complex a) {Im-[Co(corrin)]-H}^{1,1} and b) {[Co(corrin)]-H}^{1,1}.

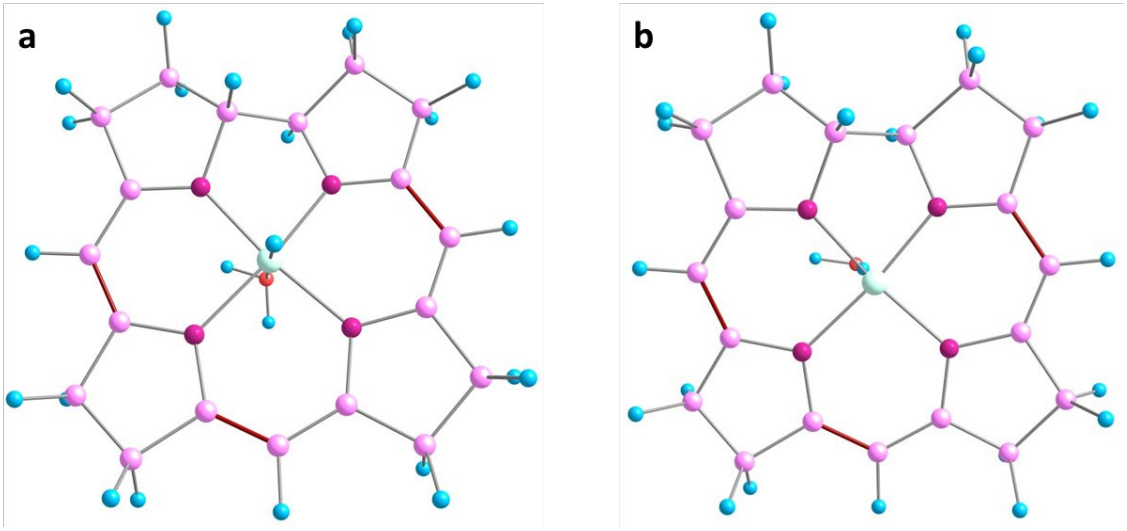

Figure A.6.3. Optimized structures of HCbl used for the *pK$_a$* calculation[a]. a) Structure of $\{H_2O\text{-}Co(corrin)\text{-}H\}^{1,1}$ optimized using BP86 and TZVP/P level of theory. b) Optimized structure of $\{H_2O\text{-}Co(corrin)\}^{0,1}$ using the same level of theory.

[a]The theoretical prediction of the pKa of the Co-H bond (aka the dissociation of the proton) corresponds to the following reaction;

$$\{H_2O\text{-}Co(corrin)\text{-}H\}^{1,1} \leftrightarrow \{H_2O\text{-}Co(corrin)\}^{0,1} + H^+$$

pK_a determined using the following equation,[1]

$$1.37\ \mathrm{pKa} = E_0\ [\mathrm{M\ (nonprotonated)}] - E_0\ [\mathrm{M\ (protonated)}] + E(H^+) + \Delta G_{solv}(H^+, 1\ \mathrm{atm}) - T\Delta S_{gas}(H^+) + \Delta ZPE + \frac{5}{2}RT$$

The solvation free energy of the proton [$\Delta G_{solv}(H^+,1atm)$] obtained from the literature is -262.11 kcal/mol[2] and the translational entropy contribution to the gas phase free energy of proton [$T\Delta S_{gas}$ (H^+)] was -7.76 kcal/mol.

1. F.G. Bordwell, J.P. Cheng, J.A. Harrelson, Homolytic Bond Dissociation Energies in Solution from Equilibrium Acidity and Electrochemical Data. *J. Am. Chem. Soc.* 110 (1988) 1229-1231.
2. T.S. Hofer, P. H. Hunenberger, Absolute proton hydration free energy, surface potential of water, and redox potential of the hydrogen electrode from first principles: QM/MM MD free-energy simulations of sodium and potassium hydration. *J. Chem. Phys.* 148 (2018) 222814.

Table A.6.1. The twenty lowest, vertical singlet electronic transitions and value of $S_1 \rightarrow S_0$ transition for {[Co(corrin)]-H}^{1,1} model complex based on the TD-DFT calculations.

	E(eV)	λ(nm)	*f*	%	Character		
S_1	2.44	507.9	0.0037	83	95 → 97	H → L+1	$d_{yz}+\pi \rightarrow \sigma^*(d_{z2})$-n
S_2	2.51	494.6	0.0362	80	95 → 96	H → L	$d_{yz}+\pi \rightarrow \pi^*$
S_3	2.60	476.4	0.0088	83	94 → 96	H-1 → L	$d_{xz}+\pi \rightarrow \pi^*$
S_4	2.69	460.5	0.0006	77	93 → 96	H-2 → L	$\pi+d_{x2-y2} \rightarrow \pi^*$
				18	92 → 96	H-3 → L	$\pi+d_{x2-y2} \rightarrow \pi^*$
S_5	2.87	432.6	0.0041	86	94 → 97	H-1 → L+1	$d_{xz}+\pi \rightarrow \sigma^*(d_{z2})$-n
S_6	3.07	404.3	0.0614	50	92 → 96	H-3 → L	$\pi+d_{x2-y2} \rightarrow \pi^*$
				23	95 → 98	H → L+2	$d_{yz}+\pi \rightarrow \pi^*+[d_{xy}$-n]
				11	93 → 96	H-2 → L	$\pi+d_{x2-y2} \rightarrow \pi^*$
S_7	3.11	398.0	0.0359	41	95 → 98	H → L+2	$d_{yz}+\pi \rightarrow \pi^*+[d_{xy}$-n]
				19	92 → 97	H-3 → L+1	$\pi+d_{x2-y2} \rightarrow \sigma^*(d_{z2})$-n
				12	93 → 97	H-2 → L+1	$\pi+d_{x2-y2} \rightarrow \sigma^*(d_{z2})$-n
S_8	3.16	392.9	0.0170	36	92 → 97	H-3 → L+1	$\pi+d_{x2-y2} \rightarrow \sigma^*(d_{z2})$-n
				27	93 → 97	H-2 → L+1	$\pi+d_{x2-y2} \rightarrow \sigma^*(d_{z2})$-n
				14	95 → 99	H → L+3	$d_{yz}+\pi \rightarrow [d_{xy}$-n]+$\pi^*$
S_9	3.17	390.5	0.0349	27	92 → 97	H-3 → L+1	$\pi+d_{x2-y2} \rightarrow \sigma^*(d_{z2})$-n
				23	95 → 98	H → L+2	$d_{yz}+\pi \rightarrow \pi^*+[d_{xy}$-n]
				21	93 → 97	H-2 → L+1	$\pi+d_{x2-y2} \rightarrow \sigma^*(d_{z2})$-n
S_{10}	3.30	375.6	0.0273	53	95 → 99	H → L+3	$d_{yz}+\pi \rightarrow [d_{xy}$-n]+$\pi^*$
				22	93 → 97	H-2 → L+1	$\pi+d_{x2-y2} \rightarrow \sigma^*(d_{z2})$-n
S_{11}	3.53	351.0	0.0007	46	91 → 96	H-4 → L	$\pi+d_{yz} \rightarrow \pi^*$
				28	93 → 98	H-2 → L+2	$\pi+d_{x2-y2} \rightarrow \pi^*+[d_{xy}$-n]
S_{12}	3.61	343.8	0.0017	69	93 → 99	H-2 → L+3	$\pi+d_{x2-y2} \rightarrow [d_{xy}$-n]+$\pi^*$
				11	92 → 99	H-3 → L+3	$\pi+d_{x2-y2} \rightarrow [d_{xy}$-n]+$\pi^*$
S_{13}	3.62	342.5	0.0024	25	91 → 97	H-4 → L+1	$\pi+d_{yz} \rightarrow \sigma^*(d_{z2})$-n
				18	93 → 98	H-2 → L+2	$\pi+d_{x2-y2} \rightarrow \pi^*+[d_{xy}$-n]
				16	93 → 99	H-2 → L+3	$\pi+d_{x2-y2} \rightarrow [d_{xy}$-n]+$\pi^*$
				16	92 → 98	H-3 → L+2	$\pi+d_{x2-y2} \rightarrow \pi^*+[d_{xy}$-n]
S_{14}	3.66	338.8	0.0039	50	92 → 99	H-3 → L+3	$\pi+d_{x2-y2} \rightarrow [d_{xy}$-n]+$\pi^*$
				25	92 → 98	H-3 → L+2	$\pi+d_{x2-y2} \rightarrow \pi^*+[d_{xy}$-n]
S_{15}	3.70	334.7	0.0064	19	93 → 98	H-2 → L+2	$\pi+d_{x2-y2} \rightarrow \pi^*+[d_{xy}$-n]
				17	95 → 100	H → L+4	$d_{yz}+\pi \rightarrow \pi^*$
				16	91 → 97	H-4 → L+1	$\pi+d_{yz} \rightarrow \sigma^*(d_{z2})$-n
				13	94 → 98	H-1 → L+2	$d_{xz}+\pi \rightarrow \pi^*+[d_{xy}$-n]
S_{16}	3.80	326.2	0.0106	71	95 → 100	H → L+4	$d_{yz}+\pi \rightarrow \pi^*$
S_{17}	3.87	320.3	0.0170	46	91 → 97	H-4 → L+1	$\pi+d_{yz} \rightarrow \sigma^*(d_{z2})$-n
				24	94 → 99	H-1 → L+3	$d_{xz}+\pi \rightarrow [d_{xy}$-n]+$\pi^*$

				19	94 → 98	H-1 → L+2	$d_{xz}+\pi \rightarrow \pi^*+[d_{xy}\text{-}n]$
S_{18}	3.97	312.6	0.0424	33	94 → 99	H-1 → L+3	$d_{xz}+\pi \rightarrow [d_{xy}\text{-}n]+\pi^*$
				24	94 → 98	H-1 → L+2	$d_{xz}+\pi \rightarrow \pi^*+[d_{xy}\text{-}n]$
				10	92 → 97	H-3 → L+1	$\pi+d_{x2\text{-}y2} \rightarrow \sigma^*(d_{z2})\text{-}n$
				10	92 → 99	H-3 → L+3	$\pi+d_{x2\text{-}y2} \rightarrow [d_{xy}\text{-}n]+\pi^*$
S_{19}	4.03	307.4	0.0934	23	90 → 97	H-5 → L+1	$\pi+d_{xz} \rightarrow \sigma^*(d_{z2})\text{-}n$
				16	92 → 98	H-3 → L+2	$\pi+d_{x2\text{-}y2} \rightarrow \pi^*+[d_{xy}\text{-}n]$
				15	90 → 96	H-5 → L	$\pi+d_{xz} \rightarrow \pi^*$
				14	91 → 96	H-4 → L	$\pi+d_{yz} \rightarrow \pi^*$
				11	92 → 99	H-3 → L+3	$\pi+d_{x2\text{-}y2} \rightarrow [d_{xy}\text{-}n]+\pi^*$
S_{20}	4.07	304.7	0.0267	51	90 → 96	H-5 → L	$\pi+d_{xz} \rightarrow \pi^*$
				12	94 → 100	H-1 → L+4	$d_{xz}+\pi \rightarrow \pi^*$
				11	92 → 100	H-3 → L+4	$\pi+d_{x2\text{-}y2} \rightarrow \pi^*$
S_1	1.74	710.6	0.0067	97	95 → 96	H → L	$d_{yz}+\pi \rightarrow \sigma^*(d_{z2})\text{-}n$ (LF)

Appendix [Chapter 7]

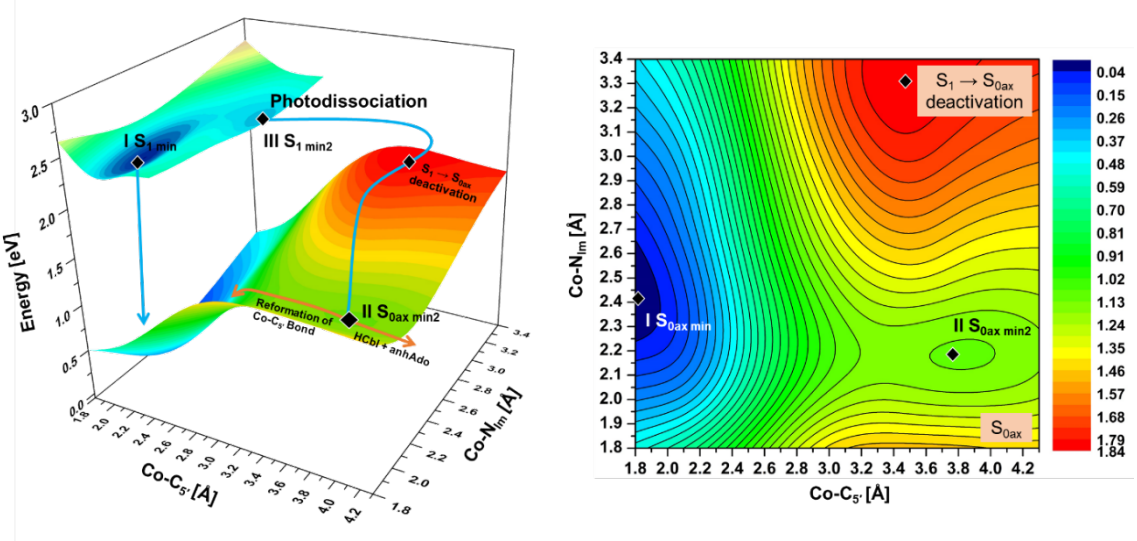

Figure A.7.1. Contour plot of S_{0ax} PES corresponding to Figure 7.3, energies are reported in eV.

ABBREVIATIONS

Abs	Absorption
Ado	5′-deoxy-5′-adenosyl
AdoCbl	Adenosylcoblamin AKA coenzyme B_{12}
anhAdo	4′,5′-anhydroadenosine
BDE	Bond dissociation energy
BS	Broken symmetry
BSSE	Basis set superposition error
CASPT2	Complete active space second-order perturbation theory
CASSCF	Complete active space self-consistent field
Cbls	Cobalamins
CC	Coupled cluster
CD	Circular dichroism
CFeSP	Corrinoid-iron/sulfur methyltransferase
CN	Cyano
CNCbl	Cyanocobalamin AKA vitamin B_{12}
Co	Cobalt
COSMO	Conductor-like screening model
CT	Charge transfer
CV	Cyclic voltammetry
CycCbl	Cysteinylcobalamin
DBI	dimethylbenzimidazole
DDH	Diol dehydratase
DFT	Density functional theory

DS	Dark state
EAL	Ethanolamine ammonia-lyase
ESP	Electrostatic potential
EOM-CCSD	Equation-of-motion coupled-cluster singles and doubles
EPR	Electron paramagnetic resonance spectroscopy
EtCbl	Ethylcobalamin
EtPh	4-ethylphenyl
EtPhCbl	4-ethylphenylcobalamin
GLM	Glutamate mutase
GS-	L-glutamyl-L-cysteinylglycine
GSCbl	Glutathionylcobalamin
GSH	Glutathione
HF	Hartree-Fock
H_2OCbl^+	Aquacobalamin
His	Histidine
HOCbl	Hydroxocobalamin
HCbl	Hydridocobalamin
IC	Internal conversion
Im	Imidazole
ISC	Intersystem crossing
KS MOs	Kohn-Sham molecular orbitals
LAM	5,6-aminomutase
LC-MS	Liquid chromatography-mass spectrometry
LF	Ligand field
LL	Ligand-to-ligand charge transfer
LRCT	Long-range charge-transfer
LS	Light state
MCD	Magnetic circular dichroism

MCM	Methylmalonyl-CoA mutase
Me	Methyl
MeCbl	Methylcobalamin
MECP	Minimum energy crossing point
MetH	Methionine Synthase
MFE	Magnetic field effect
MLCT	Metal-to-ligand charge transfer
MO	Molecular orbital
MtaBCA	methanol:CoM
NACCbl	N-acetylcysteinylcobalamin
NTO	Natural transition orbital
OH	Hydroxyl
PCM	Polarized continuum model
PhEty	2-phenylethynyl
PhEtyCbl	Phenylethynylcobalamin
PECs	Potential energy curves
PESs	Potential energy surfaces
PO_4^-	Phosphate ion
PrCbl	*n*-propylcobalamin
QM/MM	Quantum mechanics/molecular mechanics
QY or Φ	Quantum yield
RI	Resolution of Identity
RKS	Restricted Kohn-Sham
RP	Radical pair
SCbls	Thiolato-cobalamins
TAS	Transient absorption spectroscopy
TD-DFT	Time dependent-density functional theory
UKS	Unrestricted Kohn-Sham

XANES	X-ray absorption near edge structure
XMCQDPT2 theory	Extended second-order multiconfigurational quasi-degenerate perturbation
ZPE	Zero-point energy

CURRICULUM VITA

Megan J. Toda Mackintosh

Contact Information

Department of Chemistry
University of Louisville
Office 249, Chemistry Building
2320 S. Brook St., Louisville, KY, USA 40208

Phone: +1 (570) 903-8578
E-mail: mjtoda01@louisville.edu
megjtoda@gmail.com

Current Position

PhD Candidate (August 2016-*present*)
Department of Chemistry, University of Louisville
Thesis Advisor: Prof. Pawel M. Kozlowski
Thesis: *Computational Investigations of the Photochemical Properties of B_{12}-Dependent Systems: From Solution to Enzymes*
Methods: DFT, TD-DFT, QM/MM, AMBER
Software: Gaussian, Chemcraft, Chimera, Origin
Areas of Expertise: Molecular modeling, metalloenzymatic catalysis, photochemistry, B_{12}

Education

MS in Chemistry (May 2019)
University of Louisville, Louisville, KY

BS in Chemistry, *Magna Cum Laude* (December 2015)
Minor in Mathematics
Misericordia University, Dallas, PA

Research Experience

University of Louisville, *Louisville, Kentucky* (August 2016-*present*)
PhD Candidate, Theoretical Chemistry

Research Fellow, North Carolina State University, *Raleigh, NC* (Summer 2015)
National Science Foundation Research Experience for Undergraduates Program (REU)
Advisor: Dr. Felix N. Castellano

Undergraduate Researcher, Misericordia University (2013-2015)
Advisor: Dr. Anna Fedor

Awards

University of Louisville

School of Interdisciplinary and Graduate Studies Univ. Fellowship	(2016-2018)
Graduate Network in Arts and Sciences Travel Award, $250	(Fall 2018)
Graduate Student Council Travel Award, $350	(Fall 2018)
Graduate Student Council Travel Award, $350	(Spring 2018)

Misericordia University

Presidential Scholarship	(January 2012-December 2015)
Mission Award	(January 2012-December 2015)

Publications

17. **Toda, M. J.,** Lodowski, P., Mamun, A. A., Kozlowski, P. M. Electronic and Photolytic Properties of Hydridocobalamin. *J. Photochem. Photobio. B* **2021**, https://doi.org/10.1016/j.jphotobiol.2021.112295.

16. Ghosh, A. P., **Toda, M.J.,** Kozlowski, P.M. Photolytic Properties of B_{12}-Dependent Enzymes: A Theoretical Perspective. **In Book:** "Vitamin B_{12}" in series *Vitamins and Hormones.* **2021***,* Ed. Gerald Litwak*, in press.*

15. Ghosh, A. P., **Toda, M. J.,** Kozlowski, P.M. What Triggers the Cleavage of the Co-$C_{5'}$ Bond in Coenzyme B_{12}-Dependent Itaconyl-CoA Methylmalonyl-CoA Mutase? ***ACS Catal.*** **2021**, 11, 7943-7955.

14. **Toda, M. J.,** Lodowski, P., Thurman, T. M., Kozlowski, P. M. Light Mediated Properties of a Thiolato-derivative of Vitamin B_{12}. ***Inorg. Chem.*** **2020**, 59, 17200-17212.

13. **Toda, M. J.**, Mamun, A. A., Lodowski, P. Kozlowski, P. M. Why is CarH Photolytically Active in Comparison to other B_{12}-dependent Enzymes? ***J. Photochem. Photobiol. B: Biol.*** **2020**, 111919.

12. Cronin, S. P., Mamun, A. A., **Toda, M. J.**, Mashuta, M. S., Losovyj, Y., Kozlowski, P. M., Buchanan, R. M., Grapperhaus, C. A. Utilizing Charge Effects and Minimizing Intramolecular Proton Rearrangement to Improve the Overpotential of a Thiosemicarbazonato Zinc HER Catalyst. ***Inorg. Chem.*** **2019**, 58, 12986-12997.

11. Michocki, L. B.; M,iller, N. A.; Alonso-Mori, R.; Britz, A.; Deb, A.; Glownia, J. M.; Kaneshiro, A. K.; Konar, A.; Koralek, J.; Meadows, J. H.; Sofferman, D. L.; Song, S.; **Toda, M. J.**; van Driel, T. B.; Kozlowski, P. M.; Kubarych, K. J.; Penner-Hahn, J. E.; Sension, R. J. Probing the Excited State of Methylcobalamin Using Polarized Time-Resolved X-ray Absorption Spectroscopy. ***J. Phys. Chem. B*** **2019**, 123, 6042-6048.

10. Mamun, A. A., **Toda, M. J.**, Lodowski, P., Kozlowski, P. M. Photolytic Cleavage of Co-C Bond in Coenzyme B_{12}-Dependent Glutamate Mutase. ***J. Phys. Chem. B*** **2019**, 12, 2585-2598.

9. **Toda, M. J.**, Lodowski, P., Mamun, A. A., Jaworska, M., Kozlowski, P. M. Photolytic Properties of the Biologically Active Forms of Vitamin B_{12}. ***Coord. Chem. Rev.*** **2019**, 385, 20-43.

8. Mamun, A. A., **Toda, M. J.**, Kozlowski, P. M. Can Photolysis of the Co-C Bond in Coenzyme B_{12}-dependent Enzymes be used to Mimic the Native Reaction? ***J. Photochem. Photobio. B: Bio.*** **2019**, 191, 175-184.

7. **Toda, M. J.**, Kozlowski, P. M., Andruniow, T. Assessing Electronically Excited States of Cobalamins via Absorption Spectroscopy and Time-Dependent Density Functional Theory. **In book**: *Transition Metals in Coordination Environments: Computational Chemistry and Catalysis Viewpoints*. Springer. **2019**, Chapter 8, Pages 219-258. DOI: 10.1007/978-3-030-11714-6_8.

6. Wiley, T. E., Miller, N. A., Miller, W. R., Sofferman, D. L., Lodowski, P., **Toda, M. J.**, Jaworska, M., Kozlowski, P. M., and Sension, R. J. Off to the Races: Comparison of Excited State Dynamics in Vitamin B_{12} Derivatives Hydroxocobalamin and Aquocobalamin. ***J. Phys. Chem. A*** **2018**, 122, 6693-6703.

5. Lodowski, P., **Toda, M. J.**, Ciura, K., Jaworska, M., Kozlowski, P. M. Photolytic Properties of Antivitamins B_{12}. ***Inorg. Chem.*** **2018**, 57, 7838-7850.

4. Mamun, A. A., **Toda, M. J.** Lodowski, P., Jaworska, M., Kozlowski, P. M. Mechanism of Light Induced Radical Pair Formation in Coenzyme B_{12}-Dependent Ethanolamine Ammonia-Lyase. ***ACS Catalysis***. **2018**, 8, 7164-7178.

3. Miller, N. A., Deb, A., Alonso-Mori, R., Glownia, J. M., Kiefer, L. M., Konar, A., Michocki, L. B., Sikorski, M., Sofferman, D. L., Song, S., **Toda, M. J.**, Wiley, T. E., Zhu, D., Kozlowski, P. M., Kubarych, K. J., Penner-Hahn, J. E., Sension, R. J. Ultrafast X-ray Absorption Near Edge Structure Reveals Ballistic Excited State Structural Dynamics. ***J. Phys. Chem. A*** **2018**, 122, 4963-4971.

2. Lodowski, P., Ciura, K., **Toda, M. J.**, Jaworska, M., Kozlowski, P. M. Photodissociation of Ethylphenylcobalamin Antivitamin B_{12}. ***Phys. Chem. Chem. Phys.*** **2017**, 19, 30310-30315.

1. Fedor, A. M., **Toda, M. J.** Investigating Hydrogen Bonding in Phenol using Infrared Spectroscopy and Computational Chemistry. ***J. Chem. Ed.*** **2014**, 91, 2191-2194.

Presentations

7. **Toda, M. J.,** Mamun, A. A., Ghosh, A. P., Kozlowski, P.M. Comparison of the Photolytic Properties of B_{12}-dependent Enzymes. SERMACS, Augusta, GA. Physical Chemistry Division Poster Session. November **2018**.

6. **Toda, M. J.**, Lodowski, P., Ciura, K., Jaworska, M., Kozlowski, P. M. Photochemical Properties of Vitamin B_{12} Derivatives: Implications from TD-DFT Calculations. American Chemical Society National Meeting, New Orleans, LA. Computers in Chemistry Division Poster Session, **2018**.

5. **Toda, M. J.**, Lodowski, P., Ciura, K., Jaworska, M., Kozlowski, P. M. Photochemical Properties of Vitamin B_{12} Derivatives: Implications from TD-DFT Calculations. Graduate Student Regional Research Conference. University of Louisville, **2018**.

4. **Toda, M. J.**, McCusker, C., Castellano, F. N. Excited State Properties of Copper(I) *bis*-Phenanthroline Complexes. Council of Undergraduate Research's REU Symposium. NSF headquarters, Alexandria, VA, **2015**.
3. **Toda, M. J.**, McCusker, C., Castellano, F. N. Excited State Properties of Copper(I) *bis*-Phenanthroline Complexes. Undergraduate Research Symposium. North Carolina State University, Raleigh, North Carolina, **2015**.
2. Fedor, A. M. and **Toda, M. J.** Examining the Intermolecular Interactions of Ionic Liquids and Phenol Derivatives using Far-Infrared Spectroscopy and Computational Chemistry. American Chemical Society National Meeting, Boston, MA, **2015**.
1. **Toda, M. J.** and Fedor, A. M. Analysis of the Intermolecular Hydrogen Bonding Interactions of Phenol Derivatives in Solution using Infrared Spectroscopy and Density Functional Theory. American Chemical Society National Meeting, Boston, MA, **2015**.

Teaching Experience

Graduate Teaching Assistant (2018-present)
Department of Chemistry, University of Louisville
CHM 202, General Chemistry II – Recitation (Summer 2020)
CHM 207, Head TA, Intro to Chemistry Analysis I – Laboratory (Spring 2019)
CHM 207, Intro to Chemical Analysis I – Laboratory (Fall 2018, Spring 2019, Fall 2020)
CHM 208, Intro to Chemical Analysis II – Laboratory (Spring 2020, Fall 2020)
CHM 441, Elements of Physical Chemistry – Recitation (Fall 2020)
CHM 465, Physical Chemical I, Quantum Mechanics – Recitation (Fall 2018)

Research Mentor for Undergraduate Student (Spring 2017)
Department of Chemistry, University of Louisville

Professional Associations

- Member of the American Chemical Society (ACS) (2015-present)
- Member of the Kentucky Academy of Sciences (KAS) (2018-present)

Academic Leadership and Community Service

President, Chemistry Graduate Student Association (August 2018-August 2020)
University of Louisville

- Planned events for graduate students - welcome picnic for new graduate students, career information panel with University of Louisville Chemistry PhD program alumni, and Derby Lecture Series
- Organized **41st Annual Derby Lecture Series** (May 2 and 3 2019) featuring the **2016 Nobel Laureate, Sir J. Fraser Stoddart**
- Organized **42nd Annual Derby Lecture Series** (sadly postponed due to COVID-19) featuring the **2019 Nobel Laureate, M. Stanly Whittingham**
- Oversaw fundraising efforts and acquired university and corporate funding

- Led campus tours for prospective graduate students

Judge, Kentucky Junior Academy of Science, Oral Presentations (April 2018)
Tutor, Boys and Girls Haven, Louisville, KY (January 2017-December 2017)